ISSN 0911-5730
UVSOR-36
June 2009

UVSOR ACTIVITY REPORT 2008

UVSOR Facility
Institute for Molecular Science
National Institutes of Natural Sciences

Preface

This Activity Report covers the research activities carried out at the UVSOR facility in FY2008 (April 2008-March 2009). This is the sixth volume in the new series for the third decade of UVSOR, corresponding to the sixth year of the use of the low-emittance UVSOR-II storage ring. The UVSOR-II ring has been very stable in operation at the initial beam current of 350 mA for every 6-hour 0.75-GeV full-energy injection and the beam emittance of 27 nm-rad. Since last fall, the UVSOR-II has been in operation in the Top-up mode during every Thursday's night to Friday's morning. Most beamlines have been adapted to the Top-up mode. We hope all the other beamlines will be also adapted to the Top-up mode soon and the Top-up mode will be default.

The UVSOR facility is exclusively responsible for the high-brilliant VUV light source as a low-energy third generation ring. There are four 4 m-long long straight sections and four 1.5 m-long short straight sections in the present UVSOR-II ring of 53 m in circumference. We already installed three long undulators at BL3U, BL5U and BL7U and one short undulator at BL6U. We have now started design of the fifth undulator beamline BL1U with a long straight section. The BL1U will be dedicated to produce the coherent synchrotron radiation. This new research project is fully approved by the Ministry of Education, Culture, Sports, Science and Technology (MEXT) under the Quantum Beam Technology Program. Before starting the construction of BL1U, we have to move and upgrade the present BL1A and BL1B at vacant dipole ports in 2010-2011.

In UVSOR, we have four research positions for accelerator physics (1 full prof., 1 assoc. prof., and 2 assist. profs.) and four research positions for photophysics and photochemistry (2 assoc. profs. and 2 assist. profs.). In the accelerator physics division, there were two vacancies for 1 associate and 1 assistant professors. Fortunately, this April Dr. Heishun Zen has joined the accelerator division as assistant professor from Kyoto University. On the other hand, in the photophysics division, Assist. Prof. Dr. Takahiro Ito has been promoted as associate professor of Nagoya University this April.

We look forward to more exciting achievements in the coming years of UVSOR-II.

April, 2009

Nobuhiro Kosugi
Director of UVSOR

UVSOR Organization

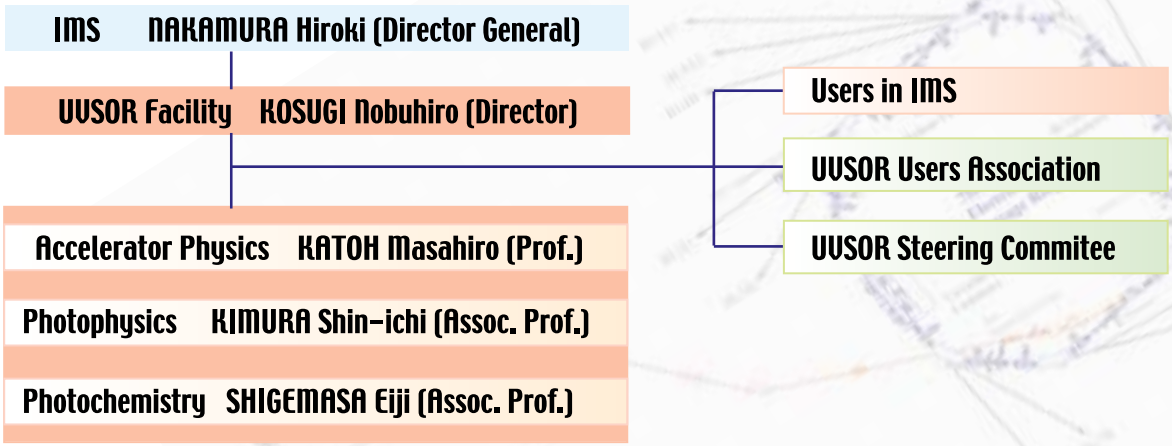

UVSOR Staff

Director

KOSUGI, Nobuhiro	Professor	kosugi@ims.ac.jp	

Light Source Division (Accelerator Physics)

KATOH, Masahiro	Professor	mkatoh@ims.ac.jp	
ADACHI, Masahiro	Assistant Professor	adachi@ims.ac.jp	
ZEN, Heishun	Assistant Professor	zen@ims.ac.jp	(since Apr. 2009)
YAMAZAKI, Jun-ichiro	Unit Chief Engineer	yamazaki@ims.ac.jp	
HAYASHI, Kenji	Engineer	h-kenji@ims.ac.jp	
TOKUSHI, Tetsuzyo	Supporting Engineer	tetsuzyo@ims.ac.jp	

Beamline Division (Photophysics)

KIMURA, Shin-ichi	Associate Professor	kimura@ims.ac.jp	
ITO, Takahiro	Assistant Professor		(until Mar. 2009)
HASUMOTO, Masami	Unit Chief Engineer	hasumoto@ims.ac.jp	
SAKAI, Masahiro	Engineer	sakai@ims.ac.jp	
TERASHIMA, Kensei	JSPS Fellow (PD)		(until Mar. 2009)
IM, Hojun	Guest Researcher		(until Nov. 2008)
TSUNEKAWA, Masanori	Guest Researcher		(until Mar. 2009)
MIYAZAKI, Hidetoshi	IMS Fellow (PD)	hmiyazak@ims.ac.jp	(since Apr. 2009)
NISHI, Tatsuhiko	Guest Researcher	tnishi@ims.ac.jp	(since Apr. 2009)

Beamline Division (Photochemistry)

SHIGEMASA, Eiji	Associate Professor	sigemasa@ims.ac.jp	
HIKOSAKA, Yasumasa	Assistant Professor	hikosaka@ims.ac.jp	
HORIGOME, Toshio	Facility Chief Engineer	horigome@ims.ac.jp	
NAKAMURA, Eiken	Unit Chief Engineer	eiken@ims.ac.jp	
KONDO, Naonori	Engineer	nkondo@ims.ac.jp	
AMEMIYA, Kenta	Adjunct Associate Professor		

Secretary

HAGIWARA, Hisayo		hagiwara@ims.ac.jp	
MASUDA, Michiko		masuda@ims.ac.jp	(since July. 2008)

UVSOR Steering Committee

KOSUGI, Nobuhiro	UVSOR, IMS	Chair
KATOH, Masahiro	UVSOR, IMS	
KIMURA, Shin-ichi	UVSOR, IMS	
SHIGEMASA, Eiji	UVSOR, IMS	
AMEMIYA, Kenta	KEK-PF(Adj. Assoc. Prof., IMS)	
YOKOYAMA, Toshihiko	IMS	
OHMORI, Kenji	IMS	
NAKAMURA, Toshikazu	IMS	
MITSUKE, Koichiro	IMS	
TAKATA, Masaki	RIKEN/SPring-8	
NAMATAME, Hirofumi	Hiroshima Univ.	
HONMA, Kenji	Univ. of Hyogo	
HINO, Shojun	Ehime Univ.	
MATSUDA, Iwao	Univ. of Tokyo	
FUKUI, Kazutoshi	Fukui Univ.	
YOSHIDA, Tomoko	Nagoya Univ.	

UVSOR Users Association

FUKUI, Kazutoshi	Fukui Univ.	Chair
HINO, Shojun	Ehime Univ.	
GEJO, Tatsuo	Univ. of Hyogo	
NAKAGAWA, Kazumichi	Kobe Univ.	
YOSHIDA, Tomoko	Nagoya Univ.	

Graduate Students

MIZUNO, Takafumi	Grad. Univ. Adv. Studies	tmizuno@ims.ac.jp
IIZUKA, Takuya	Grad. Univ. Adv. Studies	takuizk@ims.ac.jp
TANIKAWA, Takanori	Grad. Univ. Adv. Studies	tanikawa@ims.ac.jp
NAGATANI, Atsumune	Nagoya Univ.	
FURUI, Yuta	Nagoya Univ.	
TAIRA, Yoshitaka	Nagoya Univ.	
MITANI, Hiroyuki	Shinshu Univ.	
HAJIRI, Tetsuya	Nagoya Univ.	
KIKUCHI, Yoshitaka	Nagoya Univ.	

Visiting Scientists

KWON, Yong-Seung	Sungkyunkwan Univ., Korea	July-Aug. 2008, Jan. 2009
OH, Hyunjin	Masan College, Korea	July-Aug. 2008, Jan. 2009
ELAND, John	University of Oxford, UK	Aug.-Sept. 2008
BIELAWSKI, Serge	University of Lill, France	Dec. 2008
SZWAJ, Christophe	University of Lill, France	Dec. 2008
EVAIN, Clement	University of Lill, France	Dec. 2008
SONG, Yun Young	Cheju Tourism College, Korea	Jan. 2009
Hong, Jeong-Beom	Sungkyunkwan Univ., Korea	Jan. 2009
HERZOG Alexander	Max Planck Institute, Germany	Mar. 2009

Light Source in 2008

1. Status of UVSOR-II

In the fiscal year 2008, we have operated the UVSOR-II accelerators from April '08 to March '09. We had totally 37 weeks for the users operation, 33 weeks in multi-bunch mode, 2 weeks in single-bunch mode and 2 weeks as bonus runs in multi-bunch mode. We had 6 weeks dedicated for machine studies. We had one month shut-down in August for a construction work of a new undulator beam-line and also for maintenance works on accelerators. We had two 1-week shut-down in May and March, and one 2-week one around the New Years Day.

The monthly statistics of the operation time and the integrated beam current are shown in Fig. 1. The operation time per month has increased by approximately 20% on average since October. This is because of the extended operation for Top-up test runs as described later.

The weekly operation schedule is as follows. On Monday, the machine is operated for machine studies. From Tuesday to Friday, the machine is operated for users, from 9am to 9pm. In case of the multi-bunch mode, the beam injection is made twice a day, at 9am and 3pm. The filling beam current is 350 mA. In case of the single bunch mode, the injection is made three times a day, at 9am, 1pm and 5pm, and the filling current is 100 mA. Normally, it takes about 20 minutes to complete the injection.

Occasionally, we operate the machine after 9pm for beam-line conditionings, free electron laser experiments and so on. Since October, 2008, we operate the machine for 24 hours on every Thursday. After 9pm on these days, the machine is operated to test the Top-up injection scheme.

In this fiscal year, we had one rather serious trouble. In January 2009, the power supply of the bending magnets of the storage ring was malfunctioned. It took about one week to repair. We exchanged a machine study week in February with a users week to secure the beam time. Although we also had a few troubles on the linear accelerator in autumn, fortunately, it was recovered within a few days and the users time could be secured by extending the operation time during the weeks.

2. Improvements

Towards Top-up Operation

In the last two years, we have been preparing for the Top-up operation. The energy upgrade of the booster synchrotron and the beam transport lines were successfully completed. Now, we inject the electron beam at the full energy in the users runs. During the short shut-down period in April, 2008, we installed two beam scrapers and one current transformer (CT) in the beam transport line. The formers are to scrape out the unnecessary electrons in the extracted beam from the booster synchrotron. The latter is to monitor the number of the injected electrons. The signal from the CT is processed and is sent to an interlock module, which stops the injection when the integrated number of electrons reaches to a limiting value. The signal from the DCCT in the ring is also sent to the module. The module controls (starts or stops) the injection to keep the beam current almost constant, as monitoring the stored beam current in the ring.

In October, we have started testing the Top-up operation in users beam time. On every Thursday night, from 9pm to 9am, the ring is operated in the Top-up mode. The users can use synchrotron radiation and check the effects on their experiments. The beam current is kept almost constant at 300mA. The beam is injected for about 10 second every one minute with the repetition rate, 1 Hz. An example of the operational result is shown in Fig. 2. Although it is not shown in this figure, the fluctuation of the stored beam current is less than 1% when the injection efficiency is kept at the normal level.

So far, we have found several problems that have to be solved before starting the Top-up operation in daily user runs. The most serious one is the

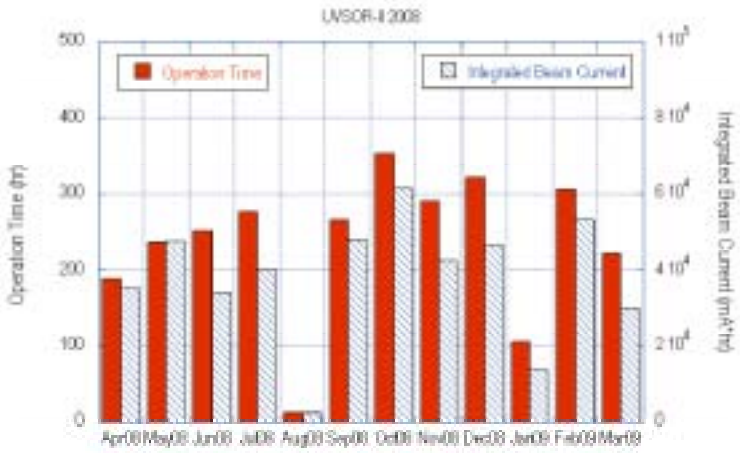

Fig. 1. Monthly statistics of the operation time (red bars) and of the integrated beam current (blue dashed bars).

instantaneous orbit movement at injection. Some beam-lines are located inside of the injection bump. Thus, the effect is inevitable. However, even in the other beam-lines, they observe the effect because of the leakage of the bump orbit. This should be suppressed by precisely adjusting the orbit in near future. In a long term, it has to be solved by introducing some sophisticated injection scheme. As an alternative approach, we are preparing a system to provide injection timing signal for the data acquisition system at the beam-lines to stop the data acquisition during the injection.

There are a few other practical problems. One is the stability of the injection efficiency. In particular, the drift of the injection efficiency from the linac to the booster synchrotron has found to be significant. Another is the discharge of the electron gun, which takes place roughly once per day. These problems should be improved in near future.

3. Researches and Developments

Coherent Synchrotron Radiation by using an External Laser

Generation of terahertz coherent synchrotron radiation has been intensively studied at UVSOR-II by using laser modulation methods. In these methods, laser pulses from an external source are injected to the storage ring to produce micro-density structures on the electron bunches. When we use sub-picosecond laser pulses, we can produce sub-picosecond dips on the bunches. In this case, broadband coherent THz radiation is emitted in the wavelength range longer than the dip size [1]. When we use amplitude modulated laser pulses, we could produce periodic density structure on the bunches. In this case, the bunches emit quasi-monochromatic coherent THz radiation at the wavelength equal to the density modulation period [2]. We have tried the laser slicing technique in a low alpha operation mode, in which the micro-density structures are kept for a longer time. Some interesting behavior was observed, which was considered to originate from a transverse-longitudinal coupling effect in the storage ring.

To get coherent radiation in the VUV range, which is hard to reach with the resonator type free electron laser, coherent harmonic generation (CHG) is under investigation. Coherent 3rd harmonics of a Ti:Sa laser was successfully produced and the properties of the radiation and the mechanisms were investigated [3, 4]. CHG in the full helical configuration was successfully demonstrated for the first time [5].

After the successes of the proof-of-principle experiments on the coherent radiation described above, we have started a new research project under Quantum Beam Technology Program of MEXT. In this five year project, we will reconstruct the beam transport line and move the injection point to produce another new 4m long straight section in the ring. We will upgrade the laser system and install new undulators, which are dedicated to the coherent radiation production. We will also construct two new beam-lines which are also dedicated to applications of the coherent radiation in the THz and VUV ranges.

[1] M. Shimada, M. Katoh, S. Kimura, A. Mochihashi, M. Hosaka, Y. Takashima, T. Hara and T. Takahashi, Jpn. J. Appl. Phys. **46** (2007) 7939.

[2] S. Bielawski, C. Evain, T. Hara, M. Hosaka, M. Katoh, S. Kimura, A. Mochihashi, M. Shimada, C. Szwaj, T. Takahashi and Y. Takashima, Nature Physics **4** (2008) 390.

[3] M. Labat, G. Lambert, M. E. Couprie, M. Shimada, M. Katoh, M. Hosaka, Y. Takashima, T. Hara and A. Mochihashi, Nucl. Instr. Meth. Phys. Res. A **593** (2008) 1.

[4] M. Labat, C. Bruni, G. Lambert, M. Hosaka, M. Shimada, M. Katoh, A. Mochihashi, T. Takashima, T. Hara and M. E. Couprie, Europhys. Lett. **81** (2008) 34004.

[5] M. Labat, M. Hosaka, M. Shimada, M. Katoh and M. E. Couprie, Phys. Rev. Lett. **101** (2008) 164803.

M. Katoh (UVSOR Facility)

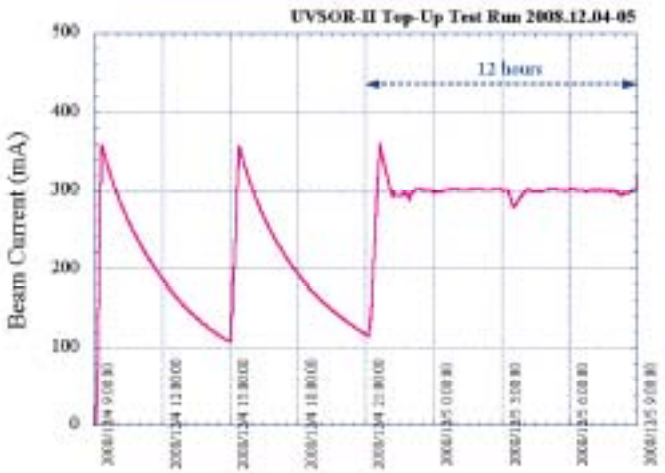

Fig. 2. Top-up Test Operation. After 9pm, the ring was operated in the Top-up mode for about 12 hours.

UVSOR Accelerator Complex

Injection Linear Accelerator

Energy	15 MeV
Length	2.5 m
Frequency	2856 MHz
Accelerating RF Field	2π/3 Traveling Wave
Klystron Power	1.8 MW
Energy Spread	~1.6 MeV
Repetition Rate	2.6 Hz

UVSOR-II Storage Ring

Energy	750 MeV
Injection Energy	750 MeV
Maximum Stored Current	500 mA (multi bunch) 100 mA (single bunch)
Natural Emittance	27.4 nm-rad
Circumference	53.2 m
RF Frequency	90.1 MHz
Harmonic Number	16
Bending Radius	2.2 m
Lattice	Extended DBA×4
Straight Section	(4 m×4)+(1.5 m×4)
RF Voltage	100 kV
Betatron Tune	
Horizontal	3.75
Veritcal	3.20
Momentum Compaction	0.028
Natural Chromaticity	
Horizontal	-8.1
Vertical	-7.3
Energy Spread	4.2×10^{-4}
Natural Bunch Length	108 ps

Booster Synchrotron

Energy	750 MeV
Injection Energy	15 MeV
Beam Current	32 mA (uniform filling)
Circumference	26.6 m
RF Frequency	90.1 MHz
Harmonic Number	8
Bending Radius	1.8 m
Lattice	FODO×8
Betatron Tune	
Horizontal	2.25
Veritcal	1.25
Momentum Compaction	0.138
Repetition Rate	1 Hz (750 MeV)

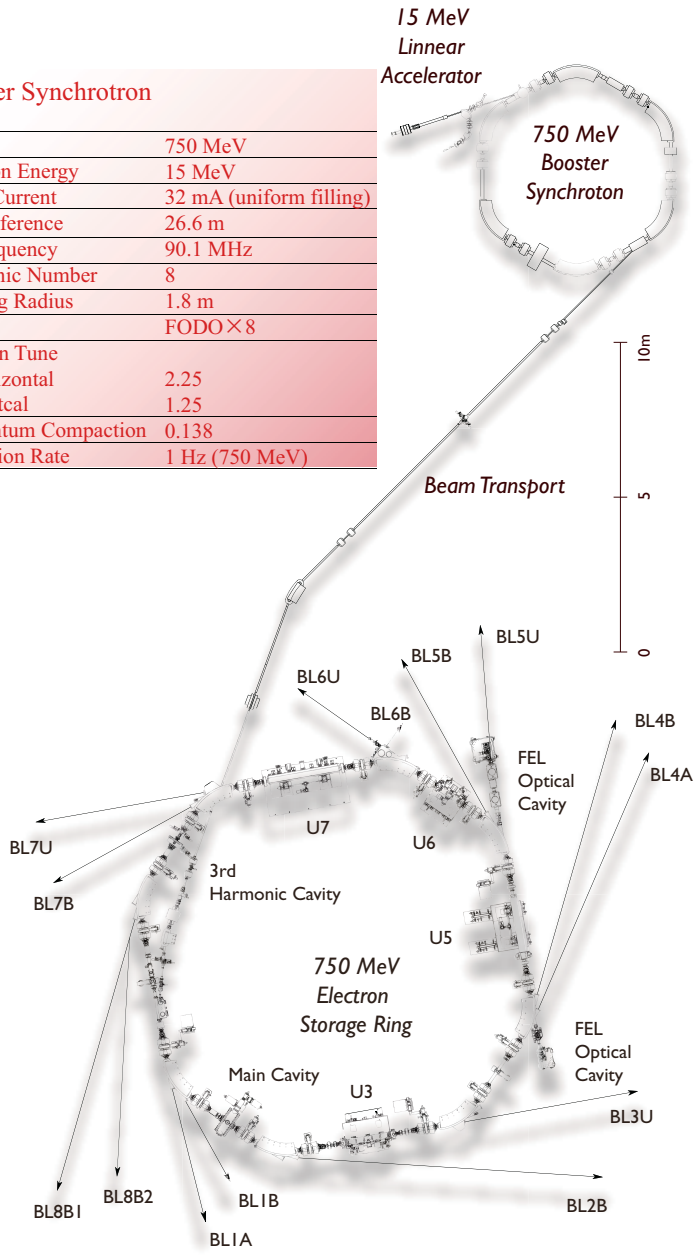

Electron Beam Optics of UVSOR-II Storage Ring

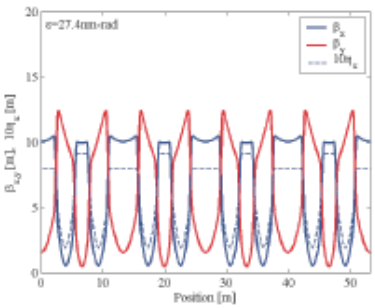

Horizontal /vertical
betatron functions
and dispersion function

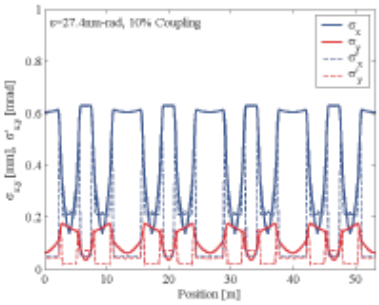

Horizontal /vertical
electron bem sizes
and beam divergences

Insertion Devices

Brilliance of Radiation

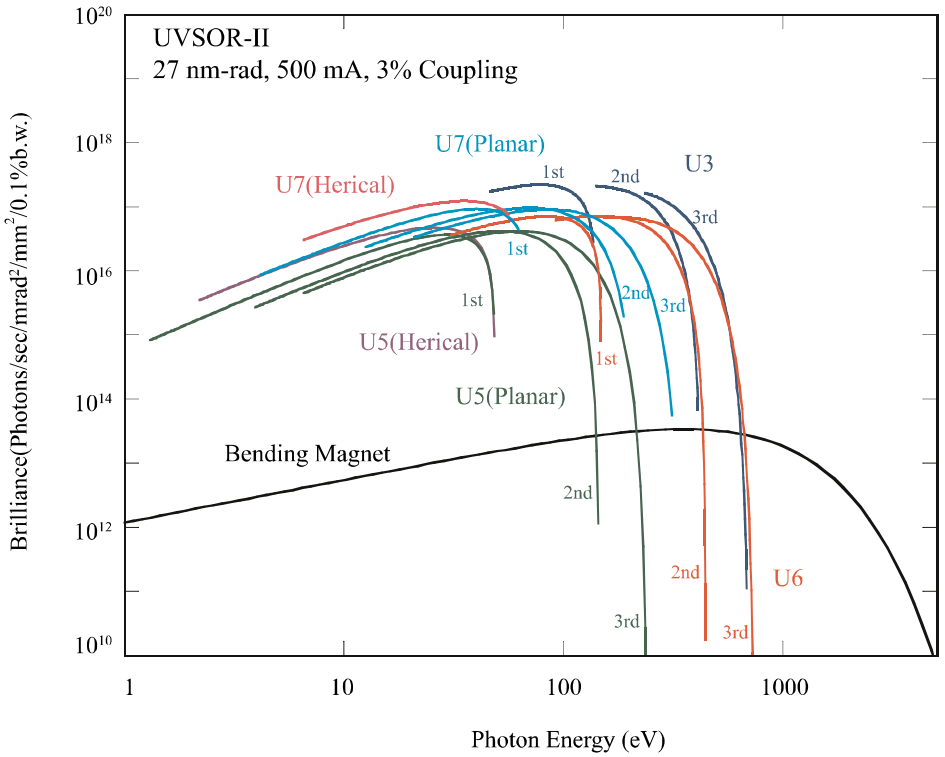

Brilliance of radiation from the insertion devices (U3, U5, U6 and U7) and a beding magnet of UVSOR-II

U3 In-vacuum Undulator

Number of Periods	50
Period Length	38 mm
Pole Length	1.9 m
Pole Gap	15 - 40 mm
Deflection Parameter	2.00 - 0.24

U6 In-vacuum Undulator

Number of Periods	26
Period Length	36 mm
Pole Length	0.94 m
Pole Gap	15 - 40 mm
Deflection Parameter	1.78 - 0.19

U5 Herical Undulator / Optical Klystron

Number of Periods	21 / 9+9 (Opt. Kly.)
Period Length	110 mm
Pole Length	2.35 m
Pole Gap	30 - 150 mm
Deflection Parameter	4.6 - 0.07 (Helical) 8.5 - 0.15 (Linear)

U7 Apple-II Variable Polarization Undulator

Number of Periods	40
Period Length	76 mm
Pole Length	3.04 m
Pole Gap	24 - 200 mm
Deflection Parameter	5.4 (Max. Horizontal) 3.6 (Max. Vertical) 3.0 (Max. Helical)

Bending Magnets

Bending Radius	2.2 m
Critical Energy	425 eV

Beamlines in 2009

Since the successful accomplishment of the upgrade project on the UVSOR storage ring (UVSOR-II project), in which the creation of four new straight sections and the achievement of much smaller emittance (27 nm-rad) were planned, the UVSOR facility has become one of the highest brilliance extreme-ultraviolet radiation sources among synchrotron radiation facilities with electron energy less than 1 GeV. Eight bending magnets and four insertion devices are available for utilizing synchrotron radiation at UVSOR. There is a total of thirteen operational beamlines (BL6U has been under construction) in 2008, which are classified into two categories. Nine of them are so-called "Open beamlines", which are open to scientists of universities and research institutes belonging to the government, public organizations, private enterprises and those of foreign countries. The rest of the four beamlines are so-called "In-house beamlines", and are dedicated to the use of research groups within IMS. We have one soft X-rays station equipped with a double-crystal monochromator, seven extreme ultraviolet and soft X-rays stations with a grazing incidence monochromator, three vacuum ultraviolet stations with a normal incidence monochromator, one infrared (IR) station equipped with Fourier-Transform interferometers, one station with a multi-layer monochromator, as shown in the appended table (next page) for all available beamlines at UVSOR.

Keeping pace with the upgrade project, the improvements and upgrades of the beamlines at UVSOR have been continuously discussed with users in a series of UVSOR workshops. Newly constructed (BL3U and BL7U) as well as the upgraded (BL5U and BL6B) beamlines synchronized with the UVSOR-II project have been routinely operated, and a number of outcome has emerged through the utilization of these beamlines. Concerning the utilization of the first in-vacuum type undulator, which has been relocated from the long straight section U7 to the short one between B05 and B06, a new project for constructing the undulator beamline BL6U has been initiated. BL6U will be initially prepared as an in-house beamline. The monochromator designed covers the photon energy ranging from 30 to 500 eV, with the resolving power higher than 10000 and the photon flux more than 10^{10} photons/sec. The practical construction of BL6U has begun from the summer shutdown in 2008. The first light has been observed and short performance tests have been carried out in December 2008. After the beamline commissioning of BL6U, BL4B will be allocated to an open beamline, and all users' activities continued at BL8B1 will be accepted at BL4B. The experimental activities conducted at BL4A will be terminated in August 2009. All the beamline components at BL4A will be removed later on, and the space thus created will be utilized for constructing a new undulator beamline.

As a research program in "Quantum Beam Technology Project" conducted by MEXT/JST, "Development and Application of Light Source Technology Based on Electron Storage Ring and Laser" proposed by the UVSOR machine group was accepted in 2008. In connection, the straight section U1 will be used for generating coherent THz and VUV radiation, where two beamlines will be constructed. Accordingly BL1A and BL1B must be moved to vacant lots. Since spectroscopic research works on solids have been conducted very actively at these beamlines, it is essential that all the users' activities there should segue at new locations. In order to discuss near future plans for BL1A and BL1B, the users' meetings have been organized separately by the UVSOR User's Union. As a result, it has been decided that BL1A will be moved to the location of the previous BL2A, and BL1B will be newly constructed at the place of the previous BL3B. The practical movement and construction will start from the spring of 2011. Further serious discussion toward utilizing the available straight sections most effectively and formulating a basic plan on the beamline construction, will be continued.

All users are required to refer to the beamline manuals and the UVSOR guidebook (the latest revision in PDF format will be uploaded on the UVSOR web page in the summer of 2009), on the occasion of conducting the actual experimental procedures. Those wishing to use the open and in-house beamlines are recommended to contact the beamline master (see next page), respectively. For updated information of UVSOR, http://www.uvsor.ims.ac.jp/.

E. Shigemasa (UVSOR Facility)

Beamlines at UVSOR

Beam-line	Monochromator, Spectrometer	Energy Region (eV)	Experiments	Beamline master
1A	Double-Crystal	600 eV – 4 keV	Solid (Absorption)	N. Kondo nkondo@ims.ac.jp
1B	1m Seya-Namioka	2 eV – 30 eV	Solid (Reflection, Absorption)	M. Hasumoto hasumoto@ims.ac.jp
2B*	18m Spherical Grating (Dragon)	24 eV – 205 eV	Gas (Photoionization, Photodissociation)	K. Mitsuke mitsuke@ims.ac.jp
3U*	Varied-Line-Spacing Plane Grating (Monk-Gillieson)	60 eV – 800 eV	Gas, Liquid, Solid (Absorption, Photoemission, Photon Emission)	N. Kosugi kosugi@ims.ac.jp
4A*	Multi-Layered-Mirror	50 eV – 95 eV	Irradiation	T. Urisu urisu@ims.ac.jp
4B*	Varied-Line-Spacing Plane Grating (Monk-Gillieson)	25 eV – 1 keV	Gas (Photoionization, Photodissociation) Solid (Photoemission)	E. Shigemasa sigemasa@ims.ac.jp
5U	Spherical Grating (SGM-TRAIN*)	5 eV – 250 eV	Solid (Photoemission)	S. Kimura kimura@ims.ac.jp
5B	Plane Grating	6 eV – 600 eV	Calibration Solid (Absorption)	M. Hasumoto hasumoto@ims.ac.jp
6U*	Variable-Included-Angle Varied-Line-Spacing Plane Grating	30 eV – 500 eV	Gas (Photoionization, Photodissociation) Solid (Photoemission)	E. Shigemasa sigemasa@ims.ac.jp
6B	Martin-Puplett FT-FIR Michelson FT-IR	0.1 meV – 2.5 eV	Solid (Reflection, Absorption)	S. Kimura kimura@ims.ac.jp
7U	10m Normal Incidence (Modified Wadsworth)	6 eV – 40 eV	Solid (Photoemission)	S. Kimura kimura@ims.ac.jp
7B	3m Normal Incidence	1.2 eV – 25 eV	Solid (Reflection, Absorption)	M. Hasumoto hasumoto@ims.ac.jp
8B1	15m Constant Deviation Grazing Incidence	30 eV – 800 eV	Solid (Absorption)	E. Nakamura eiken@ims.ac.jp
8B2	Plane Grating	1.9 eV – 150 eV	Solid (Photoemission)	T. Nishi nishi@ims.ac.jp
FEL	Free Electron Laser	1.6 eV – 6.2 eV		M. Katoh mkatoh@ims.ac.jp
CSR	Coherent Synchrotoron Radiation	0.5 meV – 5 meV		M. Katoh mkatoh@ims.ac.jp

* In-House Beamline

* Spherical Grating Monochromator with Translating and Rotating Assembly Including Normal incidence mount

BL1A

Soft X-Ray Beamline for Photoabsorption Spectroscopy

BL1A is a soft X-ray beamline for photoabsorption spectroscopy. The beamline is equipped with a focusing premirror and a double crystal monochromator [1]. The monochromator serves soft X-rays in the energy region from 586 to 4000 eV by using several kinds of single crystals such as β-Al_2O_3, beryl, KTP ($KTiOPO_4$), quartz, InSb, and Ge. The throughput spectra measured by a Si photodiode (AXUV-100, IRD Inc.) are shown in Fig. 1. Typical energy resolution (E/ΔE) of the monochromator is about 1500 for beryl and InSb. There are no experimental setups specific of this beamline, except for a small vacuum chamber equipped with an electron multiplier (EM) detector. Photoabsorption spectra for powdery samples are usually measured in a total electron yield mode, with the use of the EM detector.

[1] A. Hiraya *et al.*, Rev. Sci. Instrum. **63** (1992) 1264.

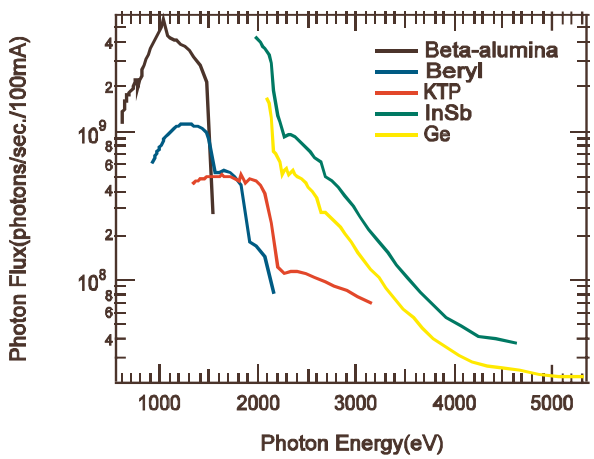

Fig. 1. Throughput spectra of the double crystal monochromator at BL1A.

Fig. 2. Side view of BL1A.

Beamline Specifications

Monochromator	Double crystal monochromator
Monochromator crystals: (2d value, energy range)	β-Al_2O_3 (22.53 Å, 586-1535 eV), beryl (15.965 Å, 827-2167 eV), KTP (10.95 Å, 1205-3158 eV), quartz (8.512 Å, 1550-4000 eV), InSb (7.481 Å, 1764-4000 eV), Ge (6.532 Å, 2020-4000 eV)
Resolution	E/ΔE = 1500 for beryl and InSb
Experiment	Photoabsorption spectroscopy

BL1B

Seya-Namioka Monochromator for General Purposes

BL1B has been constructed to perform various spectroscopic investigations such as absorption, reflectivity, and luminescence in condensed matters. This beamline consists of a pre-focusing mirror, a 1-m Seya-Namioka type monochromator, and post-focusing mirrors with different focal lengths. Three gratings of 600, 1200, and 2400 l/mm can cover the wavelength region ranging from 40 to 650 nm ($h\nu$ = 2 – 30 eV). The post mirror with a longer focal length is usually used with an LiF window to separate the vacuum condition of the monochromator from a main experimental station, which make experiments for liquids and bio-specimens possible, while the other is mainly utilized for solid-state spectroscopy. The output flux from this monochromator is about 10^{10} photons/sec. around 200 nm with 0.1 mm slit openings. The spectral distributions for two gratings measured by a conventional photomultiplyer are shown in Fig. 1. A second monochromator (Spex 270M) and a LN-cooled CCD detector (Princeton Inc.) are available for luminescence measurements, together with a liquid helium-flow type cryostat. To perform time-resolved experiments, a TAC system is also available.

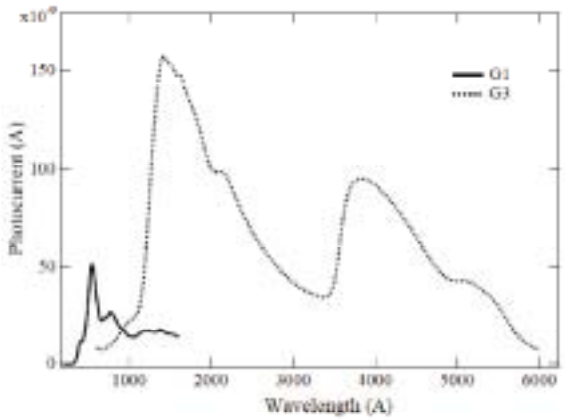

Fig. 1. Photocurrent at the sample position at BL1B.

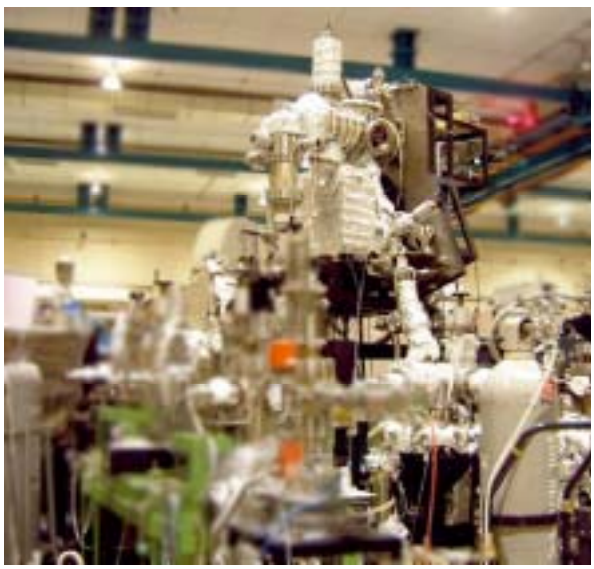

Fig. 2. Photo of BL1B.

Beamline Specifications

Monochromator	1-m Seya-Namioka type
Wavelength Range	40 to 600 nm (2-30 eV)
Resolution	E/ΔE~1000 at 100 nm (10 eV)
Experiment	Absorption, reflection, luminescence spectroscopy for solids

BL2B

Beamline for Gas Phase Photoionization and Reaction Dynamics

This beamline has been developed for the purpose of studying ionization, excitation and decay dynamics involving inner-valence electrons, 2*p* electrons of the third row atoms, and 4d electrons of the lanthanides. The monochromator is a spherical grating Dragon-type with 18-m focal length. High throughput (1×10^{10} photons s^{-1}) and high resolution ($E/\Delta E$ = 2000 - 8000) are achieved simultaneously under the condition of the ring current of 100 mA [1]. The optical system consists of two prefocusing mirrors, an entrance slit, three spherical gratings (G1 - G3), two folding mirrors, a movable exit slit and a refocusing mirror [2]. The monochromator is designed to cover the energy range of 23 - 205 eV with the three gratings: G1 (2400 lines mm^{-1}, R = 18 m) at 80 - 205 eV; G2 (1200 lines mm^{-1}, R = 18 m) at 40 - 100 eV; G3 (2400 lines mm^{-1}, R = 9.25 m) at 23 - 50 eV. The percentage of the second-order light contamination at $h\nu$ = 45.6 eV is 23 % for G2 or 7 % for G3.

We have been taking the yield curves of various fullerene ions [3]. Geometrical structures and electronic properties of fullerenes have attracted widespread attention because of their novel structures, novel reactivity, and novel catalytic behaviors as typical nanometer-size materials. However, spectroscopic information was very limited in the extreme UV region, owing to difficulties in acquiring enough amount of sample. This situation has been rapidly changed since the start of this century, because the techniques of syntheses, isolation, and purification have been advanced so rapidly that appreciable amount of fullerenes can be readily obtained.

[1] M. Ono, H. Yoshida, H. Hattori and K. Mitsuke, Nucl. Instrum. Meth. Phys. Res. A **467-468** (2001) 577.

[2] H. Yoshida and K. Mitsuke, J. Synchrotron Radiat. **5** (1998) 774.

[3] J. Kou, T. Mori, Y. Kubozono and K. Mitsuke, Phys. Chem. Chem. Phys. **7** (2005) 119.

Fig. 1. 18-m spherical grating monochromator at BL2B.

Fig. 2. End station of BL2B for gas phase spectroscopy of refractory materials.

Beamline Specifications

Monochromator	18-m spherical grating Dragon-type
Wavelength Range	6-55 nm; 24-205 eV
Resolution	2000 - 8000 depending on the gratings
Experiment	Mass spectrom.; photoelectron spectrosc.; momentum imaging spectrosc.; e^--ion coincidence spectrosc.; fullerene beam source

BL3U

Varied-Line-Spacing Plane Grating Monochromator for Molecular Soft X-Ray Spectroscopy

The beamline BL3U is equipped with an in-vacuum undulator composed of 50 periods of 3.8 cm period length. The emitted photons are monochromatized by the varied-line-spacing plane grating monochromator (VLS-PGM) designed for various spectroscopic investigations in the soft x-ray range including soft x-ray emission studies. Three holographically ruled laminar profile plane gratings are designed to cover the photon energy range from 60 eV to 800 eV. The beamline has two endstations, namely XES setup and Multi-purpose setup. The XES setup is used for soft x-ray emission spectroscopy. The beam is horizontally focused onto the sample position by plane-elliptical mirror, M2X. In the Multi-purpose setup, the beam is focused by the toroidal mirror M2. Between the sample position and M2, the differential pumping is placed.

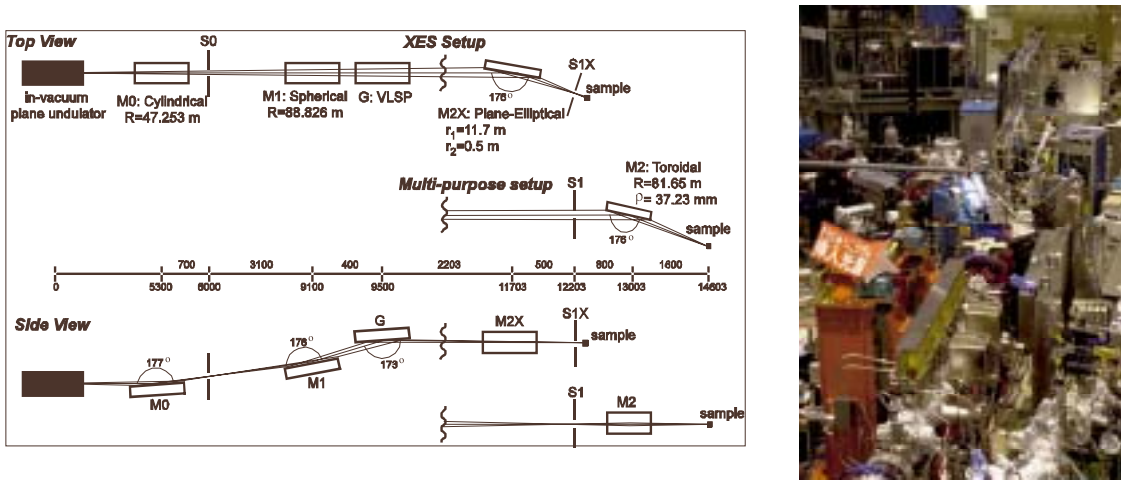

Fig. 1. Schematic layout (left) and the photography (right) of the BL3U. The distances along the beam from the center of the in-vacuum plane undulator are shown in mm. S1X and M2X can be replaced with the other exit slit S1 so that experiments can be carried out at either the XES or multi-purpose endstation. In the XES setup, the sample is placed at 5-10 mm downstream of S1X.

Beamline Specifications

Monochromator	Varied-line-spacing plane grating monochromator
Energy Range	60-800 eV
Resolution	E/ΔE > 10000
Experiment	Soft X-ray spectroscopy (XPS, XES, XAS)
Beam Size (XES Endstation)	Gaussian shape Vertical 5-20 μm; Horizontal 41 μm (FWHM)

BL4A

Multilayered Mirror Monochromator for Photochemistry

BL4A has been constructed to perform the synchrotron radiation induced etching of Si and SiO_2 using XeF_2 as an etching gas. This beam-line is composed of a multilayered mirror (MLM) monochromator, a beam condenser system, and a differential pump system. The XeF_2 pressure during the etching will reach to 0.5 Torr, so a differential pump apparatus is installed in the vacuum system and the etching chamber as shown in Fig. 1. The etching chamber is evacuated independently and is designed to achieve high pressure (0.5 Torr) keeping other vacuum system at low pressure (< 10^{-5} Torr) by an aperture flange and a sequence of pressure stages. The condenser mirror focuses the divergent radiation onto the sample surface in the etching chamber, and obtains an extreme higher photon flux can be obtained.

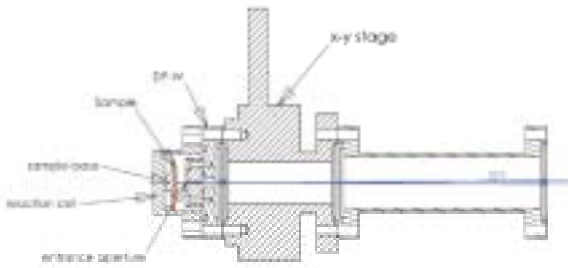

Fig. 1. Section view of differential pump apparatus installed in the etching chamber (reaction cell) and the entrance of beam.

Fig. 2. A side view of the end-station at BL4A.

Beamline Specifications

Monochromator	Multilayered mirror monochromator
Wavelength Range	13.3-22.5 nm; 55-93 eV
Resolution	5-9 eV (FWHM)
Experiment	Irradiation

BL4B

Varied-Line-Spacing Plane Grating Monochromator for Molecular Soft X-Ray Spectroscopy

The beamline BL4B equipped with a varied-line-spacing plane grating monochromator (VLS-PGM) was constructed for various spectroscopic investigations in a gas phase and/or on solids in the soft X-ray range. Three holographically ruled laminar profile plane gratings with SiO_2 substrates are designed to cover the photon energy range from 25 eV to 800 eV. The gratings with the groove densities of 100, 267, and 800 l/mm cover the spectral ranges of 25-100, 60-300, and 200-1000 eV, respectively, and are interchangeable without breaking the vacuum. Fig. 1 shows the absolute photon flux for each grating measured by a Si photodiode (IRD Inc.), with the entrance- and exit-slit openings set at 50 and 50 μm, respectively. The maximum resolving power (E/ΔE) achieved for each grating is more than 5000.

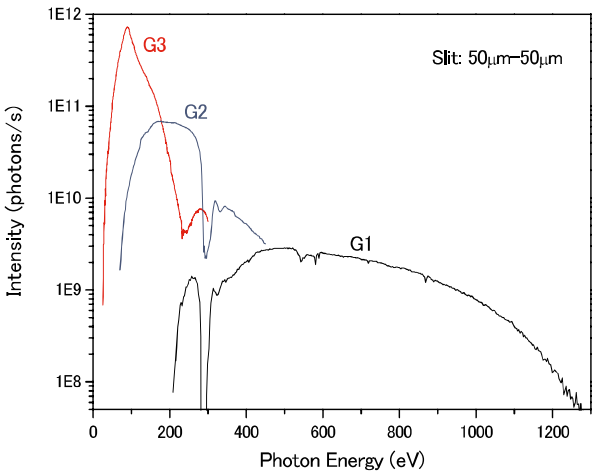

Fig. 1. Throughput from the VLS-PGM monochromator on BL4B.

Fig. 2. Photo of BL4B.

Beamline Specifications

Monochromator	Varied-line-spacing plane grating monochromator
Energy range	25-1000 eV
Resolution	E/ΔE > 5000 (at maximum)
Experiment	Soft X-ray spectroscopy (mainly, angle-resolved photoion spectroscopy for gaseous targets and photoelectron spectroscopy for gaseous and solid targets)

BL5U

Photoemission Spectroscopy of Solids and Surfaces

This beamline is designed for a high-resolution angle-resolved photoemission study on solids and surfaces with horizontal-linearly and circularly (CW, CCW) polarized synchrotron radiation from a helical undulator. The beamline consists of a Spherical Grating Monochromator with Translational and Rotational Assembly Including a Normal incidence mount (SGM-TRAIN), and a high-resolution angle-resolved photoemission spectrometer.

The SGM-TRAIN is an improved version of a constant-length SGM to aim the following points; (1) covering the wide energy range of 5-250 eV, (2) high energy resolving power, (3) use of linearly and circularly polarized undulator light, (4) reduction of higher order light, and (5) two driving modes (rotation and translation of gratings) by computer control. The second-order light is well suppressed by using laminar profile gratings and combinations of mirrors and gratings.

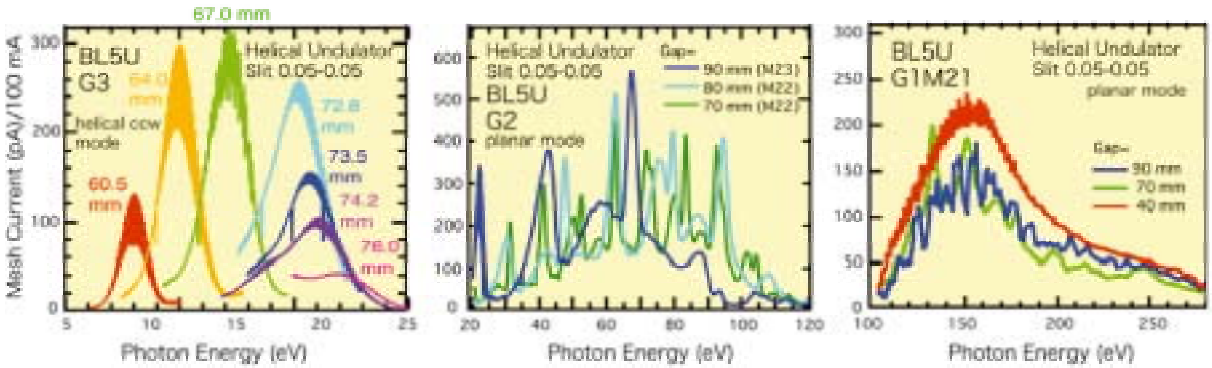

Fig. 1. Throughput spectra from the SGM-TRAIN monochromator at BL5U.

Beamline Specifications

Monochromator	SGM-TRAIN
Energy Range	5-250 eV
Resolution	hν/ΔE >2000 for < 40μm slits
Experiment	ARPES, AIPES, XAS
Flux	$<10^{11}$ photons/s for < 40μm slits (at the sample position)
Main instruments	Hemispherical photoelectron analyzer (MBS-Toyama 'Peter' A-1), LEED of reverse type (OMICRON), Liq-He flow cryostat (5-400 K)

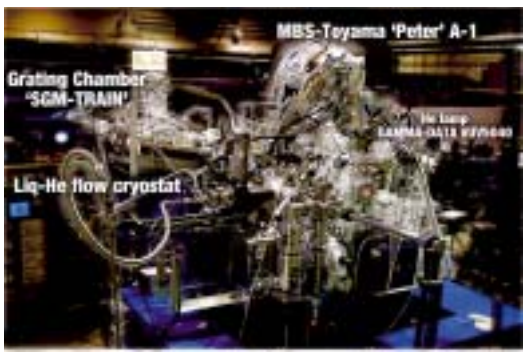

Fig. 2. High-resolution angle-resolved photoemission apparatus at BL5U.

BL5B

Calibration Apparatus for Optical Elements and Detectors

BL5B has been constructed to perform calibration measurements for optical elements and detectors. This beamline is composed of a plane grating monochromator (PGM) and three end stations in tandem. The most upstream station is used for calibration measurements of optical elements, the middle one for optical measurements for solids and the last for photo-stimulated desorption experiments. The experimental chamber at the most downstream station is sometimes changed to a chamber for photoemission spectroscopy.

The calibration chamber shown in Fig. 2 is equipped with a goniometer for the characterization of optical elements, which has six-degree-of-freedom; X-Y translation of a sample, and interchange of samples and filters. These are driven by pulse motors in vacuum. Since the polarization of synchrotron radiation is essential for such measurements, the rotation axis can be made in either horizontal or vertical direction (s- or p-polarization).

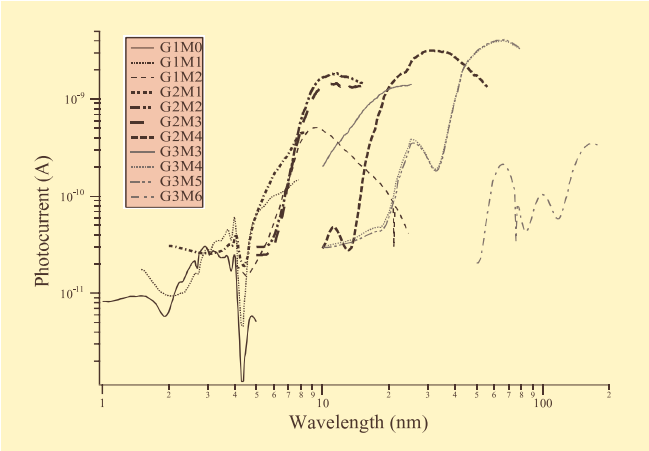

Fig. 1. Throughput spectra for possible combinations of gratings and mirrors at BL5B measured by a gold mesh.

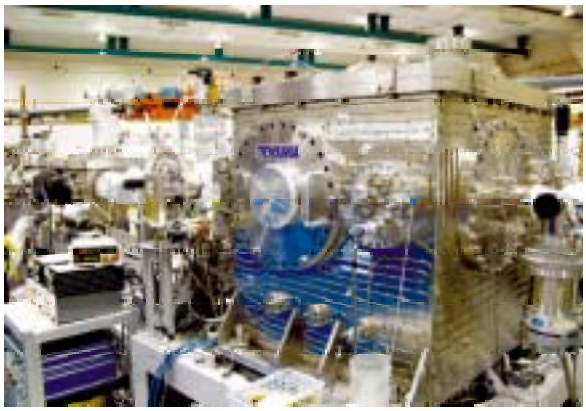

Fig. 2. A side view of the experimental chamber for calibration measurements.

Beamline Specifications

Monochromator	Plane grating monochromator
Energy range	6-600 eV (2-200 nm)
Resolution	E/ΔE ~ 500
Experiments	Calibration of optical elements, absorption of solids, photo-stimulated desorption from rare gas solids

BL6U

Variable-Included-Angle VLS-PGM for Molecular Soft X-Ray Spectroscopy

The beamline BL6U equipped with a variable-included-angle Monk-Gillieson mounting monochromator with a varied-line-spacing plane grating was constructed for various spectroscopic investigations requiring high-brilliance Soft X-rays in a gas phase and/or on solids. By a combination of undulator radiation and the sophisticated monochromator design (entrance slit-less configuration and variable-included-angle mechanism), with using one single grating, the monochromator can cover the photon energy ranging from 30 to 500 eV, with the resolving power higher than 10000 and the photon flux more than 10^{10} photons/sec. Figure 1 shows an example of the monochromator throughputs estimated from photocurrent measurements using a Au plate, with the exit-slit opening set at 30 μm, which corresponds to the theoretical resolving power of 10000 at 80 eV.

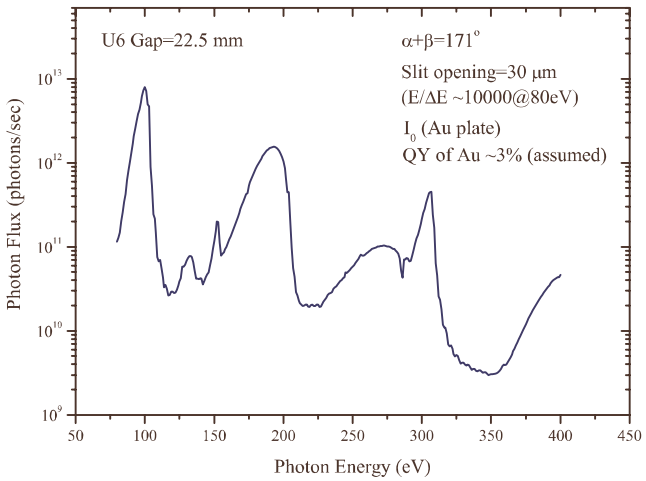

Fig. 1. Throughput from the BL6U monochromator at a given condition.

Fig. 2. Photo of BL6U.

Beamline Specifications

Monochromator	Variable-included-angle varied-line-spacing plane grating monochromator
Energy range	30-500 eV
Resolution	E/ΔE > 10000 (at maximum)
Experiment	High-resolution soft X-ray spectroscopy (mainly, photoelectron spectroscopy for gaseous and solid targets)

BL6B

Infrared and Terahertz Spectroscopy of Solids

SR has a good performance (high brilliance and high flux) not only in the VUV and SX regions but also in the infrared (IR) and terahertz (THz) regions. BL6B covers in the IR and THz regions. The previous beamline BL6A1 that has been constructed in 1985 is the pioneer of the infrared SR research. The beamline was quitted at the end of FY2003 and a new IR/THz beamline, BL6B (IR), was constructed in FY2004. The front-end part including the bending duct #6 was replaced to a new one with higher acceptance angle (215 (H) × 80 (V) mrad^2) using a magic mirror as shown in Fig. 1 [1].

The beamline is equipped with two interferometers, one is Michelson-type (Bruker IFS-66v) and the other Martin-Puplett-type (JASCO FARIS-1), to cover the wide spectral region from several to 20,000 cm^{-1} ($h\nu$ = several 100 μeV – 2.5 eV) as shown in Fig. 2. There are two end-stations; one is reflection/absorption spectroscopy for large samples (~ several mm) and the other IR/THz microscopy for tiny samples (~ several ten μm).

[1] S. Kimura, E. Nakamura, T. Nishi, Y. Sakurai, K. Hayashi, J. Yamazaki and M. Katoh, Infrared Phys. Tech. **49** (2006) 147.

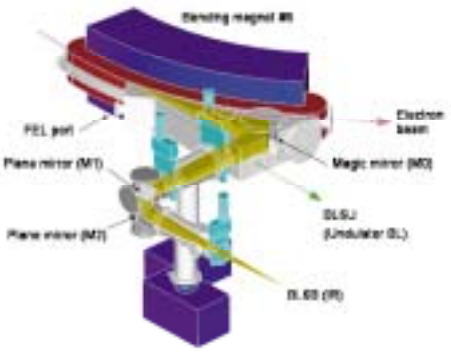

Fig. 1. The design of optics and front end of BL6B.

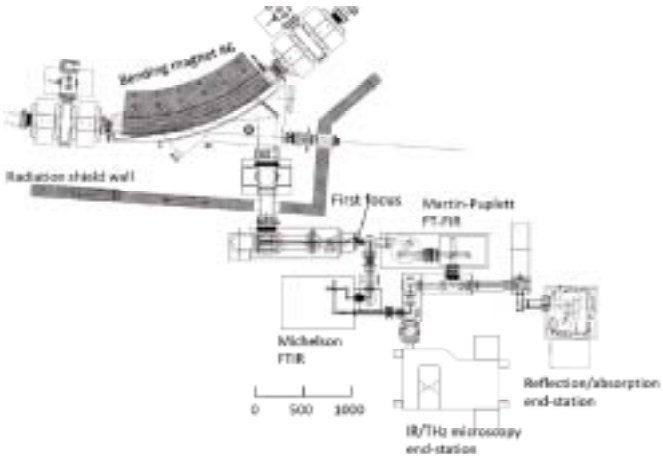

Fig. 2. Schematic figure of top view of BL6B.

Beamline Specifications

Interferometer	Michelson (Bruker IFS66v), Martin-Puplett (JASCO FARIS-1)
Wavenumber Range (Energy range)	several – 20,000 cm^{-1} (several 100 μeV – 2.5 eV)
Resolution in cm^{-1}	0.1cm^{-1} for IFS66v, 0.25cm^{-1} for FARIS-1
Experiments	Reflectivity and transmission, microspectroscopy, and magneto-optics
Miscellaneous	Users can bring their experimental system in this beamline.

BL7U

Angle-Resolved Photoemission of Solids in the VUV Region

The beamline 7U is constructed to provide the photon flux with high energy resolution and high flux mainly for high-resolution angle-resolved photoemission spectroscopy of solids. An APPLE-II-type variable polarization undulator is equipped for the light source. The undulator can make high intense VUV light with horizontal/vertical linear and right/left circular polarization. The undulator light is monochromatized by the modified Wadsworth-type monochromator with three gratings (R = 10 m; 1200, 2400 and 3600 lines/mm optimized at $h\nu$ = 10, 20, and 33 eV). The energy resolution of light ($h\nu/\Delta h\nu$) is more than 10^4 with the photon flux of more than 10^{11} – 10^{12} ph/s on samples in the whole energy region.

The beamline has a photoemission end-station which equips a 200-mm-radius hemispherical photoelectron analyzer (MB Scientific AB, A-l analyzer) with a wide-angle electron lens and a liquid-helium-cooled cryostat with a 6-axes pulse motor control (A-VC Co. Ltd., i-GONIO). The main purpose is to determine the three-dimensional Fermi surface and electronic structure of solids at low temperatures and their temperature dependence to reveal the origin of the physical properties.

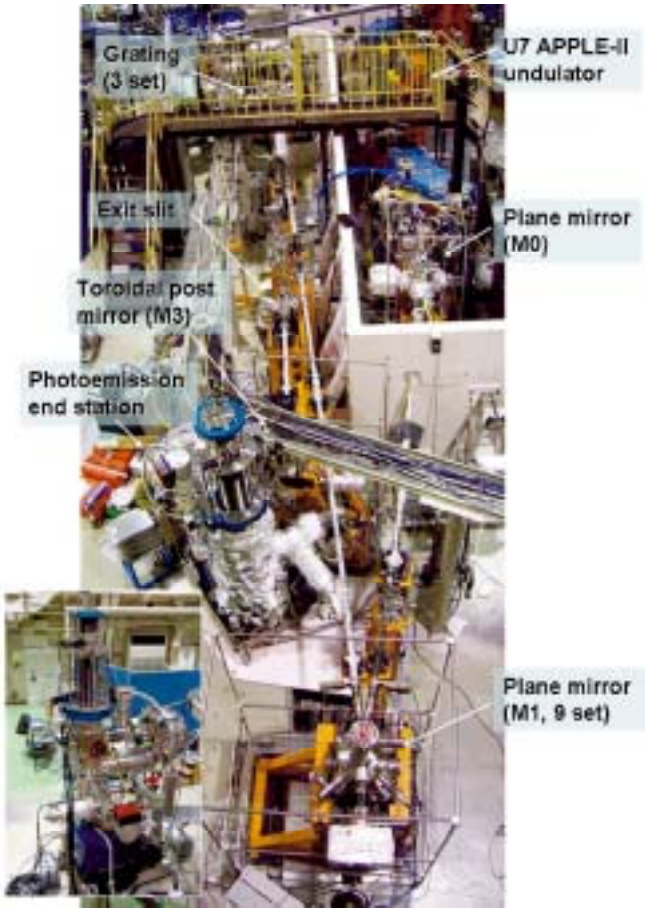

Fig.1. Top-view of BL7U.

Beamline Specifications

Light source	APPLE-II type undulator (λ_u = 76 mm, N = 36)
Monochromator	10-m normal incidence monochromator (modified Wadsworth-type)
Photon energy range	6-40 eV (λ = 30-200 nm)
Resolution ($h\nu/\Delta h\nu$)	1×10^4 - 5×10^4
Photon flux on sample	$\geq10^{12}$ - 10^{11} ph/s (depend on $h\nu$)
Beam size on sample	200(H)×50(V) μm^2
Experiment	Angle-resolved photoemission of solids (MB Scientific A-1 analyzer)

BL7B

3-m Normal Incidence Monochromator for Solid-State Spectroscopy

BL7B has been constructed to provide sufficiently high resolution for conventional solid-state spectroscopy, enough intensity for luminescence measurements, a wide wavelength coverage for Kramers-Kronig analyses, and the minimum deformation to the polarization characteristic of the incident synchrotron radiation. This beamline consists of a 3-m normal incidence monochromator which covers the vacuum ultraviolet, ultraviolet, visible and infrared, *i.e.* the wavelength region of 40-1000 nm, with three gratings (1200, 600, and 300 l/mm). Two interchangeable refocusing mirrors provide two different focusing positions. For the mirror with the longer focal length, an LiF or a MgF_2 window valve can be installed in between the end valve of the beamline and the focusing position. Figure 1 shows absolute photon intensity for each grating with the entrance and exit slit openings of 0.5 mm. A silicon photodiode (AXUV-100, IRD Inc.) was utilized for measuring the photon intensity and the absolute photon flux was estimated, taking the quantum efficiency of the photodiode into account.

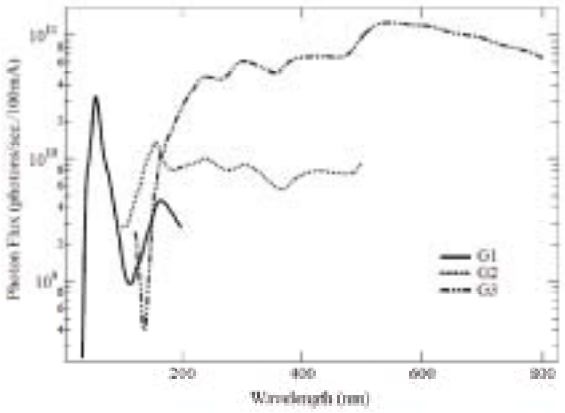

Fig. 1. Throughput spectra of BL7B measured by a silicon photodiode.

Fig. 2. Photo of BL7B.

Beamline Specifications

Monochromator	3-m normal incidence monochromator
Wavelength Range	50 to 1000 nm (1.2 - 25 eV)
Resolution	$E/\Delta E$ = 4000 – 8000 for 0.01 mm slits
Experiment	Absorption, reflection, fluorescence spectroscopy, mainly for solids

BL8B1

Spherical Grating Monochromator for Soft X-Ray Spectroscopic Studies on Solids and Surfaces

The beamline BL8B1 equipped with a constant-deviation constant-length spherical grating monochromator [1] provides soft X-ray photons in the energy range 30-800 eV with medium energy resolution. The photon energy range is covered by using three gratings (R=15 m; 1080 l/mm, R=15 m; 540l/m, and R=7.5m; 360 l/mm) which are interchangeable in vacuum. Figure 1 shows a throughput spectrum measured with the entrance- and exit-slit openings of 10 μm. Under this condition, the achievable resolving power is about 4000 at 400 eV and 3000 at 245 eV, respectively.

An experimental chamber is equipped for conventional measurements of electron yield spectra, or pseudo-photoabsorption spectra, under a ~1×10^{-6} Torr vacuum condition.

[1] A. Hiraya *et al*., Rev. Sci. Instrum. **66** (1995) 2104.

Fig. 1. Photo of BL8B1.

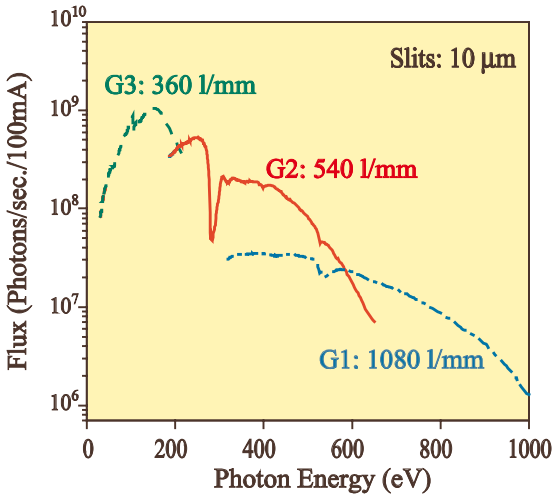

Fig. 2. Throughput of the monochromator at BL8B1.

Beamline Specifications

Monochromator	Constant-deviation constant-length spherical grating type
Energy range	30-800 eV
Resolution	E/ΔE = 4000 at 400 eV and 3000 at 245 eV
Experiment	Photoabsorption spectroscopy, electron spectroscopy and electron-ion coincidence spectroscopy for solids and surfaces

BL8B2

Angle-Resolved Ultraviolet Photoelectron Spectrometer for Solids

BL8B2 is a beamline for angle-resolved ultraviolet photoemission spectroscopy (ARUPS) system which is designed for measuring various organic solids such as molecular crystals, organic semiconductors, and conducting polymers. This beamline consists of a plane-grating monochromator (PGM), a sample preparation chamber with a fast entry Load-Lock chamber, a measurement chamber with an accurate for temperature dependence (base pressure 1×10^{-10} Torr), a cleaning chamber (base pressure 1×10^{-10} Torr), and a sample evaporation chamber (base pressure 3×10^{-10} Torr). The cleaning chamber is equipped with a back-view LEED/AUGER, an ion gun for Ar^{+} sputtering, and an infrared heating unit. The PGM consists of premirrors, a plane grating, focusing mirror, and a post-mirror, with an exit slit. It covers the wide range from 2 to 130 eV with exchanging two gratings (G1: 1200 l/mm, G2: 450 l/mm) and five cylindrical mirrors. The toroidal mirror focuses the divergent radiation onto the sample in the measurement chamber. The spot size of the zeroth-order visible light at the sample surface is about 1×1 mm^2. Figure 1 shows the throughput spectra of PGM (slit=100 μm). The energy resolution at a slit width of 100 μm was found to be E/ΔE = 1000 in the wavelength range from 2 to 130 eV. A hemi-spherical electron energy analyzer of 75 mm mean radius with an angular resolution less than 2° can be rotated around vertical and horizontal axes. The sample mounted on a manipulator can be also rotated around two axes.

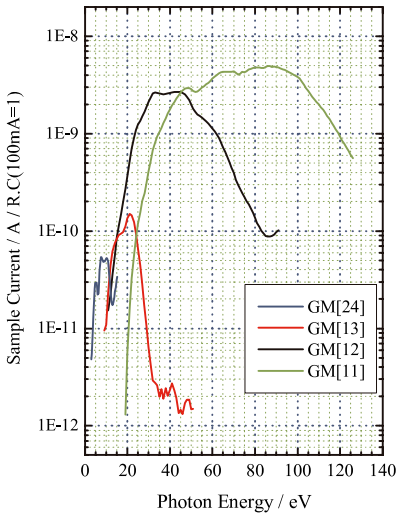

Fig. 1. Throughput spectra of plane-grating monochromator at BL8B2 (slit=100 μm).

Fig. 2. A photo of BL8B2.

Beamline Specifications

Monochromator	Plane-grating monochromator
Wavelength Range	9-600 nm (1.9-150 eV)
Resolution	E/ΔE = 1000
Experiment	Angle-resolved ultraviolet photoemission spectroscopy

FEL

Free Electron Laser

The free electron laser (FEL) at UVSOR-II is parasitically installed at BL5U. The FEL is equipped with a variably polarized optical klystron of 2.35 m long and an optical cavity of 13.3 m long. By using various multi-layer mirrors for the cavity, the FEL can provide coherent light in a wide wavelength range from 800 nm to 199 nm. The pulse width is typically several picoseconds. The repetition rate is about 11 MHz. The average output power depends on the wavelength but its typical value is several 100 mA. The output power higher than 1 W was recorded at 230 nm and 570 nm. The laser pulses are naturally synchronized with the synchrotron radiation pulses which are provided at other synchrotron radiation beam-lines. The laser beam can be transported to the beam lines by using a mirror system for pump and probe experiments if requested.

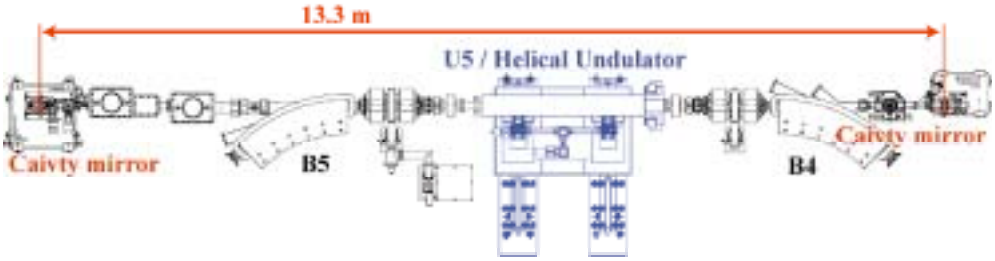

Fig. 1. The schematic of the 13.3-m long optical cavity.

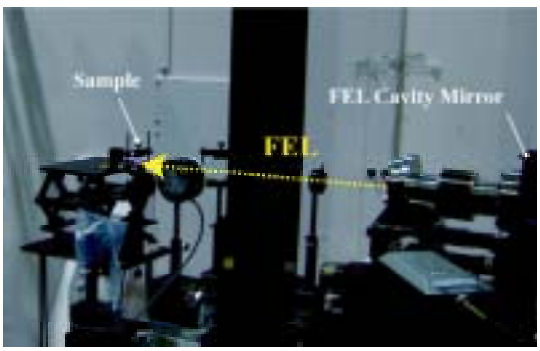

Fig. 2. Left and right circular polarized FEL is delivered to B4.

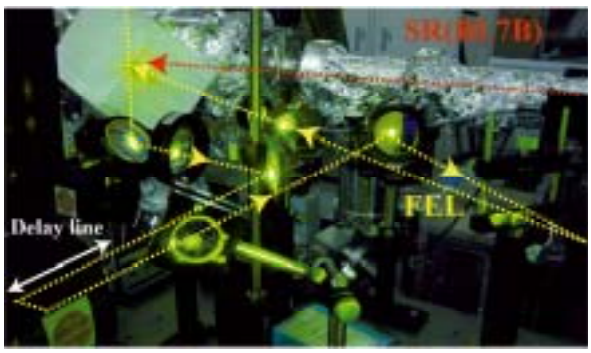

Fig. 3. The FEL is delivered to BL7B. The FEL is irradiated on a target simultaneously with the SR.

FEL Specifications

Wavelength	199-800 nm
Spectral Band Width	~10^{-4}
Polarization	Circular / Linear
Pulse Rate	11.26 MHz
Max. Average Power	~1 W
Cavity Type	Fabry-Perot
Cavity Length	13.3 m
Cavity Mirror	HfO_2, Ta_2O_5, Al_2O_3 multi-layer

FEL

Observation of CHG Spectrum at UVSOR-II

M. Hosaka[1], M. Labat[2, 3], M. Shimada[4], N. Yamamoto[1], M. Katoh[4] and M. E. Couprie[3]

[1]*Graduate School of Engineering, Nagoya University, Chikusa-ku, Nagoya 464-8603, Japan*

[2]*Centre CEA-Saclay, DSM/IRAMIS/SPAM, 91 191 Gif-sur-Yvette, France*

[3]*Synchrotron SOLEIL, Saint Aubin, BP 34, 91 192 Gif-sur-Yvette, France*

[4]*UVSOR Facility, Institute for Molecular Science, Okazaki 444-8585, Japan*

Coherent harmonic generation (CHG) FEL from a relativistic electron beam has an attractive property of producing linearly/circularly polarized short pulse light from UV to VUV region. In the CHG-FEL scheme using an optical klystron (OK), an external laser source is injected inside a first undulator-the modulator-where the energy modulation of electron beam is performed. The conversion into a density modulation occurs in a dispersive section, and coherent emission with strong harmonic content is produced in a second undulator-the radiator. Recently, we have succeeded in observing the CHG-FEL from the U5 optical klystron using a femtosecond Ti:Sa laser [1, 2]. In this report, we describe an experimental spectral analysis of the CHG-FEL as a function of the seeding laser parameter. This study serves not only for the application experiments of the CHG-FEL but also for development of the future seeded free electron lasers.

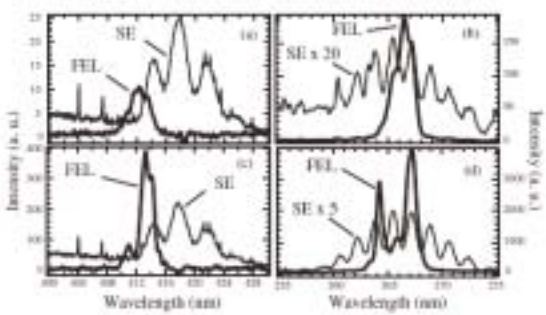

Fig. 1. CHG FEL spectra on the (a) second and (b) third harmonics with smooth focusing configuration and on the (c) second harmonic (sideband at 410.9 nm) and (d) third harmonics (sidebands at 264.2 and 267.2 nm) with the strong focusing configuration. Seeding laser power and pulse duration are 2 W and 1 pic-second-FWHM, respectively. (From ref. [3])

The experiment was performed with the single bunch electron beam at the energy of 600 MeV. The femtosecond Ti:Sa laser at 800 nm with up to 2 W of average power is focused in the middle of the modulator either with a strong focusing of corresponding to a Rayleigh length of Z_R = 0.15 m or a smooth focusing corresponding to a Rayleigh length of Z_R = 1.5 m. Detail of the experimental setup is given in the separated paper [2]. For spectral analysis, the OK radiation is transported to a spectrometer coupled to a fast intensified CCD camera. The ultrashort exposure time (down to 2 ns) of this system isolates the spectra of coherent light pulses at the laser's 1 kHz repetition rate from the 5.6 MHz incoherent light pulses.

Typical examples of the CHG and the spontaneous spectra are presented in Figs. 1(a) and 1 (b). The CHG-FEL spectral lines around 412 nm and 266 nm, are the second and third harmonics of the laser wavelengths (400 nm and 266.6 nm). The measured spectral width is $\Delta\lambda$ = 3 nm ($\Delta\lambda$ = 1 nm) on the second (third) coherent harmonics, while spontaneous emission spectral width reaches 10 nm on both harmonics. Additional spectral lines appear on each side of the initial line. In the example presented in Figs. 1(c) and 1(d), when using a strong focusing, one sideband in the shorter wavelength region of the second harmonics at 410.9 nm and two sidebands grow in the case of the third harmonics.

The growth of sidebands in the spectrum is consequence of the synchrotron motion of the trapped electrons in the ponderomotive potential. For an increasing laser power, the electrons experience a larger displacement in phase space, getting deeper in their rotations cycle. For relatively low laser power, (smooth focusing case) the bunching (density modulation) is optimum, and the associated third harmonic spectrum is monochromatic. As increasing laser power (strong focusing case), the debunching (spoiling of the density modulation) starts while sideband appears in the associated spectrum. The PERSEO simulations reproduce the sideband growth in the case of an overbunched beam. Completed simulation results are described in the separated paper [3].

In conclusion, we have shown that the laser-electron interaction has to be finely adjusted to prevent the spectral structure from being spoiled by the growth of sideband.

[1] M. Labat *et al.,* UVSOR Activity Report **33** (2006) 36.
[2] M. Labat *et al.,* Eur. Phys. J. D **44** (2007) 187.
[3] M. Labat *et al.,* Phys. Rev. Lett. **102** (2009) 014801.

Development of Orbit Feedback System at UVSOR-II

Y. Suzuki[1], M. Katoh[2,1], Y. Takashima[1], M. Hosaka[1], N. Yamamoto[1] and H. Morimoto[1]
[1]*Graduate School of Engineering, Nagoya University, Chikusa-ku Nagoya 464-8603, Japan*
[2]*UVSOR Facility, Institute for Molecular Science, Okazaki 444-8585, Japan*

Abstract

At synchrotron light sources, the drift of the orbit of the electrons in the storage ring causes a drift of the light source position, which affects user's experiments.

At UVSOR-II, an RF feedback system [1] has been operating to suppress the orbit drift on the horizontal plane caused by the thermal expansion of the storage ring floor. However, on the vertical plane, there's no system to stabilize the orbit. Here, we have developed a feedback system by using correction magnets. It was successfully demonstrated that the drift of the electron orbit was suppressed.

Feedback System

We have developed a feedback system to correct the electron orbit distortion. The following is the principle of the system. Firstly, the system gets the displacement of electron orbit from a standard orbit from the BPM (Beam Position Monitor) system, which measures the beam positions at 24 points of the ring. Secondly, the system calculates the applicable strength of correction magnet, which minimizes the displacement by minimizing the followings with SVD (Singular Value Decomposition):

$$S=|R \cdot q+z|^2$$

where R is response matrix calculated from the ring lattice data, q is the applicable strength of the correction magnets, and z is the displacement of the electron orbit. At the last, the system transfers the values of correction strength to the PC controlling the magnet power supplies. The system continues to correct electron orbit with a feedback cycle of 10 seconds.

Figure 1 shows the front panel of the system. In this panel, the operator can select/exclude the BPM or correction magnet for correction and can set previously allowable range of BPM data. If the BPM gets false data, the system would calculate abnormal value. To prevent this case, the system would cancel to transfer the values if the BPM data is out of the range previously set.

Result and Discussion

Figure 2 shows the orbit drift on the vertical plane without the feedback, and Fig.3 shows that with the feedback. The system was successfully working for 6 hours without any errors. It was demonstrated that the orbit drift was suppressed within a few tens of microns, and small oscillations (seen in Fig.2) were removed.

Conclusion

We have developed the feedback system. This system was successfully commissioned that orbit suppressed on the vertical plane. The system can be expected to contribute to high precision stabilization at UVSOR-II in the future.

Fig. 1. Front panel of Feedback System.

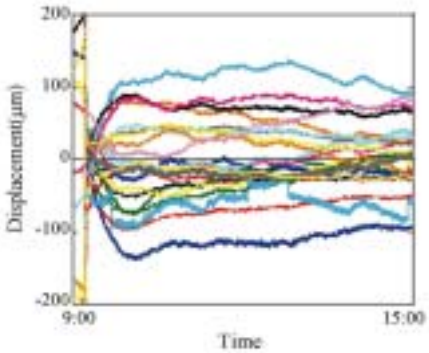

Fig. 2. Displacement of orbit before introduction of the feedback system.

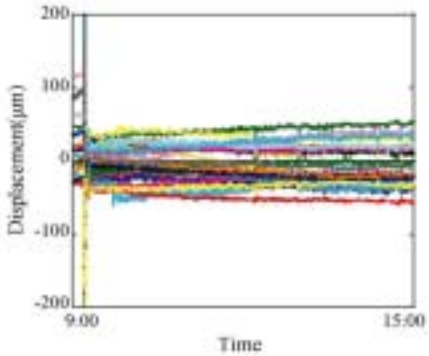

Fig. 3. Displacement of orbit after introduction of the feedback system.

[1] K. Suzumura *et al.*, UVSOR Activity Report **33** (2006) 39.

Development of Superconducting Magnets for Synchrotron Radiation Facility

M. Yoshida[1], Y. Takashima[1], M. Katoh[1, 2], M. Hosaka[1], N. Yamamoto[1], H. Morimoto[1] and M. Torikoshi[3]

[1] *Graduate School of Engineering, Nagoya University, Nagoya 464-8603, Japan*
[2] *UVSOR Facility, Institute for Molecular Science, Okazaki 444-8585, Japan*
[3] *National Institute of Radiological Sciences, Chiba 263-8555, Japan*

Abstract

By using superconducting magnets (SCM), high energy synchrotron light can be radiated. If 5Tesla(T)-SCM is introduced, hard-X ray can be generated by even small circumstance storage ring, such as UVSOR. To apply the SCM scheme for superconducting bends (SCBMs), we designed the pole and coil shapes.

SCBM

The bending angle and peak field are set 12.0 degree and 5 T. The material of the Iron core and coil is of SUY and NbTi, respectively, and the shape of the Iron core is C-type. The coil is cooled by 2 stages 4K-GM cryocooler. At first stage the temperature is cool down to 45K with the cooling power of 40W, at second stage 4.2K with 1.3W. In addition, liquid helium vessel is also set for the accidental case, such as power down of cryocooler. To decrease leak fields, two field cramps are equipped at outside of coil and iron core. The schematic view of the SCBM is shown in Fig.1.

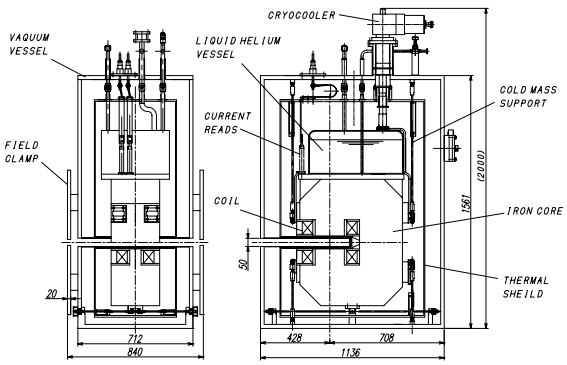

Fig. 1. The schematic view of the SCBM

To study the details of the fields and beam envelops in the SCBM, we have used the add-in program “Radia” [1], which is developed in ESRF. This program enables us to calculate 3D-field distribution with finite elements methods on analytical calculation cord “Mathematica”.

The calculation models of the coil and iron cores are shown in Figs. 2 and 3. In Fig. 3, the red and blue colors indicate the coil and iron core, respectively.

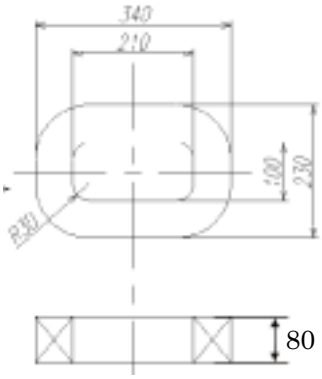

Fig. 2. coil shape

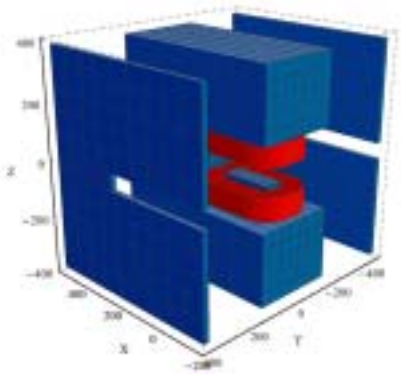

Fig. 3. SCBM simulation model.

Field mapping

We have calculated the field map on the beam orbit plane from the SCBM model, as shown in Fig. 4. In this figure, the requirement field of 5 T is obtained.

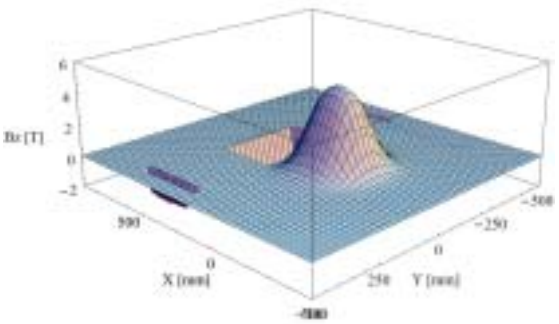

Fig. 4. SCBM field map.

[1] http://www.esrf.eu/

Stabilization of Optical Cavity of UVSOR-II Free Electron Laser

M. Koike[1], M. Hosaka[1], M. Katoh[2, 1], Y. Takashima[1], M. Adachi[2], N. Yamamoto[1], T. Tanikawa[3] and J. Yamazaki[2]

[1]*Graduate School of Engineering, Nagoya University, Nagoya 464-8603, Japan*
[2]*UVSOR Facility, Institute for Molecular Science, Okazaki 444-8585, Japan*
[3]*School of Physical Sciences, The Graduate University for Advanced Studies (SOKENDAI), Okazaki 444-8585, Japan*

Introduction

At the UVSOR storage ring, free electron laser (FEL) experiments have been made using a helical optical klystron. We have already succeeded in high power lasing around 1 W in the deep UV region and the shortest wavelength attained so far is 199nm [1]. Recently, application experiments of the FEL in the deep UV region such as photo-electron spectroscopy and irradiation on biological molecules have been carried out. Although a stable FEL is favorable for these applications, we have noticed a rapid power drop with time when the FEL is operated with a high electron beam current (~200 mA). This problem is especially disadvantage for these applications which require higher power FEL.

It was speculated that the power drop was due to distortion of a resonator mirror heated by synchrotron radiation leading to misalignment of the optical cavity. To prevent the power drop, we have developed a feedback system correcting automatically the optical cavity alignment by controlling mirror angle.

Feedback System

Figure 1 shows the outline of the feedback system. First, transmitted FEL power through a cavity mirror is measured by a photodiode, is processed and is send to a personal computer. Then the software on the personal computer decides the direction of a mirror to change. The principle of changing the mirror angle is based on comparison of FEL powers before and after the change of the mirror angle. If the FEL power after changing the mirror angle is higher than one before changing it, the software decides to change the mirror angle to the same direction again. On the other hand, if the FEL power after changing the mirror angle is lower than one before changing, it decides to change to the opposite direction.

Finally, the software transfers the determined value to a stepping motor controller, and the mirror angle is changed adjusting a gimbal by the step motor. This routine action is made every 2 seconds and it controls upstream and downstream cavity mirrors.

Result and Discussion

Figure 2 shows the FEL power variation at 230nm before and after introduction of the feedback system. It is clear that the FEL power has been stable and the rapid FEL power drop has been suppressed. Before introduction of this feedback system, FEL power decreases by a half in about 10 minutes. After the introduction, the FEL power in 10 minutes remains almost unchanged

Conclusion

We have developed a feedback system to stabilize the FEL power by changing mirror angles. The system was successfully commissioned.

As future plan, we aim more accurate correction by controlling RF frequency to synchronize the revolution frequency with the FEL round trip frequency.

Fig. 1. Block diagram of the feedback system.

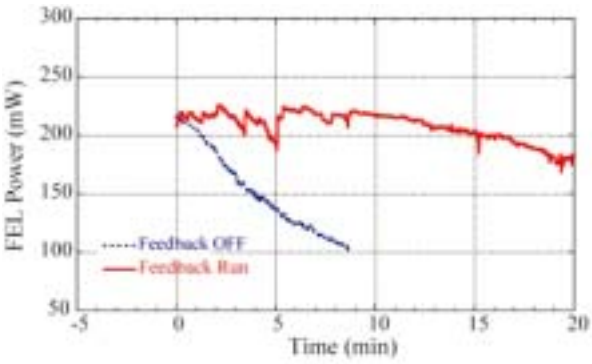

Fig. 2. FEL power variation before and after introduction of the feedback system.

[1] M. Hosaka *et al.*, UVSOR Activity Report **35** (2008) 40.

Top-Up Test Operation at UVSOR

K. Hayashi, M. Katoh, M. Adachi and J. Yamazaki
UVSOR Facility, Institute for Molecular Science, Okazaki 444-8585, Japan

Introduction

Keeping the beam current constant with intermittent injection (so-called top-up operation) has been realized at several synchrotron radiation facilities. With top-up operation, we can provide not only higher photon flux but also constant flux to beamlines. It is expected that the stability of the light beam also improves, mainly owing to temperature stabilization of the accelerator and beamline components. Thus, top-up operation has been one of the most important plan at UVSOR.

To achieve top-up operation, we had already upgraded the power sources for the booster synchrotron and the beam transport line. With this upgrade, 750MeV (full energy) injection had been enabled. To ensure radiation safety, we had installed a lead shielding wall around the storage ring.

In fiscal 2008, we prepared:

1. An interlock system to ensure the integrated charge (electron number) lower than a specified limit, and a trigger managing module to automatically keep the beam current to a fixed value.
2. Two copper slits in beam transport line.

Soon after obtaining permission of Ministry of Education, Culture, Sports, Science and Technology in October 2008, we began top-up test operation.

Injection Charge Measurement and Automatic Injection System

Injection charge measurement is necessary for radiation safety. With this system (Fig.1), we measure the weekly integration of injected charge (electron number) in top-up mode. If the integration goes over the limit, high voltage for the beam transport magnets will be turned off. Injection module automatically turn on/off the injection trigger to keep the beam current to a fixed value. Electron charge is measured using Integrated Current Transformer (Bergoz Co.).

Fig. 1. Charge integration and automatic injection module (left), Integrating Current Transformer (right).

Slits at Beam Transport Line

Two slits which utilize 60mm thick copper blocks were introduced to the beam transport line (Fig. 2). One purpose is keeping radiation at storage ring low, cutting off the electrons slipping off the central orbit which will be lost in storage ring. Another purpose is protection of magnet poles of in-vacuum type undulators.

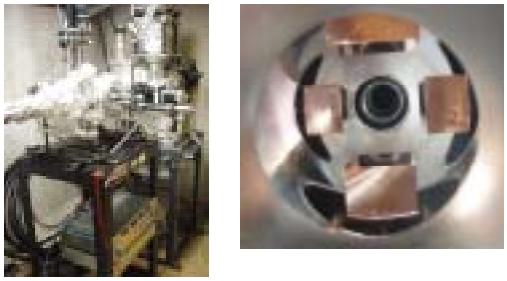

Fig. 2. A slit located at beam transport line.

Status of Top-Up Operation

An example of beam current trend is shown in Fig. 3. Short time fluctuation due to beam loss in every interval is about 1.5mA, which corresponds to 0.5 percent of stored beam. Some dips in the graph are due to decrease of the injection efficiency, which should be settled in future improving the stability of accelerator components.

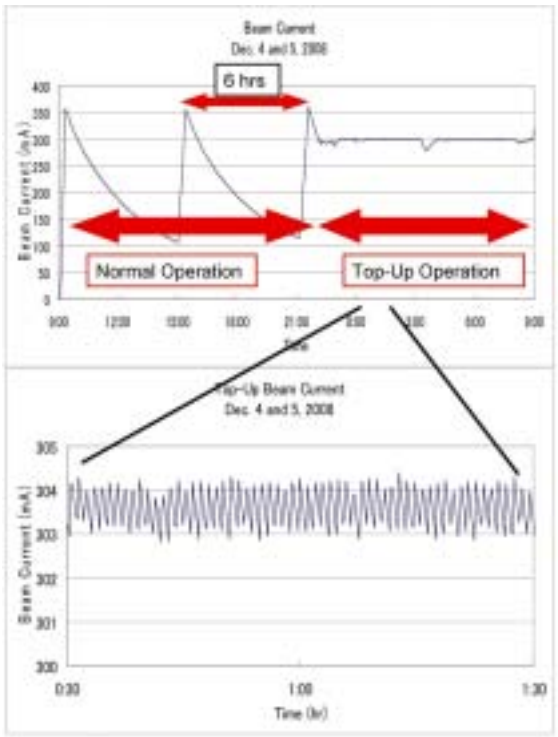

Fig. 3. A beam current trend in top-up test operation. One minute interval, up to 15 seconds injection. The data was taken every 12 second.

BL6U

Construction of New Soft X-Ray Spectroscopy Beamline BL6U

E. Shigemasa[1], Y. Hikosaka[1], E. Nakamura[1], N. Kondo[1], M. Sakai[1], T. Horigome[1] and K. Amemiya[1, 2]

[1]*UVSOR Facility, Institute for Molecular Science, Okazaki 444-8585, Japan*

[2]*Photon Factory, Institute of Materials Structure Science, Tsukuba 305-0801, Japan*

Various types of monochromators for synchrotron radiation have been proposed and constructed to realize vibrational spectroscopy in the soft x-ray range, which contains the *K*-shell thresholds of chemically important elements like C, N, and O, since the first successful observation for the vibrational structures of the π* resonance in the *K*-shell photoabsorption spectrum of nitrogen molecules [1]. Thanks to the high brilliance offered by undulator radiation, both high-resolution and high-flux are achievable simultaneously at a considerable high level. At the UVSOR, there is only one soft X-ray undulator beamline for high resolution spectroscopy, BL3U, in the photon energy region of interest.

A new project for constructing the undulator beamline BL6U has been recently initiated. The entrance slit-less configuration for the monochromator has been chosen. In order to cover a wide photon energy region (30-500 eV) with one single grating, a variable-included-angle Monk-Gillieson mounting monochromator with a varied-line-spacing (VLS) plane grating [2] has been selected. Design study for the monochromator at BL6U has been completed, with the collaboration of KEK-PF. The monochromator designed will cover the photon energy ranging from 30 to 500 eV, with the resolving power higher than 10000 and the photon flux more than 10^{10} photons/sec.

The resolution of the present monochromator was studied by ray-tracing simulation as well as analytical estimation. It is found that a resolving power E/ΔE of more than 10000 is achievable over the energy range from 30 to 500 eV with one single grating. The throughput photon flux estimated ranges from 10^{10} to 10^{12} photons/sec for the ring current of 350 mA, with a resolving power of 10000.

Figure 1 shows the overall picture of the beamline constructed, with pictorial indications for the incoming undulator radiation and important beamline components. In front of all optical elements, there is an aperture S_0, located 5.0 m from the source position. The radiation is deflected horizontally by a toroidal mirror M_0 located 1.5 m downstream of the aperture. M_0 converges the radiation vertically onto a virtual focal point behind the VLS grating G, and thus converging soft X-rays illuminate G. A plane mirror M_1 is located 1.5 m behind M_0. One laminar profile plane grating, which is ruled holographically, with the varied-line-spacing (500 l/mm at its center position), is designed to cover the energy range from 30 to 700 eV. The included angle of the grating should be changed from 167° to 176° in order to minimize the aberrations. A refocusing mirror M_2 has a toroidal shape, which focuses the monochromatized radiation at the sample position.

The practical construction of BL6U has started from the summer of 2008. After careful tuning of the whole system at BL6U, the first light was observed in December 2008. The performance tests of the monochromator have been performed, whose results are given in a separate page in this report. High resolution spectroscopic studies, not only in gas phase, but in solids or surfaces, are planned to be conducted there. The constructions of the apparatuses for high-resolution electron spectroscopy have also begun.

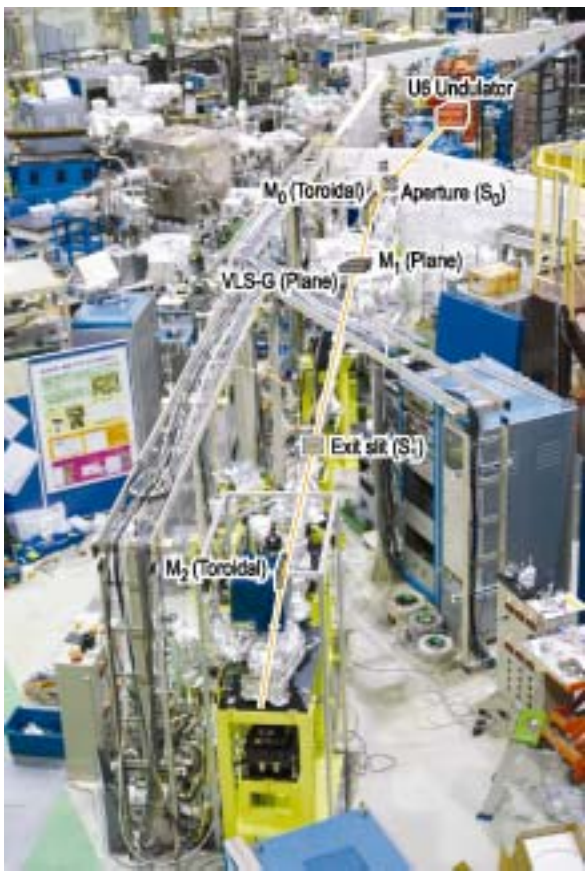

Fig. 1. Top view of the newly constructed soft X-ray spectroscopy beamline BL6U.

[1] C. T. Chen, Y. Ma and F. Sette, Phys. Rev. A **40** (1989) 6737.

[2] K. Amemiya and T. Ohta, J. Synchrotron Rad. **11** (2004) 171.

BL6U

Performance of New Soft X-Ray Spectroscopy Beamline BL6U

E. Shigemasa[1], Y. Hikosaka[1], E. Nakamura[1], N. Kondo[1], M. Sakai[1], T. Horigome[1] and K. Amemiya[1, 2]

[1]*UVSOR Facility, Institute for Molecular Science, Okazaki 444-8585 Japan*

[2]*Photon Factory, Institute of Materials Structure Science, Tsukuba 305-0801 Japan*

The in-vacuum type undulator U6, which has been relocated from the long straight section U7 to the short one U6, has 26 magnetic periods and the period length is 36 mm [1]. The spectral region from 50 eV to 140 eV, which is realized by changing the gap height from 15 mm to 40 mm, was covered with the first harmonic radiation [1]. There was an inherent energy gap between the highest and lowest photon energies, covered by the first and third harmonics, respectively. Due to the relocation of the undulator, this gap has been bridged. This is because the vertical betatron function at U6 is smaller than that at U7 and the minimum gap available becomes accordingly smaller down to 10 mm. Correspondingly the tunability covered by the undulator radiation is widened: the photon energy range from 30 to 500 eV can be covered by odd harmonics up to seventh without any energy gap. Then a new project for constructing the undulator beamline BL6U has recently been initiated.

According to the theoretical estimations by using the ray-tracing program XRAY-T [2] in combination with the synchrotron radiation calculation code named SPECTRA [3], the monochromator designed for BL6U, which possesses a variable-included angle mechanism, can cover the photon energy ranging from 30 to 500 eV by one single grating, with the resolving power higher than 10000 and the photon flux more than 10^{10} photons/sec. We have carried out short performance tests of the monochromator installed.

Figure 1 shows an example of the throughput spectra measured by a gold plate located just after the exit slit. Here the exit slit opening and the undulator gap were set at 30 μm and 22.5 mm, respectively. The included angle was fixed at 171°, which corresponds to the optimum condition for 80 eV. The measured photocurrent has been converted to the photon flux, by assuming that the quantum yield of Au is equal to 3% in the entire photon energy range of interest. The slit opening of 30 μm corresponds to E/ΔE ~ 10000 at 80 eV. It is found that the photon flux of the fundamental peak around 100 eV goes over 1×10^{12} photons/sec. The photon flux in the high energy region may be improved, by changing the included angles as satisfying their optimums during the photon energy scanning.

Figure 2 displays a total-ion yield spectrum in the vicinity of the 3d ionization thresholds of Kr, measured by an imaging spectrometer. The slit opening and undulator gap were the same as the above measurement. Two Rydberg series converging to the 3d ionization thresholds are identified as indicated here. Assuming that the natural width of the Kr $3d^{-1}$ 5p Rydberg states is 83 meV [4] and the spectral profile observed is expressed by a Voigt function, the monochromator band-pass is estimated to be ~25 meV. Since the theoretical value is about 10 meV around 90 eV, there is room for improvement on the resolving power.

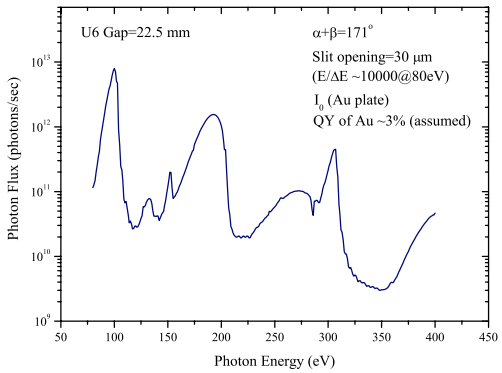

Fig. 1. Estimated throughput spectrum from the VLS-PGM at BL6U.

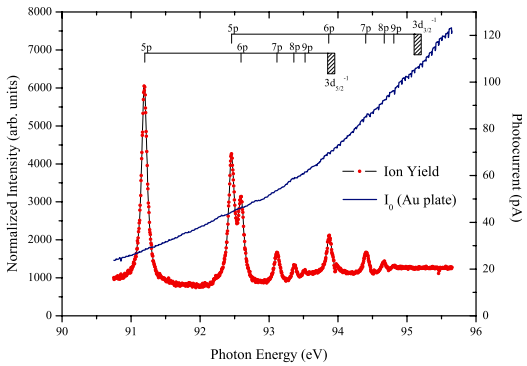

Fig. 2. Total-ion yield curve measured in the region of the 3d subshell of Kr.

[1] A. Mochihashi, M. Katoh, M. Hosaka, K. Hayashi, J. Yamazaki, Y. Takashima, Y. Hori, H. Kitamura, T. Hara and T. Tanaka, AIP Conf. Proc. **705** (2004) 259.

[2] K. Amemiya, H. Kondoh, T. Yokoyama and T. Ohta, J. Electron Spectrosc. Relat. Phenom. **124** (2002) 151.

[3] T. Tanaka and H. Kitamura, J. Synchrotron Radiat. **8** (2001) 1221.

[4] O.-P. Sairanen, A. Kivimäki, E. Nõmmiste, H. Aksela and S. Aksela, Phys. Rev. A **54** (1996) 2834.

BL7U

Present Status of UVSOR-II BL7U for VUV Angle-Resolved Photoemission Spectroscopy of Strongly Correlated Electron Systems

T. Ito[1, 2], M. Sakai[1], E. Nakamura[1], N. Kondo[1] and S. Kimura[1, 2]

[1]*UVSOR Facility, Institute for Molecular Science, Okazaki 444-8585, Japan*

[2]*School of Physical Sciences, the Graduate University for Advanced Studies (SOKENDAI), Okazaki 444-8585, Japan*

BL7U, the VUV angle-resolved photoemission (ARPES) beamline for advanced studies of strongly correlated electron systems, has been constructed in FY2006 and opened for users in FY2007 [1]. To satisfy the needs from users, especially (1) higher photon-flux, (2) reduction of higher-order light and (3) better base pressure of the photoemission chamber, we have improved the beamline in FY2008. As a result, we successfully achieved the sufficient throughput for ARPES experiments.

To improve the photon-flux especially at the bulk-sensitive low photon-energy ($h\nu$ < 15 eV), we updated the lowest photon-energy grating G3 from Au-coating to SiC-coating one. After the update of G3, we realign the beamline to be optimized with the center of the undulator light. As a result, the photon flux as well as the focusing at the sample position has intensively been improved than that in FY2007. Figures 1(a), (b) and (c) show the improved throughput spectra obtained at low (red line)-, medium (red line)-, and high (red, yellow, green, blue lines)-photon energy regions compared with the previous one (black lines), respectively. At each energy region, the spectrum becomes sharper and shifts to the higher energy side in the same condition, indicating successful alignment with the optimum parameter of the undulator light. Clear vibration sub-bands observed higher and lower energy side of the main peak of the throughput spectrum (Fig. 2), which is consistent with a calculation, ensures the correct alignment getting the center of the undulator light.

To reduce the intensity of higher order light at the low photon-energy region, we equipped a VUV filter of MgF_2 just after the exit slit. As a result, we successfully reduced the higher-order light above $h\nu$ = 11 eV (see Fig. 3). Typical loss of efficiency by the filter is less than 10%, which ensures sufficient throughput for VUV ARPES experiments with bulk-sensitive low-photon energies.

Finally, to improve the base pressure at the sample, we added a cryopump (ULVAC Cryogenic Inc., U8H) and an ion pump (ULVAC, PST-200CX2) to the photoemission chamber. As a result, we achieved the base pressure of 5×10^{-9} Pa better than before (2×10^{-8} Pa). For further improvement of base pressure, we plan to equip a thermal radiation shield around the sample in FY2009.

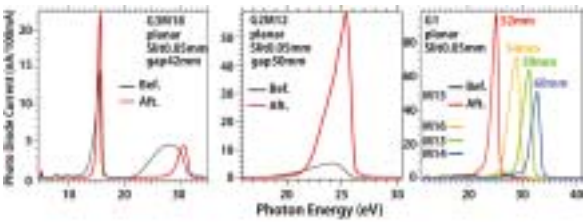

Fig. 1. Improvements of throughput spectra before and after the realignment of optics at BL7U.

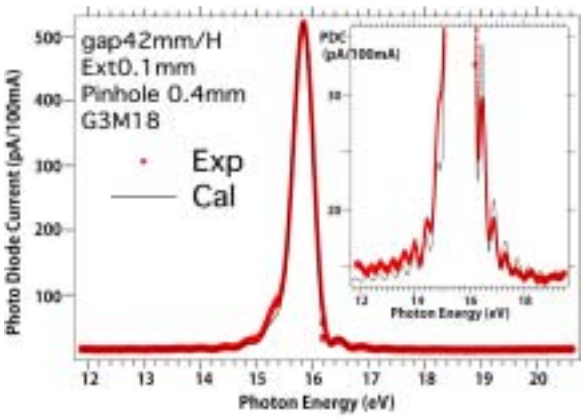

Fig. 2. Throughput spectrum at low photon-energy region in comparison with the calculation.

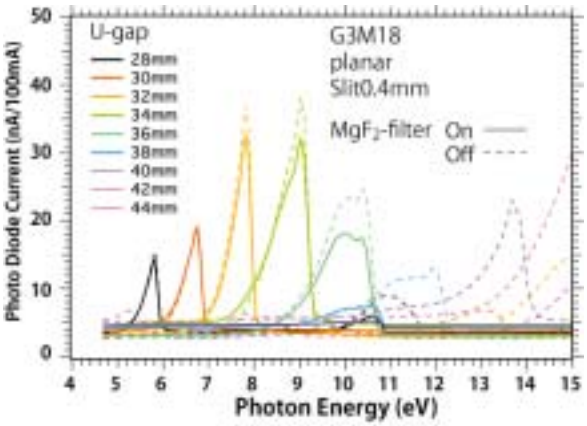

Fig. 3. Throughout spectra with some undulator gap size with and without a VUV filter, MgF_2, in the low photon-energy region.

[1] S. Kimura *et al.*, AIP Conf. Proc. **879** (2007) 527.

BL3U

Exchange Interaction of the Rydberg Electron Bound by Doubly Charged Ions in Small Krypton Clusters Studied by Resonant Auger Spectroscopy

M. Nagasaka[1], T. Hatsui[2], H. Setoyama[1], N. Kosugi[1] and E. Rühl[3]
[1]*Institute for Molecular Science, Myodaiji, Okazaki 444-8585 Japan*
[2]*XFEL Project Head Office, RIKEN, Sayo-cho, Hyogo 679-5148, Japan*
[3]*Physikalische Chemie, Freie Universität Berlin, Takustr. 3, D-14195 Berlin, Germany*

In the core-to-Rydberg excitation of small krypton clusters, we have evaluated the surface-site dependent exchange (*EX*) interaction of the Rydberg electron with the nearest neighbor atoms by using X-ray absorption spectroscopy (XAS) [1 – 3]. After the resonant Auger decay following the core-to-Rydberg excitation, the spectator-type Auger final state can be regarded as a Rydberg electron bound by a doubly charged ion. The Rydberg electron bound by a singly charged core-hole state could be decreased by a doubly charged ion, increasing the short-range *EX* interaction. In the present work, we have evaluated the site-dependent *EX* energies of the Rydberg electron with the neighbor atoms in a doubly ion by using resonant Auger electron spectroscopy (RAS).

The experiments were performed at BL3U. Kr clusters with <*N*>~15 were formed by the supersonic gas expansion method. RAS spectra were measured with a hemispherical electron energy analyzer (SCIENTA SES-200 combined with MBS A-1).

Figure 1 shows RAS spectra after the Kr $3d_{5/2}^{-1}5p$ Rydberg excitation (91.37 eV) at the edge-site atom of small Kr clusters [1 – 3]. Because the ratio of edge and face sites is 3:1 in this excitation energy, the ratio in RAS is set to be 3:1 for the fitting procedure. As shown in Table 1 and Fig. 1, the observed final-state energies of both the 5p and 6p states are redshifted from the atomic one, indicating the induced polarization (*PL*) effect is dominant. As in the case of XAS, the energy shift of the Rydberg states (i = 5, 6) is given by ΔE_i (RAS) = *PL* (+2) + EX_i (+2), where *PL* (+2) can be approximated as 4 *PL* (+1). Table 1 shows *EX* in the doubly charged ion at different surface sites. *EX* (+2) is almost proportional to the number of nearest neighbor atoms within the first coordination shell. *EX* (+2) of the 5p state is 2.3 times larger than *EX* (+1) of the 5p state, indicating contraction of the Rydberg orbital as demonstrated in Fig. 2. Table 1 shows the 6p electron bound by the doubly charged ion has a similar *EX* energy to the 5p electron bound by the singly charged ion, also indicating contraction of the Rydberg orbital.

In conclusion, RAS spectra of small krypton clusters show redshifts from the atomic peaks, indicating the *PL* effect is dominant even in the lowest Rydberg state. Furthermore, the *EX* effect is also enhanced in the Auger final state, indicating the contraction of the Rydberg orbital under the stronger potential by the doubly charged ion. The *EX* interaction of the Rydberg electron with the surrounding atoms is short-range interaction and is almost proportional to the number of the nearest neighbor atoms.

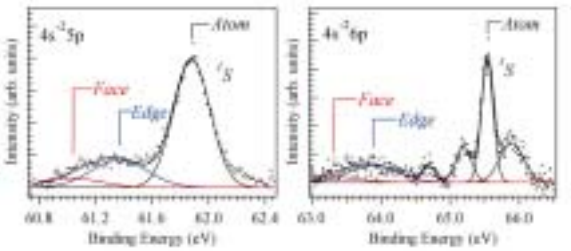

Fig. 1. RAS spectra of different surface sites in small krypton clusters for the $4s^{-2}5p$ and $4s^{-2}6p$ final states after the edge-site excitation in the $3d_{5/2}^{-1}5p$ state (91.37 eV).

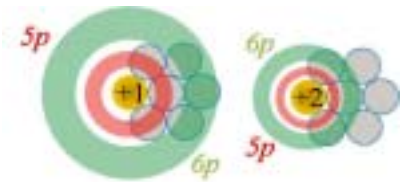

Fig. 2. Schematic Rydberg orbitals bound by singly and doubly charged ions at a surface site of small krypton clusters.

Table 1. Surface-site dependent *EX* energies (in eV) of the Rydberg electron bound by doubly charged ions of small krypton clusters. The bulk site corresponds to the large krypton clusters [4].

eV	ΔE	*PL*(+2)	*EX* (+2)	*EX* (+1)
$4s^{-2}5p$				
Edge	-0.51	-2.28	1.77	0.74
Face	-0.84	-3.16	2.32	1.01
Bulk	-1.0	-4.3	3.3	1.47
$4s^{-2}6p$				
Edge	-1.66	-2.28	0.62	0.22
Face	-2.22	-3.16	0.94	0.28
Bulk	-2.8	-4.3	1.5	0.42

[1] M. Nagasaka, T. Hatsui and N. Kosugi, in this volume.
[2] M. Nagasaka, T. Hatsui and N. Kosugi, J. Electron Spectrosc. Relat. Phenom. **166-167** (2008) 16.
[3] A. Knop, B. Wassermann and E. Rühl, Phys. Rev. Lett. **80** (1998) 2302.
[4] S. Peredkov *et al.*, Phys. Rev. A **72** (2005) 021201.

BL2B

Electron Ion Coincidence Spectroscopy of C_{60} Using Synchrotron Radiation Photoionization

C. Huang[1], H. Katayanagi[1, 2], B. P. Kafle[1], Md. S. I. Prodhan[2], H. Yagi[1], K. Nakajima[1, 3] and K. Mitsuke[1, 2]

[1]*Institute for Molecular Science, Okazaki 444-8585, Japan*

[2]*Graduate University for Advanced Studies, Okazaki 444-8585, Japan*

[3]*Science Research Center, Hosei University, Chiyoda-ku, Tokyo 102-8160, Japan*

Photoelectron-photoion coincidence (PEPICO) spectroscopy is one of the most powerful methods for studying the kinetics and dynamics of chemical reactions involving excited molecules and ions. We therefore consider that unimolecular decomposition processes of fullerenes can be closely studied using a PEPICO method. This report presents a recent results obtained with an electron detector newly incorporated into a photoionization time-of-flight mass spectrometer using synchrotron radiation of $h\nu$ = 25-120 eV.

All experiments were carried out at the bending magnet beam line BL2B. Parent C_{60}^{z+} and fragment C_{60-2n}^{z+} ions ($n \geq 1$, z = 1-3) were measured at $h\nu$ = 50 – 120 eV. Since no small ionic carbon cluster C_m^{z+} (m = 1-5) was observed, the emission of neutral C_2 rather than C_m^{z+} is the main fragmentation channel of C_{60}^{z+}. As for the singly charged fragments, C_{58}^{+} and C_{56}^{+} were detected only at a very narrow $h\nu$ range. Above 60eV, their intensities become negligibly weak. This probably means that C_{60}^{+} ions with their internal energy higher than ~60 eV are stabilized rapidly by emitting one or two electron(s), *before* being converted to high-vibrationally excited states through nonadiabatic transitions (i.e. internal conversion) followed by statistical redistribution of excess energy and sequential ejection of C_2 units [2].

Taking mass spectra with scanning the monochromator allowed us to measure the ion yield curves for C_{60}^{z+} and C_{60-2n}^{z+} as a function of $h\nu$. The relative total photoionization cross section was calculated from the total ion yield curve of C_{60} and agrees well with our former results [1]. Next, the ratio $\sigma(C_{60-2n}^{z+})/\sigma(C_{60}^{+})$ between the relative photofragmentation cross section for C_{60-2n}^{z+} ($n \geq 1$, z = 1-3) and that for C_{60}^{+} was calculated from the yield curves of the respective ions. This ratio was measured also in pulsed ion sampling by applying a positive pulsed voltage to the repeller electrode. Figure 1 shows our results of $\sigma(C_{58}^{2+})/\sigma(C_{60}^{+})$ determined by PEPICO and pulsed ion sampling, together with the previous data of Reinköster *et al.* and Juranic *et al*. [3, 4]. The two data from the literature have been measured by pulsed ion sampling.

All the results of pulsed ion sampling show that the ratio almost levels off after passing its maximum value. In contrast, our PEPICO curve exhibits a pronounced decrease after the maximum at 75 eV. The ratios of $\sigma(C_{56}^{2+})/\sigma(C_{60}^{+})$ and $\sigma(C_{54}^{2+})/\sigma(C_{60}^{+})$ have similar tendencies. The different behaviors of the $\sigma(C_{60-2n}^{2+})/\sigma(C_{60}^{+})$ curves for different detection methods can be understood [2] from expectation that the magnitude of the average internal energy remaining in nascent C_{60}^{z+} ions produced in PEPICO is larger than that in pulsed ion sampling.

The appearance energies and peak positions of the yield curves for the fragment ions were found to be shifted in the higher $h\nu$ direction than those summarized in [2].

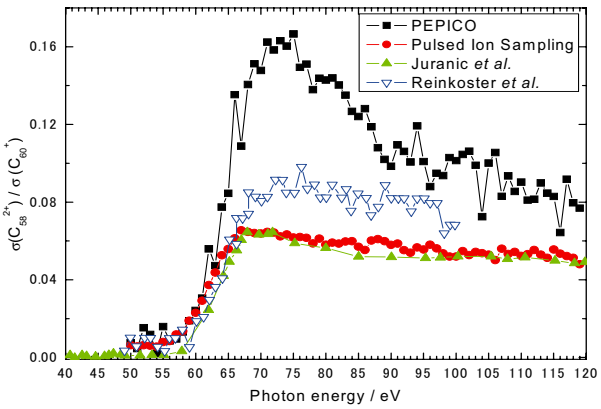

Fig. 1. Ratio between the photofragmentation cross section for C_{58}^{2+} and that for C_{60}^{+}.

[1] K. Mitsuke *et al.,* J. Phys. Chem. A **111** (2007) 8336.

[2] J. Kou *et al.,* Phys. Chem. Chem. Phys. **7** (2005) 119.

[3] B. Reinköster *et al.,* J. Phys. B **37** (2004) 2135.

[4] P. N. Juranic *et al*., Phys. Rev. A **73** (2006) 042701.

BL2B

Performance of the Mass Gate Incorporated in the Photofragment Imaging Apparatus for Measuring Momentum Distributions in Dissociative Photoionization of Fullerenes

B. P. Kafle[1], H. Katayanagi[1, 2], C. Huang[1], S. I. Prodhan[2], H. Yagi[1] and K. Mitsuke[1, 2]
[1] *Institute for Molecular Science, Okazaki 444-8585, Japan*
[2] *Graduate University for Advanced Studies, Okazaki 444-8585, Japan*

We have developed a velocity imaging spectrometer, to obtain a reliable velocity distribution of the fullerene fragments using synchrotron radiation [1-3]. Uniqueness of this apparatus is incorporation of a cylindrical *mass gate* and *retarding grid* near the end of the drift tube which are used to eliminate the overlapping of images due to other ionic fragments. Here, we will present preliminary experimental results using Kr to demonstrate their capability of separating ions with a particular charge from those with other charges. The experimental chamber was uniformly filled by Kr sample which was irradiated with a synchrotron radiation in the photoionization region lying between the repeller and extractor electrodes. A pulsed voltage of +75V was applied to the repeller electrode for pushing out photoions, while continuous voltages of 68 and 0 V were applied to the extractor electrode and drift tube , respectively.

Figure 1(a) shows the TOF mass spectra of Kr^{z+} measured in the vicinity of the $3d^{-1}_{5/2}5p^{1}$ resonance peak at $h\nu$ = 91.2 eV, with the mass gate and retarding electrode being grounded. In order to realize isolation of one of the charged state z from the others, e.g. selecting Kr^{2+} from Kr^{z+} (z = 1-3), the following method was adopted: First, setting the voltage of the mass gate (V_M) to zero, the critical voltage on the retarding grid (V_G) was optimized in such a way that no signal was observed. Now, all the ionic species were reflected back as demonstrated in the Fig. 3 of [1]. Then, a pulsed voltage was applied as V_M, at the timing when a bunch of Kr^{2+} ions arrives at the mass gate, so that they gain additional kinetic energies to overcome the potential barrier at retarding grid and can reach the detector. Figure 1(b) shows the spectrum observed at the same voltage combination as that used in Fig. 1(a) except that V_M and V_G were set to 5 and 75 V, respectively. The width of the V_M was 5 μs and its rising edge was preceded by 22 μs by that of the pulsed voltage applied to the repeller. Only a single peak assigned to Kr^{2+} appears in Fig. 1(b). This confirms that the ion selection using the mass gate works well. We also tested our spectrometer for its capability of separating a specific fragment from the other ions produced from SF_6 (not shown here). From the above observation we consider that this setup can be applied for exclusive imaging detection of C_{58}^{+} after excluding C_{60}^{+} and C_{56}^{+} with the same kinetic energies.

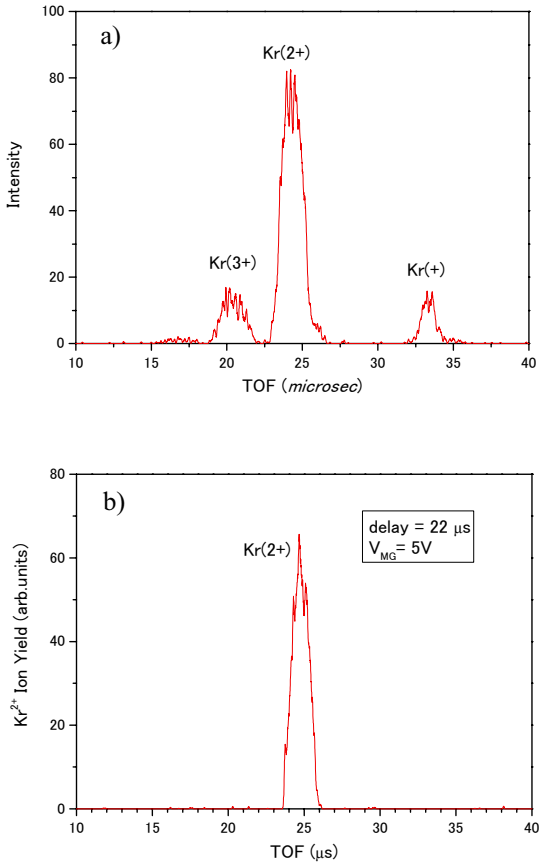

Fig. 1. (a) TOF spectrum of Kr at $h\nu$ = 91.2 eV. The mass gate and retarding grid are kept grounded. (b) TOF spectrum of Kr measured with V_M = 5 V and V_G = 75 V.

[1] B. P. Kafle, H. Katayanagi and K. Mitsuke, AIP Conf. Proc. **879** (2007) 1809.
[2] Md. S. I. Prodhan *et al.*, Chem. Phys. Lett. **469** (2009) 19.
[3] H. Katayanagi *et al.*, in preparation.

BL2B

Ion Imaging Study of Dissociative Photoionization of C_{60}

H. Katayanagi[1, 2], C. Huang[1], S. I. Prodhan[2], H. Yagi[1], B. P. Kafle[2], K. Nakajima[3] and K. Mitsuke[1, 2]

[1]*Department of Photo-Molecular Science, Institute for Molecular Science, Okazaki 444-8585, Japan*

[2]*Graduate University for Advanced Studies, Okazaki 444-8585, Japan*

[3]*Science Research Center, Hosei University, Tokyo 102-8160, Japan*

The photoion images of fullerene molecular beams, which consist of parent and fragment ions, were obtained by the velocity map imaging (VMI) technique [1]. The fragments were observed as weak shoulders in transverse profiles of the beam.

The design of our imaging setup was described elsewhere [2, 3]; we explain the experimental procedure briefly. The fullerene (C_{60}) sample was loaded in a cylindrical quartz cell and heated up by a heater around 700-800 K in vacuum. The C_{60} vapor passed through two apertures and reached the ionization region, where the C_{60} molecular beam intersected the monochromatized synchrotron radiation (SR). Ions produced at the ionization region were extracted by a VMI electrode assembly and projected on to a position sensitive detector (PSD) of 40 mm in diameter and 375 mm away from the ionization region. No mass selection was made. We thus obtained two-dimensional projections of three-dimensional scattering distributions of the ions on the PSD.

The photoion images were recorded in the photon energy range from 60 to 110 eV. Fig. 1 shows the photoion images at 60 (a) and 110 (b) eV. Vertical stripes along *x* axis correspond to the beam. Images of other photon energies resemble the images shown here. Background images obtained without the C_{60} beam was subtracted from all the images.

Figure 2 shows one-dimensional projections of the images along *y* axis with integration of pixel intensities with respect to *x*. These projections can, therefore, be regarded as the transverse intensity profiles of the beam. An intense central component of the profiles originates from parent ions of C_{60}. In addition to the intense component, we can recognize shoulders on both sides. Intensities and widths of the shoulders increased with increasing photon energy. The shoulders can be assigned to the photofragments produced by the dissociative photoionization of C_{60} with SR, since the fragments obtained translational energy by the dissociative photoionization and escaped from the central component. This assignment is supported by computer simulations of C_{60} fragmentation. The shapes of the shoulders agreed qualitatively with results of the simulations. Furthermore, the energy dependence can be interpreted as that the smaller and more highly translationally accelerated fragments can be produced with increasing photon energy. This interpretation agrees with our previous conclusions on the dissociation dynamics of fullerenes [4, 5].

In the present study, we found that the fragments could be observed even without mass selection. The mass selection will allow us more quantitative analyses on translational energy release distributions. We developed a potential switch mass gate [2], which enables us to select a specific fragment from a series of fragments. We are now testing the mass gate experimentally.

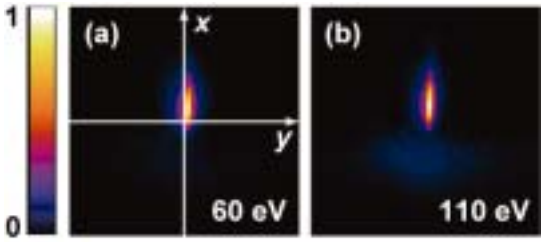

Fig. 1. Photoion images of C_{60} molecular beams (parent and fragment ions) at 60 (a) and 110 (b) eV. In panel (a), *x* axis corresponds to the direction of the molecular beam and *y* axis to the synchrotron radiation. Images are 22.5×22.5 mm in size. Pixel size is 0.176×0.176 mm.

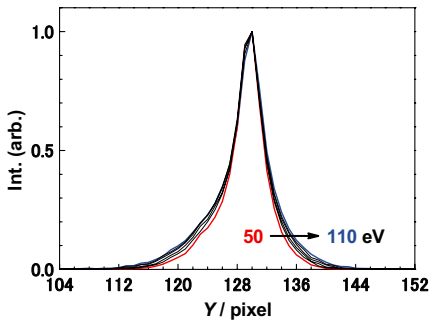

Fig. 2. Transverse intensity profiles of the beam. Curves are plotted every 10 eV in the photon energy range from 50 to 110 eV. Peak intensities of the curves are normalized to unity.

[1] A. T. J. B. Eppink and D. H. Parker, Rev. Sci Instrum. **68** (1997) 3477.

[2] B. P. Kafle *et al.*, AIP Conf. Proc. **879** (2007) 1809.

[3] S. I. Prodhan *et al.*, Chem. Phys. Lett. **469** (2009) 19.

[4] J. Kou *et al.*, Phys. Chem. Chem. Phys. **7** (2005) 119.

[5] K. Mitsuke *et al.*, AIP Conf. Proc. **811** (2006) 161.

BL2B

Dissociative Photoionization of Perfluorocyclobutane

K. Okada[1, 2], M. Sakai[1], C. Huang[2], H. Yagi[2], H. Katayanagi[2, 3], K. Mitsuke[2, 3] and K. Tabayashi[1]

[1]*Department of Chemistry, Hiroshima University, Higashi-Hiroshima 739-8526, Japan*

[2]*Institute for Molecular Science, Okazaki 444-8585, Japan*

[3]*Graduate University for Advanced Studies, Okazaki 444-8585, Japan*

Molecular photoionization and ionic fragmentation processes are of fundamental importance in the upper-atmospheric chemistry and plasma physics. Perfluorocyclobutane is extensively used as a reagent for dry etching of semiconductors. Ravishankara *et al.* [1] report that the lifetime of this molecule in the atmosphere is about 1000 years. The use of the gas in industry has atmospheric implications for global warming. Because of the absence of data above the excitation energy of 27 eV, we measured in this study yield spectra of the fragment ions produced by the photoionization of perfluorocyclobutane.

The experiments have been performed on the beamline BL2B at the UVSOR facility. The experimental setup has been described in a previous paper [2], except a minor change for the purpose in this study: A thickness monitor was removed and a needle for gas inlet was installed. Synchrotron radiation was irradiated at right angles to the effusive beam of the sample gas. Fragment ions produced in the ionization region were extracted by a pulsed electric field toward a time-of-flight (TOF) spectrometer. The pulse and ion signals were fed into the start and stop pulse inputs of a multi-stop time-to-digital converter (FAST ComTec, model P7888), respectively, to record TOF signals. Partial ion yield spectra were obtained by measuring a series of TOF spectra while scanning the photon energy. The pressure in the chamber during the measurements was kept at 1.5×10^{-6} Torr.

A variety of fragment ions such as CF_k^+ (k = 1–3), $C_2F_m^+$ (m = 1–4), $C_3F_n^+$ (n = 1–5), and $C_4F_7^+$ were detected in the TOF spectra. This is in contrast to the previous report [3], in which $C_4F_7^+$ could not be detected by the measurement of threshold photoelectron–photoion coincidence spectra acquired at photon energies of 10–27 eV. However, the production of the $C_4F_7^+$ ion is reasonable as observed in this study, if considering the fragmentation of other perfluorocarbon compounds.

Figure 1 shows partial ion yield curves of the fragment ions. The branching fractions at the photon energy of 30 eV are 46.2 % ($C_3F_5^+$), 37.5 % ($C_2F_4^+$), 7.2 % (CF_3^+), 3.0 % (CF^+), 1.7 % (CF_2^+), 1.7 % ($C_3F_3^+$), 1.1 % ($C_4F_7^+$) and others. While the $C_3F_5^+$ and $C_2F_4^+$ fragments are most abundant at all the energies studied here, the yield of these ions decreased greatly with increase in the photon energy. The yield at ~ 170 eV becomes about 1/5 of that at 25 eV. The yield of CF_3^+ gives an approximately constant value up to 55 eV, and decreases monotonically at the higher energies. The yield of CF^+ increases with the photon energy up to about 80 eV, and then gradually decreases. As a result, the yields of small fragment ions are relatively enhanced with the excitation energy.

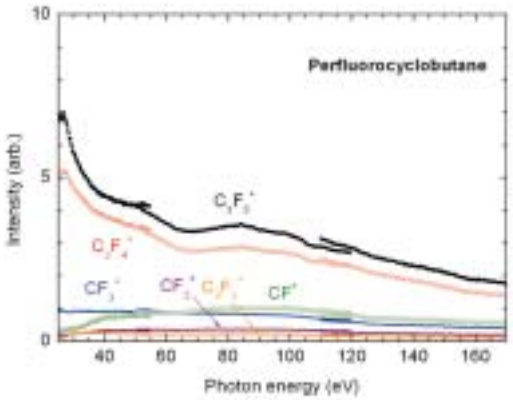

Fig. 1. Partial ion yield curves of the fragment ions produced by the photoionization of perfluorocyclobutane.

[1] A. R. Ravishankara, S. Solomon, A. A. Turnipseed and R. F. Warren, Science **259** (1993) 194.

[2] T. Mori, J. Kou, M. Ono, Y. Haruyama, Y. Kubozono and K. Mitsuke, Rev. Sci. Instrum. **74** (2003) 3769.

[3] G. K. Jarvis, K. J. Boyle, C. A. Mayhew and R. P. Tuckett, J. Phys. Chem. A **102** (1998) 3230.

BL2B

Construction of a Velocity Map Imaging Spectrometer and Its Performance Test Using Rare Gases

Md. S. I. Prodhan[1], H. Katayanagi[1, 2], C. Huang[2], H. Yagi[2], B. P. Kafle[2], K. Nakajima[2, 3], K. Mitsuke[1, 2]

[1]*The Graduate University for Advanced Studies (SOKENDAI), Okazaki 444-8585, Japan*

[2]*The Institute for Molecular Science, Okazaki 444-8585, Japan;*

[3] *Science Research Center, Hosei University, Tokyo 102-8160, Japan.*

Report is made on velocity map imaging (VMI) spectrometer based on a time-of-flight (TOF) technique. Thus we observed the momentum distributions of the scattered cations produced by dissociative photo-ionization of gaseous fullerenes by irradiation of synchrotron radiation [1, 2, 3]. The basic performance of the spectrometer was tested with rare gases for attaining high kinetic energy resolution of the photofragment images at $h\nu$ = 35 eV and 300 K. The 3D velocity distributions were reconstructed using the inverse Abel transformation (IAT) from the measured 2D images projected on a position-sensitive detector (PSD) to the cross-sectional images in the perpendicular plane of the spectrometer. Using the speed distributions extracted from these cross-sectional images, we evaluated the temperatures by the least-squares fit of the experimental data points to the Maxwell-Boltzmann distributions, as demonstrated in Fig. 1.

In addition, we have reproduced the images of rare gases at 300 K by computer simulations to compare them with those obtained experimentally. The number of He atoms in this simulation was set to 10^5. It was assumed that each He^+ ion flies from the origin with keeping its original thermal velocity of a parent He. The speed was calculated by generating random numbers utilizing Metropolis method from the Maxwell-Boltzmann distribution. The 2D image projected on the PSD was estimated by the spatial density function.

Figure 1 (a) shows the best focused 2D raw image of He^+ ions. The applied voltages at the MCP and electrodes were V_{MCP} = -2200 V, V_R = 640 V, V_T = - 350 V, and V_E = 353 V. Panel (b) represents the cross-sectional image obtained using IAT from Panel (a) [4]. The solid curve in Panel (c) denotes the Maxwell-Boltzmann distribution fitted to the data points (filled circles, extracted from (b)). The temperature obtained by the fittings was 282 ± 2 K which is explained in terms of systematic underestimate inherent in the IAT analysis. Similarly, the temperature was evaluated to be 287 ± 3 K from the simulated image of He^+ in Panel (d). A few scattered data points result from the application of IAT in the image processing.

Similar experimental works were executed for other rare gases, Ne and Ar. All the temperatures were found to be in good agreements with those from the corresponding simulated images.

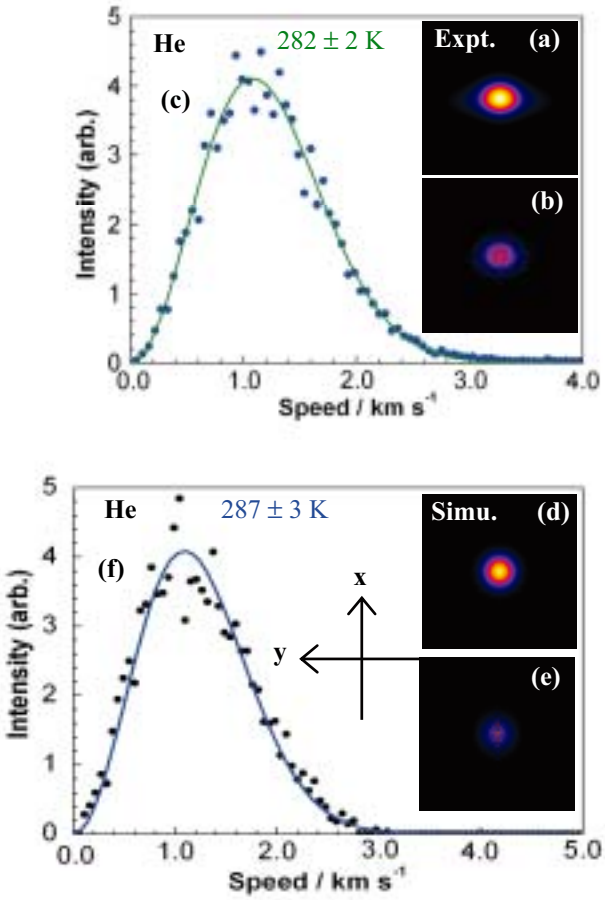

Fig. 1. Panels (a) and (d) show experimental and simulated 2D projections of He^+ ions at 300 K, respectively. Panels (b) and (e) are cross-sectional images obtained from Panels (a) and (d), respectively. Panels (c) and (f) are the speed distributions extracted from Panels (b) and (e), respectively. The solid curves denote the best fitted Maxwell-Boltzmann distributions.

[1] A. T. J. B. Eppink and D.H. Parker, Rev. Sci. Instrum. **68** (1997) 3477.

[2] B. P. Kafle, H. Katayanagi and K. Mitsuke, in "Synchrotron Radiation Instrumentation", Am. Inst. Phys., **CP879** (2007) 1809.

[3] H. Katayanagi *et al.*, Rev. Sci. Instrum. (2008) submitted.

[4] S. M. Candel, Comput. Phys. Commun. **23** (1981) 343.

BL3U

Exchange Interaction of the Rydberg Electron Bound by Singly Charged Ions in Small Krypton Clusters Studied by X-Ray Absorption Spectroscopy

M. Nagasaka[1], T. Hatsui[2] and N. Kosugi[1]

[1]*Institute for Molecular Science, Myodaiji, Okazaki 444-8585, Japan*

[2]*XFEL Project Head Office, RIKEN, Sayo-cho, Hyogo 679-5148, Japan*

Small krypton clusters show different surface sites (corner, edge, and face), and show different redshifts in the core level as a function of the number of nearest neighbor atoms in X-ray photoelectron spectroscopy (XPS) [1]. The single core hole state formed as a result of core ionization is stabilized by induced polarization (*PL*) of surrounding atoms, which leads to redshift of the cluster peaks. On the other hand, the excitation to low lying Rydberg states show blueshift of the cluster peaks in X-ray absorption spectroscopy (XAS) [2]. The blueshift behavior indicates destabilization of the excited states, which consist of the Rydberg electron bound by the singly ionized core stabilized by *PL*. The destabilization would be introduced by exchange interaction (*EX*) based on Pauli's exclusion principle for the Rydberg electron overlapping with neighbor atoms. In the present work, we have measured XAS of krypton clusters with <*N*> ~15, and discuss *EX* of the Rydberg electron in singly charged ion at different surface sites of krypton clusters [3].

The experiments were performed at BL3U. Krypton clusters were formed by the supersonic gas expansion method. XAS spectra were measured with a time-of-flight mass spectrometer to select only Kr_2^+ dimer ions.

Figure 1 shows XAS spectra of krypton clusters. The $3d_{5/2}^{-1}5p$ Rydberg states of some surface sites are blueshifted from the atomic one, whereas the $3d_{5/2}^{-1}6p$ states are redshifted. The initial state effect in van der Waals clusters is negligible; therefore, the energy shift (ΔE_i) of the Rydberg state (i = 5, 6) in XAS is simply given by ΔE_i (XAS) = *PL* (+1) + EX_i (+1), where *PL* (+1) is obtained by XPS and is not dependent on each Rydberg state *i*. Table 1 shows the surface site dependent *EX* energies of different Rydberg states. *EX* is found to be almost proportional to the coordination number of nearest neighbor atoms. It means *EX* is mainly caused by the overlap of the Rydberg electron with the nearest neighbor atoms. *EX* in the low lying 5p Rydberg electron is larger than the *PL* effect, whereas *EX* in the 6p Rydberg electron is smaller than *PL*. Therefore, the energy shift of the 5p Rydberg state in XAS is blueshifted compared to the atomic one. This is reasonable considering the radius of the 5p Rydberg orbital (3.64 Å) is close to the van der Waals distance of krypton (4.03 Å); on the other hand, the 6p orbital (8.13 Å) is distributed beyond the first coordination shell.

In conclusion, we have measured *EX* of the Rydberg electron bound by singly charged ion at different surface sites of krypton clusters, and found *EX* is derived from the repulsive and short-range interaction between the Rydberg electron and the nearest neighbor atoms of the ionized atom. *EX* is a key to understand the surrounding structure of surface sites in clusters.

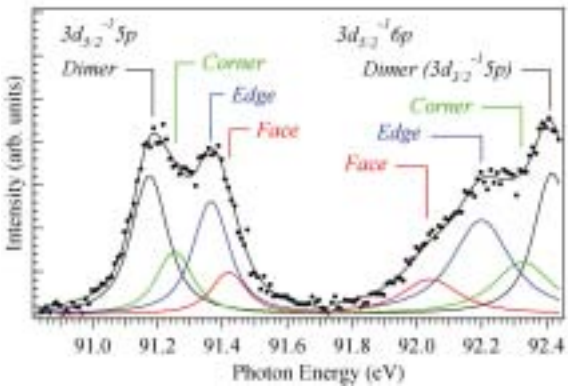

Fig. 1. XAS spectra of different surface sites in krypton clusters with the $3d_{5/2}^{-1}5p$ and $3d_{5/2}^{-1}6p$ states.

Table 1. Exchange (*EX*) energies (in eV) of Rydberg states at different surface sites of krypton clusters, together with the energy shift (ΔE) in XAS and the induced polarization (*PL*) energy determined by XPS. The bulk site corresponds to the large clusters [4].

eV	ΔE	*PL*(+1)	*EX* (+1)		*CN*
$3d_{5/2}^{-1}5p$					
Corner	0.05	-0.39	0.44	3.6	3
Edge	0.17	-0.57	0.74	6.0	5
Face	0.22	-0.79	1.01	8.2	8
Bulk	0.40	-1.07	1.47	12	12
$3d_{5/2}^{-1}6p$					
Corner	-0.22	-0.39	0.17	4.9	3
Edge	-0.35	-0.57	0.22	6.3	5
Face	-0.51	-0.79	0.28	8.0	8
Bulk	-0.65	-1.07	0.42	12	12

[1] T. Hatsui *et al.*, J. Chem. Phys. **123** (2005) 154304.

[2] A. Knop, B. Wassermann and E. Rühl, Phys. Rev. Lett. **80** (1998) 2302.

[3] M. Nagasaka, T. Hatsui and N. Kosugi, J. Electron Spectrosc. Relat. Phenom. **166-167** (2008) 16.

[4] M. Tchaplyguine *et al.*, J. Chem. Phys. **127** (2007) 124314.

BL4B

Formation of Metastable Fragments around the Cl 2p Ionization Thresholds of HCl

Y. Hikosaka, T. Kaneyasu and E. Shigemasa
UVSOR Facility, Institute for Molecular Science, Okazaki 444-8585, Japan

Formation of metastable fragments has recently been found in the inner-shell region of N_2 [1, 2]. The metastable fragments observed trace the formations of high-Rydberg N_2^+ states which dissociate into N^*+N^+ pairs. The N_2^+ states are produced through resonant Auger decay of inner-shell excited states lying below the inner-shell threshold [1] and of multiply excited states lying above the threshold [2]. The N_2^+ states are populated also in the near-threshold region through photoelectron recapture due to the post-collision interaction [1]. These previous works demonstrate that the observation of metastable fragments enables us to probe the decay dynamics of molecular inner-shell excited states [1] and also to perform detailed spectroscopic studies on the multiply excited states embedded in the inner-shell ionization continuum [2].

In this work, we have investigated metastable formation in the vicinity of the Cl 2p ionization thresholds of HCl [3]. The monochromatized SR light and the target gas beam effusing from a hypodermic needle crossed each other at a right angle. Two microchannel plate (MCP) detectors with an active diameter of 14.5 mm, facing each other across the interaction region, were placed at pseudo-magic angles with respect to the electric vector of the light and at right angles with respect to the gas beam [1]. The acceptance solid angle of each MCP detector was estimated to be 0.18 sr. Two grids (80% transmission each) were mounted in front of each detector, and the grids facing the interaction region were grounded. One of the detectors was dedicated to neutral particle observation and the other to fragment ions: the second grid of the neutral particle detector was held at +50 V while that of the fragment-ion detector was held at +5 V. Both the front plates of the two MCP stacks were held around -2 kV in order to prevent detection of electrons. The neutral particle detector was sensitive to neutral metastable particles with sufficient internal energy (> ~9 eV), as well as both VUV and SX photons.

Figures 1(a) and (b) show a fragment ion and a neutral particle yield spectrum measured in the photon energy range of 203.5 - 211.0 eV. The neutral particle yields are due to the detection of neutral metastable fragments, as well as VUV/SX photons. Here, the metastables of the parent HCl cannot be detected with our experimental geometry in which the neutral particle detector is placed perpendicular to the gas flow. Blow the Cl 2p ionization thresholds, Rydberg structures are seen in both the spectra. An intriguing characteristic of the neutral particle yield spectrum is the broad peaks around the Cl 2p thresholds, which are completely absent from the ion yield spectrum. A similar enhancement of the neutral particle yield is observed around the N 1s ionization threshold of N_2 [1]. In analogy to the N_2 case, we attribute the enhancements in HCl to the observation of metastable fragments formed via either spectator Auger decay from high-Rydberg states or by photoelectron recapture due to the post-collision interaction. Coincidence detections of neutral particle and ions reveal pair formation of H^*+Cl^{n+} [3]. It is found that efficient H* formation around the ionization thresholds is related to the high-Rydberg HCl^+ states, which are populated via either spectator resonant Auger decay or photoelectron recapture. In addition, H* is revealed to be produced by the dissociation of the HCl^{2+} states formed by normal Auger decay of the Cl 2p core-ionized states [3].

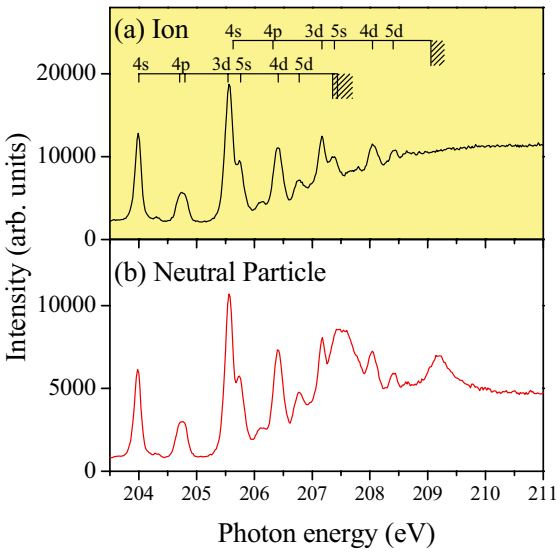

Fig. 1. (a) Ion yields and, (b) neutral particle yields in the vicinity of the Cl 2p ionization thresholds of HCl. The photon energy resolution is set to about 40 meV. The ion yield spectrum was measured with a retardation of +5 V.

[1] Y. Hikosaka, P. Lablanquie and E. Shigemasa, J. Phys. B: At. Mol. Opt. Phys. **38** (2005) 3597.
[2] Y. Hikosaka, T. Gejo, T. Tamura, K. Honma, Y. Tamenori and E. Shigemasa, J. Phys. B: At. Mol. Opt. Phys. **40** (2007) 2091.
[3] Y. Hikosaka, T. Kaneyasu and E. Shigemasa, J. Korean Phys. Soc. **53** (2008) 3798.

BL4B

High-Resolution Multi-Electron Coincidence Spectrometer for Studies of Atomic and Molecular Auger Processes

Y. Hikosaka and E. Shigemasa
UVSOR Facility, Institute for Molecular Science, Okazaki 444-8585, Japan

When an inner-shell electron in an atom or molecule is removed, the core-hole state decays via the Auger transition. The kinetic energy of the Auger electron is element-specific, and thus Auger electron spectroscopy is widely used as a powerful analytical tool in many different fields of research. However, the detailed interpretation of Auger spectra is difficult, even for atoms and small molecules. This is because inner-shell ionization is concomitant with the excitation and ionization of valence electrons, and all of these core-hole states contribute to the conventional Auger electron spectra. In theory, it is possible to filter out structures due to individual contributions by using the photoelectron-Auger electron coincidence method, which allows one to correlate initial core-hole states with the relevant Auger decays. In practice, the acceptance solid angle of a conventional electron spectrometer is too small to allow the recording of such a coincidence spectrum with sufficient statistics. The experimental limitation was fully solved by the introduction of the magnetic bottle electron spectroscopic technique [1], and highly-efficient coincidence studies using this technique have been successfully performed [2-4]. However, since this technique is based on time-of-flight analysis, the energy resolutions for fast electrons are often insufficient to observe individual Auger lines.

While the retardation of electron kinetic energy improves the energy resolution of time-of-flight analysis in general, the adequateness is not established for the magnetic bottle electron spectroscopic technique using a strong inhomogeneous magnetic field. In this work, we have tested an electric retardation for a magnetic bottle electron analyzer. Our analyzer is essentially the same as that developed by Eland et al. [1], except for the 1.5-m flight path in the present analyzer instead of the original 5-m path. A strong permanent magnet is located close to the interaction region, and the magnetic field guides electrons through a long solenoid toward a position sensitive detector. Electrodes which retard electrons are located around the entrance of the flight tube. The energy resolution was evaluated by measuring He 1s photoelectrons at different photon energies.

Figure 1 shows the evolutions of energy resolution (FWHM) with electron energy, which were observed with a 100-eV retardation or no retardation. It is shown that the retardation improves the energy resolutions. The coincidence measurement of Ar 2p Auger lines demonstrates more clearly the improved resolution. Figure 2 shows Auger spectra obtained in coincidence with $2p_{3/2}$ photoelectrons; thus, Auger lines associated with the $2p_{1/2}$ core are removed from the ordinary Auger spectrum. While the components of the band structures are not resolved on the spectrum observed without retardation, a 180-eV retardation clearly separates the individual Auger lines.

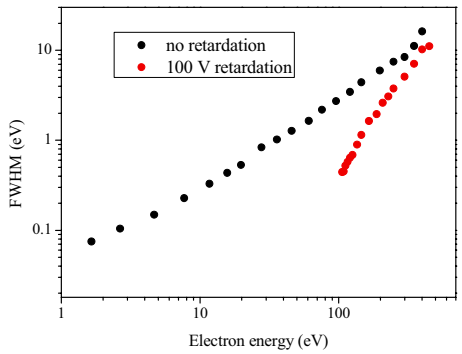

Fig. 1. Evolutions of energy resolution (FWHM) with electron energy, observed with a 100-eV retardation (red dots) and no retardation (black dots).

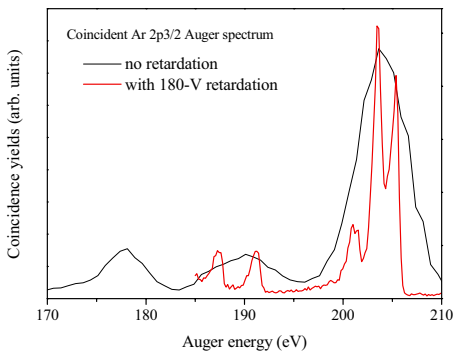

Fig. 2. Ar 2p Auger spectra obtained in coincidence with $2p_{3/2}$ photoelectrons: with a 180-eV retardation (red) and no retardation (black).

[1] J. H. D. Eland *et al.*, Phys. Rev. Lett. **90** (2003) 053003.
[2] Y. Hikosaka *et al.*, Phys. Rev. Lett. **97** (2006) 053003.
[3] Y. Hikosaka *et al.*, Phys. Rev. Lett. **98** (2007) 183002.
[4] Y. Hikosaka *et al.*, Phys. Rev. Lett. **102** (2009) 013002.

BL4B

Dissociation Pathways of $C_2D_2^{2+}$ Studied by an Auger-Electron–Ion Coincidence Method

E. Shigemasa[1], T. Kaneyasu[1, 2], Y. Hikosaka[1], M. Fushitani[3] and A. Hishikawa[3]
[1]*UVSOR Facility, Institute for Molecular Science, Okazaki 444-8585, Japan*
[2]*Kyushu Synchrotron Light Research Center, Tosu 841-0005, Japan*
[3]*Dept. of Photo-Molecular Science, Institute for Molecular Science, Okazaki 444-8585, Japan*

The acetylene dication is one of the smallest metastable polyatomic dications, whose dissociation and isomarization from the acetylene (HCCH) into the vinylidene (H_2CC) configurations have been extensively investigated. By using the PEPIPICO technique, it was found that the acetylene dications dissociate from excited states above 34 eV, where five three-body reactions and three two-body reactions including the dissociation channel via the vinylidene form ($CH_2^+ + C^+$: V-channel) have been identified. The isomarization time of the acetylene decation produced following the Auger decay was estimated to proceed within 60 fs [1]. Very lately, the visualization of ultrafast hydrogen migration in deuterated acetylene dication, which occurs in a recurrent manner, was nicely demonstrated by using intense ultrashort laser pulses [2].

An attempt to identify the fragmentation patterns for specific electronic states of the acetylene dication was made more recently, where the momenta of two positively charged ions were measured in coincidence with the Auger electrons [3]. In addition to the V-channel, the other two channels in the two-body reactions, such as the acetylene channel ($CH^+ + CH^+$: A-channel) and deprotonation channels ($C_2H^+ + H^+$: P-channel), were correlated with some Auger final states. In order to gain a further insight into the dissociation mechanism of the Auger final states, we have performed an Auger-electron–ion coincidence study on fragmentations of deuterated acetylene dication, $C_2D_2^{2+}$, formed via Auger decay. With the use of our Auger-electron–ion coincidence spectrometer [4], we have identified Auger final states relevant to the individual fragmentations including the three-body reaction, as well as to the formation of metastable $C_2D_2^{2+}$.

Figure 1 shows the coincidence Auger spectra extracted from the coincidence data sets, with the maximum intensity in each spectrum normalized to unity. It is found that the atomic fragment ions tend to be produced in the entire region of Auger electrons, while the molecular ions except for CD^+ exhibit specific productions for certain Auger final states. The parent dications are mainly observed at the lowest band, which shows a clear maximum around 33.3 eV. The shaded area in the $C_2D_2^{2+}$ spectrum displays the CD^+ spectrum multiplied by an appropriate factor. We come to the conclusion that the parent dications are essentially produced only from the lowest energy states with the $1\pi_u^{-2}$ configurations. The second lowest peak in the $1\pi_u^{-2}$ band lies at 34.7 eV, where C_2D^+ and C_2^+ fragments are produced. The CD_2^+ fragments related to the V-channel, as well as the atomic fragments C^+ and D^+ yield the highest energy peak in the $1\pi_u^{-2}$ band at 35.0 eV. The second band around 40 eV in the Auger spectrum seems to be composed of at least three components: 38.5 eV for C_2D^+ and D^+, 40.6 eV for CD^+ and D^+, and 42.4 eV for C_2^+. The highest binding energy band centered at 50 eV enhances violent fragmentation leading to the productions of C^+, D^+, CD^+, and C_2^+.

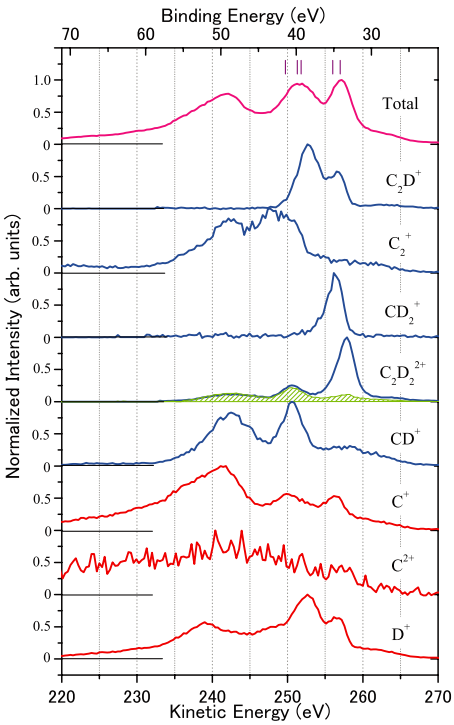

Fig. 1. *KVV* Auger spectrum of C_2D_2 (pink), in comparison with coincidence Auger spectra related to molecular ions (blue), and atomic ion formation (red).

[1] T. Osipov *et al.*, Phys. Rev. Lett. **90** (2003) 233002.
[2] A. Hishikawa, A. Matsuda, M. Fushitani and E. Takahashi, Phys. Rev. Lett. **99** (2007) 258302.
[3] T. Osipov *et al.*, J. Phys. B **41** (2008) 091001.
[4] T. Kaneyasu, Y. Hikosaka and E. Shigemasa, J. Electron Spectrosc. Relat. Phenom. **156-158** (2007) 279.

BL4B

Study of Magnetic Anisotropy in NO/Ni/Cu(001) Using X-Ray Magnetic Circular Dichroism

T. Nakagawa, Y. Takagi, I. Yamamoto and T. Yokoyama

Department of Electronic Structure, Institute for Molecular Science, Okazaki 444-8585, Japan

Magnetic anisotropy in a magnetic thin film is sensitive to its surface modification since the contribution of the surface to the entire film is significant and the surface atoms may exhibit non-collinear anisotropy due to their lower symmetry. It is known that the orbital moment, which is usually large at the surface and interface, is an origin of the magnetic anisotropy. To support this concept, the quantitative relationship between the orbital moment and the magnetic anisotropy needs to be examined. For this aim, X-ray magnetic circular dichroism (XMCD) under a strong magnetic field enough to saturate the magnetization is an ideal method.

XMCD experiments were carried out at BL4B, which delivers circular polarized light (circular polarization = 0.67). The end station was an ultra high vacuum chamber equipped with a superconductive magnet (7 T) and a low temperature insertion of 5 K. [1] 4 ML Ni films grown on a Cu(001) sample were used, which had magnetic easy axis within the surface, and NO adsorption did not change its easy axis. Adsorption of NO was done at 5 K, and the coverage of NO was estimated to be 0.5 ML as judged from XAS spectra.

Figure 1 shows XMCD spectra for grazing and normal incidences. From the XMCD sum rule, spin magnetic moment (m_s) and orbital magnetic moments for the in-plane ($m_{orb}^{//}$) and out-of-plane ($m_{orb}^{\perp}$) components are separately evaluated. The m_{orb} components are larger for the in-plane direction before and after NO adsorption, which is in agreement with the direction of the magnetization easy axis. Upon the NO adsorption the difference in m_{orb} between the out-of-plane and in-plane directions becomes smaller, suggesting that NO adsorption makes the in-plane anisotropy weaker.

Figure 2 shows magnetization hysteresis curves with the magnetic field normal to the surface, which were taken on the same sample as that for Fig. 1. The magnetization curves are results of Ni-L_3 intensity variation as a function of magnetic field. The anisotropy fields, H_a, are 2.1 and 1.0 T for clean and NO adsorbed surfaces respectively, resulting in anisotropy energies, K_u, of 5.1 x 10^5 and 1.9 x 10^5 J/m^3. The obtained anisotropy energies contain contributions from the shape anisotropy due to the dipole-dipole interaction and the electron orbital anisotropy (crystalline anisotropy). After the subtraction of the shape anisotropy (the clean and NO adsorbed surfaces are 1.6 x 10^5 for the clean surface and 1.2 x 10^5 J/m^3 for NO adsorbed surface), the crystalline magnetic anisotropy energies are obtained as 3.5 x 10^5 and 0.7 x 10^5 J/m^3, respectively.

A theoretical model indicates that the difference of m_{orb} for in-plane and out-of-plane directions, Δm_{orb}, is simply proportional to the magnetic anisotropy energy. [2] From our result, the Δm_{orb} ratio between the clean and NO adsorbed surfaces is 0.013/0.002 ~ 6.5, which is in reasonably agreement with the crystalline anisotropy energies ratio (~5).

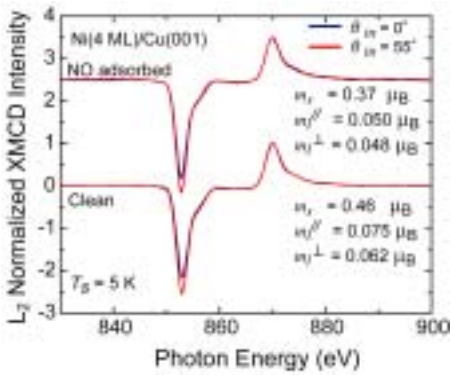

Fig. 1. XMCD spectra in Ni L edge for the clean and NO adsorbed surface. The calculated spin and orbital moments are indicated.

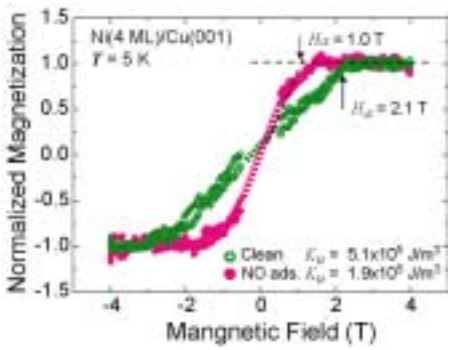

Fig. 2. Magnetization curves for clean Ni (4 ML)/Cu(001) and NO adsorbed one. Both the magnetic field and the photon incident direction are perpendicular to the surface. Anisotropy fields, H_a, are indicated.

[1] T. Nakagawa, Y. Takagi, Y. Matsumoto and T. Yokoyama, Jpn. J. Appl. Phys. **47** (2008) 2132.
[2] P. Bruno, Phys. Rev. B **39** (1989) 865.

BL1B

Photoionization Threshold of Aromatic Molecules on the Surface of Ionic Liquid/Water Mixture

T. Ishioka, N. Inoue and A. Harata

Department of Molecular and Material Science, Kyushu University, Kasuga 816-8580, Japan

Photoionization threshold of aromatic molecules has been measured on the surface of the mixture of an ionic liquid and water. The threthold energy of pyrene was nearly unchanged with the content of water while the value of perylene was largely dependent on the ratio of water. This result suggests the solvation structure of pyrene at the surface is largely different from those of perylene.

Introduction

Ionic liquids have attracted much attention due to its unique characteristics such as low melting point, high conductivity, negligible vapor pressure, and designable solubility to other solvents. Their interfacial properties also attract large interest because interface structures play a crucial role in transport kinetics and they are related directly to the applications of ionic liquids such as solvent extraction and rechargeable batteries.

Interfacial characteristics of ionic liquids have been studied theoretically and experimentally. Surface tension measurements, X-ray techniques, neutron reflection, nonlinear optical methods, and molecular dynamic simulations have been used and their common conclusion on air/ionic liquid structure is that cations are present at the surface with long alkyl chains directed to the air. This conclusion implies surface molecules suffer different dielectric environment from those in bulk solutions.

The dielectric environment is directly related to the solvation conditions of solute molecules. However, it is difficult to know solvation conditions experimentally at the liquid surfaces. Photoionization is one of such methods to inform dielectric conditions at the surface because the threshold energy is lowered by the polarization energy of cations produced by photoionization.

In this report, photoionization thretholds of two aromatic molecules, pyrene and perylene, were measured at the surface of the mixture of ethylammonium nitrate and water. The water content was varied from 0-100% and the solvation characteristics were discussed.

Experimental

The monochromated synchrotron light (4-8 eV) was obtained from BL1B at the UVSOR facility and emitted from the chamber to the He-purged cell through an MgF_2 window. The emitted light was reflected on an Al mirror and vertically irradiated on the solution surface through a Cu-mesh electrode. The electrode was set at 5 mm high above the liquid surface and high voltage (400 V) was applied to the electrode so that emitted electrons were trapped. The photocurrent (~100 fA) was measured by a picoammeter and the incident photon intensity was monitored by measuring fluorescence intensity from sodium salicylate plate.

Solution samples were prepared by spreading dilute hexane solution of pyrene or perylene on the surface of the mixture of ethylammonium nitrate and water.

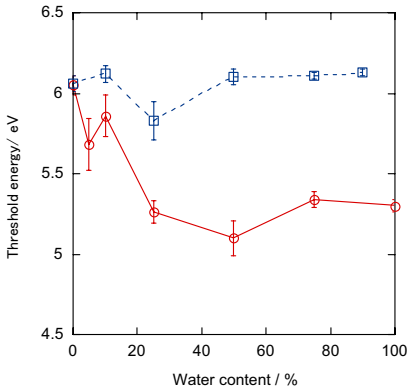

Fig. 1. Photoionization threshold energy of aromatic molecules on the surface of ethylammonium nitrate / water mixture. Solid line: perylene. Broken line: pyrene. The threshold value was derived from the mathematical fitting of $I = C(E-E_{th})^{2.5}$. I : photocurrent, C: constant, E: Photon energy.

Results and Discussion

Photoionization threshold energy (E_{th}) on the solution surface can be explained by

$$E_{th} = IP + P^{+} \qquad (1)$$

where IP is ionization potential in vacuum and P^{+} is the polarization energy. IPs of pyrene and perylene are 7.43 eV and 6.96 eV, respectively. From Fig. 1 measured photoionization threshold shows 0.9-1.8 eV lower value than each IP, indicating P^{+} values. P^{+} is the function of surrounding solvent properties such as dielectic constant and coordination numbers. In the case of pyrene, the threshold value is independent of water content. This result suggests dielectric condition of pyrene is not affected by bulk water content. While this, photoionization threshold of perylene decreases by increasing the water content showing large solvation energy by surrounding molecules. It is suspected that the average molecular distribution from the surface of perylene is deeper than pyrene.

BL1B

Optical Properties of TiO_2 Thin Films Prepared by a Sol-Gel Method

T. Kawai[1], R. Sato[1] and K. Kifune[1, 2]

[1]*Department of Physical Science, Graduate School of Science, Osaka Prefecture University, Osaka 599-8531, Japan*

[2]*Faculty of Liberal Arts and Sciences, Osaka Prefecture University, Osaka 599-8531, Japan*

Titanium dioxide (TiO_2) is one of technologically important materials from the view point of applications, such as pigments, photocatalyst, and dye sensitized solar cell [1]. Though a lot of studies on TiO_2 have been performed for structural and photocatalytic properties, the studies on optical properties of TiO_2 in the energy region above the band edge, especially up to the vacuum ultraviolet (VUV) energy region, have been considerably limited. In this study, we prepared TiO_2 thin films on the quartz substrate by using a conventional sol-gel method and performed the optical measurements up to the VUV energy region at the BL-1B line of UVSOR.

Figure 1 shows the absorption spectrum of the TiO_2 thin film. The absorption spectrum exhibits the rise at 3.32 eV, whose value is almost equal to the band gap of anatase TiO_2 crystals [2, 3]. Reflecting the ultra thinness of the sample, the several absorption peaks and shoulders can be seen in the energy region above the absorption band edge. We decompose the absorption spectrum of the TiO_2 thin film into the several Gaussian shape bands. The Gaussian shape bands obtained by decomposing the absorption spectrum are represented by blue curves in Fig. 1. These results are consistent with the absorption spectra calculated from the reflection spectra by Kramers-Kronig (K-K) transformations [2]. The experimental and theoretical studies for anatase TiO_2 crystals present that the highest valence band is composed of oxygen 2p states and the conduction bands below about 8 eV consist mainly of titanium 3d states [2, 3]. Therefore, these absorption bands are attributed to the transitions from oxygen 2p to titanium 3d states.

Figure 2 shows the luminescence and excitation spectra of the TiO_2 thin films at 10 K. Under the excitation above the band edge, the broad luminescence band is observed at 2.23 eV. The band shape and peak energy are similar to those of the anatase TiO_2 crystals reported previously [3, 4]. The excitation spectrum for the luminescence exhibits the response rising sharply from 3.32 eV, which corresponds to the rise on the absorption spectrum of the TiO_2 thin film. In the energy region from 3.5 to 7.0 eV, the excitation spectrum has no remarkable structure and an almost constant response.

It should be noted that the small peak around 7.8 eV and the increase of intensity with increasing photon energy from 8.0 eV are observed in the excitation spectrum above 7.0 eV. The absorption spectra calculated by K-K transformations demonstrate the absorption peak around 9.0 eV and the decrease of the absorption coefficient with increasing photon energy from 9.0 to 12.0 eV. This fact implies that the increase of the excitation spectrum from 8.0 eV is not attributed to that of the light intensity absorbed in the sample. The increase of the excitation spectrum would come from the change of the relaxation processes. In order to make the relaxation processes clear, the optical measurements over the VUV energy region are needed for the anatase TiO_2 single crystals.

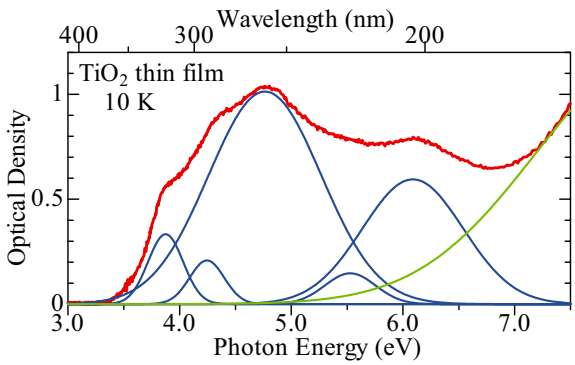

Fig. 1. Absorption spectrum (red) of the TiO_2 thin film, Gaussian components (blue) decomposing the absorption spectrum, and the background (green) consisting of the absorption tail and the substrate.

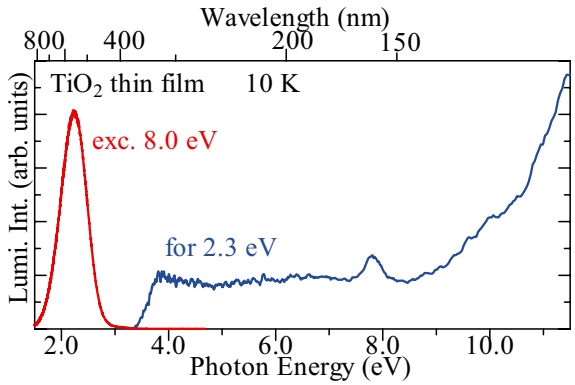

Fig. 2. Luminescence (red) and excitation (blue) spectra of the TiO_2 thin film at 10 K.

[1] A. Fujishima *et al.*, Surf. Sci. Reports. **63** (2008) 515.
[2] N. Hosaka *et al.*, J. Phys. Soc. Jpn. **66** (1997) 877.
[3] T. Sekiya *et al.*, J. Lumi. **108** (2004) 69.
[4] M. Watanabe *et al.*, J. Lumi. **112** (2005) 88.

BL3U

Field Effect on the Electronic States of Pentacene Thin Films Studied by Fluorescence-Yield X-Ray Absorption Spectroscopy

H. S. Kato[1], F. Yamauchi[1, 2], M. Kawai[1, 2], H. Yamane[3], M. Nagasaka[3], T. Hatsui[4] and N. Kosugi[3]

[1]*RIKEN (The Institute of Physical and Chemical Research), Wako 351-0198, Japan*
[2]*Department of Advanced Materials Science, University of Tokyo, Kashiwa 277-8501, Japan*
[3]*Institute for Molecular Science, Okazaki 444-8585, Japan*
[4]*PRESTO, JST and XFEL Project Head Office, RIKEN, Sayo 679-5148, Japan*

Introduction

In order to extend new functionality of electronic devices, the molecular devices have recently been investigated with great efforts. The organic field effect transistor (OFET) is a typical molecular device that controls electric conductivity by injection of carriers into the organic thin film under the applied electric field. Since the organic materials consist of molecular units having their own molecular orbitals, it is not clear that the energy diagram of OFET is exactly the same as that of the inorganic semiconductors, i.e., band bending at the interface in the semiconductor side. Therefore, the direct observation of electronic states in the organic thin films under operative conditions has been required.

In this study, we aim to elucidate the electronic state of organic thin films in OFET under the electric field. The fluorescence-yield X-ray absorption spectroscopy (FY-XAS) should be a promising method for detection of inner electronic states of organic devices, because the fluorescent X-ray has a long penetration depth of about 100 nm in most of materials even for the soft X-ray region. In addition, X-rays are not disturbed by applied electric fields, different from emitted electrons. Thus, we have attempted to utilize FY-XAS for investigation of inner electronic states of OFETs.

Experimental

To investigate the electronic states of OFET, pentacene (Pn) thin films on the SiO_2-covered Si substrates were fabricated using a molecular beam deposition system at RIKEN. The quality of their morphology and crystallinity was high enough in comparison with that reported in previous work. The performance as FETs of the fabricated Pn thin films was also confirmed with additive deposition of Au electrodes (35 nm thick) on the films. By the same preparation, the fully Au-covered Pn thin-film samples were made to evaluate the field effects under uniform electric fields in the films.

The FY-XAS measurements were performed at the BL3U beamline of the UVSOR facility in IMS. The samples were set in a BL3U end-station through a sample-entry system. The fluorescence intensities were measured using a retarding field detector consisting of MCP plates.

Results and Discussion

Figure 1(a) shows the gate bias dependence of the C K-edge FY-XAS spectra of the Pn films (20 nm thick), in which the spectra at the bias of 0 V and -90 V are plotted. The bias voltage was applied with a square wave (7 Hz) synchronized to the veto signals to the two fluorescence signal counters for each of the bias conditions, which enabled reliability of the difference spectrum. Figure 1(b) shows the spectral change at the biases from 0 V to -90 V, in which the sharp peaks at the photon energies around 285 eV on the spectra are absent, while broad components are found at the higher photon energies. In Fig. 1(b), the spectral change of a Pn-lacked sample at the same bias conditions is also shown. Although a small fluctuation possibly originates from imperfection of X-ray intensity monitoring, no meaningful signals were confirmed. It is, therefore, concluded that the observed spectral change is caused by an electronic change of the Pn thin films in FET under the applied bias, though its origin has been under debate.

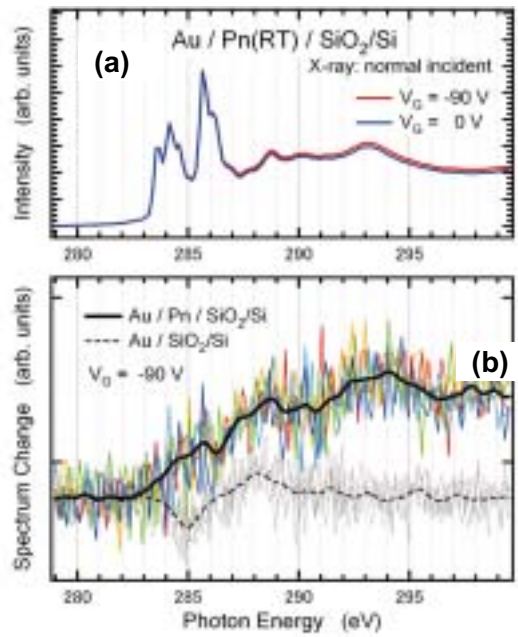

Fig. 1. Bias dependence of the C K-edge fluorescence-yield XAS spectra of the Au-covered Pn films (20 nm thick) measured at normal incidence geometry: (a) the spectra at the biases of 0 V and -90 V, (b) spectral changes at the biases form 0 V to -90 V (solid lines) as compared with that of a Pn-lacked sample (broken lines).

BL4A

Synchrotron-Radiation-Stimulated Etching of PDMS Using XeF_2 as Reaction Gas

T.-C. He[1], T. Makimura[2], S. Torii[2], T.-Y. Chiang[3], R. Tero[3], C.-S. Wang[1] and T. Urisu[3]
[1]*Department of Physics, Shanghai Jiao Tong University, Shanghai 200240, China*
[2]*Institute of Applied Physics, University of Tsukuba, Tsukuba 305-8573, Japan*
[3]*Institute for Molecular Science, Okazaki 444-8585, Japan*

PDMS elastomer is used in many applications including micro fluidic circuits, insulation or micro/nanoelectro-mechanical (MEMS) devices and soft lithography, and it is also biocompatible and effective for fluid seals. The ability to reliably pattern PDMS in the form of both thick substrates and thin membranes or films is critical to expand the scope of its applications. In the past years, many methods for patterning PDMS have been developed, such as molding method, wet chemical etching, dry (plasma) etching, photolithography and bond-detach lithography. However, these methods can be only applicable to very thin PDMS membranes. We think that development of reliable removing type microfabrication technique applicable to thick PDMS membranes is an important issue and this will realize new 3D microstructures of PDMS by combining with molding type technique. In this work, high speed SR etching beam line using XeF_2 as reaction gas has been constructed (Fig.1) and high spatial resolution, area selective and anisotropic etching of elastic material PDMS has been demonstrated for the first time. Extremely high etching rate of 40-50 μm/10 min was easily obtained (Fig.2) at the XeF_2 gas pressure of 0.2-0.4 Torr. This suggests that SR etching using XeF_2 gas provides a new microfabrication technology for thick PDMS membranes. Figure 3 shows the optical microscope image of the patterning formed on the PDMS substrate surface by the SR etching under the conditions of 0.4 Torr XeF_2 gas and 110 mA ring current. In our following plan, the research will be extended to apply the etched surface structures to the 3D microstructures biosensor.

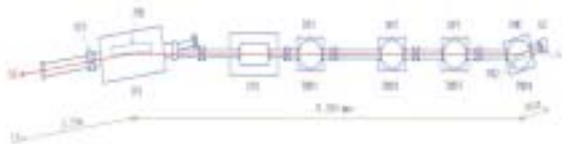

Fig. 1. Schematic diagram synchrotron radiation XeF_2 etching beam line at UVSOR. LS: light source, FCV: fast closing valve, FM1, FM2: first and second focusing mirrors, FMC: second focusing mirror chamber, DPi (i = 1 - 3): differential pumping chambers, IPi (i = 1 - 2): ion pumps, TMPi (i = 1 - 4): turbo molecular pumps, EC: etching chamber, A: aperture. Distances from the light source are written in the figure.

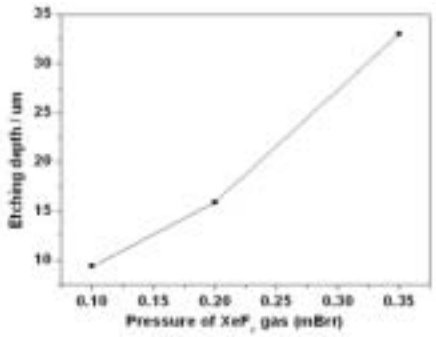

Fig. 2. Observed dependence of etched depth on XeF_2 pressure of 0.35, 0.2 and 0.1 mTorr. These data show that a high speed, area selective and anisotropic etching is realized for PDMS by the SR etching using XeF_2 as an etching gas.

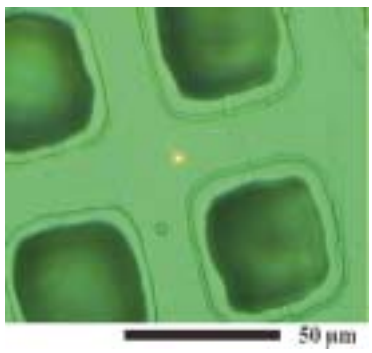

Fig. 3. The optical microscope image of the pattern formed on the PDMS by the SR etching using XeF_2 as reaction gas.

BL4B

Evaluation of Magnetism of MnSi Ultra-Thin Films on Si(111)

S. Higashi[1], Y. Takagi[2], T. Nakagawa[2], T. Yokoyama[2] and H. Tochihara[1]

[1]*Department of Molecular and Material Sciences, Kyushu University. Kasuga 816-8580, Japan*

[2] *Institute for Molecular Science, Okazaki 444-8585, Japan*

We report on a study of surface magnetism of MnSi ultra-thin films on Si(111) by means of X-ray magnetic circular dichroism (XMCD) at BL4B, equipped with a superconducting magnet system.

It has been revealed that the deposition of Mn atoms on the Si(111)-7×7 surface at room temperature (RT) followed by subsequent annealing at elevated temperature results in the Volmer-Weber type growth of a manganese silicide [1]. The structure of the silicide is considered to be the B20 type structure of MnSi, based on results of photoemission spectroscopy and transmission electron microscopy studies.

Recently, we reported a recipe for fabrication of atomically flat MnSi ultra-thin films on Si(111) : 3ML (ML; 1ML = 7.83×10^{14} atoms/cm^2) of Mn deposition at RT followed by subsequent annealing at relatively low temperatures (~250˚C) [2]. According to recent DFT calculations, the ferromagnetic ordering is slightly more stable than other magnetic structures. In addition, the structure has 50% of spin polarization at the Fermi level [3].

In this study, we grew the atomically flat MnSi ultra thin-film and evaluated the surface magnetism of the film. Samples were prepared in the preparation chamber, and then transferred to the XMCD measurement chamber under ultra-high vacuum conditions (< 3×10^{-10} Torr).

First, we measured XAS spectra of Mn $L_{III,II}$-edge under the magnetic field of 5 T at a sample temperature of 5 K with different light incident angles (0° and 55°) for the sample of Mn-3ML. For both incident angles, weak MCD signals were observed. The XAS and XMCD spectra for Mn $L_{III,II}$-edge at an incident angle of 55° are shown in Fig. 1.

In order to know the magnetic easy axis of the MnSi film, the dependence of Mn L_{III}-edge intensity under the external magnetic field up to ±5T was measured. The magnetization was not saturated at an incident angle of 0° even under 5 T, while it was saturated around 2 T at 55° incident angle (see Fig. 2). Thus we conclude that the magnetic easy axis of MnSi of Mn-3ML is in-plane.

Then, we increased the Mn amount to 10 ML and measured XAS and XMCD spectra. The XMCD signal for Mn-10ML was as weak as the sample of Mn-3ML. Additionally, The M-H curve recorded as Mn L_{III} XAS intensity indicated that the magnetic easy axis was in-plane. These results imply the magnetic moment of MnSi thin-film is independent of the thickness of the film up to 10 ML.

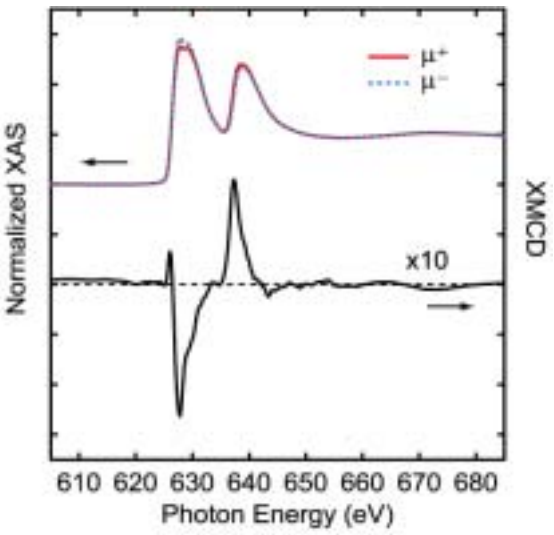

Fig. 1. Mn $L_{III,II}$-edge circularly polarized X-ray absorption spectra (blue and red lines) and XMCD spectrum (black line) of the Mn-3ML MnSi film on Si(111) at 5 K with light incident angle of 55°. μ^+ and μ^- denote those for the X-ray helicities parallel and anti-parallel to the electron spins in the specimen, respectively.

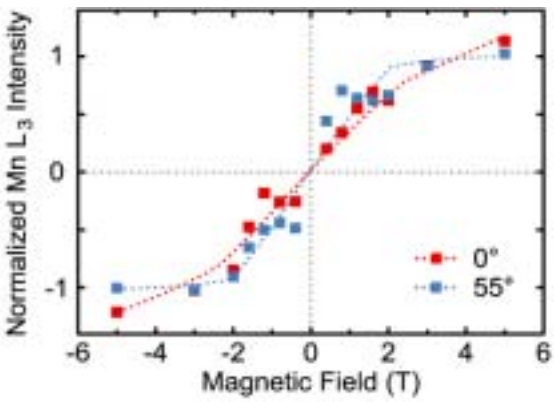

Fig. 2. M-H curves for Mn-3ML at 5.0 K, recorded as Mn L_{III} XAS intensity. The light incident angles were 0° (red) and 55° (blue). The signals were normalized by the intensity at an incident angle of 55° under 5 T. The dotted lines were drawn for eye guide.

[1] M. M. R. Evans, J. C. Glueckstein and J. Nogami, Phys. Rev. B **53** (1996) 4000.
[2] S. Higashi, Y. Ikedou, P. Kocán and H. Tochihara, Appl. Phys. Lett. **93** (2008) 013104.
[3] M. Hortamani, P. Kratzer and M. Scheffler, Phys. Rev. B **76** (2007) 235426.

BL4B

Spin-Dependent Transport in Codeposited C_{60}-Co Films with Giant Tunnel Magnetoresistance

Y. Matsumoto[1], S. Sakai[1], Y. Takagi[2], T. Nakagawa[2] and T. Yokoyama[2]
[1]*Advanced Science Research Center, JAEA, Tokai, Naka 319-1195, Japan*
[2]*Institutes for Molecular Science, Okazaki 444-8585, Japan*

The spin transport in the organic molecule-based materials has attracted for its capabilities in the spintronics fields, and several groups have reported significant magnetoresistance (MR) effects in the hybrid systems of the π-conjugated molecules and ferromagnetic transition metals. In particular, the large tunnel magnetoresistance (TMR) effects were found for the granular C_{60}-Co films consisting of a C_{60}-Co compound matrix and Co nanoparticles [1]. However, the mechanism of these MR effects have not been clarified due to the absence or limited insights into the electronic and spin states essential for the magnetotransport properties.

In the present study, the electronic and spin states of the C_{60}-Co films are investigated by employing the X-ray absorption spectroscopy (XAS) and magnetic circular dichroism (MCD) measurements.

XAS and MCD measurements were carried out in the TEY mode at the magic angle. For the MCD measurements, the magnetic field (H) was applied parallel and antiparallel to the propagating direction of the circularly polarized X-ray (P_c=0.80±0.03) by using a superconducting magnet [2]. C_{60}-Co films (30nm thick) with the different Co contents ($C_{60}Co_x$, x: the number of Co atom per a C_{60} molecule) were prepared with the codeposition method under the UHV condition (<10^{-7}Pa) [1]. The prepared samples were transferred into the analysis chamber without breaking the UHV condition.

Figure 1(a) and (b) show the Co $L_{3,2}$-edge XAS spectra of $C_{60}Co_{4.3}$ sample which corresponds to the C_{60}-Co compound [3], and the MCD spectra of the respective samples measured at T=6K under H=50kOe, respectively. Fig. 1(c) and (d) show the H-dependence of the spin and orbital magnetic moments (M_{spin} and M_{orb}). The T-dependence of the total magnetic moment (M_{tot}=M_{spin}+M_{orb}) are also shown in Fig. 2(a).

For the $C_{60}Co_{4.3}$ sample, the peak of the MCD spectrum is observed close to the characteristic energy position to the C_{60}-Co compound (A_0 resonance). The magnitude of the M_{tot} exhibits a strong T-dependence, which is roughly proportional to the inverse of the temperature. These results indicate the paramagnetic-like spin-polarization of the Co 3d-derived states in the C_{60}-Co compound.

Figure 2(b) shows the T-dependences of the zero-bias MR ratios (MR_0) for the granular C_{60}–Co films, and of the model-calculated MR ratios (MR_{calc}) as shown in the following. By virtue of the Julliere's model, the MR ratio is given as $MR_{calc}=m^2P^2/(1+m^2P^2)$ in case of the granular systems, where P denotes the spin-polarization of tunneling electrons and $m=M/M_S$ (M: magnetization, M_S: saturation magnetization). In the present work, MR_{calc} is calculated by substituting m with $m=M_{tot}$(50kOe)/M_{sat} for the $C_{60}Co_{4.3}$ sample and by assuming P≈1 in consideration of the remarkably high MR ratios. As shown in the figure, the MR_{calc}–T dependence is found to agree well with the MR_0–T dependences of the granular C_{60}–Co films. This suggests that the spin-polarized Co 3d-derived states in the C_{60}–Co compound affect on the spin-dependent tunneling process. We speculate that the high spin-polarization of the tunneling electrons is induced at the interfaces of the spin-polarized C_{60}–Co compound and Co nanoparticles.

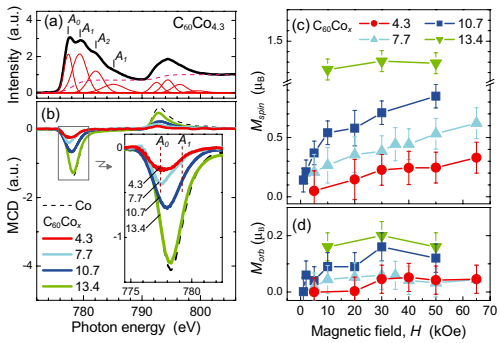

Fig. 1. (a) The Co $L_{3,2}$-edge XAS and MCD spectra of the $C_{60}Co_{4.3}$ sample, and (b) the MCD spectra of the respective samples measured at T=6K under H=±50kOe. The H-dependences of the (c) spin and (d) orbital magnetic moments (M_{spin} and M_{orb}).

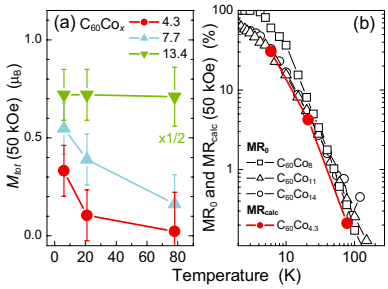

Fig. 2. (a) Temperature dependences of the total magnetic moment (M_{tot}) for the C_{60}-Co films, and (b) the zero-bias MR ratios (MR_0) under H=±50kOe and the model calculated MR ratios (MR_{calc}).

[1] S. Sakai *et al.*, Appl. Phys. Lett. **91** (2007) 242104.
[2] T. Nakagawa *et al.*, Jpn. J. Appl. Phys. **47** (2008) 2132.
[3] S. Sakai *et al.*, Thin Solid Films **515** (2007) 7758.

BL4B

Magnetic Properties of Iron Nitride Thin Films on Cu(001)

Y. Takagi[1, 2], K. Isami[2], I. Yamamoto[1], T. Nakagawa[1, 2] and T. Yokoyama[1, 2]
[1]*Institute for Molecular Science, Okazaki, Aichi 444-8585, Japan*
[2]*The Graduate University for Advanced Studies, Okazaki, Aichi 444-8585, Japan*

We report on a study of the surface magnetism of iron nitride thin films on Cu(001) by means of X-ray magnetic circular dichroism (XMCD) at BL4B, equipped with a superconducting magnet systems.

The iron nitride films on Cu(001) were prepared as follows. First, The Cu(001) single crystal was cleaned by Ar^+ ion sputtering and 900K annealing cycles in ultrahigh vacuum (UHV) chamber. Next, 1ML Fe was deposited on the substrate at room temperature (RT). Then, the 1ML Fe film was exposed to low energy (150eV) N^+ bombardment with pressure = 5×10^{-6} Torr at RT for 15 min. Finally, the 1 ML iron nitride film was formed after annealing the sample in UHV at 670K for 10min. The deposition and annealing processes were repeated for more than 1ML.

The results of scanning tunneling microscopy and low energy electron diffraction studies revealed that the iron nitride films epitaxially grew on the Cu(001) substrate with the surface structure of *p4gm*(2×2). The 1ML thickness film have a 2:1 Fe:N composition, where the N atoms locate at fourfold hollow site of 1ML fcc Fe on Cu(001). On the other hand, the Fe:N composition is 4:1 for more than 1ML film. These films have the similar structure as the bulk γ-Fe_4N.

Figure 1 gives magnetization curves obtained by recording the electron yield with the photon energy fixed at the Fe L_{III} peak top (~707 eV). The spectra for the grazing incidence (θ=55°) had the step-like shape, while the smoothed shape of the magnetization curves appeared for the normal incidence (θ=0°). Therefore, the magnetic easy axis was found to be in-plain. Moreover, the magnetization at normal incidence was not saturated even under 5 T in 1ML and 2ML, while that of more than 2ML film was saturated around 3 T, as the result of decreasing the magnetic anisotropy with increasing the thickness.

The XMCD spectra of Fe $L_{III,II}$-edge were measured under the magnetic field of 5 T at a sample temperature of 5 K (Fig. 2). The spin (m_{spin}) and orbital (m_{orb}) magnetic moments obtained by each experimental XMCD spectra are indicated in the figure. Because the magnetization of 1ML and 2ML was not saturated even at 5 T at normal incidence, the spin and orbital magnetic moments of them were obtained by the spectra of the magic angle arrangement (θ=55°). On the other hand, the in-plane and perpendicular orbital magnetic moments ($m^{\parallel}_{orb}$ and $m^{\perp}_{orb}$) were analyzed for the spectra of 3ML and 4ML. The spin magnetic moment increases with increasing the thickness and is saturated at 1.8μ_B around 3ML. In addition, the total magnetic moment is almost the same as the bulk γ-Fe_4N of 2.2μ_B.

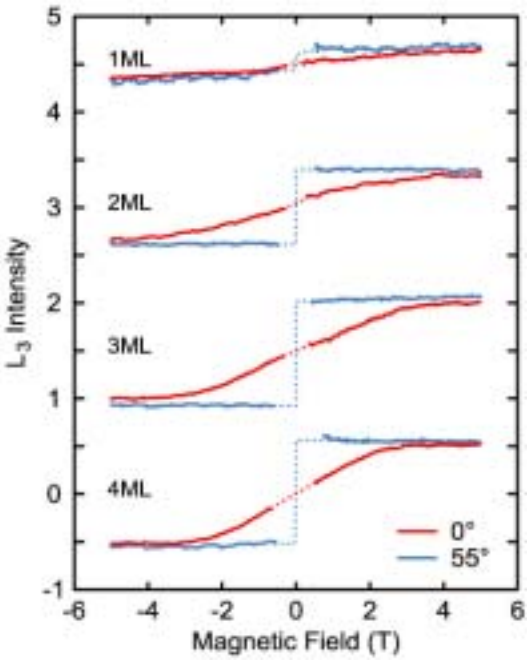

Fig. 1. The M-H curve of 1 - 4 ML iron nitride films obtained by recording the electron yield with the photon energy fixed at the Fe L_{III} peak top (707 eV) at incident angles θ = 0° (red line) and θ = 55° (blue line) from the surface normal.

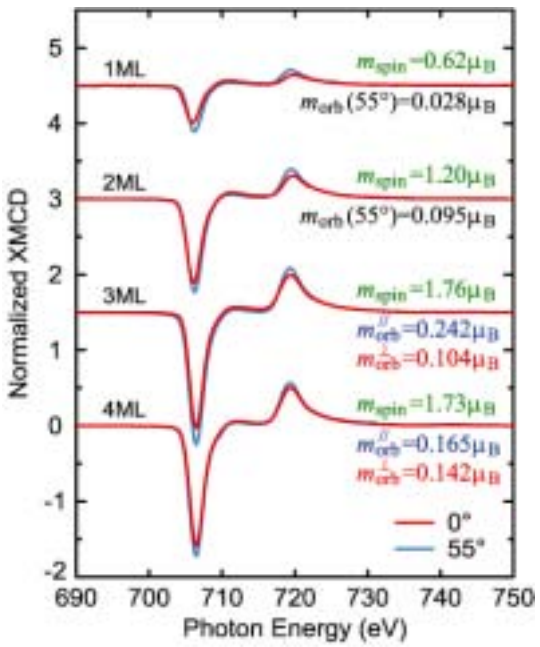

Fig. 2. Fe L_{III-II}-edge XMCD spectra of 1 - 4 ML iron nitride films under H = ±5.0T at incident angles θ = 0° (red line) and θ = 55° (blue line), normalized with the $L_{III,II}$-edge jump.

BL4B

Spin Reorientations of Fe/Ni/Pd(111) Films Studied by XMCD

I. Yamamoto, T. Nakagawa, Y. Takagi and T. Yokoyama
Institute for Molecular Science, Okazaki 444-8585, Japan

Surface magnetic anisotropy of magnetic thin films is one of the critical factors in determining the magnetization easy axis. The surface anisotropy is sensitive to surface modifications such as the adsorption of gases and metals, which induce sometimes spin reorientation transition (SRT). In this work, we have investigated Fe-induced SRTs for Ni/Pd(111) system by x-ray magnetic circular dichroism (XMCD).

Fe and Ni thin films were prepared by electron-beam evaporation method at room temperature. The angle-dependent Fe L-edge and Ni L-edge XMCD measurements were performed with a total electron mode using a UHV-compatible superconducting magnet (7 T) XMCD system with a liq. He cryostat [1]. The XMCD spectra were recorded with reversal of magnetic field, and using the circularly polarized synchrotron radiation. All XMCD measurements were done at 55 K.

Figure 1 shows magnetization curves for various Fe thicknesses on Ni(6 ML)/Pd(111) along the surface normal, recorded with the Ni L_{III} XMCD intensity. The magnetic fields of ±5 T are thus confirmed to be enough to saturate the magnetization even along the hard axis. The magnetization easy axis of Ni/Pd(111) system, which shows no thickness-driven SRT, is in-plane. By depositing Fe, two opposite SRTs was observed. Initially submonolayer Fe deposition causes a transition to perpendicular magnetization, and further Fe deposition (~3 ML) induces a return transition to in-plane magnetization. The anisotropic magnetic fields H_a were 0.8 T and 1.8 T for Fe 3 ML and 0 ML (bare Ni 6 ML), respectively (Fe 1 ML and 2 ML is the easy axis). The effective magnetic anisotropy energy K^{eff} were obtained as -38 μeV/atom (Fe 3ML) and -25 μeV/atom (bare Ni 6 ML).

The angular dependent Ni $L_{III,II}$-edge and Fe $L_{III,II}$-edge XMCD spectra for Fe/Ni(6 ML)/Pd(111) at T= 55 K and H= 5 T are shown in Fig. 2. All the XMCD spectra are normalized at L_{II}-edge. The orbital magnetic moments (perpendicular: $m_{orb}^{\perp}$, in-plane: $m_{orb}^{//}$) and spin magnetic moments m_{spin} were obtained by applying the sum rule. The obtained orbital magnetic moments of both Ni and Fe along the magnetization easy axis are larger than that of the hard axis. This result indicates that the orbital magnetic moments contribute to determining the magnetization easy axis.

[1] T. Nakagawa, Y. Takagi, Y. Matsumoto and T. Yokoyama, Jpn. J. Appl. Phys. **47** (2008) 2132.

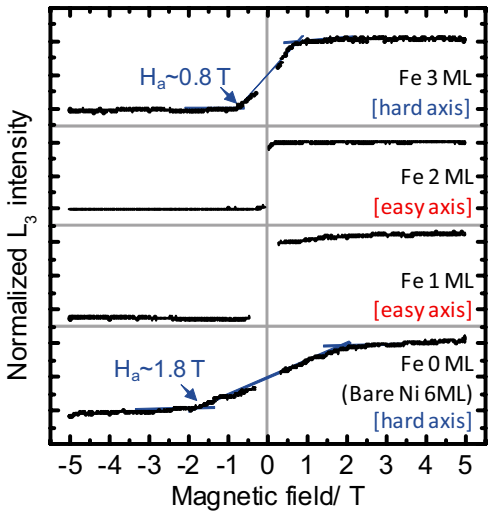

Fig. 1. Magnetization curves of Fe(0-3 ML) on Ni(6 ML)/Pd(111) at 55 K, recorded as Ni L_{III} XMCD intensity.

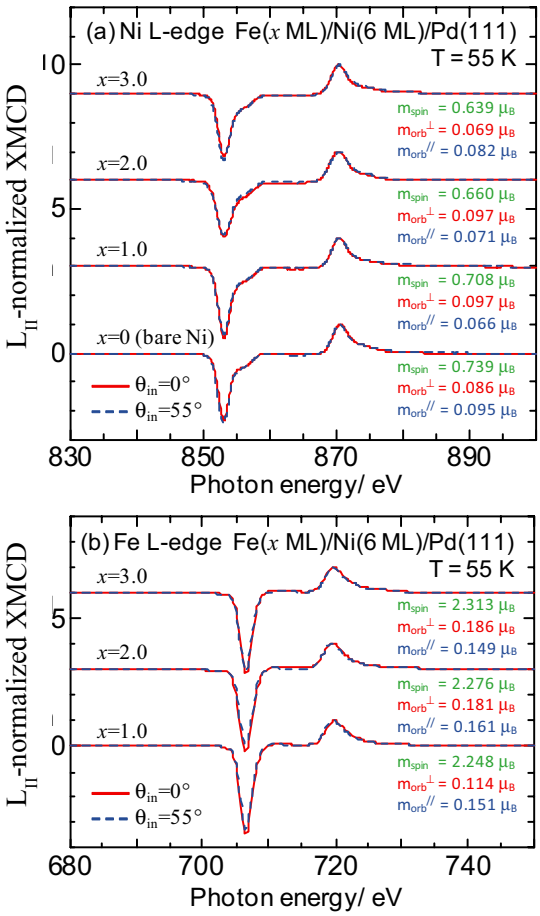

Fig. 2. XMCD results for Fe/Ni(6 ML)/Pd(111). (a) Ni L-edge XMCD spectra. (b) Fe L-edge XMCD spectra.

BL4B

Angular Dependent XMCD Study of Perpendicularly Magnetized $Fe_{1-x}Co_x$/Rh(001)

F. Yildiz[1], M. Przybylski[1], Y. Takagi[2], T. Nakagawa[2], I. Yamamoto[2] and T. Yokoyama[2]

[1]*Max-Planck-Institut f˙ur Mikrostrukturphysik, Weinberg 2, 06120 Halle, Germany*
[2]*Institute for Molecular Science, Okazaki, 444-8585, Japan*

Perpendicular magnetic anisotropy is one of the most important subjects in thin film magnetism because of its technological requirements and fundamental interest in physics. Recently, Yildiz *et al*. [1] discovered extremely strong perpendicular magnetic anisotropy in $Fe_{1-x}Co_x$ alloy films on Rh(001). The maximum critical thickness achieves as much as 15 monolayer (ML) when x=0.6. It was speculated from the remanent XMCD measurements that the orbital magnetic moment of Co dominantly contributes to magnetic anisotropy. In this work, we have measured *in situ* Fe and Co L-edge XMCD (x-ray magnetic circular dichroism) spectra using a superconducting magnet (±7 T) and a liq. He cryostat.

The experiments were carried out at BL4B. Fe and Co were codeposited on clean Rh(001). The concentration ratio Fe:Co was determined by the Fe and Co edge jumps. The XMCD spectra were taken at H=±5 T and T=4.9 K with the incidence angles θ_{in} of 0° (normal incidence) and 55°. The helicity of the x-rays was fixed positively (P_c=+0.67), while the magnetic field was reversed.

The XMCD spectra shown in Figs. 1 and 2 were analyzed using the well-known sum rules. The orbital magnetic moments $m_{orb}(\theta_{in})$ and the effective spin magnetic moments $m_{spin}^{eff}(\theta_{in})$ obtained experimentally yielded the perpendicular and in-plane orbital magnetic moments $m_{orb}^{\perp}$ and $m_{orb}^{//}$, the magnetic dipole moments $m_T^{\perp}$ and $m_T^{//}$, and the intrinsic spin magnetic moment m_{spin}.

The obtained perpendicular and in-plane orbital magnetic moments $m_{orb}^{\perp}$ and $m_{orb}^{//}$ are found to be quite large in both Fe and Co. Especially, it should be noted that the orbital magnetic moments of Fe are large, although the bulk Fe shows much smaller orbital magnetic moment. Moreover, Fe shows more significant angular dependence of the orbital magnetic moment, implying that the strong perpendicular magnetic anisotropy originates mainly from the Fe orbital magnetic moment of Fe, not from the Co one. The present work successfully demonstrates the importance of the hard-axis measurement at a sufficiently high magnetic field using a superconducting magnet for the discussion of magnetic anisotropy.

[1] F. Yildiz, F. Luo, C. Tieg, R. M. Abrudan, X. L. Fu, A. Winkelmann, M. Przybylski and J. Kirschner, Phys. Rev. Lett. **100** (2008) 037205.

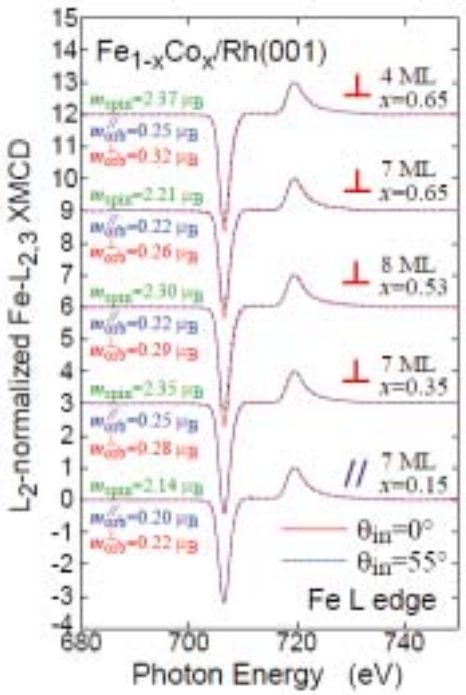

Fig. 1. Fe L-edge XMCD of $Fe_{1-x}Co_x$/Rh(001) at H=±5 T and T=4.9 K. "⊥" and "//" imply that the corresponding films show the perpendicular and in-plane easy axes, respectively.

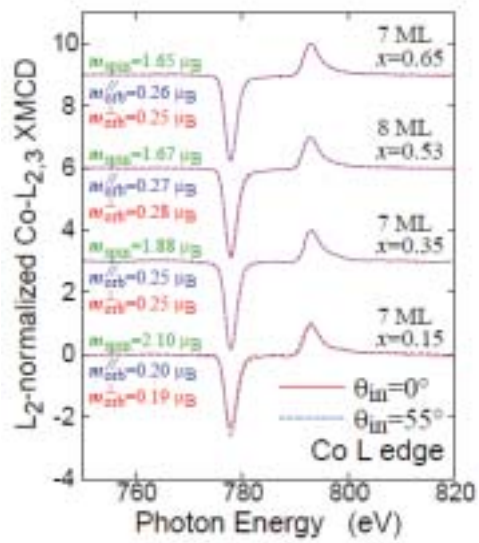

Fig. 2. Co L-edge XMCD of $Fe_{1-x}Co_x$/Rh(001) at H=±5 T and T=4.9 K.

BL7B

VUV Reflection Spectroscopy of PdO, PtO and $Pt_{1-x}Pd_xO$ Thin Films

Y. Iwai, K. Nakagawa, T. Mizunuma, T. Yabumoto, Y. Takayanagi,
S. Matsumoto and H. Matsumoto
School of Science & Technology, Meiji University, Kawasaki 214-8571, Japan

Both PdO and PtO have the same crystal structure and atomic coordinate, and extremely near lattice constants. Extensive experimental and theoretical studies have been performed for the electronic structures of PdO [1]. On the other hand, there are a few reports for PtO in experimental data obtained by electric and optical measurements. Various reports have been done about the existence of the band gap of PtO. In recent yeas, a small gap was expected [2]. To verify the result of the theoretical results, we try to take a wide view of the electronic structure of PtO by obtaining a wide range optical properties experimentally. As part of this work, we designed to use PdO as an object of comparison of PtO [3]. In the present study, $Pt_{1-x}Pd_xO$ thin films were prepared, and they were added to the target for comparison.

Experiment

$Pt_{1-x}Pd_xO$ thin films ($0 \leq x \leq 1$) were deposited by RF reactive sputtering on fused quartz substrate, at a temperature of 673 K. Metal palladium and platinum plate were used as the target, and the sputtering was carried out in argon and oxygen mixture gases. The film thickness was about 150 nm. Composition ratio, chemical bonding states and crystallinity of the films were investigated by RBS, XPS and XRD.

Reflection spectra of the films were measured under the vacuum ultraviolet region up to 30 eV with the 3-m normal incident monochromator (grating: G1 and G2) at BL-7B of UVSOR-II. And a silicon photodiode sensor was used as a detector for the reflection light.

Results and Discussion

According to the analysis techniques mentioned above, all the films prepared for this work ware composed of polycrystalline of $Pt_{1-x}Pd_xO$.

Figure 1 shows the reflection spectra of $Pt_{1-x}Pd_xO$ thin films in room temperature. In the reflection spectra of PdO and PtO, many similar features were seen and some possibility about the relation between the peaks of PdO and PtO remained: 6 eV-peak in PdO (peak-B) is related to 4 eV-peak or 8 eV-peak in PtO; 19.4 eV-peak in PdO (peak-E) is related to 17.5 eV-peak or 21 eV-peak in PtO.

As Pt composition ratio is increased in $Pt_{1-x}Pd_xO$ thin films, peak-B and peak-E exhibited continuous shift to lower energy. Hence, it may be concluded that peak-B and peak-E in PdO are related to 4 eV-peak and 17.5 eV-peak in PtO, respectively, and peak-C in PdO is related to 8 eV-peak in PtO. Since the relations of the peaks become clear, it is possible to discuss the differences of the features of each reflection spectrum.

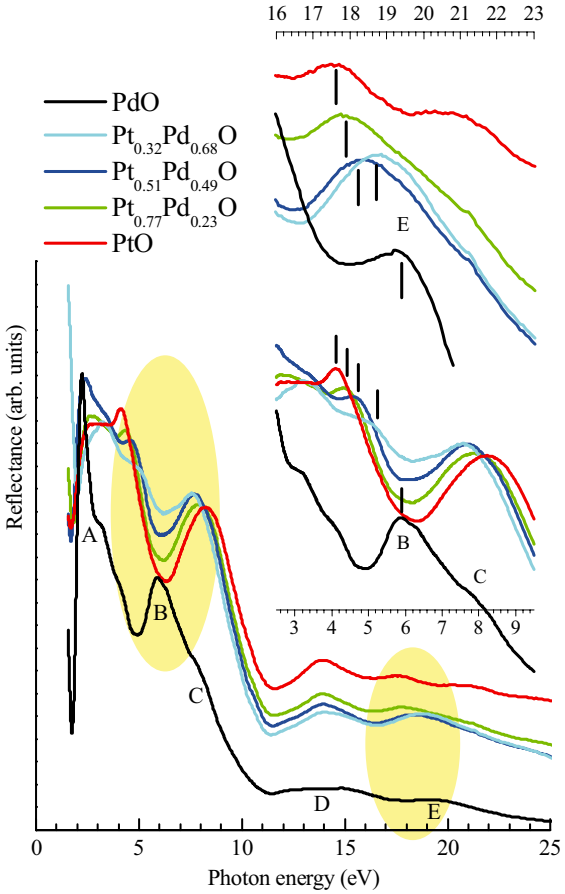

Fig. 1. Reflection spectra of $Pt_{1-x}Pd_xO$ thin films. The data below 6 eV in photon energy was measured elsewhere with deuterium and xenon lamps. The insets are expanded spectra in specific range.

The energy positions of peak-B and related peak in PtO is remarkable. In the spectrum of PdO, it is separated from peak-A by a dip. On the other hand, 4 eV-peak in PtO overlaps the reflection band below the peak. Our theoretical calculation [3] have predicted that the energy levels of Pd5s and Pd5p orbital will form at higher energy than unoccupied Pd4d orbital, and the energy levels of Pt6s and Pt6p orbital will overlap the energy levels of Pt5d orbital. Therefore, the origin of the reflection peak-B and corresponding peak in PtO is considered to be the metal s and p orbital.

[1] H. A. E. Hagelin *et al.*, J. Electron. Spectrosc. Relat. Phenom. **124** (2002) 1.
[2] J. Uddin *et al.*, Phys. Rev. B **71** (2005) 155112.
[3] Y. Iwai *et al.*, UVSOR Activity Report **35** (2008) 96.

BL7B

Photoabsorption Cross Section of C_{70} Thin Films from the Visible to Vacuum Ultraviolet

H. Yagi[1], K. Nakajima[1, 2], K. R. Koswattage[3], K. Nakagawa[3], H. Katayanagi[1] and K. Mitsuke[1]
[1]*The Institute for Molecular Science and Graduate University for Advanced Studies, Okazaki 444-8585, Japan*
[2]*Science Research Center, Hosei University, Chiyoda-ku, Tokyo 102-8160, Japan*
[3]*Faculty of Human Development, Kobe University, Nada-ku, Kobe 657-8501, Japan*

Since Krätschmer *et al*. established the method for synthesizing macroscopic amount of C_{60} and C_{70}, optical properties of solid C_{70} have been studied by various techniques. But to our knowledge these studies were restricted to the photon energies below 6.2 eV. In the present study, we have determined the absolute photoabsorption cross section of C_{70} thin film from 1.3 to 42 eV.

Polycrystalline C_{70} films with the thickness of 11 to 57 nm were prepared by the vacuum deposition method. The collodion thin film substrate and a surface thickness monitor (Inficon, XTM/2) were mounted 90mm above the C_{70} vapor source so that their centers were equidistant from the vapor source. Thus the thickness t of the C_{70} film on the substrate was calculated from $t=M_{TM}/A_{TM}\rho$, where M_{TM} is the total mass of C_{70} deposited on the thickness monitor, A_{TM} is the effective area of the thickness monitor and ρ = 1.68 g cm^{-3} is the mass density of solid C_{70} at room temperature.

Optical absorption measurements were carried out by means of photon attenuation method. The absolute photoabsorption cross section σ_{film} of the C_{70} thin film was estimated by using the Lambert-Beer law.

$$\sigma_{film} = \frac{1}{tN}\ln\frac{I_0}{I} = \frac{A_{TM}M}{M_{TM}L}\ln\frac{I_0}{I}$$

Here, N is the number density of C_{70} in the sample, I is the light intensity measured downstream of the collodion substrate covered with a C_{70} film, I_0 is the light intensity measured downstream of the collodion substrate without C_{70}, L is the Avogadro constant, and M is the molar mass of C_{70}. I_0 and I were measured successively and normalized by the ring current of the storage ring.

At $h\nu$ < 6 eV, present data were affected by the reflection at the sample surface and/or scattering at the grain boundaries. Therefore, instead of using present data, we calculated σ_{film} from the dielectric function $\varepsilon(\nu)$ reported by Kataura *et al*. [1] at $h\nu$ < 6 eV. Thus determined σ_{film} curve is shown in Fig. 1 (black solid curve). From the σ_{film} curve in Fig. 1, we calculated the complex refractive index $n(\nu)$ = $n'(\nu)+in''(\nu)$, and the complex dielectric function $\varepsilon(\nu)$ = $\varepsilon_1(\nu)+i\varepsilon_2(\nu)$ by using Kramers-Kronig analysis. The $\varepsilon(\nu)$ curves obtained from present σ_{film} curve agree well with those obtained from the EELS results by Sohmen *et al*. [2].

In the case of C_{60}, the absolute photoabsorption cross section of a single molecule σ_m can be calculated from σ_{film} by considering the correction of the Lorentz-Lorenz local field by surrounding C_{60} molecules [3]. In the previous paper, we actually demonstrated that σ_m curve of C_{60} calculated from the σ_{film} curve shows good agreement with the absolute photoabsorption cross section σ_{gas} curve of gaseoou C_{60} [4]. The Lorentz-Lorenz local field correction is also applicable to our C_{70} thin films because most part of solid C_{70} prepared by vacuum deposition shows fcc structure at room temperature. The blue solid curve in Fig. 1 shows the σ_m of C_{70} calculated from present σ_{film} curve. Unlike the case of C_{60}, no experimental data of σ_{gas} of C_{70} is available above $h\nu$ ~5 eV. Therefore we calculated σ_{gas} of C_{70} from the EELS spectrum of gaseous C_{70} [5]. Red dots in Fig. 1 represent thus calculated σ_{gas} of C_{70}, which appears to agree with the present σ_m except at several fine structures.

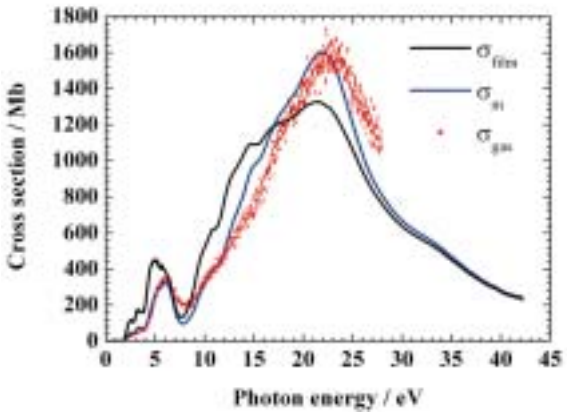

Fig. 1. Photoabsorption cross section of C_{70} thin film (black curve), C_{70} single molecule (blue curve) calculated from σ_{film}, and gaseous C_{70} (red dots).

[1] H. Kataura *et al*., J. Phys. Chem. Solids **58** (1997) 1913.
[2] E. Sohmen *et al*., Z. Phys. B: Condense. Matter **86** (1992) 87.
[3] J. Andersen and E. Bonderup, Eur. Phys. J. D **11** (2000) 435.
[4] H. Yagi *et al*., Carbon, **47** (2009) 1152.
[5] N. Ju *et al*., Phys. Rev. B **48** (1993) 9071.

BL8B2

Angle-Resolved UPS of Perfluoropentacene Monolayer on Graphite

S. Kera, S. Hosoumi, T. Aoki, S. Duhm, S. Nagamatsu and N. Ueno

Graduate School of Advanced Integration Science, Chiba University, Chiba 263-8522, Japan

A newly synthesized molecule of perfluoropentacene (**PFP**) was reported to act as n-channel OFET and fabricated ambipolar transistors with pentacene [1]. We have investigated the electronic structure and molecular orientation of **PFP** in a monolayer film by using angle-resolved ultraviolet photoelectron spectroscopy (ARUPS). ARUPS has been known as a powerful technique to obtain crucial information on electronic band structure for various kinds of materials. Moreover, for organic thin films, information on the geometrical structure of the thin films can be also discussed in accordance with a quantitative analysis of the ARUPS intensity using photoelectron scattering theory.

In this report, we show the observed electron-emission-angle (θ) dependence of HOMO band in ARUPS spectra for the **PFP** monolayer deposited on the graphite substrate.

Experiments

ARUPS spectra were measured at photon incidence angle α=45°, hν=35 eV, and T=295 K. The purified molecules were carefully evaporated onto the graphite (HOPG) substrate at 295 K. The nominal thickness of the monolayer is confirmed by the work function of the condensed monolayer film of 4.6 eV. θ dependence was analyzed using the multiple-scattering theory combined with molecular orbital calculation (MST/MO) [2]. We have calculated the θ pattern from a free molecule itself.

Results and Discussion

Figure 1 (a) shows the θ dependence of ARUPS of **PFP** (0.3nm) on the HOPG. The intensity is normalized to the incidence photon flux. A top feature appeared around 1.5 eV is ascribed to HOMO band of **PFP**. Figures 1 (c) and (d) show the comparison between observed and calculated θ dependences of the HOMO intensity. The HOMO intensities are evaluated after background subtraction and shown to normalize at the maximum intensity. The observed intensity gives the maximum at around 37°. The calculated intensities are shown for the molecular tilt angles β, which is inclined angle from the long-molecular axis, and γ, which is angle from the short axis (see Fig.1 (b)). Azimuthal angle ϕ is integrated due to the polycrystalline HOPG surface in Fig.1 (c). Among them, the molecular tilt angles of β=0° and γ=0° gives the best agreement with the observed θ pattern. However, the calculated pattern is still broader than the observed one. In Fig.1 (d), calculated θ patterns, where the patterns are obtained at fixed ϕ = 36° or 38°, are compared to the observed one, giving the best agreement. It indicates that the molecules are perfectly oriented flat to the substrate and form a uniform monolayer film, where the molecular single domain is large enough unexpectedly.

In fact, one can see a relatively large energy shift of the HOMO about 210 meV depending on the θ (see the guide lines) in Fig.1(a). The intermolecular HOMO-HOMO overlapping might be large enough to detect an energy-band dispersion. Accordingly we expect that the DOS structure in the HOMO feature of UPS, which comes from the HOMO band dispersion, could be observed even for polycrystalline **PFP** films as in pentacene standing film [3]. Note that one should also consider the large anisotropic vibronic coupling for such an ordered film. Nevertheless, ARUPS study for the well-ordered **PFP** film on the single crystal would be fascinating.

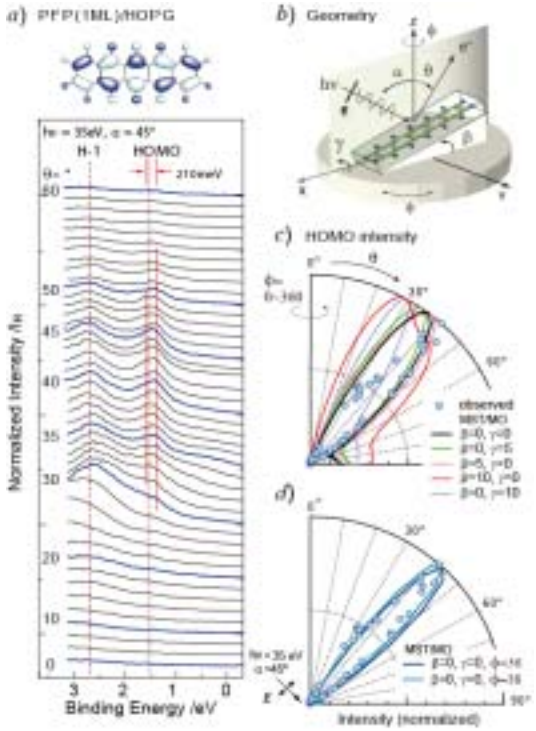

Fig. 1. (a) θ dependence of ARUPS of PFP monolayer on HOPG. (b)Computation geometry for the MST/MO method. (c) and (d) Observed and calculated θ patterns of the HOMO. ϕ is integrated for 0~360° in (c). Schematic view of the HOMO pattern is also shown.

[1] Y. Sakamoto *et al.*, J. Am. Chem. Soc. **126** (2004) 8138.

[2] S. Nagamatsu *et al.*, e-J. Surf. Sci. Nanotech **3** (2005) 461.

[3] H. Fukagawa *et al.*, Phys. Rev. B **73** (2006) 245310.

BL8B2

Electronic Structures of Single Crystalline Rubrene Studied by Photoemission Measurement Techniques

Y. Nakayama[1], S. Machida[2], T. Kubo[1, 3], A. Funakoshi[2], N. Ogawa[3], T. Minari[4], K. Tsukagoshi[4] and H. Ishii[1, 2]

[1] *Center for Frontier Science, Chiba University, Chiba 263-8522, Japan*

[2] *Graduate School of Advance Integration Science, Chiba University, Chiba 263-8522, Japan*

[3] *Faculty of Engineering, Chiba University, Chiba 263-8522, Japan*

[4] *National Institute for Materials Science, Tsukuba, Ibaraki 305-0047, Japan*

Rubrene (5,6,11,12-tetraphenyltetracene) is one of the most promising materials for organic field effect transistor application due to its high hole mobility. To understand the transport nature and improve the device performance, information about the electronic structures is indispensable. There have been a number of reports about the electronic states of amorphous thin films (TFs) of rubrene studied by photoelectron spectroscopy (PES) [1, 2]. On the other hand, sufficiently high field effect mobility has not been realized for the rubrene TFs but only for the crystalline phase. It has been known that rubrene molecules in the single crystals (SCs) have different conformation from those in the TFs [3]. This fact implies different electronic states of rubrene SC from those of its TF phase. However, experimental observation of the electronic structures of rubrene SCs has not been reported. It is mainly because PES measurement on organic crystals has been awkward due to the sample charge-up problem.

In this study, we conducted direct observation of the electronic structures of rubrene SCs by two types of photoemission measurement techniques to overcome the aforementioned issues. The one was photoelectron yield spectroscopy (PYS) that gives us information about ionization potentials (IPs) of specimens excluding any effects of the charge-up [4]. The other was PES with special tactics, illumination of visible laser light and positive biasing on the samples, in order to relieve the charge-up problem.

Rubrene SCs were produced by a physical vapor transport technique and were fixed on conductive substrates (indium-tin-oxide (ITO) or Au) with silver paste. Rubrene TFs that were formed on ITO by *in-situ* vacuum deposition were also examined for comparison. Details of the PYS apparatus were described elsewhere [5]. PES measurement was performed at BL8B2 in UVSOR.

As shown in PYS spectra (Fig. 1), rubrene SCs exhibited apparently lower threshold energy of photoelectron emission compared to its TFs [6]. It means that crystallization lifts the highest occupied molecular orbital (HOMO) of rubrene upward to the vacuum level.

Figure 2 shows PES spectra of a SC and a TF of rubrene. Laser light (405 nm, 1 mW) and positive bias (+20 V) were applied on the SC sample during measurement. The HOMO peak of the SC appeared at a lower binding energy position compared to that of the TF, whereas positions of the other peaks are roughly same for the both spectra This result also supports the upshift of the HOMO energy of rubrene caused by crystallization. Mapping of the electronic band structures of rubrene SC by angle resolved PES is now underway by utilizing these techniques.

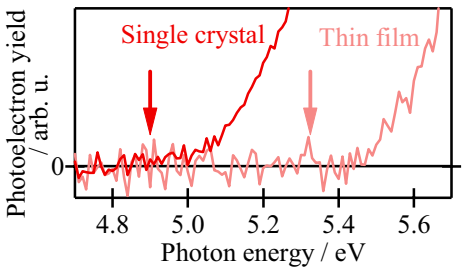

Fig. 1. PYS spectra of a SC and a TF of rubrene. Estimated IPs are indicated as arrows.

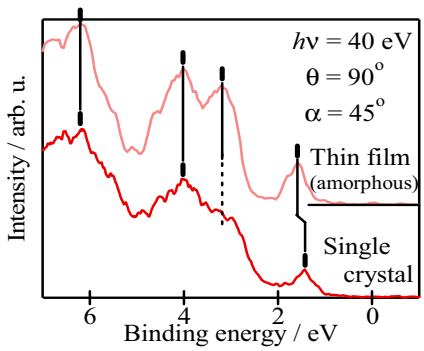

Fig. 2. PES spectra of a SC and a TF of rubrene.

[1] Y. Harada *et al.*, Chem. Phys. Lett. **62** (1979) 283.
[2] L. Wang *et al.*, Appl. Phys. Lett. **90** (2007) 132121.
[3] D. Käfer *et al.*, Phys. Rev. Lett. **95** (2005) 166602.
[4] Y. Nakayama *et al.*, Appl. Phys. Lett. **92** (2008) 153306.
[5] H. Ishii *et al.*, J. Surf. Sci. Soc. Jpn. **28** (2007) 264.
[6] Y. Nakayama *et al.*, Appl. Phys. Lett. **93** (2008) 173305.

BL8B2

Interaction between 11,11,12,12-Tetracyano-2,6-Naphthoquinodimethan (TNAP) and Bismuth (001)

T. Nishi[1], S. Nagamatsu[2], T. Aoki[2], K. Kato[2], S. Hara[2], M. Tsunekawa[3], K. Sakamoto[2] and N. Ueno[2]

[1]*Center for Frontier Science, Chiba University, Chiba 263-8522, Japan*

[2]*Graduate School of Advanced Integration Science, Chiba University, Chiba 263-8522, Japan*

[3]*Research Center for Materials Science, Nagoya University, Nagoya 464-8602, Japan*

The energy level alignment at the interface between molecule and electrode is one of the most important subjects in organic thin film devices, since the phenomena at the interface such as charge injection barrier affects their performance. Complicated several factors render understanding phenomena at the interface very difficult. For example, in the case of the vacuum level (VL) shift, which is one of the most important phenomena in the energy level alignment of organic/metal interface, six factors in molecule-substrate that closely relate each other must be considered [1].

In the case of 11,11,12,12-tetracyanonaphtho-2,6- -quinodimethane (TNAP, Fig.1.), which is an electron accepter π-conjugated organic molecule shows interesting correlation on noble metal substrates. That is, a diffusion of Cu atoms to TNAP thin film, a charge transfer and a weak interaction have been observed on Cu (work function, Φ = 4.9), Ag (Φ = 4.7) and Au (Φ = 5.3), respectively [2]. On the other hand, Bismuth is considered to be a low active material despite the low work function of its (001) surface, Φ = 4.22 [3], which is smaller than those of Cu, Ag and Au. In this paper, the electronic structure of TNAP / Bi (001) is reported.

Sample was prepared by depositing TNAP (Tokyo Kasei) on a Bi(001) film formed on a Si(111)-(7×7) substrate in a ultra high vacuum chamber. The quality of the Si(111)-(7×7) reconstruction was checked by low energy electron diffraction (LEED). The thickness of Bi deposited on the Si substrate was 10 bi-layers. TNAP powder crystals were loaded in Pyrex glass crucible. The deposition rate of TNAP was less than 0.025 nm/min. UPS measurements were performed using photon energies of 21.2 eV and 50 eV. DFT calculations were carried out using the B3LYP functional, with 6-311G (p,d) and 6-311G ++ (p,d) split valence plus polarization basis set for neutral and anion state by Gaussian 03, respectively [4]. The geometry of TNAP was optimized via DFT. The angular distributions of photoemission were obtained by the multiple-scattering approximation combined with the molecular orbital (MS/MO) calculation [5].

Figure 2 shows the valence band region of UPS spectra of Bi(001) and TNAP, the thickness is ~0.3nm corresponding to 1 monomolecular layer (ML). At TNAP spectrum, a density of state was observed just below the Fermi energy like the case of 2,3,5,6-tetrafluoro-7,7,8,8-tetracyanoquinodimethane (F4-TCNQ) / Au [6]. The calculations have been done assuming that TNAP lies flat on the Bi(001) substrate by taking into account the STM image. The results indicate that the interaction between Bismuth and TNAP is strong. There is a possibility of charge transfers from Bismuth to TNAP like F4-TCNQ / Au case.

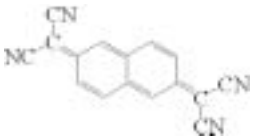

Fig. 1. Molecular structure of TNAP.

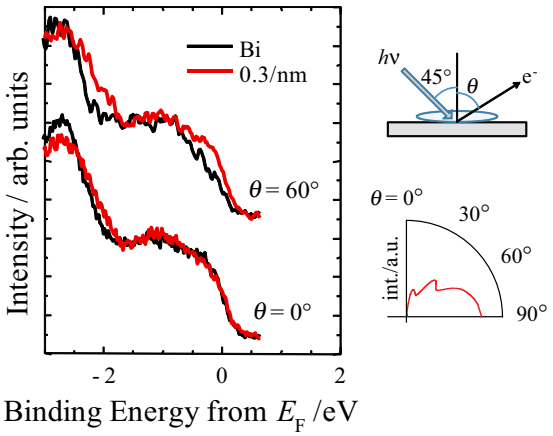

Fig. 2. UPS spectra of Bi(001) and TNAP, 1 ML, on Bi(001) and angular distribution of photoemission of $TNAP^-$ HOMO by MS/MO calculation.

[1] H. Ishii *et al.,* Adv. Mat. **11** (1999) 605.
[2] K. Kanai *et al.,* MRS symp. Proc. **871E** (2005). K. Kanai and K. Seki, J. Vac. Soc. Jpn. **50** (2007) 722.
[3] H. Kakuta *et al.,* Phys. Rev. Lett. **98** (2007) 247601.
[4] Gaussian 03, Revision C.02, M. J. Frisch *et al.*, Gaussian, Inc., Wallingford CT, 2004.
[5] S. Nagamatsu *et al.*, e-J. Surf. Sci. Nanotech. **3** (2005) 461.
[6] N. Koch *et al.*, Phys. Rev. Lett. **95** (2005) 247601.

BL8B2

Molecular Orientation of P3HT Thin Film by ARUPS

K. K. Okudaira, Y. Suzuki and N. Ueno
Association of Graduate Schools of Science and Technology, Chiba Univererity, Chiba 263-8522, Japan

Introduction

The structure-property relationship of solution-processible conducting polymers with π-conjugated electronic structures have been explored extensively due to their significant impact in optoelectronic applications. Solution-processed regioregular conjugated poly(3-hexylthiophene) (P3HT) thin films can easily lead to well-organized conformation leading to highly oriented polymer films.[1] The long-range order and π-π interchain stacking in the P3HT thin films play an important role on the charge transport process and the device performance. However, few studies on structural characteristics such as quantitative determination of surface molecular orientation were reported.

In this report we observed angle-resolved ultraviolet photoelectron spectra (ARUPS) of P3HT spin-casted thin films with various coating parameters to clarify the molecular orientation (tilt angle of polymer backbone)

Experimental

ARUPS measurements were performed at the beam line BL8B2 of the UVSOR storage ring at the Institute for Molecular Science. The take-off angle (θ) dependencies of photoelectron spectra were measured at incident angle of photon (α) = 45° with the photon energy (hν) of 40 eV.

The polymer thin films were prepared on gold coated Si(100) wafers by spin casting.. The spin casting was performed 60s with speeds of 4500 and 400 rpm for solution concentrations of 5 and 0.5 mg/mL, respectively.

Results and Discussion

Figures 1 (a) and (b) show the θ dependencies of ARUPS spectra of P3HT thin film with speeds of 4500 and 400 rpm, respectively. In Figure 1 peak 1 located at about binding energy of 3-4 eV corresponds to the localized π states contributed from S 3pz.[2] For both sample, the intensities of peak 1 show θ dependence..

The observed θ dependencies of the peak 1 (π band) intensities of the P3HT thin film with different spin-cast speeds are plotted in Fig. 2. It was found that the θ dependence of the π band (peak 1) intensity for the thin film with spin-casted speed of 4500rpm is different from that with 400 rpm. It indicates that the molecular orientation (tilt angle of polymer backbone) was affected by process parameter. To determine the molecular orientation quantitatively, it needs to compare the observed θ dependencies with the calculated ones.

[1] H. Sirringhaus *et al.*, Nature **401** (1999) 685.
[2] X. T. Hao *et al.*, J. Phys. Chem. B. **111** (2007) 10365 .

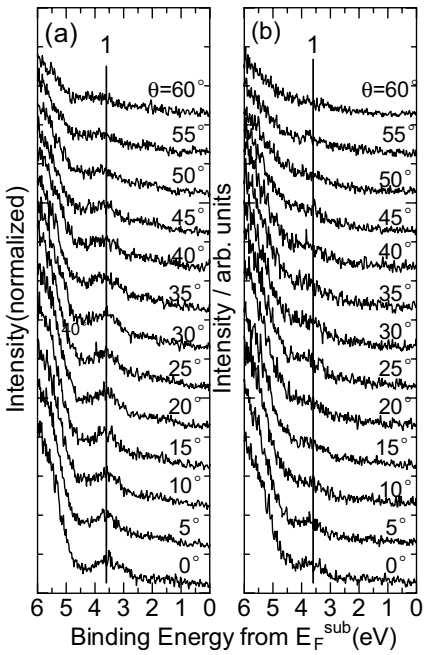

Fig. 1. Take-off angle (θ) dependence of ARUPS of P3HT spin-casted thin films with speeds of 4500 (a), 400 rpm (b), respectively.

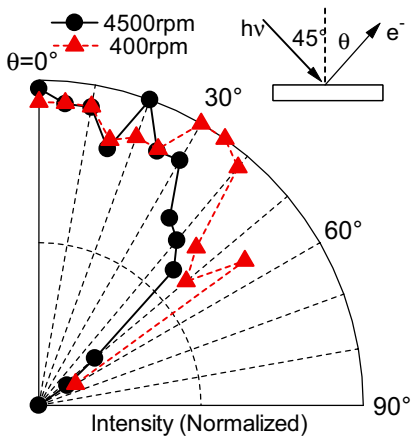

Fig. 2. Take-off angle (θ) dependencies of photoelectron intensities of peak 1 (indicated in Fig. 1) for P3HT spin-casted film with speeds of 4500 (●) and 400 rpm (▲).

BL8B2

Formation of Interface State at the Zinc-Phthalocyanine/In Interface

S. Tanaka, K. Watanabe, S. Mizuta and I. Hiromitsu

Department of Material Science, Interdisciplinary Faculty of Science and Engineering, Shimane University, Matsue 690-8504, Japan

Organic electronics devices, such as organic light emitting diodes, organic solar cells, organic thin film transistor, etc…, are expected as a candidate of the electronics devices for the next generation. The property of metal/organic interface has a critical role for the performance of such organic electronics devices.

In this study, we focused on the interface electronic structure of the zinc phthalocyanine (ZnPc)/In interface. ZnPc is a semiconducting material and plays an important role in the organic devices. In has a small work function (~4.1 eV) and is used as a cathode (or electron injection) metal.

The electronic structure of ZnPc and In interface was investigated by using the photoelectron spectroscopy. Figure 1 shows photoelectron spectra of In incrementally deposited on the ZnPc layer. The abscissa is the binding energy relative to the Fermi energy of substrate. The light with photon energy of 40 eV was used for the measurements. The deposition rate of In was ~ 0.2 nm/min. The peak at 1.5 eV in the ZnPc (30 nm) spectrum is the highest occupied molecular orbital (HOMO) of ZnPc. In the spectrum of 0.5 nm of In on the ZnPc layer, an in-gap peak was observed at around 0.5 eV (The hatched area in the figure). In addition, the intensity of HOMO of ZnPc was decreased drastically with a slight shift toward higher binding energies. Similar behavior has been observed in the experiments about the In deposition on the organic layers [1, 2]. The origin of the interface states of the In-on-ZnPc interface was considered as the electron transfer from In to ZnPc by analogy with the study of In on copper phthalocyanine system [2]. On the secondary electron cutoff, an abrupt shift (~ 0.6 eV shift to higher binding energy) was observed at the deposition of 0.5 nm In (not shown here). This may also relate to the charge transfer between In and ZnPc, although further studies are needed.

With the increase of the In thickness, the intensity of in-gap state was decreased. In addition, the signal from the HOMO of ZnPc was observed on the spectrum with 20 nm deposition of In. These results indicate that: (i) the distance between the In atom and the ZnPc molecule was an important parameter for the formation of the in-gap state, (ii) In atoms were diffused into the ZnPc layer.

Note that the interface state was not observed in the spectra of ZnPc on the In layer. (Fig. 2) This result indicates that the order of the deposition critically affects the electronic state of the interface. A driving force of the diffusion of In atoms into the ZnPc layer is probably needed for the formation of the in-gap state.

Based upon these results it is expected that there is a difference in the carrier transfer properties between the In-on-ZnPc interface and the ZnPc-on-In interface. It is known that the rectifying contact is formed at the In-on-ZnPc interface [3]. Investigations of the effects of the interface states on the electric properties of the ZnPc/In interface are now in progress.

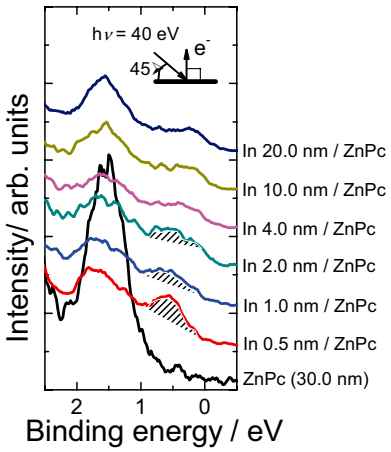

Fig. 1. Photoelectron spectra of In incrementally deposited on the ZnPc layer. An in-gap state (hatched) was observed for the low-thickness region.

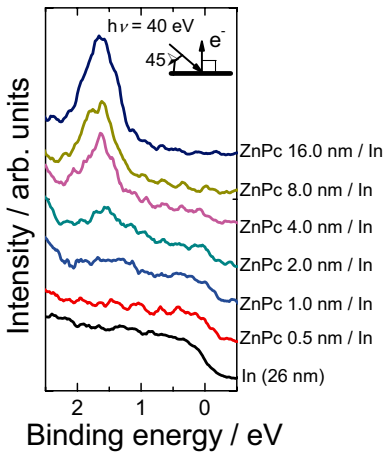

Fig. 2. Photoelectron spectra of ZnPc incrementally deposited on the In layer.

[1] Y. Hirose *et al.*, Phys. Rev. B **54** (1996) 13748.
[2] V. Yu. Aristov *et al.*, Phys. Rev. B **72** (2005) 165318.
[3] M. Nonomura *et al.*, Appl. Phys. Lett. **88** (2006) 042111.

BL1B

Magneto-Optical Kerr Effect in $Nd_2(Mo_{1-x}Nb_x)_2O_7$

S. Iguchi[1], S. Kumakura[1], Y. Onose[1, 2] and Y. Tokura[1, 2, 3]

[1]*Dept. of Applied Physics, Univ. of Tokyo, Tokyo 113-8656, Japan*

[2]*Multiferroics Project, ERATO, JST, Wako 351-0198, Japan*

[3]*Cross-Correlated Materials Research Group, ASI, RIKEN, Wako 351-0198, Japan*

The origin of the anomalous Hall effect (AHE) has long been discussed since 1960's in terms of the band effect by Karplus-Luttinger, the spin fluctuation, and the side jump, etc. Recent theoretical studies on the AHE due to the Berry phase or the spin-chirality mechanism are the quantum theoretical extension from the traditional perturbative treatment by Karplus-Luttinger, and have revealed the significance of the resonant effect [1] at a small gap in band structure due to some kind of interaction, such as the spin-orbit interaction or the spin chirality.

Magneto-optical Kerr effect (MOKE) is an extension of AHE with respect to the energy range. The MOKE measurements for $Nd_2Mo_2O_7$ with spin chirality and $Gd_2Mo_2O_7$ without it have revealed that there is an enhancement in the mid-IR region of the off-diagonal optical conductivity $\sigma_{xy}(\omega)$ originated from the spin chirality [2]. The scaling relation between the anomalous Hall conductivity and the longitudinal resistivity in $Nd_2(Mo_{1-x}Nb_x)_2O_7$ (NMNO) with spin chirality [1] is in good agreement with the theoretical prediction, which should be considered as the resonant effect among the slightly gapped t_{2g} bands by the spin chirality. Thus, the direct observation of the resonant effect in $\sigma_{xy}(\omega)$ is desired for the investigation on the origin of the AHE. The NMNO is suitable for the possible observation of the resonant structure in $\sigma_{xy}(\omega)$ and its systematic change with the electron doping by Nb^{5+} (Fig. 1).

All the specimens used in this study were of single crystals synthesized by a floating-zone method. The reflectivity measurement has been performed from 20 meV to 40 eV for $E\|(100)$. Especially for the energy range of 4-40eV, we used the spectrometer equipped in BL-1B at UVSOR (see Fig. 2). Thus the highly accurate optical conductivity ($\sigma_{xx}(\omega)$) was acquired. Then the $\sigma_{xy}(\omega)$ was calculated with the obtained $\sigma_{xx}(\omega)$ and the MOKE spectrum for the energy range of 0.1-4.5 eV.

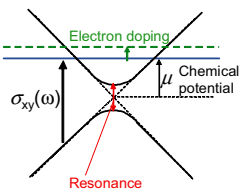

Fig. 1. The schematic picture of the resonant structure and the electron doping effect in $\sigma_{xy}(\omega)$.

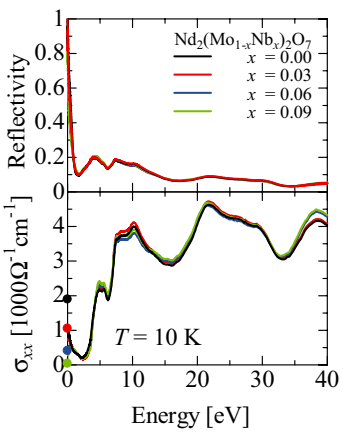

Fig. 2. The reflectivity and conductivity in NMNO. The temperature is 300 K for 4-40 eV range.

Figure 3 shows the spectra of the optical conductivity, the real and imaginary components of $\sigma_{xy}(\omega)$ in NMNO at 10 K. The $\sigma_{xx}(\omega)$ shows the correspondent change with the dc conductivity (metallic to insulating with increasing x) without remarkable anomaly such as a peak. In contrast, the characteristic peak structure was observed in the mid-IR range in the $\sigma_{xy}(\omega)$ as well as the continuity to the dc value represented by the dots in the Fig. 2. Especially, some of the peak-top values are larger than dc ones meaning the resonance effect is intrinsic for the off diagonal conductivity. The shift of the peak to higher energy is considered as the increase in the chemical potential by Nb doping as depicted in Fig. 1.

In conclusion, we have demonstrated the resonance effect of bands in $\sigma_{xy}(\omega)$, which is in good accordance with the Berry phase theory, and revealed the $\sigma_{xy}(\omega)$ is subject to the band structure.

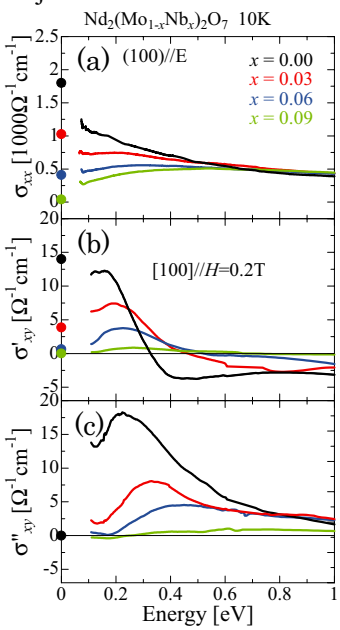

Fig. 3. (a) The optical conductivity, (b) the real and (c) the imaginary part of off-diagonal optical conductivity in NMNO at 10 K.

[1] S. Onoda *et al.*, Phys. Rev. B **77** (2008) 165103.
[2] I. Kézsmárki *et al.*, Phys. Rev. B **72** (2005) 094427.
[3] S. Iguchi *et al.*, Phys. Rev. Lett. **99** (2007) 077202.

BL1A

Investigfation of Al K-Edge of Local Structure in Mesoporous Alumina Bulk with Fe Addtion

A. Nakahira, T. Nishimoto, T. Kubo and T.Onoki
Faculty of Engineering, Osaka Prefecture University, Gakuencho, Sakai 599-8531, Japan

Introduction

Much attentions have been paid to mesoporous materials. Among them, mesoporous alumina is also one of unique mesoporous materials because of their possible usages as a support material for catalysts and adsorption. However, the application of mesoporous alumina was restricted since mesoporous alumina was obtained only as a powder. The development of solidification of mesoporous alumina will expand the possibility of its application to various fields. After Nakahira et al reported that the dense bulk of zeolite was successfully synthesized using hydrothermal hot-pressing (HHP) method [1], it was found that the mesoporous materials could be also densified by hydrothermal hot-pressing (HHP) method. Here, we attemped to fabricate the dense bulks for mesoporous alumina containing with Fe salt. In this study, the local structure around Al of bulks of mesoporous alumina with Fe salt prepared by HHP method were invetigated by XANES measurements.

Experiments

Mesoporous alumina powder was synthesized as a starting material by a reference [2]. 2we% Fe salt ($Fe(NO_3)_2$) was added to mesoporous alumina powder, suffiently mixed with alumina mortar and dried at 323 K. Mixture of these mesoporous alumina powders containing with Fe salt and water was heated at 110℃ with uniaxial pressing under 40 MPa for 2 hours. Mesoporous alumina bulks obtained by hydrothermal hot-pressing (HHP) method were heat-treated at 723K in air atmosphere. Mesoporous alumina bulks were identified by XRD measurement.

Al K-edge XANES spectra for mesoporous alumina bulks were obtained in a total electron yield mode at room temperature using a KTP double–crystal monochrometer at BL1A station of UVSOR. The spectra were collected in the photon energy range from 1520 to 1600 eV at intervals of 0.05 eV with a dwell time of 1 s.

Results

Dense mesoporous alumina bulks containing with Fe salt were successfully obtained by hydrothermal hot-pressing (HHP) method and after heat-treatment at 723K in air atmosphere. XRD pattern of these showed that mesoporous alumina HHP bulk was also retained the mesoporous structure after HHP. Fe oxide as an additive was not detected by XRD for mesoporous alumina bulks containing with Fe salt obtained by hydrothermal hot-pressing (HHP) method. Figure 1 shows the results of Al K-edge XANES of mesoporous alumina powder with Fe salt, HHP bulk from mesoporous alumina powder with Fe salt, and reference material powder (α-alumina, γ-alumina, and $Al(OH)_3$). The spectrum of HHP bulk was significantly similar to those of starting powder and γ-alumina. Consequently. these results of XANES spectra revealed that the local structure around Al enviroment was almost unchanged before or after HHP treatment.

[1] A. Nakahira, S. Takezoe and Y. Yamasaki, Chemistry Letters **33** (2004) 1400.
[2] H. Nagata, M. Takimura, Y. Yamasaki and A. Nakahira, Materials Transactions **47** (2006) 2103.

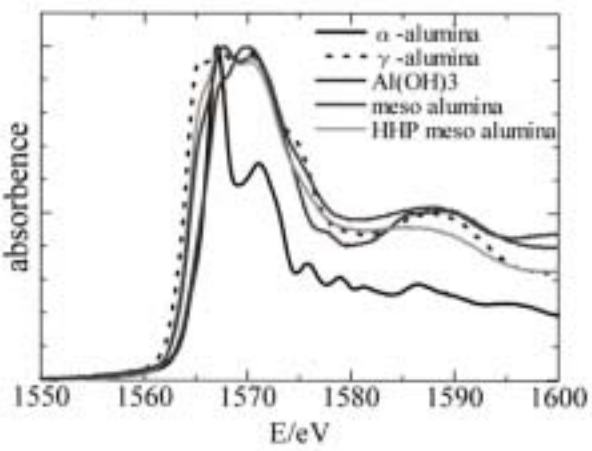

Fig. 1. Al K-edge XANES of mesoporous alumina powder with Fe salt, HHP bulk from mesoporous alumina powder with Fe salt, and reference material powder (α-alumina, γ-alumina, and $Al(OH)_3$).

BL1B

Excitonic Structures of Reflection Spectra of $Bi_4Ge_3O_{12}$ and $Bi_{12}GeO_{20}$

T. Aoki[1], H. Mitani[1], T. Katagiri[1], M. Itoh[1] and M. Fujita[2]

[1]*Dept. of Electrical and Electronic Engineering, Shinshu University, Nagano 380-8553, Japan*

[2]*Japan Coast Guard Academy, Kure 737-8512, Japan*

Bismuth germinate, $Bi_4Ge_3O_{12}$, and bismuth germanium oxide, $Bi_{12}GeO_{20}$, are usually abbreviated as BGO in common. The former (e-BGO) is a cubic crystal (space group $I\bar{4}3d$) of the eulytine-type structure. The latter (s-BGO) is also cubic (space group $I23$) with the sillenite-type structure. In the present experiment, the reflection spectra of e-BGO and s-BGO have been measured on the cleaved surfaces at T = 5 and 300 K. Both crystals were obtained from Dr. Y. Usuki of Furukawa Co.

Figures 1(a) and 1(b) show the reflection spectra of e-BGO and s-BGO in a wide spectral range up to 35 eV at 5 K, respectively. The e-BGO exhibits a sharp lowest-energy peak at 4.81 eV followed by a weak peak at 5.15 eV, as clearly seen in Fig. 2(a). When T is increased from 5 to 300 K, the 4.81 and 5.15 eV bands are considerably broadened, the latter merging into the low-energy part of a broad band at around 6.25 eV. Such a feature reveals that these two bands are related to the excitonic transitions; i.e., the 4.81 and 5.15 eV bands are ascribed to the n = 1 and n = 2 excitons, respectively. The s-BGO exhibits a clear peak at 3.65 eV. This peak is also assigned to the excitonic 6s → 6p transition of Bi^{3+} ions. The n = 2 exciton peak is not observed in s-BGO (Fig. 2(b)).

Assuming the simple hydrogen-like model of exciton, the energy of the nth level, E_n, is expressed as $E_n = E_g - E_B/n^2$, where E_g is the band-gap energy and E_B the exciton binding energy. By substituting the values of E_1 and E_2, we obtain E_g = 5.26 eV at 5 K and 5.17 eV at 300 K for e-BGO. Therefore, the value of E_B is estimated to be 0.45 ± 0.02 eV at 5 and 300 K. On the other hand, the value of E_g in s-BGO is roughly determined to be 3.8 eV from the beginning of the rise of the reflectivity after the excitonic band, thus leading to $E_B \approx 0.15$ eV.

The exciton binding energy is given by $E_B = \mu e^4/2\hbar^2\varepsilon_\infty^2$, where μ is the reduced exciton mass, e the electron charge, $\hbar$ the Planck constant, and ε_∞ the optical dielectric constant. From ε_∞ (e-BGO) = 4.67 and ε_∞ (s-BGO) = 7.13, one can obtain $\mu = 0.72m$ (m: free electron mass) for the exciton in e-BGO and $\mu \approx 0.56m$ for s-BGO.

The reflection spectra above the band gap are briefly discussed by referring to our theoretical results calculated by the DV-$X\alpha$ method [1]. We ascribe the structures in the region of 5.5–12.5 eV in e-BGO and of 4.5–11.0 eV in s-BGO to the transitions from the valence band formed from the hybridized O 2p-Bi 6s states to the bottom of the conduction band. The structures in the region of 12.5–22.5 eV in e-BGO and of 11.5–22.0 eV in s-BGO are attributed to the transitions from the isolated Bi 6s state locating below the valence band to the entire conduction band. Three peaks appearing in the 25–30 eV region in both BGOs are apparently due to the Bi 5d → 6p core exciton transitions.

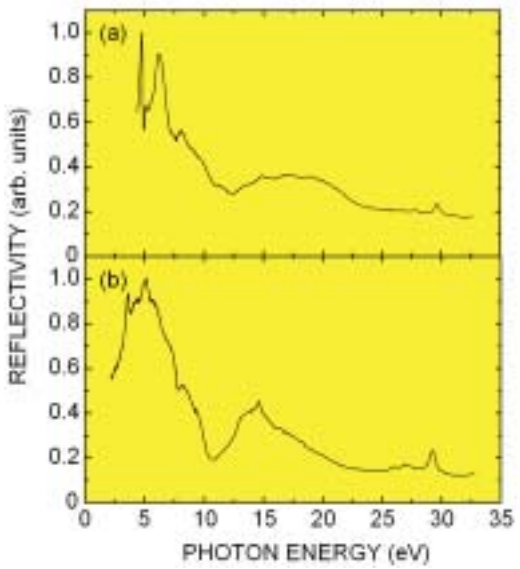

Fig. 1. Reflection spectra of (a) e-BGO and (b) s-BGO in a wide spectral range up to 35 eV measured at 5 K.

Fig. 2. Expanded spectra in the low-energy region of (a) e-BGO and (b) s-BGO shown in Fig. 1.

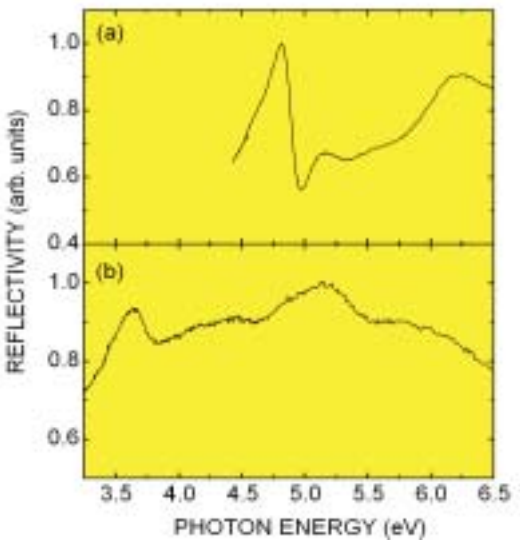

[1] M. Itoh, T. Katagiri, H. Mitani, M. Fujita and Y. Usuki, Phys. Status Solidi B **245** (2008) 2733.

BL1B

Polarization Dependence of Optical Transitions in $CdMoO_4$ and $CdWO_4$

M. Fujita[1], T. Katagiri[2], D. Iri[2], M. Itoh[2], M. Kitaura[3] and V. B. Mikhailik[4]

[1]*Japan Coast Guard Academy, Kure 737-8512, Japan*

[2]*Faculty of Engineering, Shinshu University, Nagano 380-8553, Japan*

[3]*Fukui National College of Technology, Sabae 916-8507, Japan*

[4]*Physics Department, University of Oxford, Oxford OXI 3RH, United Kingdom*

Metal tungstates and molybdates are widely used as scintillating detectors in high-energy particle physics, rare event searches, and medical diagnoses. It is interesting to compare the optical spectra of $CdMoO_4$ with those of $CdWO_4$, since the former crystallizes in the scheelite structure and the latter in the wolframite structure. In $CdMoO_4$ crystal, each Mo site is surrounded by four equivalent O sites to form MoO_4^{2-} molecule of approximately tetrahedral symmetry. In $CdWO_4$ crystal, each W site is surrounded by six O sites in approximately octahedral symmetry. The WO_6^{6-} octahedra form a chain by edge sharing. In the present study, the optical spectra of $CdMoO_4$ and $CdWO_4$ have been investigated in order to clarify their electronic structures.

Reflectivity spectra were measured at 10 K for oriented single crystals of $CdMoO_4$ and $CdWO_4$ using the polarized light parallel to the a-axis (**E**//**a**) and c-axis (**E**//**c**). The real (ε_1) and imaginary (ε_2) parts of the dielectric functions were calculated from the reflectivity spectra using a Kramers-Kronig analysis.

Figures 1(a) and 1(b) show the ε_2 spectra of $CdMoO_4$ and $CdWO_4$, respectively. It appears that there is no obvious similarity in the ε_2 spectra between $CdMoO_4$ and $CdWO_4$. The valence bands of both materials consist of the O 2*p* state. The conduction band is mainly made of the Mo 4*d* or W 5*d* states. The lower and upper parts of the conduction band are associated with the *e* and t_2 states, respectively, in the scheelite crystals, and vice versa in the wolframite crystals, due to the crystal-field splitting of the *d* state. The structures in regions I and II of $CdMoO_4$ in Fig. 1(a) are assigned to the transitions to the lower part of the conduction band with the *e* character and to the upper part with the t_2 character, respectively. As for $CdWO_4$, the structures in regions I and II in Fig. 1(b) are ascribed to the transitions to the lower t_2 state and to the upper *e* state, respectively.

According to theoretical calculations by the DV-*Xα* method [1, 2], the Cd 5*s* state significantly contributes to the bottom of the conduction band in both materials. For scheelite $CdMoO_4$, we propose an energy-level diagram shown in Fig. 2. In a free MoO_4^{2-} molecule of T_d symmetry, the highest occupied orbital made of the O 2*p* state is of t_1 symmetry, while the lowest unoccupied orbital made of the Mo 4*d* state is of *e* symmetry. In the scheelite crystal they split into sublevels, because the site symmetry of the MoO_4^{2-} molecule is lowered to S_4. The Cd 5*s* state forms an energy level, which couples with a sublevel of the same symmetry originating from the Mo 4*d* state. The dichroism in region I in Fig. 1(a) can be explained in terms of the assignment in Fig. 2.

In wolframite $CdWO_4$, the WO_6^{6-} octahedra form chains along the *c* axis. It is supposed that the intensity of the transition from the O site in the chain to the Cd site outside of the chain highly depends on the direction of the polarization with respect to the chain axis. Then the structures exhibiting the dichroism on the broad band in region I in Fig. 1(b) are attributed to the transitions to the Cd 5*s* state, which hybridizes with the W 5*d* conduction state.

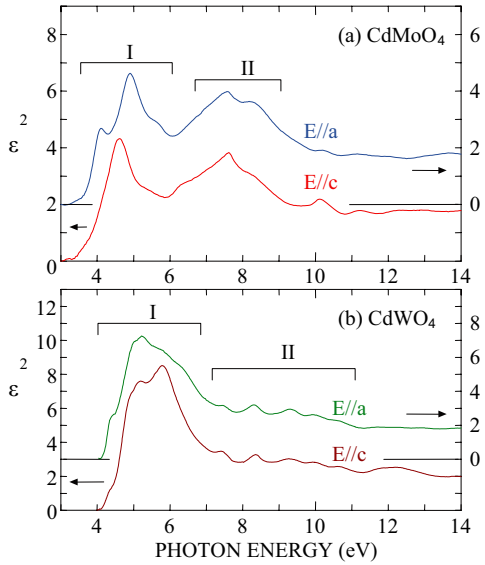

Fig. 1. Imaginary parts of the dielectric functions of (a) $CdMoO_4$ and (b) $CdWO_4$ for **E**//**a** and **E**//**c** at 10K.

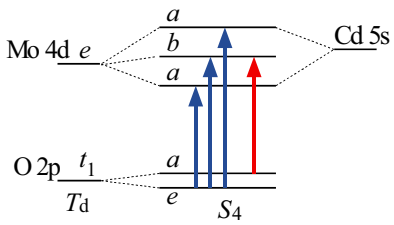

Fig. 2. Schematic diagram of the energy levels of $CdMoO_4$. Blue and red arrows indicate the optical transitions allowed for **E**//**a** and **E**//**c**, respectively.

[1] M. Itoh, N. Fujita and Y. Inabe, J. Phys. Soc. Jpn. **75** (2006) 084705.

[2] M. Fujita *et al.*, Phys. Rev. B **77** (2008) 155118.

BL1B

Effect of Crystallization on the Photoluminescence in $LaAlO_3$ Induced by Ultraviolet Photons

T. Iikura, E. Hirata and Y. Ohki

Dept. Electrical Engineering and Bioscience, Waseda University, Shinjuku 169-8555, Japan

Lanthanum aluminate ($LaAlO_3$) has been attracting much attention as a promising candidate for a gate insulator in advanced metal-oxide-semiconductor devices. In order to analyze its photoluminescence (PL) properties, we have been measuring PL and PL excitation (PLE) spectra for amorphous and crystalline $LaAlO_3$.

Experimental

The samples examined are $LaAlO_3$ (100) single crystals grown by the Czochralski method and $LaAlO_3$ thin films prepared by a spin-coating method. The films were annealed in oxygen at designated temperatures between 600 and 1000 °C. Using synchrotron radiation under multibunch operation at the BL1B line of UVSOR Facility as a photon source, PL, PLE, and absorption spectra were measured at 10 K. Crystallization of thin films was confirmed by in-plane X-ray diffraction (XRD) measurements.

Results and Discussion

Figure 1 shows PL spectra of $LaAlO_3$ excited at 5.1 and 6.4 eV. Although the films annealed at 600 and 700 °C have no PL peaks, those annealed at 800, 900, and 1000 °C and the single crystal have three sharp PL peaks at around 1.60, 1.65, and 1.68 eV. The PL excited at 6.4 eV is much more intense than the one excited at 5.1 eV. Figure 2 shows PLE spectra measured for the three PLs. Note that each PLE spectrum is normalized to each maximum intensity. For all the samples, the PLE spectrum starts to rise at around 5.7 eV.

As shown in Fig. 3, both the single crystal and the film annealed at 900 °C show a sharp increase in absorption at 5.7 eV, while the film annealed at 600 °C shows a similar increase at 6.2 eV. The two energies agree with the band-gap energies of $LaAlO_3$ reported for its crystalline and amorphous states [1]. Furthermore, 5.7 eV corresponds to the energy at which the PLE spectra detected at 1.60, 1.65, and 1.68 eV show an abrupt increase in Fig. 2. From these results, the three PLs at around 1.60, 1.65, and 1.68 eV are assumed to be caused by de-excitation of electrons excited to the conduction band.

The XRD patterns shown in Fig.4 indicate the formation of a perovskite structure in the films if they are annealed at 800 °C or higher. Namely, the three sharp PL peaks around 1.60, 1.65, and 1.68 eV appear only in crystalline $LaAlO_3$. The luminescence due to Cr^{3+} in Al_2O_3 has been reported to appear only when the sample is crystalline, and the mechanism underlying this is that the corresponding spin-forbidden transition in Cr^{3+} becomes possible owing to spin-orbit mixing induced by the crystal field [2,3].Taking these facts into consideration, the three PLs in $LaAlO_3$ are assumed to be due to impurities.

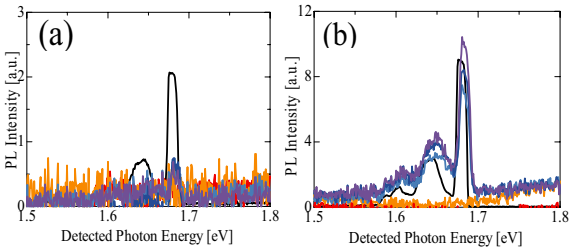

Fig. 1. PL spectra at 10 K induced by 5.1 eV photons (a) and by 6.4 eV photons (b) observed in $LaAlO_3$ films annealed at 600 °C (—), 700 °C (—), 800 °C (—), 900 °C (—), and 1000 °C (—), and similarly obtained PL spectra of single crystal $LaAlO_3$ (—). The numerals on the vertical axes should be multiplied by 10 only for the PL intensity of the single crystal (—).

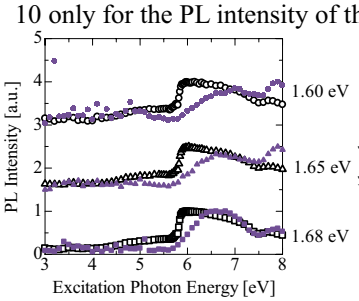

Fig. 2. PL intensities at 10 K detected at 1.60, 1.64, and 1.68 eV, induced in $LaAlO_3$ by photons with various energies. Solid symbols are for the film annealed at 1000 °C (●, ▲, ■), while open symbols are for the single crystal (○, △, □).

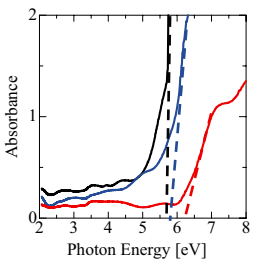

Fig. 3. Absorption spectra observed for $LaAlO_3$ films annealed at 600 °C(—) and 900 °C(—), and for single crystal (—).

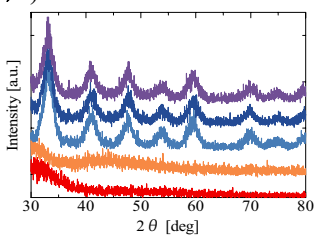

Fig. 4. XRD patterns of the $LaAlO_3$ films annealed at 600 °C (—), 700 °C (—), 800 °C (—), 900 °C (—), and 1000 °C (—).

[1] L. F. Edge *et al.*, Appl. Phys. Lett. **84** (2004) 726.
[2] J. Kákoš and L. Baca, J. Sol–gel Sci. Technol. **21** (2001) 167.
[3] G. Carturan *et al.*, J. Matr. Sci. **25** (1990) 2705.

BL1B

Luminescence Properties of Undoped and N-Doped TiO_2 Powders Prepared by a Conventional Sol-Gel Method

T. Kawai[1], Y. Kishimoto[1] and K. Kifune[1, 2]

[1]*Department of Physical Science, Graduate School of Science, Osaka Prefecture University, Osaka 599-8531, Japan*

[2]*Faculty of Liberal Arts and Sciences, Osaka Prefecture University, Osaka 599-8531, Japan*

Recently, R. Asahi *et al*. reported that substitutional doping of nitrogen into TiO_2 contributed to narrowing of the band gap, thus providing a visible-light response [1]. According to other groups' studies, though the nitrogen doping induces new optical absorption bands in the visible-light region, absorbance is not linearly proportional to the photocatalytic activity [2]. The contribution of the nitrogen doping may be revealed by luminescence properties, because photoluminescence (PL) and excitation (PLE) spectra have been widely used to investigate the trapping, migration, and relaxation of the photo-excited carriers. In this study, we measure the PL and PLE spectra of undoped and N-doped TiO_2 powder specimens at the BL-1B line of UVSOR.

Undoped TiO_2 powders were prepared by a conventional sol-gel method. The TiO_2 powders obtained were annealed for 1 h in air at 500 ℃ in order to transform into anatase phase. N-doped TiO_2 powders were obtained by sintering the anatase TiO_2 powders together with urea at 500 ℃.

Figure 1 shows the PL spectra of the undoped and N-doped TiO_2 powder specimens at 10 K. The broad luminescence bands around 2.23 and 2.63 eV are observed for the undoped and N-doped TiO_2 powders, respectively. In the undoped TiO_2 specimen, the luminescence bands exhibit the Gaussian-like band shape. On the other hand, the luminescence bands of the N-doped TiO_2 specimen have the shoulder structures at 2.46 and 2.83 eV and the lower energy tail. The difference of the peak energy and band shape between both the specimens implies that of the origin of the luminescence. The origin of the luminescence band in anatase TiO_2 is considered to be self-trapped excitons, excitons or electrons trapped around oxygen defects [3]. Many studies on N-doped TiO_2 demonstrate that N-related levels are formed above the valence band composing of oxygen 2p states [2, 4]. Therefore, the luminescence bands in the N-doped TiO_2 powder would be attributed to the radiative recombination of the electron with holes bound to the N-related levels.

Figure 2 shows the PLE spectra for the luminescence of the undoped and N-doped TiO_2 powder specimens at 10K. In the undoped TiO_2 powder, the PLE spectrum exhibits the response rising sharply from 3.32 eV, reflecting the band gap of anatase TiO_2. On the other hand, the PLE spectrum for the 2.64 eV luminescence of the N-doped TiO_2 powder has the rise from 2.83 eV and the step-like shoulder at 3.23 eV. The energy position of the step-like shoulder is close to the band gap energy of anatase TiO_2. Thus, the response below 3.23 eV would be attributed to the nitrogen doping, that is to say, the transitions from the N-related levels to the conduction band. In order to clarify the contribution of nitrogen doping, the further studies on the luminescence properties are needed for TiO_2 with various amount of doped nitrogen.

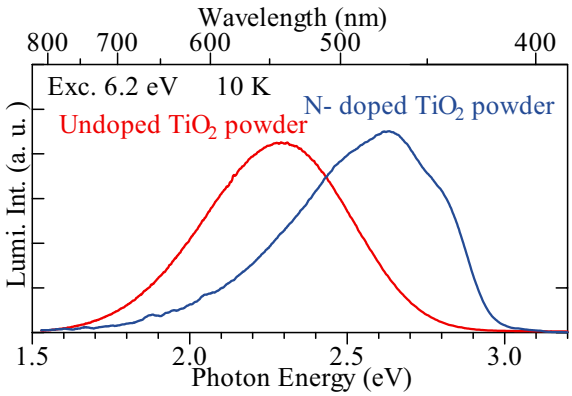

Fig. 1. PL spectra of undoped (red) and N-doped (blue) TiO_2 powder specimens at 10K.

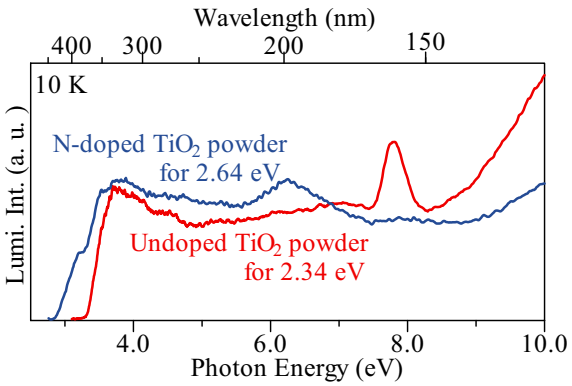

Fig. 2. PLE spectra of undoped (red) and N-doped (blue) TiO_2 powder specimens at 10 K.

[1] R. Asahi *et al*., Science **293** (2001) 269.
[2] R. Nakamura *et al*., J. Phys. Chem. B **108** (2004) 10617.
[3] S. Mochizuki *et al*., Physica B **340-342** (2003) 956.
[4] C. D. Valentin *et al*., Chem. Phys. **339** (2007) 44.

BL1B

Secondary Excitation Process by Hot Photocarriers in Inorganic EL Phosphors

M. Kitaura[1], H. Mitani[2] and M. Itoh[2]
[1]*Fukui National College of Technology, Sabae 916-8507, Japan*
[2]*Department of Electrical and Electronics Engineering, Shinshu University, Nagano 380-8553, Japan*

In general, it is known that electroluminescence (EL) of inorganic phosphors is caused by the impact excitation of valence electrons by hot electrons; hot electron excitation. On the other hand, hot hole excitation has been found to occur in narrow-gap semiconductors, but there is no report on it in EL phosphors. Recently, Tanaka and Okamoto have reported that the hot hole excitation predominantly takes place in single insulating EL devices with $SrGa_2S_4:Eu^{2+}$ thin film [1]. Similar phenomena are also found in $EuGa_2S_4$ [2] and $BaAl_2S_4:Eu^{2+}$ [3]. In contrast, they claim that hot electrons play a predominant role for the impact excitation in $SrGa_2S_4:Ce^{3+}$ thin film [1].

The aim of the present study is to inspect the above mentioned difference on hot carrier type between $SrGa_2S_4:Eu^{2+}$ and $SrGa_2S_4:Ce^{3+}$ phosphors. These phosphors show the green emission around 536 nm and the blue emission around 445 nm, respectively, under excitation with uv photons. We have measured photoluminescence excitation (PLE) spectra for the green and blue emission at 300 K, in order to investigate the lowest energy excitation process due to the creation of hot photocarriers. For better understanding of the structures in PLE spectra, we have also calculated the energy level structure of $SrGa_2S_4$ by using the relativistic DV-Xα method [4].

Figures 1(a) and 1(b) show the PL and PLE spectra of $SrGa_2S_4:Eu^{2+}$ and $SrGa_2S_4:Ce^{3+}$, respectively. Both spectra were corrected for the spectral distribution of excitation light by using the sodium salicylate phosphor. The PL spectrum is also shown in each figure by a red line. As seen in both PLE spectra, the PL intensity is large below 4.4 eV, where the 4f→5d absorption occurs efficiently. As the photon energy increased, the PL intensity is rapidly decreased at 4.4 eV, the energy of which is in good agreement with the fundamental absorption edge energy of $SrGa_2S_4$, determined from an analysis of the transmittance spectrum. Further increase in photon energy leads to the PL enhancement around 10 eV. This feature is interpreted as an indication of hot carrier excitation, because the hot carriers can gain the energy enough to excite valence electrons by the interband Auger mechanism.

In our calculation, the energy gap E_g and the valence band width E_{VB} were determined to be 4.57 eV and 6.56 eV, respectively. The value of E_{VB} is larger than that of E_g, and thus the condition for hot hole excitation $E_{VB} > E_g$ is satisfied in host $SrGa_2S_4$. However, since the optical transition from the valence band (VB) to the upper conduction band (CB) is expected to predominantly occurs in the 11-21 eV region, the hot hole excitation should be negligibly small even if it happens. Therefore, it is more likely that the PL enhancement around 10 eV is caused by hot photoelectron excitation.

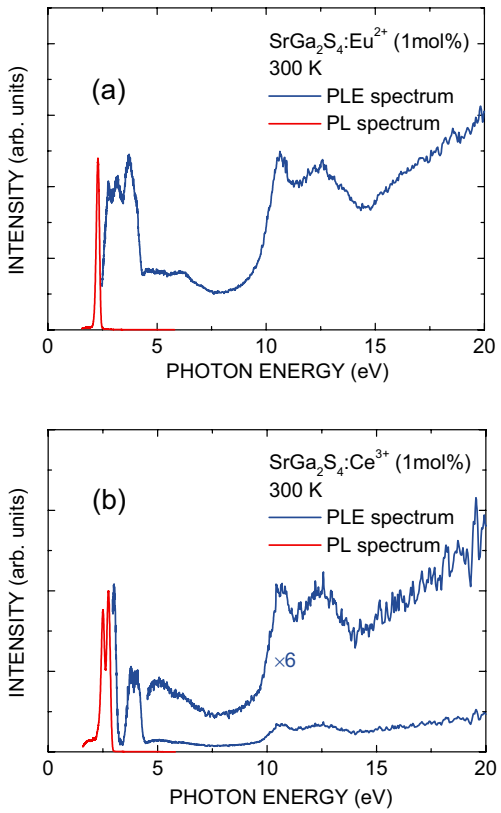

Fig. 1. Photoluminescence excitation (PLE) spectra of $SrGa_2S_4:Eu^{2+}$ (a) and $SrGa_2S_4:Ce^{3+}$ (b) phosphors. Both spectra were measured at 300 K. The PL spectra are also shown in the figures.

[1] K. Tanaka and S. Okamoto, Appl. Phys. Lett. **89** (2006) 203508.
[2] K. Tanaka and S. Okamoto, Appl. Phys. Lett. **83** (2003) 647.
[3] K. Tanaka and S. Okamoto, Proc. of IDW'06 (2006) 1207.
[4] H. Adachi, M. Tsukada and C. Satoko, J. Phys. Soc. Jpn. **45** (1978) 875.

BL1B

Photoluminescence of Hydroxyapatite Irradiated by Ultraviolet Synchrotron Orbital Radiation Light (5)

M. Ohta

Department of Material Science and Technology, Faculty of Engineering, Niigata University, Niigata 950-2181, Japan

It was known that rare earth ions dosed for oral administration to mouse and rat are transferred to blood vessel through the ileum and deposited its teeth and bone, which mainly consists of hydroxyapatite ($Ca_{10}(PO_4)_6(OH)_2$) [1-2]. Recently, rare earth is also useful as a contrast medium for magnetic resonance imaging, restriction enzyme, biocatalyst, and so on in fields of biochemistry, physiology, medicine, etc. However, the behavior of rare earth in the living body system remains an open question until now. We have found that Eu ion substituted Ba ion in Eu doped $Ba_{10}(PO_4)_6Cl_2$ phosphor, which matrix is apatite structure [3]. The Eu ions, Gd ions or Yb ions are also found to substitute easily for calcium ions in hydroxyapatite which is soaked in $EuCl_3$, $GdCl_3$ or $YbCl_3$ aqueous solution, and to play on emission center.

In this study, hydroxyapatite samples doped with $SmCl_3$ aqueous solution were prepared in order to apply to phosphor. Their characteristics were investigated by photoluminescent property of Sm ion-doped hydoxyapatite samples excited by ultraviolet synchrotron orbital radiation light.

Sm-doped hydroxyapatite samples were prepared as follows: hydroxyapatite was soaked in $SmCl_3$ aqueous solution. After 72 hr, Sm doped hydroxyapatite was separated from $SmCl_3$ aqueous solution by filtation and then dried by using with infrared ray.

The photoluminescent property of each sample exited by ultraviolet synchrotron orbital radiation light (BL1B) was observed by using with a multi-channel analyzer.

Figure 1 shows photoluminescence spectra of Sm ion-doped hydroxyapatite samples excited by BL-1B. The photoluminescence spectra of fired sample have the peak due to $^4G_{5/2} \rightarrow {}^6H_{5/2}$ (570nm), $^4G_{5/2} \rightarrow {}^6H_{7/2}$ (606nm), $^4G_{5/2} \rightarrow {}^6H_{9/2}$ (652nm) and $^4G_{5/2} \rightarrow {}^6H_{11/2}$ (713 nm), regardless of excitation wave length from 100 to 240 nm. The peak intensity is higher at 160 and 190 nm of excitation wave length. The peak intensity decreases with the wave length form 100nm to 130nm. This phenomenon is thought to be due to the multi-electron excitation.

[1] S. Hirano and K. T. Suzuki, Environ. Health Perspect. **104** (Supplement 1) (1996) 85.
[2] K. Kostial, B. Kargacin and M. Lendeka, Int. J. Radiat. Biol. Relat. Stud. Phys. Chem. Med. **51** (1987) 139.
[3] M. Sato, T. Tanaka and M. Ohta, J. Electrochem. Soc. **141** (1994) 1851.

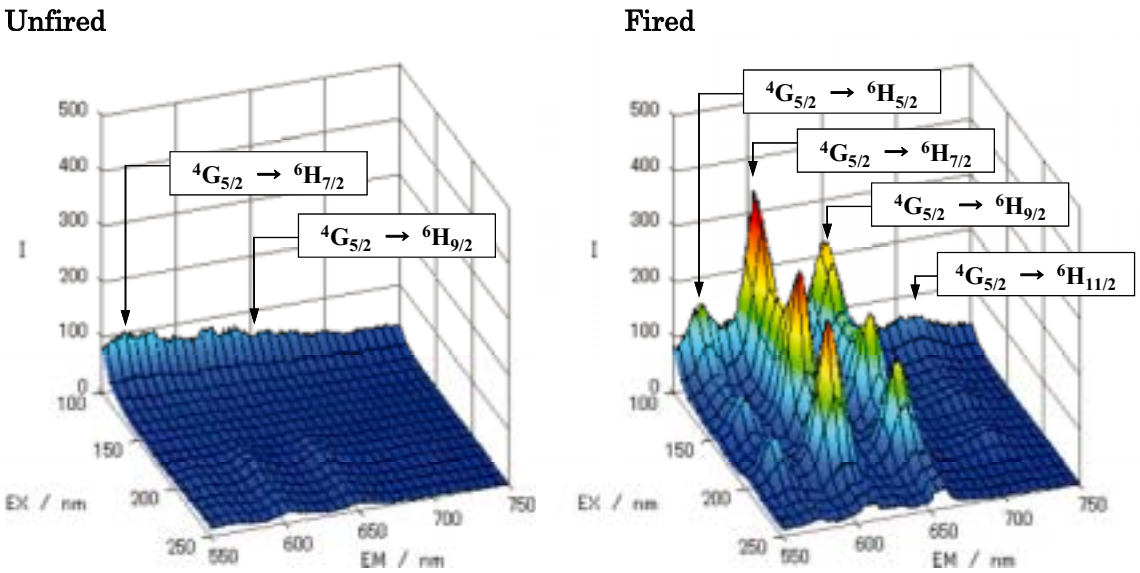

Fig. 1. Photoluminescent spectra of Sm ion-doped hydroxyapatite samples excited by ultraviolet synchrotron orbital radiation light.

BL3U

Local Electronic Structure Near the Energy Gap of Organic Solids Studied by X-Ray Emission Spectroscopy: The Case of Phthalocyanines

H. Yamane[1], T. Hatsui[2] and N. Kosugi[1]

[1] *Institute for Molecular Science, Okazaki 444-8585, Japan*

[2] *XFEL Project Head Office, RIKEN and PRESTO, JST, Sayo-gun, Hyogo 679-5148, Japan*

Introduction

Photon-in-photon-out techniques using synchrotron radiation such as fluorescence-yield X-ray absorption spectroscopy (FY-XAS) and X-ray emission spectroscopy (XES) measure the intensity distribution of emitted X-rays by the decay process of an inner-shell excitation, which gives unoccupied and occupied partial density-of-states of non-ionized or ionized materials. In these techniques, problems encountered with usual electron spectroscopies, such as charging, sample atmosphere, or disturbance from electric/magnetic fields, are negligible. The FY-XAS and XES are therefore powerful techniques for studies of large energy-gap materials and electric/magnetic-field-applied materials. Furthermore, the attenuation length of photons in the soft X-ray region is typically tens or hundreds of nanometers, which realizes an inherent bulk-sensitive method. In addition, such bulk sensitivity makes it possible to study buried interfaces of functional materials covered by different materials such as metal electrodes [1].

In this study, in order to understand the local electronic structure of organic semiconductors in the bulk phase, which is in principle difficult to study just by using the conventional ultraviolet photoemission spectroscopy (UPS) due to the charging problem of the sample, we have performed the FY-XAS and XES experiments on various metal-phthalocyanine (M-Pc: M = Zn, Cu, Mn, and H_2) crystalline films.

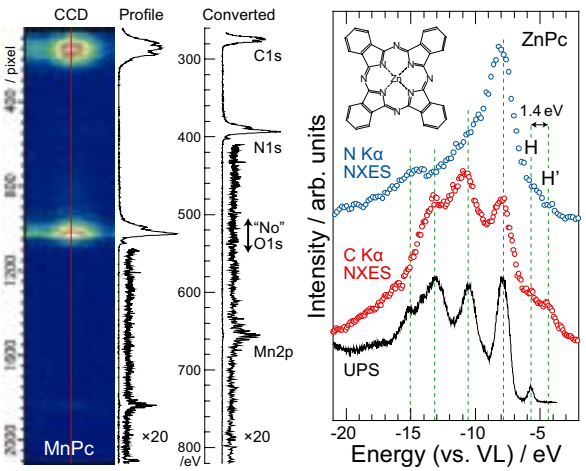

Fig. 1. (Left) The observed CCD image, its lineprofile, and a converted XES spectrum of the MnPc crystalline film. (Right) The C Kα and N Kα normal XES spectra of the 200-nm-thick ZnPc crystalline film, compared with a UPS spectrum of a 10-nm-thick ZnPc film.

Experimental

The purified M-Pc materials were deposited onto the SiO_2/Si(111) surface at room temperature. The deposited 200-nm-thick films show clear polar-angle dependence in the FY-XAS spectra (not shown), indicating a good crystallinity of the film. All the crystalline films were introduced to the spectrometer chamber at BL3U. The XES spectra were obtained by using a transmission-grating spectrometer [2]. Since the combination between a small photon-beam spot of 20 μm (vertical) × 40 μm (horizontal) with a photon flux of 10^{11} ph/sec and an exposure time of 40–60 min induces significant radiation damage in organic solids, samples were translated at a rate of 20 μm/min during the XES measurements. Judging from the observed XES spectra, no oxygen-related contamination (see, Fig. 1 left panel) and no damage-induced defects exist in the present samples.

Results and Discussion

The right panel in Fig. 1 shows the comparison of the C Kα and N Kα normal XES (NXES) spectra of the ZnPc crystalline film ($h\nu_i$ = 295 eV and 420 eV for C Kα and N Kα, respectively) with an UPS spectrum of a 10-nm-thick ZnPc thin film ($h\nu_i$ = 40 eV). The relative energies of the transition peaks in NXES correspond well with those of the valence-level peaks in UPS, except for the topmost NXES peak as labeled H', in which no corresponding UPS peak exists. The energy difference between the second NXES peak (H) and the peak H' is about 1.4 eV. Due to the presence of the chemical shift of the C sites in the molecule of about 1.3 eV (not shown), one may assign the peaks H and H' to the transitions from the HOMO to the ring and pyrrole C1s holes, respectively. However, this assignment cannot be applied to the N Kα NXES spectrum, which also shows the double peaks of H and H', since the chemical shift of the N sites in the molecule is only 0.2 eV (not shown).

As a possible origin of the peaks H and H' in the XES spectra, intermolecular interaction in the bulk phase may play a crucial role. For detailed discussion on relationship of the crystalline structure to the bulk electronic structure, the FY-XAS and XES experiments on amorphous films and single crystals of M-Pc molecules are now in progress.

[1] H.S. Kato *et al.*, UVSOR Act. Rep. **35** (2008) 114; a separate page in this volume.

[2] T. Hatsui *et al.*, AIP Conf. Proc. **705** (2004) 921; UVSOR Act. Rep. **34** (2007) 42.

BL4B

In Situ Magnetic Circular Dichroism Experiment on Ferromagnetic Semiconductor EuO Thin Films

H. Miyazaki[1, 2], T. Ito[1, 3], K. Terashima[1], H. J. Im[4], Y. Takagi[3, 5], T. Nakagawa[3, 5], Y. Yamamoto[5], S. Kimura[1, 3], S. Yagi[2], M. Kato[2], K. Soda[2] and T. Yokoyama[3, 5]

[1]*UVSOR Facility, Institute for Molecular Science, Okazaki 444-8585, Japan*

[2]*Graduate School of Engineering, Nagoya University, Nagoya 464-8603, Japan*

[3]*School of Physical Sciences, The Graduate University for Advanced Studies, Okazaki 444-8585, Japan*

[4]*Department of Advanced Physics, Hirosaki University, Hirosaki 036-8560, Japan*

[5]*Department of Molecular Structure, Institute for Molecular Science, Okazaki 444-8585, Japan*

Europium monoxide (EuO) is a ferromagnetic semiconductor with the Curie temperature (T_C) at around 70 K [1, 2]. In the electron doping case by the Eu excess or substitute Gd^{3+} or La^{3+} from Eu^{2+} ion, T_C increases up to 150 K and the electrical resistivity drops twelve-order of magnitude below T_C originating in a metal-insulator transition (MIT) [2, 3]. To reveal the origin of these physical properties of EuO, it is important to clarify the relation of the electronic structure to the magnetic property. The soft X-ray Magnetic Circular Dichroism (XMCD) is powerful technique to determine the magnetic configuration of the electronic structure. Using this technique we observed the electronic structure of the Eu 4*f* states under the magnetic field.

Single-crystalline EuO thin films with a thickness of about 50 nm were fabricated by the molecular beam epitaxy (MBE) method. Epitaxial growth of the single-crystalline EuO thin films with the 1 x 1 EuO (100) patterns was confirmed with low energy electron diffraction (LEED) and reflection high energy electron diffraction (RHEED) methods. The T_C measured with a superconducting quantum interference device (SQUID) magnetometer was 71 K [4]. The *in situ* Eu *M*-edge X-ray adsorption spectra (XAS) and XMCD measurements were performed using a total electron yield mode at the bending magnet beamline 4B of UVSOR-II combined with the MBE system. The EuO thin films were prepared in the growth chamber and were transferred to the superconducting magnet chamber under the UHV condition.

Figure 1 shows the Eu $M_{4,5}$ XAS of an EuO (100) thin film recorded at the temperature of 5 K and the magnetic field of ± 1 T. The magnetic field was applied perpendicular to the sample surface. Observed XAS spectra mainly have two structure at the photon energy 1130.6 and 1134.4 eV. Since the peaks from the Eu^{3+} 3*d* states are not observed, the EuO does not contain impurities such as Eu_2O_3. The XMCD spectrum, which is obtained by the subtraction of the XAS spectrum of H = -1 T from that of 1 T, is good agreement with previously results and theoretical spectrum for a Eu^{2+} ion with $L = 0$ and $S = 7/2$ [6, 7].

To summarize, we succeeded to measure XMCD spectra of single-crystalline EuO thin films *in situ*. The method is good for the excluding the extrinsic effect such as oxidization, impurity and so on. The detailed analysis and the further study for EuO thin films are in progress.

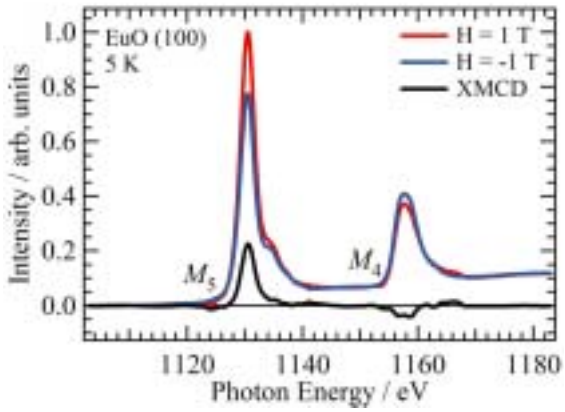

Fig. 1. Eu $M_{4,5}$ XAS of EuO thin films recorded at 5 K with 1 (red line) and -1 T (blue line), respectively. The lowest curves (black line) shows the difference between both, which is called the XMCD spectrum.

[1] N. Tsuda *et al*., Electronic Conduction in Oxides (Springers College) (1976).
[2] A. Mauger *et al*., J. Phys. (paris) **39** (1978) 1125.
[3] Y. Shapira, S. Foner, and T. B. Reed, Phys. Rev. B **8** (1973) 2299. ; **8** (1973) 2316.
[4] H. Miyazaki *et al*., Jpn. J. Appl. Phys. (2008) (in press).
[5] H. Lee *et al*., J. Appl. Phys. **102** (2007) 053903.
[6] J. Holroyd *et al*., J. Appl. Phys. **95** (2004) 6571.
[7] J. B. Goedkoop *et al*., Phys. Rev. B **37** (1988) 2086.

BL5U

Ce 4d-4f Resonant Photoemission Studies in Ce Dilute Kondo System

H. J. Im[1], M. Tsunekawa[2, 3, 4], H. Miyazaki[3, 5], T. Ito[3, 6], S. Kimura[3, 6], K. E. Lee[7], J. B. Hong[7] and Y. S. Kwon[7]

[1]*Department of Advanced Physics, Hirosaki University, Hirosaki 036-8561, Japan*
[2]*Research Center for Materials Science, Nagoya University, Nagoya 464-8602, Japan*
[3]*UVSOR Facility, Institute for Molecular Science, Okazaki 444-8585, Japan*
[4]*Faculty of Education, Shiga University, Otsu 520-0862, Japan*
[5]*Graduate School of Engineering, Nagoya University, Nagoya 464-8603, Japan*
[6]*School of Physical Sciences, The Graduate University for Advanced Studies, Okazaki 444-8585, Japan*
[7]*Department of Physics, Sungkyunkwan University, Suwon 440-746, Korea*

Localization of electrons in metals has been in the center of condensed matter physics. The intrigue phenomena take place, when the localized electrons hybridize with conduction electrons. For example, heavy fermion systems show a variety of the ground states from magnetic to non-magnetic states via the quantum critical point (QCP) as a function of the hybridization. In order to understand the localization in terms of electronic structure, we have performed resonant photoemission (RPES) studies of $Ce_{1-x}Gd_xCoSi_3$, where the ground state changes antiferromagnetism to non-magnetism via the QCP (x = 0.4) [1]. In previous report, the large Kondo resonance (KR) peak near the Fermi-level (E_F) is retained from x = 0 to 0.6, indicating the continuous change of Ce 4f-character across the QCP unlike a local quantum critical scenario [2,3]. This gives rise to a long-standing fundamental question, i.e., how the KR peak behaviors in the different states (the periodic and impurity) of Ce 4f-electron and what the fate of the KR peak is in a dilute state.

In this report, Ce 4d-4f RPES measurements were carried out for the Ce-dilute system, $Ce_{0.1}Gd_{0.9}CoSi_3$, at BL5U. The used photon energies are 120 (on) and 113 eV (off). Total energy resolution is about 65 meV for the photon energies of 120 eV. Measurement temperature is 10 K. Sample surfaces were prepared by *in situ* fracturing under 2×10^{-8} Pa. Sample cleanliness is checked by the absence of oxidization peak around -6 and -10 eV.

Figure 1 shows the Ce 4d-4f on- and off-RPES spectra. The spectra are normalized to the intensity of Gd $4f^6$ peak at ~ -8.4 eV, whose cross-section should be almost the same in on- and off-photon energies. We observe the additional weight of the on-spectrum in valence band from -5 eV to E_F in comparison with the off-spectrum, indicating Ce 4f-state.

Figure 2 is the obtained Ce 4f-spectrum near E_F by subtraction of the off- from on-spectrum. The two peaks are clearly observed at about -0.2 eV and E_F, which are separated by spin-orbit interaction. The former is Ce $4f^1_{7/2}$ final-state and latter Ce $4f^1_{5/2}$ final-state (the tail of KR peak). Moreover, it is recognized that the intensity of KR peak is much larger than that of Ce $4f^1_{7/2}$ peak, indicating strong hybridization strength in Ce dilute Kondo system.

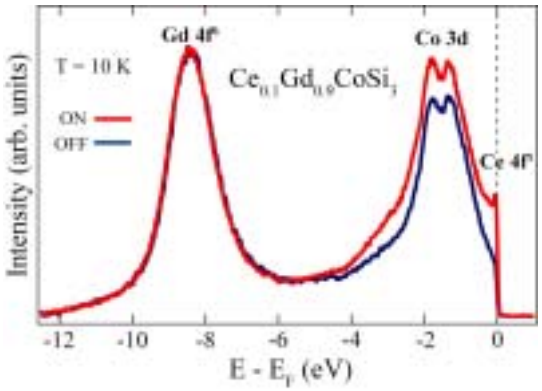

Fig. 1. Ce 4d-4f on- and off-RPES spectra of $Ce_{0.1}Gd_{0.9}CoSi_3$.

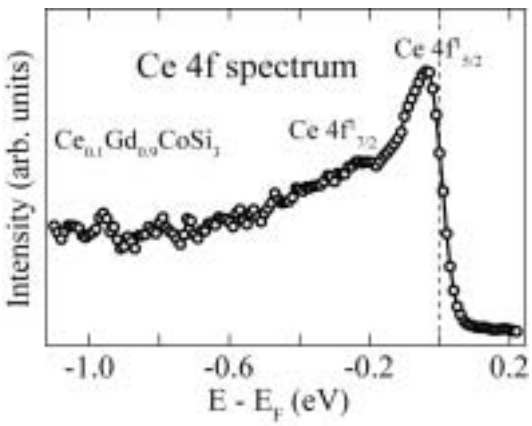

Fig. 2. Ce 4f spectrum of $Ce_{0.1}Gd_{0.9}CoSi_3$.

[1] J. B. Hong *et al.*, Physica B **403** (2008) 911.
[2] H. J. Im *et al.*, UVSOR Activity Report **35** (2008) 119.
[3] H. J. Im *et al.*, Phys. Rev. B **72** (2005) 220405.

BL5U

Photoemission Study of CTAB-Passivated Au Nanorods

M. Imamura, A. Matsumoto, T. Kitagawa, S. Fujimasa and H. Yasuda
Department of Mechanical Engineering, Kobe University, Kobe 657-8501, Japan

Recently, chemically synthesized cethyltrimathyl ammonium bromide(CTAB)-passivated Au nanorods attract much attention due to their characteristic optical properties. CTAB-passivated Au nanorods are generally prepared with the seed-mediated growth method. The aspect ratio of Au nanorods is easily controlled by Ag ion concentration during the preparing process. However, the detailed structure of CTAB-passivated Au nanorod and the role of Ag in the growth process and are still unclear. In order to elucidate the structure of CTAB-passivated Au nanorod and the role of Ag ions, we have carried out the core-level photoemission study.

The CTAB-passivated Au nanorods are prepared by seed-mediated growth method developed by M. A, El-sayed *et al*..[1] We performed the X-ray and synchrotron-radiation photoemission measurements. The synchrotron photoemission study was carried out with the incident photon energy of 190 eV at BL-5U of UVSOR facility.

Figure 1 shows the Ag 3*d* core-level X-ray photoemission spectrum of CTAB-passivated Au nanorods with the aspect ratio of 4.1 supported on the HOPG substrate. The Ag 3*d* core-level photoemission spectrum measured from the bulk surface is also shown as a reference. The Ag 3*d* core-level X-ray photoemission spectrum of CTAB-passivated Au nanorods shifted to lower binding energy, and shows asymmetric spectral shape in the higher binding energy side compared with that of the bulk surface. In order to elucidate the chemical states of Au nanorods, we have carried out the line-shape analysis of the photoemission spectrum. The photoemission spectrum of Ag 3*d* in Au nanorods consists of two components. The higher binding energy component is considered to be the interface component that originates from the bonding between the Ag atoms and Br atoms, which indicates the passivation of Ag atoms by the CTAB molecule. The lower binding energy component in the photoemission spectrum of the Au nanorods shifted to lower binding energy side compared with the bulk component in the spectrum of bulk Ag, and is assigned as Au-Ag interface component. Thus, it is considered that Ag atoms are passivated by Br and bond to Au atoms of the nanorods.

Figure 2 shows the Au 4*f* photoemission spectrum of Au nanorods measured with synchrotron radiation light source. The results of the line shape analysis are also shown in the figure. As shown in Fig. 2, Au 4*f* photoemission spectrum of Au nanorods consist of one component, and no surface component appears. The disappearance of Au-Ag interface component in fig. 2 is consistent with the result of line-shape analysis of the Ag 3*d* spectrum. The charge transfer between Au and Ag is considered to be very small, since the electron affinity of Au and that of Ag are quite similar. In addition, the volume fraction of Ag atoms are small compared with that of Au. Therefore Au-Ag interface component was not observed. From these results, it is concluded that Ag layer formed on the Au nanorod surface is monolayer, and the Ag layer is passivated by the CTAB molecules.

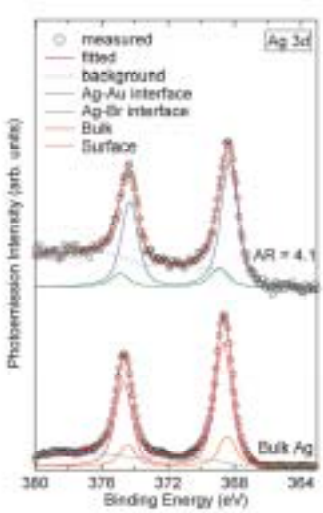

Fig. 1. Ag 3*d* core-level X-ray photoemission spectrum and the results of line shape analysis of CTAB-passivated Au nanorod with the aspect ratio of 4.1.

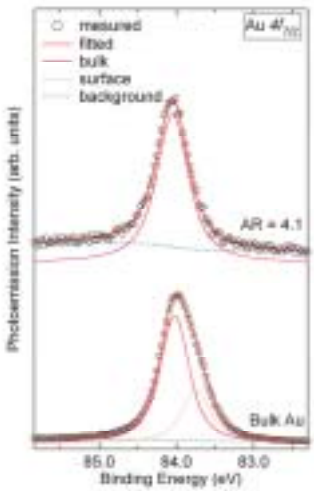

Fig. 2. Au $4f_{7/2}$ core-level synchrotron photoemission spectrum and the results of line shape analysis of CTAB-passivated Au nanorod with the aspect ratio of 4.1.

[1] B. Nikoobakht and M.A. El-Sayed, Chem. Mater. **15** (2003) 1957.

BL5U

Ce 4*d*-4*f* Resonant Photoemission Study on Single-Crystalline Cerium

T. Ito[1, 2], H. Miyazaki[1, 3], S. Kimura[1, 2] and K. Maesawa[4]

[1]*UVSOR Facility, Institute for Molecular Science, Okazaki 444-8585, Japan*

[2]*School of Physical Sciences, the Graduate University for Advanced Studies (SOKENDAI), Okazaki 444-8585, Japan*

[3]*Graduate School of Engineering, Nagoya University, Nagoya 464-8603, Japan*

[4]*Department of Liberal Arts and Sciences, Toyama Prefectural University, Toyama 939-0398, Japan*

Cerium is one of the most fascinating model systems to clarify the essential origin of strong electron correlations, causing the anomalous magnetic/electronic properties. This is because metallic cerium shows a unique first-order isostructural (fcc → fcc) phase transition from the high-temperature γ phase to the low-temperature α phase with a huge (15 %) volume reduction. According to the Kondo volume collapse theory based on the Anderson impurity model (AIM), γ - α phase transition has been described by the change of the effective hybridization intensity of the conduction *spd* electrons with the *f* electron, from weak (γ; localized) to strong (α; itinerant) one [1]. Photoemission spectroscopy has been used to directly estimate the applicability of AIM on various kinds of strongly correlated *f* electron systems by comparing the Kondo scaling parameter between the photoemission experiment and the AIM theory [2]. On the other hand, a recent angle-resolved photoemission (ARPES) result suggests that *f* states have band dispersions and cannot be treated as a local spin state based on AIM [3]. Thus the direct observation of the 4*f* band structure by using ARPES is indispensable to clarify the origin of γ - α phase transition in cerium.

Figure 1 shows the change of valence band photoemission spectra of single-crystalline cerium as a function of Ar^+-sputtering time. After 22 hours, extrinsic contamination peaks at 6.5 and 11 eV and CeO_2 features at 2 and 5 eV almost disappear, which can be attributed to successful cleaning of the sample surface. However, unexpected peak remained at 6eV. Though the origin of the peak is not clear at present, we think the peak is not come from CeO_2 but from chemically free oxygen contained in the single-crystalline cerium, since the peak intensity suddenly decreases at low temperature.

Figure 2 shows the temperature dependence of the on-resonant angle-integrated photoemission spectrum of the clean cerium above and below γ - α phase transition temperature. According to AIM, the peaks at the Fermi level (E_F) and 2.5 eV has been attributed to the spin-orbit splitted $4f^1$ and the $4f^0$ final states, respectively, originating from the strong *cf* hybridization [1]. We observed a sudden enhancement of $4f^1_{5/2}$ peak below the transition temperature, which is consistent with the previous study. To clarify the change of the electroic structure due to the γ-α transition, an ARPES measurement on the single-crystalline cerium wll be performed in the near future.

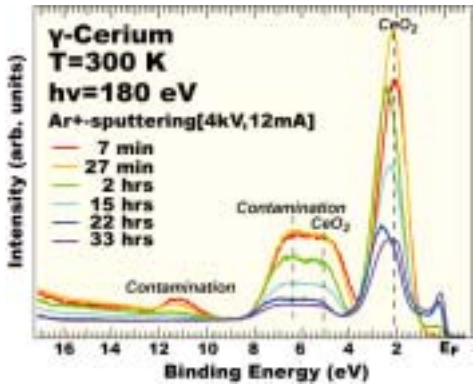

Fig. 1. Change of photoemission spectra due to the surface cleaning by the Ar^+-sputtering measured at T=300 K using hν = 180 eV photons.

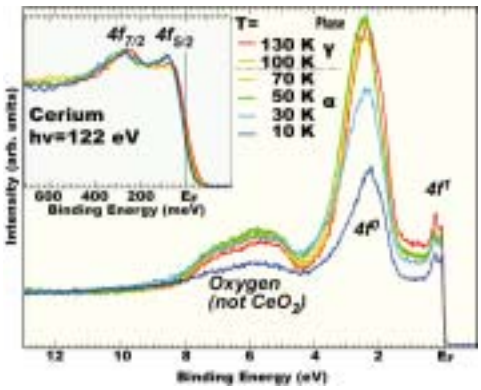

Fig. 2. Temperature-dependence of Ce 4*d*-4*f* on-resonance spectra (hν=120 eV). (Inset) the enlargement near E_F. The intensities are normalized at $4f^1_{7/2}$.

[1] J. W. Allen *et al.*, Adv. Phys. **35** (1986) 275.
[2] D. Malterre, M. Grioni and Y. Baer, Adv. Phys. **45** (1996) 299.
[3] H. J. Im *et al.*, Phys. Rev. Lett. **100** (2008) 176402.

BL5U

Electronic Structure of $Ba_3Co_2O_6(CO_3)_{0.7}$

M. Kikuchi[1], S. Ogawa[1], H. Miyazaki[2], M. Inukai[2], K. Iwasaki[2], T. Matsui[2, 3], M. Kato[2], S. Yagi[2] and K. Soda[2]

[1]*School of Engineering, Nagoya University, Nagoya 464-8603, Japan*
[2]*Graduate School of Engineering, Nagoya University, Nagoya 464-8603, Japan*
[3]*EcoTopia Science Institute, Nagoya University, Nagoya 464-8603, Japan*

Cobalt oxides such as Na_xCoO_2 have received much attention because of their fascinating transport and magnetic properties. Recently it has been found that a barium cobalt oxycarbonate $Ba_3Co_2O_6(CO_3)_{0.7}$ shows metallic behavior of its electric conductivity above 300 K and fairly large power factor of 0.9 $mWm^{-1}K^{-2}$ at 300 K with positive thermoelectric power of about 120 μVK^{-1} [1]. $Ba_3Co_2O_6(CO_3)_{0.7}$ has pseudo-one dimensional structure with Co-O chains consisting of face-sharing CoO_6 octahedra along the *c* axis. In the present study, we have investigated its electronic structure by photoelectron spectroscopy, in order to understand the physical properties.

Single crystalline specimens of $Ba_3Co_2O_6(CO_3)_{0.7}$ in size of 5 x 0.5 x 0.5 mm^3 was prepared by a flux method [1], and their clean surfaces for photoelectron measurement was obtained by *in situ* cleaving the specimens in perpendicular to the *c* axis.

Valence band photoelectron spectra recorded at 20 K are summarized in Fig. 1. Excitation photon energy $h\nu$ is indicated in the right side of each spectrum, and each spectrum is normalized with the integrated intensity. We recognize features A to H in the spectra; we ascribe the features A to C to the hybridized bands of the Co 3*d* and O 2*p* states, comparing with reported spectra of Na_xCoO_2 [2], which is composed of triangular planes of edge-sharing CoO_6 octahedra. The resonance behavior at the Co 3*p* threshold around $h\nu$ = 60 ~ 70 eV indicates the relatively large characters of Co 3*d* states to the features A and B and of the O 2*p* state to the feature C. The bands D, F, G and H are assigned to the CO_3-derived states, Ba 5*p* spin-orbit doublets and O 2*s* state, respectively. We ascribe the feature E to the surface components.

Figure 2 shows detailed spectrum near the Fermi level E_F measured at 20 K and $h\nu$ = 40 eV in comparison with a reference Au spectrum. The spectrum of $Ba_3Co_2O_6(CO_3)_{0.7}$ reveals large reduction in intensity towards E_F but clear finite intensity at E_F. This may suggest the electron doping into the low-spin bands of $Co^{4+}(t_{2g}\ 3d^5)$, which in turn might lead to the positive thermoelectric power of 81 or 141 μVK^{-1} at high temperatures for the Co^{4+} concentration *x* of 0.7 [3], consistent with the observed value.

A 1/8-power-law dependence on the binding energy, which may be expected in one-dimensional fermion system [4], is also shown in Fig. 2 after the convolution with a Gaussian function presenting an experimental energy resolution of 34 meV. It seems to explain the spectral feature near E_F fairly well. For definite conclusion, further study is intended with an improved energy resolution and statistics.

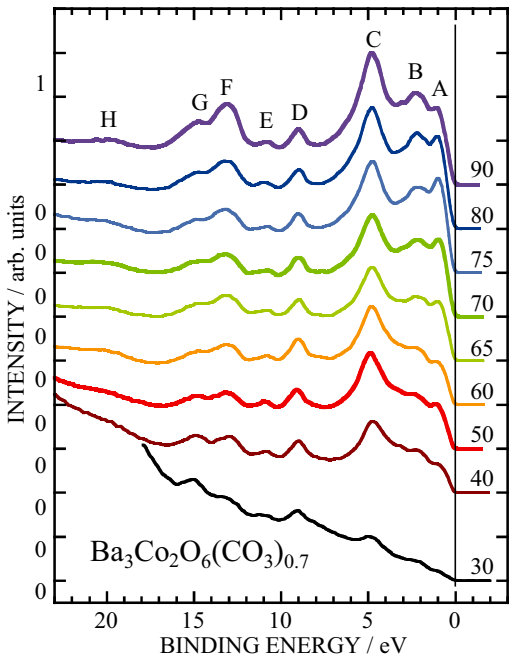

Fig. 1. Valence-band spectra of $Ba_3Co_2O_6(CO_3)_{0.7}$.

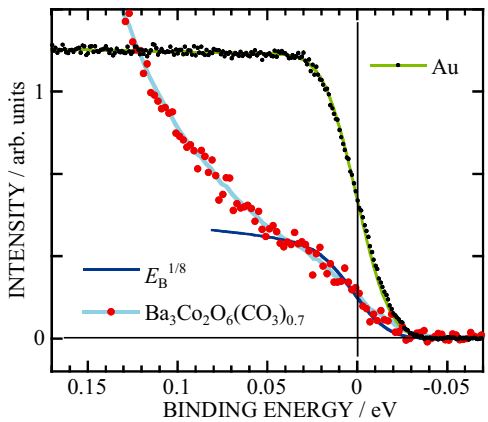

Fig. 2. Detailed spectra near the Fermi level.

[1] T. Yamamoto *et al.*, Proc. Int. Symp. on EcoTopia Science 2007, p.145.
[2] M. Z. Hasan *et al.*, Phys. Rev. Lett. **92** (2004) 246402.
[3] W. Koshibae *et al.*, Phys. Rev. B **62** (2000) 6869.
[4] J. Voit, Pep. Prog. Phys. **57** (1994) 977.

BL5U

Temperature Dependent Angle-Resolved Photoemission Spectra of La-Doped EuO

H. Miyazaki[1, 2], T. Ito[1, 3], K. Terashima[1], H. J. Im[4], S. Yagi[2], M. Kato[2], K. Soda[2] and S. Kimura[1, 3]

[1]*UVSOR Facility, Institute for Molecular Science, Okazaki 444-8585, Japan*
[2]*Graduate School of Engineering, Nagoya University, Nagoya 464-8603, Japan*
[3]*School of Physical Sciences, The Graduate University for Advanced Studies, Okazaki 444-8585, Japan*
[4]*Department of Advanced Physics, Hirosaki University, Hirosaki 036-8560, Japan*

Pristine europium monoxide (EuO) is a ferromagnetic semiconductor with the Curie temperature (T_C) at around 70 K [1, 2]. In the electron doping case by the Eu excess or substitute Gd^{3+} or La^{3+} from Eu^{2+} ion, T_C increases up to 150 K and the electrical resistivity drops twelve-order of magnitude below T_C originating in a metal-insulator transition (MIT) [2, 3]. Recently, we reported that the origin of the magnetic properties of EuO is caused by the hybridizations of the Eu 4*f* – O 2*p* and Eu 4*f* – 5*d* [4, 5]. To reveal the origin of increase of T_C due to the electron doping, it is important to clarify the electronic structure. Three dimensional angle-resolved photoemission spectroscopy (3D-ARPES) using a synchrotron radiation is the most powerful technique to directly determine the electronic band structure. Using this technique we observed the change of the electronic structure across T_C.

Single-crystalline La-doped EuO thin films with a thickness of about 50 nm were fabricated by a molecular beam epitaxy (MBE) method. Epitaxial growth of the single-crystalline La-doped EuO thin films with the 1 x 1 EuO (100) patterns was confirmed by a low energy electron diffraction (LEED) method. T_C measured with a superconducting quantum interference device (SQUID) magnetometer was around 200 K. The 3D-ARPES measurements were performed at the beam line 5U of UVSOR-II combined with the MBE system. The total energy and momentum resolutions for the ARPES measurement were set 123 meV and 0.020 $Å^{-1}$ at the Γ point and 45 meV and 0.014 $Å^{-1}$ at the X point, respectively.

Figures 1 (a) and (b) show the 3D-ARPES results for La-doped EuO near the Γ and X points, respectively. The local minimums on the second-derivative energy distribution curves (EDCs) indicate the peaks and shoulders of the EDCs. EDCs at binding energies (E_B) of 0.5 – 3.5 eV and of 4.0 – 6.5 eV are attributed to the Eu 4*f* and O 2*p* states, respectively. In comparison with the temperature-dependent 3D-ARPES spectra of pristine EuO [6], the temperature dependence is similar, but the photoemission intensity near the Fermi energy (E_F, E_B = 0 eV) at the X point appears indicating the metallic electronic structure. Since there is no intensity at E_F at the Γ point, the conduction band has the momentum dependence. According to the electronic resistivity data of an electron-doped EuO [2, 3], metallic electronic structure is expected to appear only below T_C. Though the origin of the observed conduction band is not clear yet, therefore, the doped electrons may appear in the ARPES spectrum and play an important role for the increasing of T_C. The detailed analysis and the further study for electron-doped EuO thin films are in progress.

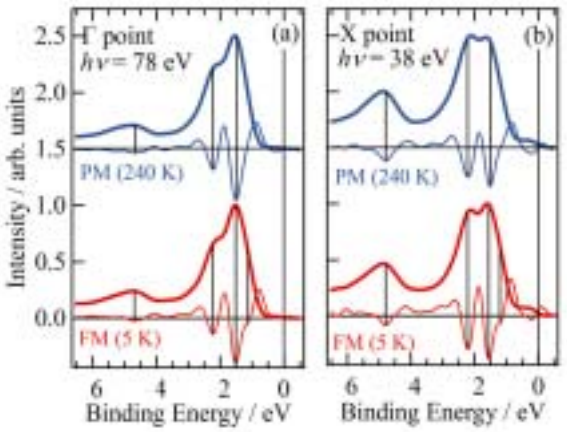

Fig. 1. Temperature dependence of the energy distribution curves (EDCs, thick line) and their second-derivative EDCs (thin line) of a La-doped EuO (100) thin film at the Γ (a) and X (b) points.

[1] N. Tsuda *et al*., Electronic Conduction in Oxides (Springers College) (1976).
[2] A. Mauger *et al*., J. Phys. (paris) **39** (1978) 1125.
[3] Y. Shapira, S. Foner, and T. B. Reed, Phys. Rev. B **8** (1973) 2299.; **8** (1973) 2316.
[4] H. Miyazaki *et al*., Physica B **403** (2008) 917.
[5] H. Miyazaki *et al*., Jpn. J. Appl. Phys. (2009) (in press).
[6] H. Miyazaki *et al*., submitted.

BL5B

Dilute Multi Ferroic Semiconductor GaCrN

S. Emura[1], K. Tokuda[1], H. Tambo[1], F. Suzuki[2] and K. Fukui[2]
[1]*ISIR, Osaka University, Mihoga-oka 8-1, Ibaraki, Osaka 567-0047, Japan*
[2]*Faculty of Engineering, University of Fukui, Bunkyo 3-9-1, Fukui 910-8507, Japan*

Multi-ferroic materials, which simultaneously show ferro-magnetism, ferro-electricity, and ferro-elasticity or two of those, and exist the coupling among them, attract much attention because of the physical interest in the coupling mechanism and for the potentiality of the various applications. We may be opening the door of new materials in the multi-ferroic research field, that is, dilute multi-ferroic semiconductors (DMS). Here, we will describe on DMS, GaCrN (GaN:Cr), where the Cr ion is a dilute dopant up to ~1.5%. In higher concentration, multi-ferroic phenomena are quenched (concentration quenching). This dilute alloy GaCrN is well known as a dilute magnetic semiconductor. The specimen studied here is a single crystal in the thin layer form on an Al_2O_3 substrate.

Analysis of XAFS spectra around Cr K-edge leads to the discovery the spontaneous elastic deformation (quasi Jahn – Teller effect) involving the local electric polarization. The polarization dependence of the absorption spectra in VUV energy region gives the evidence of the ordering of the elastic deformation and consequently of the electric polarization.

Figure 1 presents the radial distribution functions (RDFs) from the Cr ion site. We can see a doublet peak at around 1.3 ~ 1.7Å corresponding to Cr – N bonds and a single peak at 2.9Å corresponding to Cr – Ga bond. This finding means that there exist two different lengths for the first nearest neighbor (Cr – N), and one distance for the second nearest neighbor (Cr – Ga), resulting in the simply parallel shift of the four nitrogen ions as shown in Fig. 2. This deformation is originated in quasi Jahn – Teller effect. Involving the deformation, it is apparent from the figure that the local spontaneous electric polarization is induced around the doped Cr ion. Here, it should be noticed that there are four nearly equivalent legs because the original site symmetry is nearly Td, and we cannot distinguish these four legs from the XAFS analysis, which merely gives the one-dimensional structural information. The parallel shifts may randomly be distributed in the matrix or ordered along some direction of the matrix. The answer will come from the polarization effect of the absorption spectra. Figure 3 shows the incident angle dependence of the absorption spectra in VUV region observed at BL5B at UVSOR. At zero angles, the electric field of incident photon is vertical to the crystal c-axis of GaCrN. The absorption band around 28 nm (44.3 eV), which is tentatively assigned to the transition from 3p of the Cr atom to the s-like conduction band of matrix because of the wide halfwidth, strongly depends on the direction of the electric polarization of the incident photon. In the parallel electric field to the c-axis, the band vanishes, indicating anisotropy along the c-axis. This is clear evidence of the ordering of the deformation and consequent electric polarization.

The GaCrN alloy is one of the dilute magnetic semiconductors. From our observation, it is found that it behave as a ferro-electric and elastic material [1]. The coupling among those leads to substances of a new category in multi-ferroic research field.

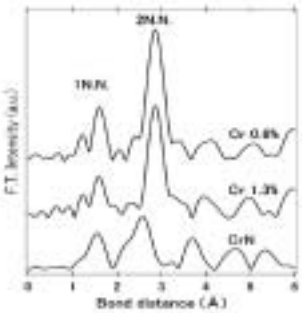

Fig. 1. RDFs from Cr ion site.

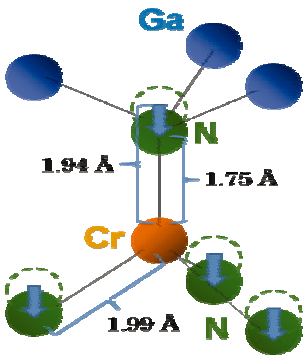

Fig. 2. Schematic drawing of relative positions.

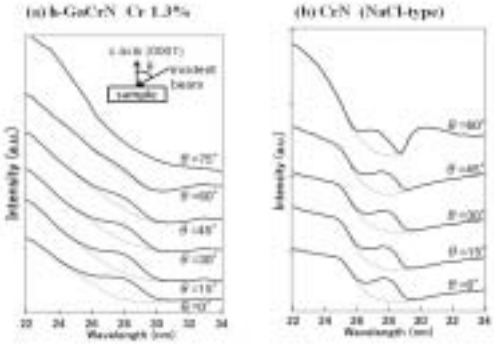

Fig. 3. Angular dependence of the absorption.

[1] submitted to Phys. Rev. Lett.

BL6B

Terahertz Spectroscopy of Bromides-Doped Silver Phosphate Superionic Conducting Glasses

T. Awano

Department of Electronic Engineering, Tohoku Gakuin University, Tagajo 985-8537, Japan

The enhancement of ionic conductivity by metal iodide doping into silver phosphate glass has been reported with BiI_3, CdI_2 and other metal iodides [1]. The increase of ionic conductivity is proportional to dopant concentration and valence number of the metal ion. Meanwhile, silver bromide- doped silver phosphate glass has less ionic conductivity than the iodide-doped one [2]. These facts suggest the following mechanism of the enhancement of ionic conductivity; the doped metal ion substitutes silver ions which was connected with non-bonding oxygen according to their valence and the released silver ions contribute to ionic conduction. The halogen ions expand conduction channel for the silver ion between glass network chains of PO_4 tetrahedra. This expansion is small in the case of bromide-doping therefore the conduction channel is narrow than in the case of iodide-doping. This abstract reports results of far-infrared spectra of metal bromides doped silver phosphate glasses to confirm the above mentioned model.

Figure 1 shows absorption spectra of $(AgBr)_x(AgPO_3)_{1-x}$ glass obtained from reflectivity spectra. Intensity of the band around 120 cm^{-1} increases as the bromine content increases. Peak position shifts slightly from 113 cm^{-1} (x=0.4) to 120 cm^{-1} (x=0.1).

Figure 2 shows absorption spectra of $(BiBr_3)_{0.05}(AgPO_3)_{0.95}$ glass obtained from reflectivity spectra. Fig. 3 shows absorption spectra of $(CdBr_2)_{0.1}(AgPO_3)_{0.95}$ glass. Intensity of the band around 120 cm^{-1} is almost the same as that of $(AgBr)_{0.4}(AgPO_3)_{0.6}$ glass in Fig. 1. Peak positions in Figs. 2 and 3 are around 130 cm^{-1} and different from that of $(AgBr)_{0.4}(AgPO_3)_{0.6}$ glass.

In the above mentioned model of structural change of the glass, the number of the released silver ions is proportional to the dopant concentration and also the valence number of the doped metal ion. Therefore intensities of newly induced absorption band by Ag-Br is expected to proportional to the product of the dopant concentration and the valence number. On the other hand, intensities of newly induced absorption band by Cd- or Bi-O is expected to proportional only to the dopant concentration. The intensity of Ag-O vibration should also decrease with the product of the dopant concentration and the valence number. The far-infrared spectral change seems to coincide with such mechanism of the structural change of the glass.

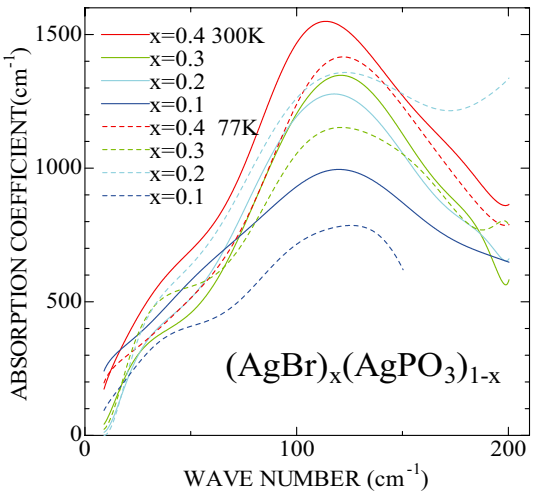

Fig. 1. Absorption spectra of AgBr-$AgPO_3$ glasses obtained from reflectivity.

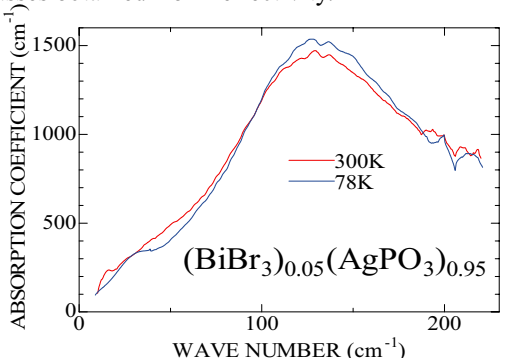

Fig. 2. Absorption spectra of $BiBr_3$-$AgPO_3$ glass obtained from reflectivity.

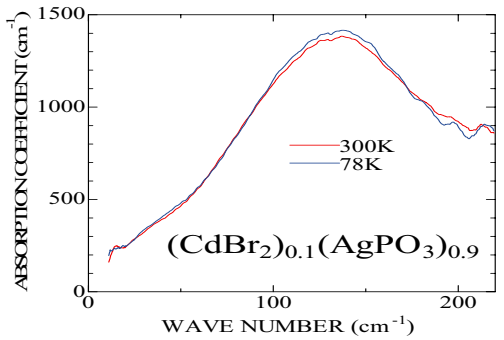

Fig. 3. Absorption spectra of $CdBr_2$-$AgPO_3$ glass obtained from reflectivity.

[1] H. Takahashi, H. Nakanii and T. Sakuma, Solid State Ionics **176** (2005) 1067.

[2] M. Hanaya, T. Okubayashi, T. Sakurai and M. Oguni, Thermochimika Acta **266** (1995) 79.

BL6B

Pressure-Dependent Far-Infrared Reflectivity Spectra of $CeIn_3$ at 9K

T. Iizuka[1], T. Mizuno[1], K. E. Lee[2], H. J. Im[3], T. Ito[4, 1], Y. S. Kwon[2] and S. Kimura[4, 1]

[1]*School of Physical Sciences, The Graduate University for Advanced Studies (SOKENDAI), Okazaki 444-8585, Japan*

[2]*Department of Physics, Sungkyunkwan University, Suwon 440-746, Korea*

[3]*Department of Advanced Physics, Hirosaki 036-8561, Japan*

[4]*UVSOR Facility, Institute for Molecular Science, Okazaki 444-8585, Japan*

Introduction

In recent years, some compounds called "heavy fermion"(HF) attract attention because of their various physical properties, which originate from the hybridization between itinerant conduction electrons and local 4*f* electrons. One of the characteristic physical properties is unconventional superconductivity due to HF, which appears near a quantum critical point (QCP) located in between the local and itinerant characters of 4*f* electrons.

$CeIn_3$ has an $AuCu_3$-type simple cubic crystal structure with the ground state located in the local regime (T_N = 10 K). With applying pressure, due to the increasing of the hybridization intensity between the conduction and 4*f* electrons, the ground state can be changed from antiferro magnetic (AFM) to nonmagnetic HF state via QCP. So $CeIn_3$ is one of suitable samples to study the hybridization dependence of electron structure near QCP. From the result of a de Haas-van Alphen (dHvA) effect measurement of $CeIn_3$ at 82 mK [1], the effective mass is enhanced at around the AFM ordering pressure of P_C = 2.6 GPa. On the other hand, another typical material located near QCP, $YbRh_2Si_2$, has another boundary (T^*) at which the carrier density probed by the Hall coefficient measurement drastically changes [2]. To reveal the relation of the mass enhancement of $CeIn_3$ to the enhancement of the carrier density of $YbRh_2Si_2$ at T^*, the pressure-dependent reflectivity spectrum in the terahertz (THz) region below T_N = 10 K were measured.

Experimental

Single phase $CeIn_3$ samples were synthesized by an arc melting method under argon atmosphere, and then annealed at 600 °C for three weeks inside an evacuated quartz tube. The THz reflection spectroscopy under pressure was performed at the THz micro-spectroscopy end station of UVSOR-II BL6B. A diamond anvil cell was employed to produce high pressure. KBr and Au film were used for media and for a background spectrum, respectively.

Results and Discussion

We obtained pressure-dependent reflectivity spectra [$R(\omega,P)$] of $CeIn_3$ at 9.5 K in the pressure region from 0.6 to 3.3 GPa as shown in Fig. 1. All spectra were divided by that at 2.0 GPa to highlight the pressure dependence. With increasing pressure, $R(\omega,P)$ of $CeIn_3$ mainly changes below 300 cm^{-1} region. To derive the pressure dependence of the spectra, the spectrum is divided into three parts, and the integrated intensities of each area are plotted as a function of pressure in Fig. 2. The area at around 150 cm^{-1} has a bottom at around 2.5 GPa and recovers above the pressure, in spite that the other lines monotonically increase with increasing pressure. The pressure of 2.5 GPa is close to the QCP of $CeIn_3$. The spectral change suggests that the Drude weight of heavy quasiparticles enhance below 150 cm^{-1} near the QCP and become smaller in the HF region. This result is consistent with the mass enhancement of CeIn3 at QCP and the increasing of the carrier density at T^* in $YbRh_2Si_2$, i.e., a large Fermi surface due to the heavy quasiparticles appears at P_C. One possibility of the origin is the valence transition from Ce^{3+} to Ce^{4+} at P_C.

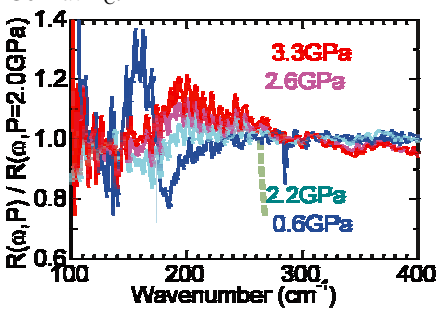

Fig. 1. Pressure-dependent reflectivity spectra $R(\omega,P)$ divided by $R(\omega,P = 2.0$ GPa) at 9.5K.

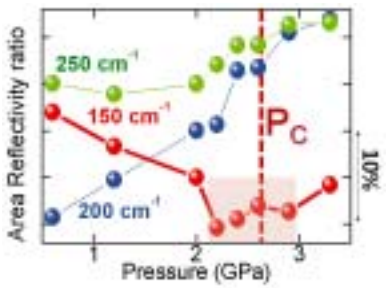

Fig. 2. The pressure dependence of the areas classified in Fig.1. Successive curves are offset by 5 % for clarity. P_C is the pressure of the QCP.

[1] R. Settai *et.al.*, J. Phys. Soc. Jpn. **74** (2005) 3016.
[2] S. Paschen *et.al.*, Nature **432** (2004) 881.

BL6B

Phonon-Polariton of GaN Observed by Far-Infrared Synchrotron Radiation

T. Inushima[1], Y. Ota[1], T. Yanagawa[2] and K. Fukui[2]
[1]*Department of Electronics, Tokai University, Hiratsuka, 259-1292, Japan*
[2]*Department of Electronics and Electrical Engineering, University of Fukui, Fukui 910-8507, Japan*

Temperature dependence of the reflectivity of GaN with a film thickness from 1 to 4 μm is investigated from 50 to 750 cm^{-1} by means of infrared synchrotron radiation. The phonon-polariton of GaN is observed in the energy range below E_1(TO) phonon. From the temperature dependence of the damping factor of the phonon, it is found that the E_1(TO) phonon decays primarily into phonons with a renormalized frequency of 226 cm^{-1}. Compared with the damping factor of superconducting InN, GaN grown on sapphire has more defects in the film.

All of the GaN films investigated have a hexagonal structure and their c-axes are perpendicular to the sapphire (0001) planes. Therefore, one E_1 optical phonon is observed in this configuration. Figure 1 shows the reflectivity spectrum of GaN with a thickness of 4 μm. A clear Reststrahren band is seen above 560 cm^{-1}, which is due to the E_1 optical phonon. The spectrum is analyzed using the following dielectric function,

$$\varepsilon(\omega) = \varepsilon_\infty - \frac{(\varepsilon_0 - \varepsilon_\infty)\omega_{TO}^2}{\omega^2 - \omega_{TO}^2 + i\omega\Gamma}. \qquad (1)$$

Using Eq. (1), the reflectivity spectrum is well reproduced and obtained fitting parameters are given in the figure.

The phonon-polariton is observed below the E_1(TO) phonon in Fig. 1, from which the damping factor Γ is obtained as a function of temperature shown in Fig. 2. The Γ of InN is also plotted for comparison. The Γ is the energy dissipation factor of the E_1(TO) oscillation and 1/Γ is regarded as the phonon lifetime. The lifetime was explained by Klemens in terms of a three-phonon process[1]. The three-phonon process is a decay process of the zone-center TO or LO phonon into two LA or TA phonons of equal frequencies and opposite wave vectors. In this consideration the temperature dependence of the Γ is expressed by the following equation;

$$\Gamma = \Gamma_0 + \Gamma_1 \coth\left(\frac{\hbar\omega_0}{2kT}\right). \qquad (2)$$

As is shown in Fig. 2, Γ(T) is reproduced by ω_0=226 cm^{-1} and 0.2 and 0.5 meV for Γ_0 and Γ_1, respectively. This indicates that the E_1(TO) phonon decays into two TA phonons with ω_0=226 cm^{-1}. As the value of Γ_0 is a measure of the defects in GaN, the measurement of the phonon-polariton is a tool for examining the crystal quality dynamically.

The ratio of Γ/ω_{TO} is the energy dissipation rate for the E_1 vibration and is 1.0×10^{-2} for GaN and 3.3×10^{-3} for InN. When we regard this as an unharmonic factor of the crystal, GaN grown on sapphire has much dislocation than InN.

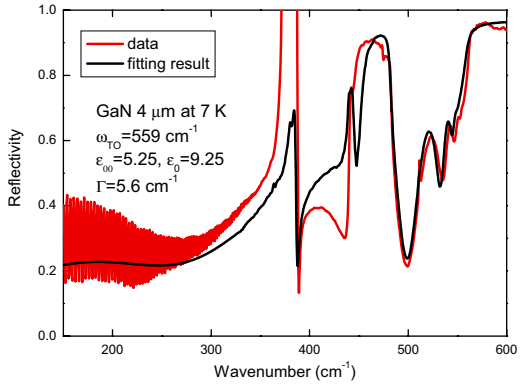

Fig. 1. Reflection spectrum of GaN at 7 K. The fitted line (black line) is drawn using Eq. (1). The fitting parameters are; ω_{TO}=559 cm^{-1}, ε_∞=5.25, Γ=0.0007 eV, d=3.9 μm.

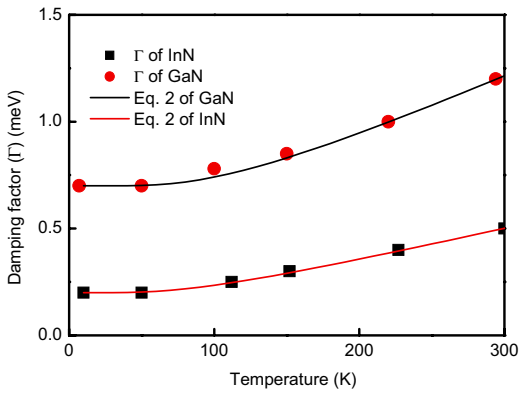

Fig. 2. Temperature dependence of the damping factors (Γ) of GaN and those of InN. The fitting is done using Eq. (2). For GaN, Γ_0 and Γ_1 are 0.2 and 0.5 meV, respectively and ω_0=226 cm^{-1} is obtained. As for InN, Γ_0 and Γ_1 are 0 and 0.2 meV, respectively, and ω_0=177 cm^{-1} is obtained.

[1] P. G. Klemens, Phys. Rev. **148** (1966) 845.

BL6B

Origin of Middle-Infrared Peaks in $CePd_3$

S. Kimura[1, 2], T. Iizuka[2] and Y. S. Kwon[3]

[1]*UVSOR Facility, Institute for Molecular Science, Okazaki 444-8585, Japan*

[2]*School of Physical Sciences, The Graduate University for Advanced Studies (SOKENDAI), Okazaki 444-8585, Japan*

[3] *Department of Physics, Sungkyunkwan University, Suwon 440-746, Korea*

Heavy fermion as well as mixed-valence materials, such as cerium (Ce), ytterbium (Yb), and uranium compounds, commonly have a characteristic peak structure (namely, the mid-IR peak) in the middle-infrared (mid-IR) region below 1 eV in their optical conductivity [$\sigma(\omega)$] spectra [1]. The origin of the mid-IR peak has remained a long debated issue so far. To investigate the origin of the mid-IR peaks of Ce compounds, we calculate the $\sigma(\omega)$ spectrum of $CePd_3$, which is a typical heavy fermion material, from the first principle band calculation with the spin-orbit interaction (SOI).

Band structure calculation was performed by the full potential linearized augmented plane wave plus local orbital (LAPW+lo) method including SOI implemented in the WIEN2K code [2]. $CePd_3$ forms a Cu_3Au-type cubic crystal structure (*Pm3m*, No. 221) with lattice constants of 4.1280 Å [3]. The band structure and $\sigma(\omega)$ spectrum of $LaPd_3$ (lattice constant = 4.235 Å [4]) were also calculated for reference.

The calculated $\sigma(\omega)$ spectra with and without SOI are plotted in Fig. 1. The experimental $\sigma(\omega)$ spectrum of $CePd_3$ at T = 8 K [5] is also plotted in the figure. The experimental spectrum has three large peaks at 0.25, 0.55, and 0.78 eV, and one small peak at 0.04 eV. The calculated $\sigma(\omega)$ spectrum with SOI also has three peaks at 0.3, 0.56, and 0.75 eV and one shoulder at 0.1 eV, despite the very low $\sigma(\omega)$ intensity of $LaPd_3$. This structure can be assigned to the experimental structure as follows: The peaks mainly appear in the Γ–X–R–M plane in the first Brillouin zone and the initial state of all peaks is commonly the highly dispersive conduction band [6]. The peaks at 0.3 and 0.78 eV in the calculated spectrum originate from the optical transitions to the Ce $4f_{7/2}$ state near the Γ-point and near the bottom of the Λ-axis, respectively. The small peak at 0.55 eV originates from the transition near the Δ- and S-axes. The shoulder structure at 0.1 eV in the calculation originates from the transition from the occupied flat band to the unoccupied Ce $4f_{5/2}$ state near the Γ-point. Therefore, all of the mid-IR peaks of $CePd_3$ can be explained by the band structure calculation with SOI.

In the calculated spectrum without SOI, one large peak at 0.7 eV appears, as shown in Fig. 1. The spectrum cannot reproduce the experimental triple-peak structure. The SOI of the Ce 4*f* state therefore plays an important role in the mid-IR triple-peak structure of $CePd_3$; i.e., the mid-IR peaks originate from the band structure including the SOI of the Ce 4*f* state [7].

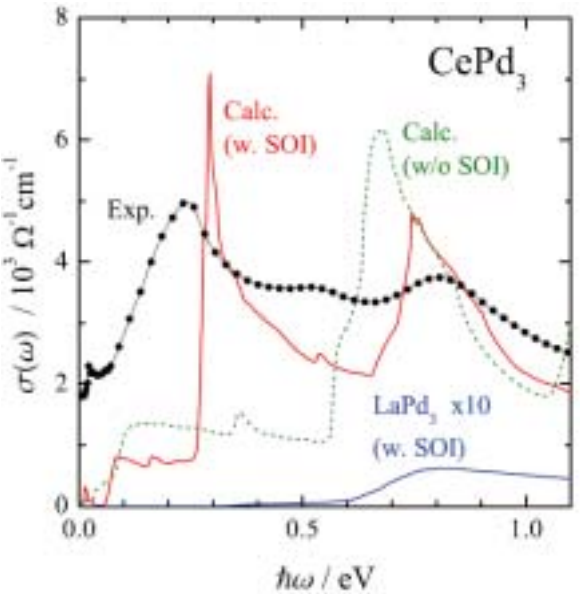

Fig. 1. Experimental and calculated optical conductivity [$\sigma(\omega)$] spectra of $CePd_3$. The calculated $\sigma(\omega)$ spectrum of $LaPd_3$ is also plotted for reference. Two different calculations with and without SOI were performed. The experimental spectrum, which was obtained at T = 8 K, is derived from that reported elsewhere [5].

[1] L. Degiorgi, Rev. Mod. Phys. **71** (1999) 687.
[2] P. Blaha, K. Schwarz, P. Sorantin and S. B. Trickey, Comput. Phys. Commun. **59** (1990) 399.
[3] K. H. J. Buschow, Rep. Prog. Phys. **42** (1979) 1373.
[4] C. Koenig and M. A. Khan, Phys. Rev. B **38** (1988) 5887.
[5] S. Kimura, H. Iwata, K. Kanai, S. Shin, G. Schmerber, J. P. Kappler and J. C. Parlebas, Acta Phys. Pol. B **34** (2003) 975.
[6] A. Hasegawa and A. Yanase, J. Phys. Soc. Jpn. **56** (1987) 3990.
[7] S. Kimura, T. Iizuka and Y. S. Kwon, J. Phys. Soc. Jpn. **78** (2009) 013710.

BL6B&7B

Optical Response of a New Type of Pyrochlore Oxides $Sm_2Mo_2O_7$ and $Pb_2Ir_{2-x}O_7$

M. Nishiyama[1], K. Shoji[1], A. Irisawa[1], T. Nanba[1], K. Miyoshi[2] and K. Matsuhira[3]
[1]*Kobe University, Nada-ku, Kobe 657-8501, Japan*
[2]*Shimane University, Matsue 690-8504, Japan*
[3]*Kyushu Institute of Technology, Tsukuba 305-0047, Japan*

Introduction

$Sm_2Mo_2O_7$ and $Pb_2Ir_{2-x}O_7$ are well known as typical pyrochlore oxides and have been recently synthesized. These oxide compounds crystallize in a so-called pyrochlore-type structure in which rare earth and transition metal element form respectively 3-dimensional network and Ir element locates at the central position of the tetragon of oxygen atoms. The recent electrical resistivity experiment revealed that at atmospheric pressure, both specimens exhibit a metallic property but their magnetic properties have attracted significant attention due to the geometrical frustration inherent in its crystal structure. That is, $Sm_2Mo_2O_7$ exhibits paramagnetic states to a spin-glass state at low temperature. On the other hand, $Pb_2Ir_{2-x}O_7$which contains nonmagnetic element instead of rare earth element is considered to be a good a reference material. To study its fundamental electronic states close to the Fermi level at ambient pressure, we measured the temperature dependence of optical reflectivity spectra R (ω) of $Sm_2Mo_2O_7$ and $Pb_2Ir_{2-x}O_7$.

Experimental

The optical reflectivity spectra R at ambient pressure were measured in the wide photon energy range from 7 meV to 30 eV in the temperature range of 8-300 K. The measurements were performed using a Fourier-transform interferometer combined with a thermal light source and synchrotron radiation source at the beam line BL6B & 7B of UVSOR. The optical conductivity $\sigma_1(\omega)$ and complex dielectric function $\varepsilon_1(\omega)$ were obtained from a standard Kramers-Kronig (K-K) transformation of the measured reflectivity (R) spectrum.

Results and discussions

Figure 1 shows the temperature dependence of the R-spectra of $Sm_2Mo_2O_7$. The spectra in the low energy region exhibit a strong Drude component due to the free conduction electrons which grows with cooling. The peaks at 2.6, 8.0 and 20 eV from a visible to vacuum ultraviolet originate to the electronic interband transition.

Figure 2 shows the temperature dependence of the R-spectra of $Pb_2Ir_{2-x}O_7$. The spectra at room temperature exhibit a metallic property, but with decreasing of temperature, the overall spectra change to insulating properties. Particularly, in the low energy part of the R-spectra around 0.08-0.8 eV, a distinct decrease in the reflectivity. This clear appearance of the structure means the occurrence of the stabilization of the insulating phase which induces the formation of the energy gap. The analysis is now on progress.

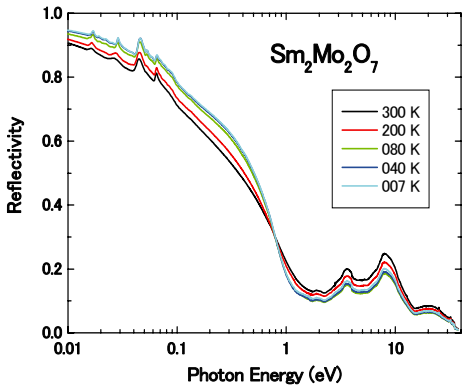

Fig. 1. Temperature dependence of R-spectra of $Sm_2Mo_2O_7$. Note to the abscissa in logarithmic scale.

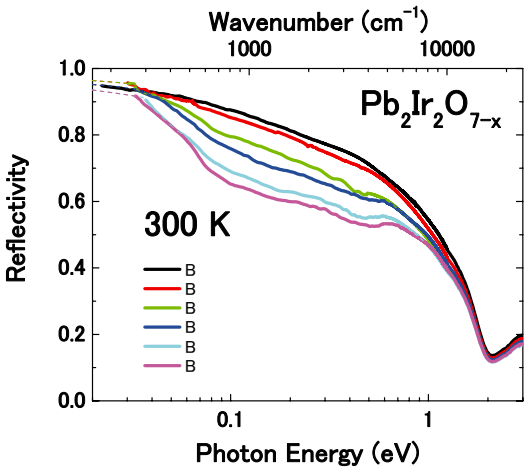

Fig. 2. Temperature dependence of R-spectra of $Pb_2Ir_{2-x}O_7$. Note to the abscissa in logarithmic scale.

[1] K. Miyoshi *et al.*, J. Phys. Jpn. **75** (2006) 065001-1.

BL7U

Angle-Resolved Photoemission Study on $EuFe_2As_2$

T. Ito[1, 2], J. B. Hong[3], Y. R. Jang[3], S. Kimura[1, 2] and Y. S. Kwon[3]

[1]*UVSOR Facility, Institute for Molecular Science, Okazaki 444-8585, Japan*

[2]*School of Physical Sciences, the Graduate University for Advanced Studies (SOKENDAI), Okazaki 444-8585, Japan*

[3]*Department of Physics, Sungkyunkwan University, Suwon 440-749, Korea*

Recent discovery of a new high-temperature (T_c) superconductor, iron (Fe) pnictides, has triggered intensive researches, since the foregoing common sense that the magnetism must be the obstacle for superconductivity has been disproved [1]. Since the compounds commonly exhibit a collinear antiferromagnetic (AF) spin density wave (SDW), which can be connected to the pseudo-gap phase of cupurate high-T_c superconductors [2], the relation between SDW and superconductivity becomes a new topic on strongly-correlated electron systems.

$EuFe_2As_2$, which exhibits a SDW transition around T_0=190 K at Fe_2As_2 layer, shows the antiferromagnetic ordering at T_N = 20 K of the localized Eu^{2+} moments [3]. With applying pressure, the SDW temperature decreases in spite of the constant T_N. Furthermore, superconductivity T_c = 30 K appears under high pressure or due to the K doping [4]. Thus $EuFe_2As_2$ is an ideal system to study the essential role of the SDW formation to the mechanism of high-T_c superconductivity.

Figure 2(b) shows the band structure near E_F of $EuFe_2As_2$ at the SDW phase (T = 25 K). From the comparison with the results of $Ba_{0.6}K_{0.4}Fe_2As_2$, observed Fermi surfaces (FSs) (see Figs. 1 and 2(a)) are attributed to a tetragonal shaped hole-like FS (β) around the Γ point and an ellipsoidal shaped electron-like one (γ) around the M point. When we focus on to the hole-pocket, we found a faint dispersive feature that can be attributed to the folded band originating from the electron-pocket at the M point shifted by an antiferromagnetic SDW vector. It should be noted that the SDW formation has been expected between the electron-like FS (γ) at the M point and the smaller hole-like FS (α) at the Γ point in $Ba_{0.6}K_{0.4}Fe_2As_2$ system [1], though the latter seems to be fully occupied at the present $EuFe_2As_2$ case. With the further investigation of the folded feature along hole-like FS, we found clear anisotropy (not shown) in consistent with the SDW formation between the electron-like FS (γ) and the observed hole-like FS (β). To further insight into the essential role of the observed SDW feature, its temperature dependence across SDW transition temperature as well as T_N, and the doping dependence are intended.

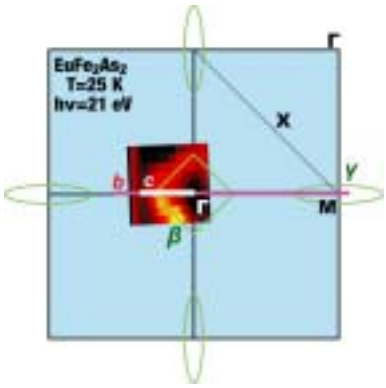

Fig. 1. Fermi surface image of $EuFe_2As_2$ compared with the expected Fermi surface topology from the previous report on $Ba_{0.6}K_{0.4}Fe_2As_2$ [1].

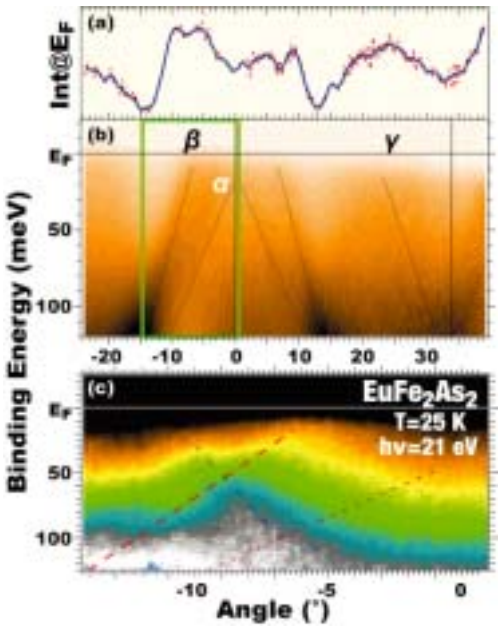

Fig. 2. (a) Angular distribution curve at E_F and (b) band structure near E_F of $EuFe_2As_2$ at the SDW phase (T = 25 K). (c) Band structure near E_F enlarged around the hole-pocket (β). Dashed lines are guide for eyes.

[1] H. Ding *et al.*, Eur. Phys. Lett. **83** (2008) 47001.
[2] S. V. Borisenko *et al.*, Phys. Rev. Lett. **100** (2008) 196402.
[3] H. S. Jeevan *et al.*, Phys. Rev. B **78** (2008) 020503(R).
[4] H. S. Jeevan *et al.*, Phys. Rev. B **78** (2008) 092406.

BL7U

High-Resolution Angle-Resolved Photoemission Study of High-T_c Cuprate Superconductors: Observation of Bulk Electronic States

K. Nakayama[1], T. Arakane[1], S. Souma[2], K. Terashima[3], T. Sato[1] and T. Takahashi[1, 2]

[1]*Department of Physics, Tohoku University, Sendai 980-8578, Japan*

[2]*WPI Research Center, Advanced Institute for Material Research, Tohoku University, Sendai 980-8577, Japan*

[3]*UVSOR Facility, Institute for Molecular Science, Okazaki 444-8585, Japan*

Low-energy excitations play an essential role in characterizing various physical properties such as superconductivity and the metal-insulator transition. In copper-oxide (cuprate) high-T_c superconductors (HTSC), low-energy excitations are intensively studied by the high-resolution angle-resolved photoemission spectroscopy (ARPES). Numerous amounts of ARPES researches have been focused on a bilayered Bi-based HTSC $Bi_2Sr_2CaCu_2O_8$ (Bi2212), because of its high T_c value and good surface condition suitable for ARPES. Previous ARPES studies of Bi2212 clarified several characteristic features essential to the high-T_c superconductivity, such as the large Fermi surface centered at the (π, π) point of the Brillouin zone, the $d_{x^2-y^2}$-wave superconducting gap, the emergence of well-defined Bogoliubov quasiparticles below T_c in antinodal region, and the pseudogap above T_c in an underdoped regime. However, it is still unclear whether or not these characteristic low-energy excitations are generic feature of all HTSCs. Hence the universality of essential character of CuO_2 plane should be examined by performing ARPES of other families of HTSCs. In this regard, $YBa_2Cu_3O_{7-\delta}$ (Y123) is most suitable candidate since it is also a bilayered system with similar maximum T_c, and the bosonic excitations are intensively studied by other experiments. However, it is well known from the earlier stage of ARPES investigations on Y-based HTSCs that the electronic structure is fairly complicated owing to the experimental facts that the superconducting gap is not as robust as that of Bi2212 and is not clearly observed even below T_c, and strong emission from the surface-state in the antinodal region dominates the low-energy excitations, causing a difficulty in distinguishing bulk electronic signal from the CuO_2 plane.

In this study, we overcome these difficulties by utilizing the low-energy and variable polarization characters of the beamline BL-7U, and we have succeeded in directly observing the signature of bulk superconducting gap in Y123.

Figure 1(a) shows the ARPES spectral intensity plot of Y123 (T_c = 92 K) at E_F measured at 15 K with 24.5-eV photons using a linearly polarized light whose polarization direction is shown in (a). ARPES intensity at E_F is obtained by integrating the intensity within 10 meV with respect E_F. We clearly identify large hole-like Fermi surfaces centered at the (π, π) point of the Brillouin zone, consistent with the previous ARPES study with higher energy photons [1]. These features mainly originate in the surface-derived bonding and antibonding bands. In order to see dispersive feature of energy bands, we have measured energy distribution curves along a cut shown by a blue line in (a). The result is illustrated in Fig. 1(b). We clearly observed a highly dispersive band which apparently crosses E_F. This band is attributed to the surface band, since it is metallic even below bulk T_c. Moreover, as indicated by markers, we find less dispersive feature at ~30 meV which does not cross E_F. This band is assigned as a bulk band showing a superconducting gap of 30 meV in the antinodal region. We thus conclude from the present experimental result that bulk electronic structure of Y123 can be clearly resolved when we optimize the photon energy and the polarization vector of incident light.

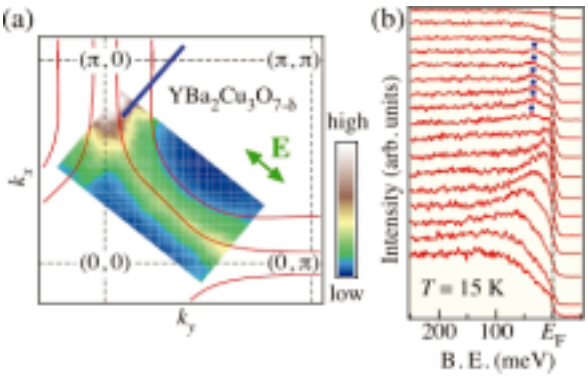

Fig. 1. (a) ARPES intensity of Y123 measured at 15 K with $h\nu$ = 24.5 eV plotted as a function of in-plane wave vector, together with the tight-binding fitting result of the surface band (solid curves). Polarization direction of light is indicated in the inset. (b) Energy distribution curves measured along the cut indicated by a blue line in (a).

[1] K. Nakayama *et al.*, Phys. Rev. B **75** (2007) 014513.

BL7U

Extremely Low-Energy Photoemission Study of $Sm_{1-x}Eu_xB_6$

A. Sekiyama[1], J. Yamaguchi[1], S. Komori[1], H. Sugiyama[1], M. Y. Kimura[1], S. Yeo[2], S. Lee[3], H. Kim[4], T. Ito[5], S. Kimura[5] and S. Suga[1]

[1]*Graduate School of Engineering Science, Osaka University, Toyonaka, Osaka 560-8531, Japan*

[2]*Korea Atomic Energy Research Institute, Daejeon 305-600, Korea*

[3]*Department of Physics, Sogang University, Seoul 121-742, Korea*

[4]*Pohang Accelerator Laboratory, Pohang 790-784, Korea*

[5]*UVSOR Facility, Institute for Molecular Science, Okazaki 444-8585, Japan*

SmB_6 and YbB_{12} are known as Kondo semiconductors showing a nonmagnetic semiconducting behavior at low temperatures. It is thought that this nature originates from the formation of the hybridization gap in the vicinity of the Fermi level (E_F), which reflects the periodicity of the 4f sites. Recently, we have found the collapse of the 4f lattice coherence is collapsed for a partially Lu-substituted system $Yb_{1-x}Lu_xB_{12}$ by temperature-dependent hard x-ray photoemission (HAXPES), suggesting that the hybridization gap is no longer opened for x = 0.125 due to the lack of the 4f periodicity [1]. On the other hand, it is also found that the temperature dependence of the 4f HAXPES spectra for $Sm_{0.85}Eu_{0.15}B_6$ (x = 0.15) is qualitatively similar to that for pure YbB_{12} while the bulk spectra of $Sm_{0.5}Eu_{0.5}B_6$ (x = 0.5) could be explained by the single impurity Anderson model without considering the 4f periodicity. These results imply that the hybridization gap is still present for the Eu-substituted system $Sm_{0.85}Eu_{0.15}B_6$. In order to directly verify the presence of the gap, we have performed the extremely low-energy photoemission (ELEPES) study for $Sm_{1-x}Eu_xB_6$.

ELEPES was performed at BL7U by using a photoelectron spectrometer of MB Scientific A1 analyzer. In order to obtain clean surfaces, the bulk $Sm_{1-x}Eu_xB_6$ samples were fractured *in situ* at 15 K. We measured the photoemission spectra by controlling hν from 7 to 17 eV. The energy resolution was set to <10 meV at hν = 7 eV. We checked the reproducibility of the temperature dependence of the spectra for $Sm_{0.85}Eu_{0.15}B_6$ by measuring the spectra on heating from 15 to 200 K and those on cooling from 200 to 15 K for the same sample without any surface treatment after fracturing at 15 K.

Figure 1 shows the hν dependence of the valence-band spectra near E_F for $Sm_{0.85}Eu_{0.15}B_6$. A narrow peak located at about 15 meV is seen in the spectra at hν = 7, 8.4 and 9.7 eV. This peak is strongly smeared in the spectra at hν = 12 and 14 eV, and seems to disappear in the spectrum at hν = 17 eV. The spectral weight in the vicinity of E_F seems to increase slightly but gradually with hν. Considering that the spectral line shape does not change among the spectra at hν = 7, 8.4 and 9.7 eV, we conclude that the narrow peak at ~15 meV reflects the bulk band structure at low temperatures, and that ELEPES is surely bulk-sensitive at hν < 10 eV. The leading-edge, the binding energy at which the spectral intensity is half of that at the peak or shoulder nearest to E_F, is apparently in the occupied side in the spectra at hν < 10 eV, which indicates that the finite gap is open even for the Eu-substituted system $Sm_{0.85}Eu_{0.15}B_6$.

The temperature-dependent spectra of x = 0.15 at hν = 7 eV (not shown here) indicate that the spectral weight in the vicinity of E_F is gradually enhanced with temperature up to 200 K, suggesting that the gap is closed at high temperatures. On the other hand, such a temperature dependence is not seen for x = 0.5, which gives a metallic Fermi cut-off in the spectra at 15 and 200 K. This result reflects that the hybridization gap as well as the 4f lattice coherence collapses even at low temperatures for the "heavily" substituted x = 0.5. From these results, we would conclude that SmB_6 is a "robust" Kondo semiconductor against a rare-earth substitution, which is in strong contrast to the case for YbB_{12}.

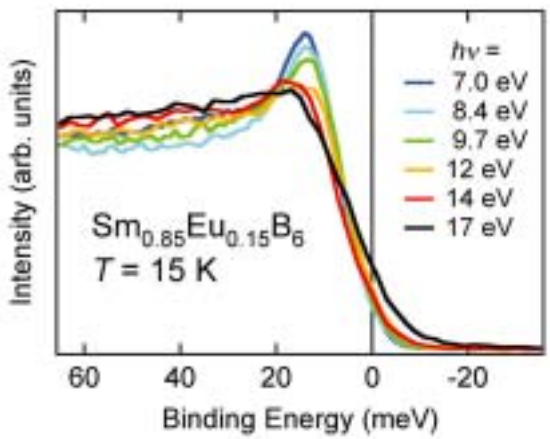

Fig. 1. hν dependence of the valence-band photoemission spectra near E_F for $Sm_{0.85}Eu_{0.15}B_6$.

[1] J. Yamaguchi *et al.*, Phys. Rev. B, in press.
[2] J. Yamaguchi *et al.*, unpublished.

BL7U

Anisotropic Electron-Scattering and Thermoelectric Power of $La_{2-x}Sr_xCuO_4$ and $Nd_{2-x}Sr_xCuO_4$ Superconductors

T. Takeuchi[1, 2], H. Komoto[2], Y. Hamaya[2], S. Arita[2], T. Ito[3] and S. Kimura[3]

[1]*EcoTopia Science Institute, Nagoya Univeristy, Nagoya 464-8603, Japan*

[2]*Depaertment of Crystalline Materials Science, Nagoya University, Nagoya 464-8603, Japan*

[3]*UVSOR Facility, Institute for Molecular Science, Okazaki 444-8585, Japan*

After the prediction of the potential of low-dimensional systems as a practical thermoelectric material [1, 2], a considerable attention has been attracted in the materials with low dimensional crystal structure. High-T_c superconductors, such as $La_{2-x}Sr_xCuO_4$ (LSCO) and $Nd_{2-x}Sr_xCuO_4$ (NCCO), are typical materials possessing two-dimensional atomic and electronic structures. Notably, LSCO and NCCO with small x possess a large thermoelectric power exceeding 100 μV/K and metallic electrical conduction.

Although important role of two-dimensional electronic structure was predicted from the theoretical considerations [1, 2], the relation between the theory and the good thermoelectric properties of LSCO and NCCO has not been clearly understood yet. The small magnitude of thermoelectric power observed for $Bi_2Sr_2CuO_{6+\delta}$ possessing an electronic structure similar to that of LSCO and NCCO might indicate less important role of two-dimensional electronic structure. It is, therefore, of great importance to study the origin of the characteristic thermoelectric properties observed for LSCO and NCCO.

LSCO possess positive sign in its thermoelectric power over a wide temperature range while NCCO negative one. This fact seemingly sounds natural because LSCO and NCCO are obtained by doping some holes or electrons in the Mott insulator, respectively, and the Mott insulator has the fully occupied lower Hubbard-band and upper Hubbard-band separated from each other by an energy gap. These Hubbard-bands, however, are known to disappear in LSCO and NCCO and to be replaced by a single band crossing the Fermi level. This experimentally revealed fact definitely indicates that the sign and magnitude of thermoelectric power of LSCO and NCCO cannot be simply accounted for with the Mott-Hubbard bands.

In this study, therefore, we investigated the energy-momentum dispersion and the lifetime of the coherent states (Bloch states or quasiparticles) in LSCO and NCCO using the high-resolution angle resolved photoemission spectroscopy (APRES) measurements. By using the obtained information about the electric states, we calculated thermoelectric power by using the semi-classical Boltzmann equation and compared it with the measured data.

By accumulating ARPES data over the whole momentum space, we realized that the energy-momentum dispersion of these two compounds looks very similar to each other except for the clear difference in the Fermi level, and that the electron scattering exhibits strong anisotropy, which is characterized by the "*hot spot*" and "*cold spot*", in both compounds. We also realized by analyzing the spectral shape at each Fermi momentum that the "*hot spot*", where the quasiparticles are most frequently scattered, is located near (π, π) in LSCO, while it stays at the momentum near (π/2, π/2) in NCCO. This fact is naturally understood by assuming that the "*hot spot*" is created by the fluctuation of anti-ferromagnetic ordering and hence it is located at the momentum where the Fermi surface (FS) crosses the anti-ferromagnetic zone boundary (AFZB). Indeed the large holelike Fermi surface in LSCO intersects AFZB near (π, π) while the small holelike FS in NCCO near (π/2, π/2).

We calculated thermoelectric power with considering the strong scattering effect at the AFZB. The calculated thermoelectric power is shown in Fig. 1 together with the measured data. Obviously, the calculation quantitatively reproduced the measured data at least in the temperature range we used in the calculation. We also calculated thermoelectric power without the effect of strong scattering at the AFZB, and found that the large magnitude nor the sign of thermoelectric power are unable to be reproduced without the AFZB-effect. We conclude, therefore, that the large magnitude of the thermoelectric power is caused by the anisotropic electron-scatterings while the two-dimensionality has less important role on it.

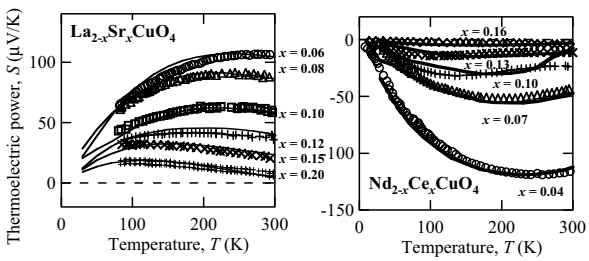

Fig. 1. The calculated and measured thermoelectric power of $La_{2-x}Sr_xCuO_4$ and $Nd_{2-x}Ce_xCuO_4$.

[1] L. D. Hicks and M. S. Dresselhaus, Phys. Rev. B **47** (1993) 12727.

[2] L. D. Hicks and M. S. Dresselhaus, Phys. Rev. B **47** (1993) 16631.

BL7B

Valence Band Structure Study of AlN

T. Ito[1], R. Ikematsu[1], M. Kishida[1], K. Fukui[1], K. Hiramatsu[2], H. Amano[2] and H. Hirayama[3]

[1]*Department of Electrical and Electronics Engineering, University of Fukui, Fukui 910-8507, Japan*

[2]*Department of Material Science Engineering, Meijo University, Aichi 468-8507, Japan*

[3]*RIKEN, Saitama 351-0198, Japan*

Aluminum nitride (AlN) has the widest direct band-gap in III-V nitride compound semiconductors, so that AlN is expected such applications as UV light emitting diodes, *etc*. It is known that the uppermost valence band (VB) of AlN splits into three levels (CH, HH and LH bands in increasing band-gap order) due to crystal-field splitting and spin orbit interaction, and transition between each level and conduction band (CB) has the different polarization character. These three transitions are usually labeled as A (from CH to CB), B (HH to CB), and C (LH to CB). B and C transitions are mainly allowed under $\boldsymbol{E} \perp c$ condition, while A transition is only allowed under $\boldsymbol{E} \parallel c$ condition, where $\boldsymbol{E}$ and c represent the electric field vector of the excited light and the crystal axis of wurtzite AlN, respectively. It means that the transition at the minimum band-gap (A transition) becomes forbidden, because c-axes of AlN thin films grown on both sapphire and SiC substrates are usually perpendicular to the surface. Then, an understanding of the VB structure is necessary not only for basic science but also for application. Therefore, optical reflectance (OR) spectra, photoluminescence (PL), and PL excitation (PLE) spectra measurements at low temperature have been performed to observe all transitions near band edge (including A to C transitions and estimation of both the crystal-field splitting energy Δ_{cr} and spin-orbital splitting energy Δ_{so}) and their polarization characters. To measure all transitions including forbidden transitions under normal incidence light configuration, OR and PLE spectra measurements have been carried out with rotating incident light angle under p optical configuration using highly linear polarized synchrotron radiation excitation light.

AlN films were grown on the sapphire substrates by MOCVD method. Thicknesses are 1 ~ 3.5 μm for avoiding the stress by the lattice constant mismatch with the substrate. The rotation angle of the incident light is defined as the angle between excitation light and normal vector of sample surface (c axis).

Figure 1 shows OR spectra at 20 K. OR spectrum at 60 degree clearly shows the structure due to the excitonic absorption around 6.05 eV. It shows that the transition energy of A transition is 6.05 eV, because this strucutre has clear incident light angle dependence and increases its intensity under $\boldsymbol{E} \parallel c$ configuration. Adjacent two excitonic structures due to B and C transitions around 6.1 ~ 6.4 eV are analyzed by the line shape fitting using the theoretical function of exciton absorption [1], and B and C transitions are located at 6.24 and 6.28 eV, respectively. Therefore, based on theoretical model [3], Δ_{cr} and Δ_{so} are -205 meV and 55 meV, respectively. Figure 2 shows PLE spectra and inset figure shows PL spectrum at 20 K. PL spectrum does not show the incidence light angle dependence. PL peak at 6.05 eV is the main peak and two small peaks at low energy side are LO replicas. Integrated intensities of main PL peaks at 0 and 60 degrees as the function of the excitation photon energy are plotted as PLE spectra. Two peaks which correspond to B and C transitions and two other peaks above 6.4 eV are clearly observed. They are all excited both $\boldsymbol{E} \perp c$ and $\boldsymbol{E} \parallel c$ conditions. However, significant difference is shown below 6.24 eV (B transition).

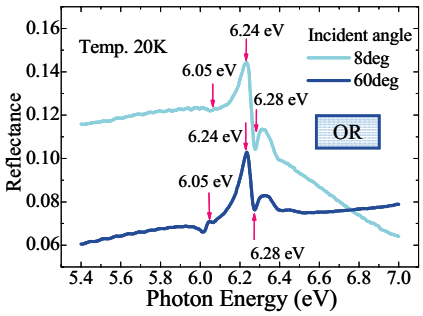

Fig. 1. Incident angle dependence of OR spectra

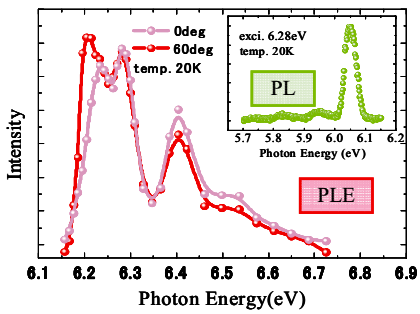

Fig. 2. Incident angle dependence of PLE spectra with PL spectrum (inset).

[1] T. Onuma, S. F. Chichibu, T. Sota, K. Asai, S. Sumiya, T. Shibata and M. Tanaka, Appl. Phys. Lett. **81** (2002) 652.

[2] A. Sedhain, J. Y. Lin and H. X. Jiang, Appl. Phys. Lett. **92** (2008) 041114.

BL7B

Electronic Structures of YbS and Yb Studied by Optical and Photoemission Spectroscopies

H. Okamura[1], M. Matsunami[2], T. Nanba[1] and A. Ochiai[3]

[1]*Graduate School of Science, Kobe University, Kobe 657-8501, Japan*

[2]*Institute for Solid State Physics, University of Tokyo, Kashiwa, Chiba 277-8581, Japan*

[3]*Center for Low Temperature Science, Tohoku University, Aoba-ku, Sendai 980-8578, Japan*

In the field of strongly correlated f electron physics, it is often important to estimate the average valence of rare earth element such as Ce and Yb, since the average valence is directly related to the degree of *f* electron localization and delocalization. Such a localization/delocalization duality is believed to be closely related with interesting phenomena such as heavy fermion formation and magnetic quantum criticality. Along with the thermodynamic techniques such as magnetic susceptibility, spectroscopic techniques such as X-ray absorption (XAS) and photoemission (PES) spectroscopies have been very useful in estimating the average valence of a Ce or Yb compound. However, these spectroscopic techniques have sometimes yielded an average valence inconsistent with that given by the thermodynamic properties. For example, YbS and Yb metal are both believed to be divalent compounds from their thermodynamic properties and general considerations on their electronic structures, yet some XAS and PES results have suggested that they are in mixed-valent states [1-3]. In the case of PES, the estimation of average valence usually involves a comparison of spectral weight between the Yb^{2+} and Yb^{3+} components. It is sometimes difficult to distinguish between a Yb^{3+} component and a satellite associated with the Yb^{2+} component, which may have resulted in the inconsistent results.

To resolve this question, we have measured X-ray PES spectra of YbS and Yb at SPring-8, and have compared the results with their optical spectra measured at BL7B of UVSOR [4]. Regarding the optical spectra, the reflectivity R(ω) of YbS and Yb was measured at BL7B, and their complex dielectric function ε was obtained from the Kramers-Kronig analysis of R(ω). Then the bulk and surface energy loss functions were calculated as Im(1/ε) and Im[1/(ε+1)], respectively. Figure 1 shows the measured Yb 3d core-level PES of YbS (a) and Yb (b), measured with incident photon energy of 7.94 keV at SPring-8, and the energy loss functions obtained at BL7B as described above. The sharp peak near 1520 eV is the Yb^{2+} main peak. For the more bulk-sensitive, θ=0 (normal incidence) spectrum, the satellite located to the left of the main peak has fine structures that correspond to peaks in the bulk loss function very well. In contrast, the more surface-sensitive, θ=80° (grazing incidence) spectrum has a satellite that corresponds to the surface loss function very well. Based on this set of data and the valence band PES spectra measured with soft X-ray incident light, it is concluded that the Yb^{3+} component in YbS and Yb is negligibly weak, and these compounds are in fact purely divalent in terms of spectroscopic point of view. Namely, the *f* electrons in YbS and Yb are completely localized and forming a closed 4*f* shell.

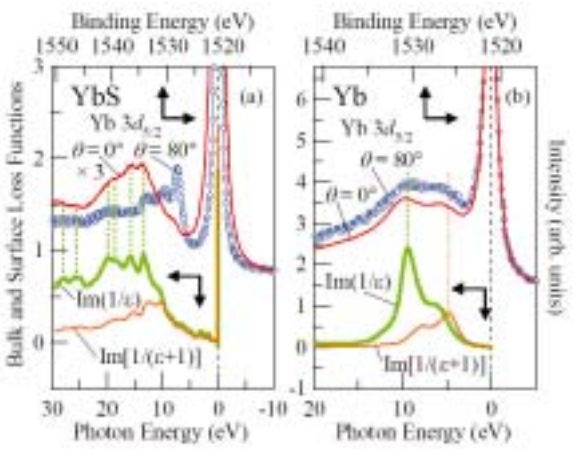

Fig. 1. Yb 3d5/2 core-level PES spectra of YbS (a) and Yb metal (b), measured at SPring-8, and the bulk and surface loss functions Im(1/ε) and Im[1/(ε+1)], respectively, measured at BL7B of UVSOR [4].

[1] E. Annese, J. P. Rueff, G. Vanko, M. Grioni, L. Braicovich, L. Degiorgi, R. Gusmeroli and C. Dallera, Phys. Rev. B **70** (2004) 075117.

[2] A. Fuse, G. Nakamoto, M. Kurisu, N. Ishimatsu and H. Tanida, J. Alloys Compounds **376** (2004) 34.

[3] C. Dallera, O. Wessely, M. Colarieti-Tosti and O. Eriksson, Phys. Rev. B **74** (2006) 081101.

[4] M. Matsunami, A. Chainani, M. Taguchi, R. Eguchi, Y. Ishida, Y. Takata, H. Okamura, T. Nanba, M. Yabashi, K. Tamasaku, Y. Nishino, T. Ishikawa, Y. Senba, H. Ohashi, N. Tsujii, A. Ochiai and S. Shin, Phys. Rev. B **78** (2008) 195118.

BL7B

Near Band Edge Photoluminescence and Photoluminescence Excitation Spectra of Mg-Doped $Al_XGa_{1-X}N$

M. Suzuki[1], S. Sawai[1], K. Fukui[1], K.Nagamatsu[2] and H.Amano[2]

[1] *Department of Electrical and Electronics Engineering, University of Fukui, Fukui 910-8507, Japan*

[2] *Department of Material Science Engineering, Meijo University, Nagoya 468-8502, Japan*

The undoped AlGaN alloys always show the n-type conduction due to the Nitrogen defects. Then, p-type AlGaN alloys are expected to achieve electronic devices, and Mg has been used for the typical dopant. However, it seems that the optical investigations of Mg doped AlGaN (AlGaN:Mg) are mainly concentrated to the Mg related broad emission band (Mg-related band) which is located between near band edge (NBE) emission band and impurity related broad emission band (so-called Yellow emission). However, NBE emission is also affected by Mg doping. Then, in this study, we investigate the Mg doping effects by the NBE photoluminescence (PL) and PL excitation (PLE) spectra of $Al_xGa_{1-x}N$:Mg in the wide x range, though we observe both Mg-related band and impurity related broad emission band.

The wurtzite AlGaN:Mg films of 1.5 μm thickness are grown on the c-plane sapphire substrates covered with 2 μm thickness highly crystalline AlN layers by MOVPE [1]. The measurement temperature is from 10 to 160 K.

Figure 1 shows the PL and PLE peak energies of four AlGaN:Mg samples as a function of Al fraction at 10 K. Two curves represent calculated PL and PLE peaks of undoped AlGaN. The peaks of AlGaN:Mg are in agreement with those of AlGaN. Figure 2 shows the temperature dependence of NBE emission peak energy shifts of $Al_{0.65}Ga_{0.35}N$:Mg. Temperature dependence of the peak energy shows *S*-shaped (decrease – increase – decrease) behaviour with increasing temperature, which is well observed in that of undoped AlGaN. These two results suggest that the mechanism of NBE PL of AlGaN:Mg is basically similar to that of undoped AlGaN. Figure 3 shows the PL spectrum of $Al_{0.65}Ga_{0.35}N$:Mg at 10 K and the fitting result of spectrum deconvolution. This deconvolution is based on the model that NBE PL band of undoped AlGaN consists of a main peak and 2 ~ 3 LO phonon replicas, and is in good agreement with experimental results of undoped AlGaN. However, an additional (A) band is required in the case of AlGaN:Mg. Then, one possibility model is that A band is assigned as the transition to Mg acceptor level. According to this model, activation energies of Mg acceptor which corresponds to the energy difference between PLE peak and A band peak becomes 370 and 320 meV for $Al_{0.65}Ga_{0.35}N$:Mg and $Al_{0.27}Ga_{0.73}N$:Mg, respectively.

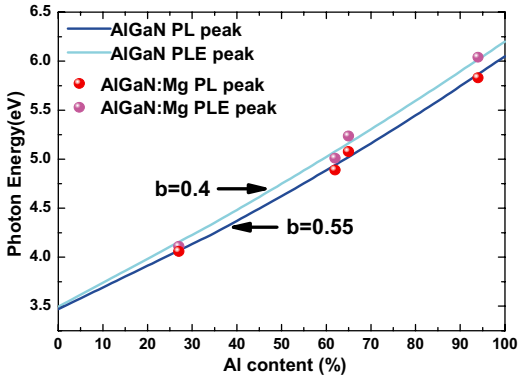

Fig. 1. PL and PLE peaks of AlGaN:Mg and undoped AlGaN as a function of Al fraction.

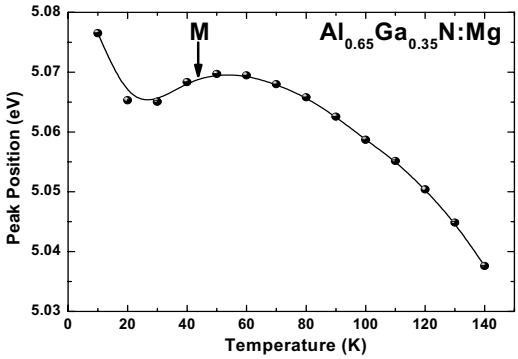

Fig. 2. The temperature dependence of (M) peak energy shifts of $Al_{0.65}Ga_{0.35}N$:Mg.

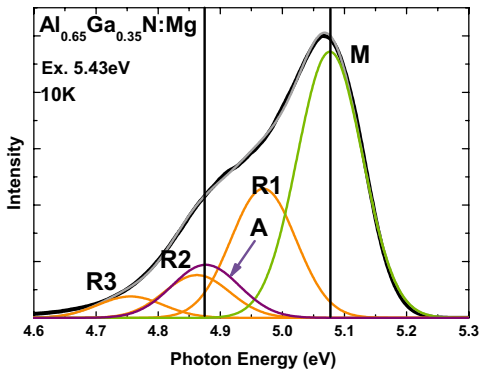

Fig. 3. PL spectrum of $Al_{0.65}Ga_{0.35}N$:Mg and fitting result of spectrum deconvolution.

[1] H. Imura, N. Kato, N. Okada, K. Balakrishnan, M. Iwaya, S. Kamiyama, H. Amano, I. Akasaki, T. Noro, T. Takagi and A. Bandoh, Phys. Stat. Sol. **4** (2007) 2502.

BL8B1

Characterization of Lithium in Minerals by an XAFS Method

T. Kurisaki[1], Y. Sakogawa[1], D. Tanaka[1] and H. Wakita[1, 2]

[1]*Department of Chemistry, Faculty of Science, Fukuoka University, Jonan-ku, Fukuoka 814-0180, Japan*

[2]*Advanced Materials Institute, Fukuoka University, Jonan-ku, Fukuoka 814-0180, Japan*

Lithium compounds are generally used in industrial and commercial applications such as lithium batteries, lithium glasses and other materials. Sometimes, the lithium is included in minerals, and was tried extract from the minerals. Therefore, it is very interesting to investigate the chemical condition of lithium in minerals. The XAFS method has not been widely used to estimate the electronic structure of lithium in minerals owing to the low energy (below about 70 eV) of Li K edge. However, there are a few reports about Li-K XANES spectra [1,2].

In this work, we applied the X-ray absorption near edge structure (XANES) spectroscopy to lithium in minerals. X-ray absorption spectra of near Li K absorption edges were (XAFS) measured at BL8B1 of the UVSOR in the Institute of Molecular Science, Okazaki [3]. The energy of the UVSOR storage ring was 750 MeV and the stored current was 110-230 mA. The absorption was monitored by the total electron yield using a photomultiplier. We employed the discrete variational (DV)-Xα molecular orbital (MO) method to perform calculated spectra, and compared observed spectra with calculated spectra.

The Li *K* XANES spectra of a lepidolite contained lithium and three reference lithium compounds are shown in Fig. 1. A remarkable change of the spectral patterns was observed for the three reference lithium compounds. But the peak was not observed to a spectrum of the lepidolite. This reason is because lithium ion content in the lepidolite is very small amount (1.5~3%). We are going to try to measured Al K edge XANES of the lepidolite and calculated spectra by DV-Xα molecular orbital calculations.

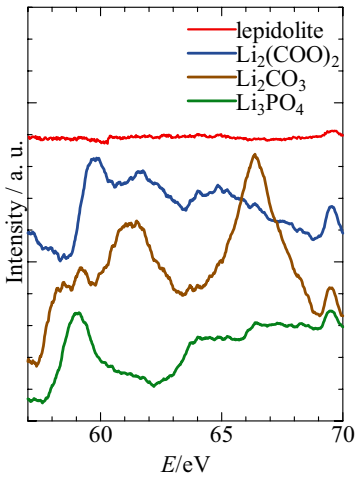

Fig. 1. Li K-edge XANES spectra of a lepidolite and reference lithium compounds.

[1] J. Tsuji, K. Kojima, S. Ikeda, H. Nakamatsu, T. Mukoyama and K. Taniguchi, J. Synchrotron Rad. **8** (2001) 554.

[2] T. Kurisaki, Y. Nakazono, S, Matsuo, R.C.C. Perera, J. H. Underwood and H. Wakita, Adv. Quantum Chem. **54** (2008) 315.

[3] S. Murata, T. Matsukawa, S. Naoè, T. Horigome, O. Matsudo and M. Watanabe, Rev. Sci. Instrum. **63** (1992) 1309.

BL1A

Modification of Gallium Oxide Photocatalyst with Mg Ions

K. Shimura[1], T. Yoshida[2] and H. Yoshida[1]

[1] *Department of Applied Chemistry, Graduate School of Engineering, Nagoya University, Nagoya 464-8603, Japan*

[2] *Department of Materials, Physics and Energy Engineering, Graduate School of Engineering, Nagoya University, Nagoya 464-8603, Japan*

The development of a hydrogen production method from renewable resources and natural energy would be important to realize a sustainable society. Photocatalytic steam reforming of methane (PSRM; $CH_4+2H_2O \rightarrow 4H_2+CO_2$) is an attractive reaction because it has a potential to produce hydrogen from water and biomethane by using solar energy. We reported that Pt-loaded semiconductor photocatalyst such as Pt/TiO_2 showed activity for this reaction around room temperature [1, 2]. In the present study, we applied the Ga_2O_3 photocatalyst for PSRM and examined the loading effect of Mg ions on the structure and the activity of Ga_2O_3.

Mg^{2+}-loaded Ga_2O_3 was prepared from β-Ga_2O_3 and an aqueous solution of $Mg(NO_3)_2$ by impregnation method, followed by calcination in air at various temperatures for 6 h. Then, Pt (0.01 wt%) co-catalyst was loaded on it by impregnation method followed by calcination in air at 773 K.

Photocatalytic reaction was carried out with a fixed- bed flow type reactor. The quartz cell was filled with the catalyst (0.8 g). The reaction gas (H_2O 1.5%, CH_4 50%, Ar balance) was introduced at a flow rate of 50 mL min^{-1}, and the light of the entire wavelength region from a 300 W Xe lamp was irradiated. The outlet gas was analyzed by on-line gas chromatography with a thermal conductivity detector.

X-ray absorption spectra were measured in the total electron yield mode at room temperature with a beryl double-crystal monochromator at the BL-1A station of UVSOR-II. The powder sample was put on the first dynode of the electron multiplier with carbon adhesive tape.

Pt/β-Ga_2O_3 promoted PSRM to produce H_2 and CO_2 and the high activity sustained for a long time (Fig. 1a). Further modification of Ga_2O_3 by Mg^{2+} through calcination at 1273 K enhanced the activity (Fig. 1b). However, characterization by XRD, UV-vis and N_2 adsorption exhibited no differences among these samples.

Mg K-edge XANES spectrum of MgO shows some peaks and Ga L_I-edge XANES of Ga_2O_3 was broad spectrum although both absorption edges are known to appear at 1307 eV (Fig. 2 a and f). The spectra of Mg^{2+}-loaded Ga_2O_3 samples calcined at various temperatures were much different from each other (Fig. 2 b-d). For the sample calcined at 773 K, the spectrum was similar to that of MgO. When the calcination temperature was higher than 1073 K, the spectra were the same as that of $MgGa_2O_4$ spinel. It was suggested that Mg ions would form $MgGa_2O_4$ spinel-like local structure by substituting for Ga ions at tetrahedral site when the calcination temperature was higher than 1073 K. The Mg ions in the bulk would improve the property of the Ga_2O_3 photocatalyst.

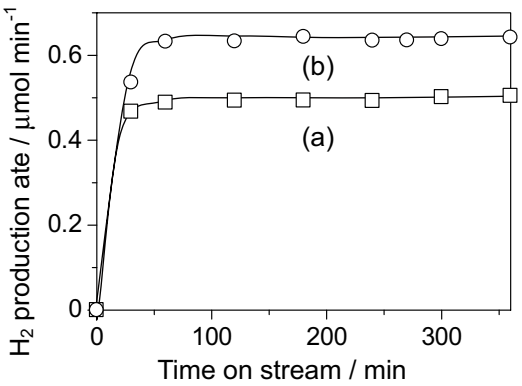

Fig. 1. Time course of the hydrogen production rate over (a) Pt/Ga_2O_3 and (b) Pt/Mg^{2+}-loaded Ga_2O_3 prepared at 1273 K.

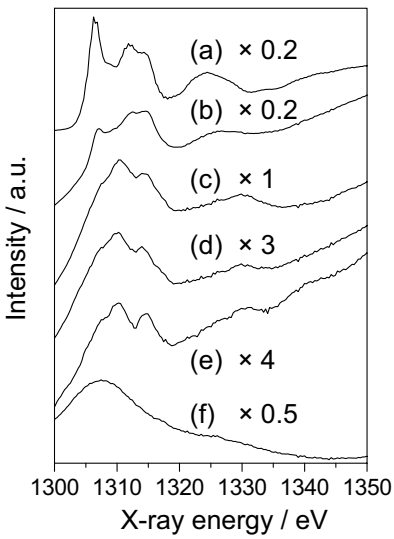

Fig. 2. X-ray absorption spectra of (a) MgO, (b)-(d) Mg^{2+}-loaded Ga_2O_3 samples, (e) $MgGa_2O_4$ and (f) Ga_2O_3. Loading amount was 2 mol%. The calcination temperature was (b) 773 K, (c) 1073 K and (d) 1273 K, respectively.

[1] H. Yoshida *et al.*, Chem. Lett. **36** (2007) 430.
[2] H.Yoshida *et al.*, J. Phys. Chem. C **112** (2008) 5542.

Asymmetric Synthesis and Decomposition of Amino Acids by Using UVSOR-FEL

K. Kobayashi[1], S. Shima[1], T. Suzuki[1], T. Kaneko[1], H. Mita[2], J. Takahashi[3], M. Hosaka[4], M. Adachi[5] and M. Kato[5]

[1]*Graduate School and Faculty of Engineering, Yokohama National University, Yokohama 240-8501, Japan*

[2]*Faculty of Engineering, Fukuoka Institute of Technology, Fukuoka 811-0295, Japan*

[3]*NTT Microsystem Integration Laboratory, Atsugi 243-0198, Japan*

[4]*Graduate School of Engineering, Nagoya University, Nagoya 464-8601, Japan*

[5] *UVSOR Facility, Institute for Molecular Science, Okazake 444-8585, Japan*

Introduction

Amino acids in terrestrial organisms are fundament- ally L-enantiomers. A number of hypotheses have been presented on the origin of such biochemical homochirality. One of them is that enantiomeric excesses (e. e.'s) of amino acids were generated by circularly polarized ultraviolet light (CPL-UV) ejected from a neutron star. In order to examine this hypothesis, we irradiated amino acids or metal complexes of amino acids with circularly polarized ultraviolet light (CPL-UV). Isovaline (Fig. 1 a), a non-proteinous amino acid without a-hydrogen atom, was selected as a target amino acid since relatively large e. e. of isovaline was found in Murchison meteorite [1]. A small e. e. formed by CPL-UV might have been enlarged by autocatalytic reactions in primordial ocean. From such a point of view, histidine (Fig. 1 b) was used because it has catalytic activity. Aqueous solution of histidine, isovaline, and metal complexes of them were irradiated with CPL-UV. We also studied possible introduction of chirality to amino acids in thin films by CPL-UV irradiation.

Experimental

The following aqueous solutions in quartz cuvettes were irradiated with CPL-UV light at 217 nm from a free electron laser (FEL) of UVSOR II: DL-Alanine, DL-histidine, Cu-complex of DL-histidine, DL-isovaline and Cu-complex of DL-isovaline. After irradiation, amino acids in the resulting solutions were analyzed by HPLC with chiral columns.

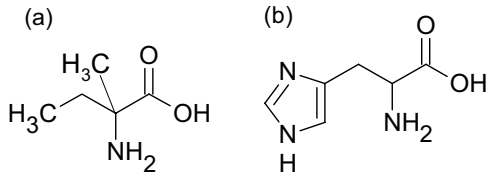

Fig. 1. Isovaline (a) and histidine (b)

Thin films of isovaline and alanine made by vacuum deposition, and they were irradiated with CPL-UV. CD spectra of the resulting thin films were observed.

Fig. 2. CPL-UV irradiation of amino acid solution.

Results and Discussion

Isovaline gave DL-alanine as major amino acid products after irradiation, but only a small part of histidine was decomposed under the present condition. No significant enantiomeric excesses of each amino acid were detected. We irradiated amino acids in neutral solution this time, which might be the reason why no e. e. was found. We are planning to irradiate acidic / basic solution of amino acids and their metal complexes with CPL-UV.

After the irradiation with the CPL on DL-alanine film, peaks appeared in the CD spectra at 180 nm (carboxyl group (π-π*)) and 215 nm and (carboxyl group (n-π*)) with an opposite sign. Intensity ratio of the two peaks and the intensity and the sign of the CD peaks changed with CPL dose. After the irradiation with the CPL on DL-isovaline film, vague peaks appeared in the CD spectra at 175 nm (carboxyl group (π-π*)) and 200 nm (carboxyl group (n-π*)) with an opposite sign. These results suggest that a chiral construction was introduced into the racemic film by the CPL.

[1] J. R. Cronin and S. Pizzarello, Science **275** (1997) 951.

Transient Fluorescence Spectroscopy of Dye Sensitized Solar Cells

K. Mitsuke[1], K. Nakajima[1, 2], H. Katayanagi[1],
M. Adachi[3], T. Tanikawa[3], N. Yamamoto[4], M. Hosaka[4] and M. Katoh[3]
[1]*Dept. Photo-Molec. Sci., Inst. Molec. Sci., Okazaki 444-8585, Japan*
[2]*Sci. Res. Center, Hosei Univ., Tokyo 102-8160, Japan*
[3]*UVSOR Facility, Inst. Molec. Sci., Okazaki 444-8585, Japan*
[4]*Grad. Sch. Engin., Nagoya Univ., Nagoya 464-8603, Japan*

The dye sensitized solar cell (DSSC) has attracted worldwide attention in the last two decades because of its high-solar-energy-to-electricity conversion efficiencies and relatively low cost of its manufacturing. In DSSC solar light is primarily absorbed by a sensitizer dye which is anchored to the surface of a wide band gap semiconductor. The efficiency of sensitization depends critically on the ratio between the rate of electron injection and that of charge recombination. Thus, intensive research has been carried out focusing on the analysis of the dynamics of interfacial electron transfer processes. In this study we assembled a DSSC using a Ru dye and irradiated them with free electron laser (FEL) to observe the kinetics of electron injection using time-resolved fluorescence spectroscopy.

Electron injection is known to occur in a time scale of 10 ps or faster, if TiO_2 film together with Ru dyes is covered in inert solvents. In contrast, the rate of injection is drastically reduced by one or two orders of magnitude in a typical redox active electrolyte. Several authors argued that the additives in the electrolyte used for reducing unwanted electron-hole recombination have an effect of raising the conduction band edge of TiO_2. Eventually the high-efficiency DSSCs often show lifetimes as long as 1 ns with respect to electron injection, that is, injection dynamics which is just fast enough to compete with the fluorescence decay (10 ~ 100 ns) of the excited state of the Ru dyes.

We fabricated the DSSC composed of a nanocrystalline mesoporous TiO_2 film, sensitizer dye ("N719" or "Black dye"), electrolyte (50 mM tri-iodide in acetonitrile, ionic liquid and 4-*tert*-butyl pyridine), and a Pt thin film. All these materials were sandwiched by two electrode plates of FTO glass. The formula of N719 is written as $RuL_2(NCS)_2$:2TBA (L = 2,2'-bipyridyl-4,4'-dicarboxylic acid; TBA = tetrabutylammonium). Here, dye molecules are firmly grafted onto the surface of the titania through their carboxylate substituents. The assembled DSSC exhibits a maximum energy conversion efficiency of ca. 6.5 %. Fluorescence decay was observed by time-resolved single photon counting using FEL of ~ 580 nm at a repetition rate of 11.3 MHz.

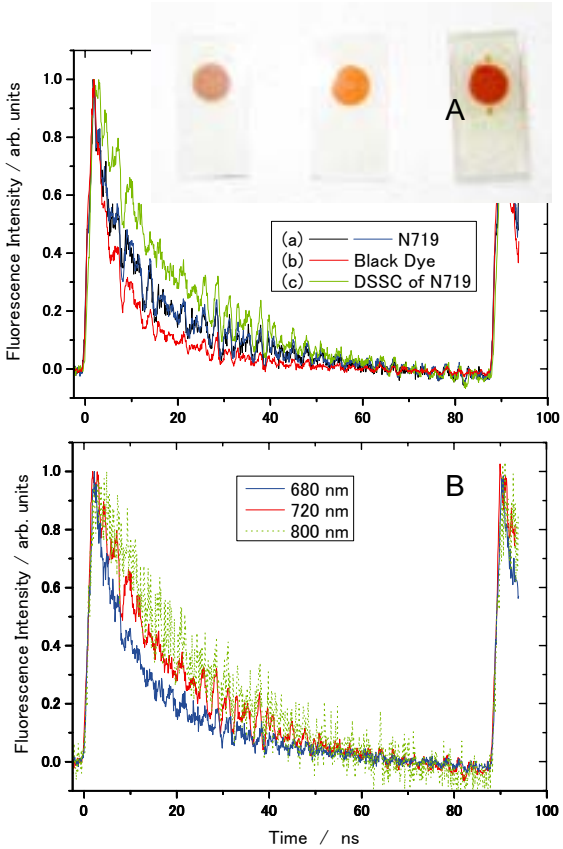

Fig. 1. Fluorescence decay curves of DSSC and photovoltaic electrodes, obtained by FEL photolysis.

Fluorescence decay curves in Fig. 1A were monitored at 720 nm for (a) a photovoltaic electrode of TiO_2 film prepared with N719, (b) that with Black dye, and (c) a complete DSSC fabricated using N719. The apparent fluorescence lifetime of the complete DSSC is longer than those of the two photovoltaic electrodes, probably due to slower electron injection induced by one of the additives in the electrolyte. Figure 1B shows the dependence of the decay curves of the DSSC on the fluorescence wavelength. The rate of electron injection appears to increase with decreasing wavelength. This suggests that the vibrational redistribution of the internal energy in the excited state of the dyes proceeds in competition with the electron injection and fluorescing emission.

This research was partly supported by a grant from Hosei University.

BL1A

Local Environment Analysis of Al Atoms in Proton-Conducting Amorphous $Al_{0.1}Si_{0.9}O_x$ Thin Films

Y. Aoki and H. Habazaki

Graduate School of Engineering, Hokkaido University, N13W8, Sapporo 060-8628, Japan

Zeolitic compounds are attractive as an unhydrated proton conductor due to the presence of large number of native acid sites. Although gas permeation through the micropore poses difficulty in fuel cell application, they exhibit excellent proton conductivity even in dry atmosphere at elevated temperatures. Previously, we reported that amorphous aluminosilicate thin films exhibit the enhanced proton conductivity in nonfumidified atmosphere in the intermediate temperature range [1]. Amorphous metal oxides have intrinsic advantages for their application to thin film electrolyte, since they tend to be non-granular, dense layer without void formation at grain boundary due to the covalently-bonded M-O-M-O network. Furthermore, we discovered that the films reveal the power-law increment of proton conductivity by reduction of thickness into the sub-100 nm regime [2]. This conductivity scaling behavior was not completely understood, but it is speculated to be involved in the acidic nature of films. Here, we study the local environment of Al atoms in amorphous $Al_{0.1}Si_{0.9}O_x$ thin film thin films by XANES in order to identify the acid site.

The $Al_{0.1}Si_{0.9}O_x$ film was prepared on an ITO substrate (Aldrich) by multiple spin-coating of precursor solutions of tetraethoxysilane (TEOS) (Kanto) and aluminum *sec*-butoxide ($Al(O^sBu)_3$) (Kanto) at the Al/Si atomic ratio of 5/95. The details of the procedure were described elsewhere. [1] The metal concentration (Al+Si) in the precursor mixture sol was adjusted in 30 mM for the film of < 100 nm-thickness and 100 mM for the film of > 100 nm-thickness. A film with thickness of 100 nm was prepared from both of these sols. The precursor sols were spin-coated onto the ITO substrate at 3000 rpm for 40 sec by a Mikasa 1H-D7 spin coater. The deposited gel layer was hydrolyzed by blowing hot air for 30 sec (Iuchi hot gun), and the substrate was cooled to room temperature by blowing cold air for 20 sec. These cycles of spin-coating, hydrolysis and cooling were repeated 10-20 times and the gel film thus obtained was calcined at 400°C for 15 min. The combination of deposition and calcination was repeated more than 3 times, and the final calcination was performed at 450°C for 1 h.

Al K-edge XANES spectroscopy was carried out with $Al_{0.1}Si_{0.9}O_x$ films of 50 nm, 120 nm and 300 nm-thickness (Fig. 1). It is reported that Al K-edge spectra is very sensitive to the coordination number and geometry of AlO_x moieties in oxides. [3] Here, the Y-zeolite (Wako) was used as a reference material of tetrahedral AlO_4 configuration and α-Al_2O_3 (Wako) as that of octahedral AlO_6 configuration, respectively. Y-zeolite shows a sharp peaks at 1566 eV and a broad peak at 1571 eV in agreement with the spectral features of tetrahedral AlO_4 compounds. α-Al_2O_3 shows two sharp peaks at 1568 and 1572 eV, which are identical to the features of the compound given by the previous reports. The $Al_{0.1}Si_{0.9}O_x$ films possess the same features of XANES in every thickness. They show a sharp peak at 1566 eV and a broad peak at 1571 eV, which are identical to that of Y-zeolite. Therefore, it is clear that Al atom in these films preferably takes the tetrahedral AlO_4 configuration. These results suggest that $Al_{0.1}Si_{0.9}O_x$ films have the zeolite-like aluminosilica network, where the SiO_4 tetrahedron and AlO_4 tetrahedron are 3-dimensionally linked by corner-sharing. Thus, our films can retain amounts of Brønsted acid site by the protonation onto the negative charge of -Si-O-Al- hetero bond as is the case with zeolite.

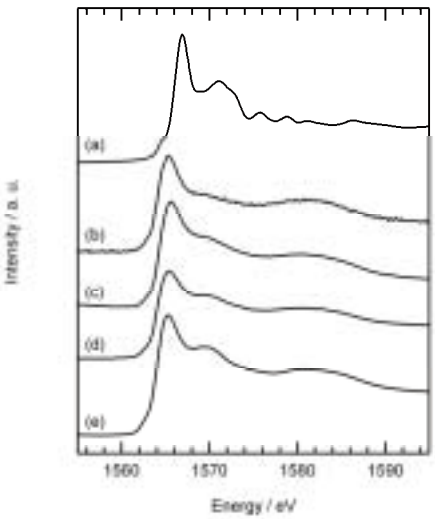

Fig. 1. Al K-edge XANES spectra of amorphous $Al_{0.1}Si_{0.9}O_x$ films and reference materials. (a)α-Al_2O_3 powder, (b) 300 nm-thick film, (c) 120 nm-thick film, (d) 50 nm-thick film and (e) Y-zeolite powder.

[1] Y. Aoki *et al*., Adv. Mater. **20** (2008) 4387.
[2] Y. Aoki *et al*., Electrochem. Solid state Lett. **11** (2008) 13.
[3] Y. Kato *et al*., PCCP **3** (2001) 1925.

BL1A

Mo L_{III}-Edge XANES Study on Redox Behavior of Supported Mo Species on H-MFI for Methane Dehydroaromatization Catalysts

H. Aritani[1], K. Nagashima[1], M. Morioka[1], H. Shibasaki[1] and A. Nakahira[2]

[1]*Faculty of Engineering, Saitama Institute of Technology, Fukaya 369-0293, Japan*

[2]*Graduate School of Engineering, Osaka Prefecture University, Sakai 599-8531, Japan*

MoO_3-modified H-MFI catalyst is typical for exhibiting quite high activity and selectivity for CH_4 dehydroaromatization in absence of oxygen. On the reaction, reduction of Mo species is brought about in contact with methane in initial step. The Mo ions react methane to form carbide and/or oxycarbide species in the next step. The carbide species is active for methane dehydroaromatization, however, deactivation is brought about by carbon deposition on the catalyst surface at the same time. Therefore, red-ox performance of active Mo ions (such as Mo^{2+} and others) is one of a key role for catalytic dehydroaromatization activity. In our previous study, pretreatment with CO and H_2 co-feed with CH_4 reactant give a significant effect for high activity. However, excess hydrogen may affect a reduction of Mo species during the reaction. Thus, the effect of hydrogen with methane is also very important to give an effect on Mo state on H-MFI. This study addresses the effects of CO pretreatment and H_2 co-feed with CH_4 reactant for Mo sites on H-MFI. Characterization by Mo L_{III}-edge XANES can be applied to evaluate the red-ox performances of Mo sites in detail.

Catalysts were prepared by impregnation of H-MFI (Si/Al_2=72) synthesized hydrothermally with $MoO_2(acac)_2$–$CHCl_3$ solution, and followed by drying overnight and calcination at 773 K. MoO_3-loading amount is 5.0 wt% in all the catalysts. Mo L_{III}-edge XANES spectra were collected in BL1A of UVSOR-IMS in a total-electron yield mode using InSb double crystal monochromator. Photon energy was calibrated by using Mo metal-foil at Mo L_{III}-edge, and normalized XANES spectra and their second derivatives were obtained. Catalytic activity was evaluated in a fixed bed flow reactor. Each catalyst (0.25 g) was placed in a quartz-tube reactor, and pretreated in He–CO(0-2%) flow (30 mL min^{-1}) at 973 K for 1 h. Then CH_4(20%)– H_2(0-3%)–He reactant gas was fed at 973 K (30 mL min^{-1}: SV = 7.2 L g^{-1} h^{-1}). Products were analyzed by online GC.

After pretreatment with CO (shown in Fig. 1(A)) at 973 K, small amount of reduced Mo is formed. After the reaction with CH_4 or CH_4-H_2 (Fig. 1(B)(C)), reduced Mo (Mo^{2+} in major) species because of the large intensity of minimum peaks (at 2522.5 eV) of 2nd derivatives of L_{III}-XANES spectra [1]. The reduced Mo species after the reaction is not similar to bare Mo_2C, suggesting the formation of carbonized MoC_x species [2]. In these cases, the catalysts are almost deactivated by contamination of hydrocarbon and/or carbon deposition. After the following treatment with H_2(2%)-He or He, the amount of deposited species decreased by species, whose results are evaluated by thermogravimetry. In addition, catalytic activity is restored by their treatments. On these cases (Fig. 1(D)(E)), the ratio of reduced (carbonized) Mo species becomes small. These results suggest that carbonized Mo species are formed on H-MFI after the CH4 dehydroaromatization, and excess carbon and/or hydrocarbon species are deposited on Mo sites as MoC_x species. By not only H_2 but also He treatments, excess carbonaceous species can be desorbed and restore the dehydroaromatization activity. It is concluded that deactivation can exhibit the gas treatment with no red-ox atmosphere because of enhancement of desorption of carbonaceous species.

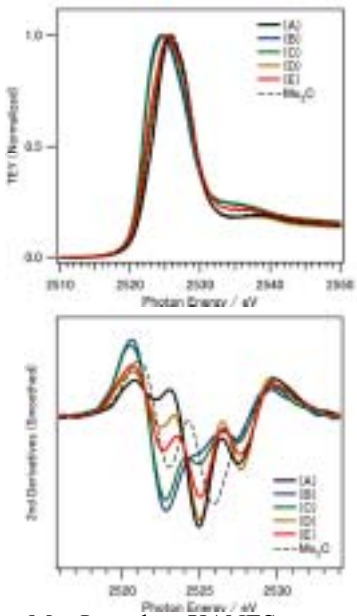

Fig. 1. Mo L_{III}-edge XANES spectra (top) and their second derivatives (bottom) of 5.0 wt% MoO_3-modified H-MFI (Si/Al_2=72) catalysts. (A) After CO(2%)-He pretreatment; (B) After reaction with CH_4(20%)-He on sample (A); (C) After H_2(2%)-He treatment on sample (B); (D) After reaction with CH_4(20%)-H_2(2%)-He on sample (C); (E) Reacted with CH_4(20%)-He on sample (A), and then He treated and followed by reaction with CH_4(20%)-H_2(2%)-He.

[1] H. Aritani *et al*., UVSOR Activity Report **35** (2008) 106.

[2] H. Aritani *et al*., J. Environm. Sci., in press.

BL1A

Characterization of Various Phosphate Compounds by an XAFS Method

T. Kurisaki[1], D. Tanaka[1], Y. Sakogawa[1] and H. Wakita[2]

[1] *Department of Chemistry, Faculty of Science, Fukuoka University, Jonan-ku, Fukuoka 814-0180, Japan*

[2] *Advanced Materials Institute, Fukuoka University, Jonan-ku, Fukuoka 814-0180, Japan*

A phosphate compound is a very important compound constituting DNA and ATP. In addition, these compounds have widely used such as production of the manure, a catalyst of the ethylene production, cement for dentistry, a metal surface treatment agent, the coagulant of the rubber milky liquid, and medicine. For various light element compounds, we have studied the electronic structure by X-ray absorption spectroscopy [1,2,3]. These results suggested that there is a correlation between XANES spectra and the local structures.

In this work, we applied the X-ray absorption near edge structure (XANES) spectroscopy to phosphate compounds. The results of the measurement indicate unoccupied and occupied electronic structure of phosphate compounds. The X-ray absorption spectra were measured at BL1A of the UVSOR in the Institute of Molecular Science, Okazaki [4]. The ring energy of the UVSOR storage ring was 750 MeV and the stored current was 110-230 mA. P K-edge absorption spectra were recorded in the regions of 2125-2270 eV by use of two InSb crystals. The absorption was monitored by the total electron yield using a photomultiplier. The samples were spread into the carbon tape on the first photodynode made of CuBe of the photomultiplier.

Figure 1 shows the observed P K-edge XANES spectra for the phosphate compounds. The P-K XANES spectra of hydroxyapatite, octacalcium phosphate, and standard phosphate compounds show different peak profiles. These phosphate compounds have different electronic state. We are going to try to calculate the spectra by DV-Xα molecular orbital calculations.

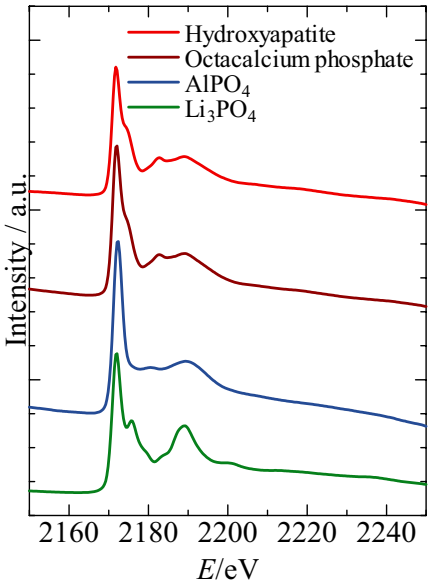

Fig. 1. Observed Al K-edge XANES spectra of phosphate compounds.

[1] H. Ichihashi, T. Kurisaki, T. Yamaguchi, T. Yokoyama and H. Wakita, Jpn. J. Appl. Phys. Part 1 **38(suppl.)** (1999) 101.

[2] S. Matsuo, K. Shirouzu, Y. Tateishi and H. Wakita, Adv. Quan. Chem. **42** (2002) 407.

[3] T. Kurisaki, Y. Nakazono, S, Matsuo, R.C.C. Perera, J. H. Underwood and H. Wakita, Adv. Quantum Chem. **54** (2008) 315.

[4] S. Murata, T. Matsukawa, S. Naoè, T. Horigome, O. Matsudo and M. Watatabe, Rev. Sci. Instrum. **63** (1992) 1309.

BL1A

Defect Formation Mechanism in $Ce_{1-x}Y_xO_{2-x/2}$

Y. Nakade and T. Yamamoto
Faculty of Science and Engineering, Waseda University, Shinjuku 169-8555, Japan

$Ce_{1-x}Y_xO_{2-x/2}$ is known as a solid oxide electrolyte of fuel cell, which shows high oxygen ion conductivity. In order to know the reasons for this high conductivity, it is essential to know the defect formation mechanism in $Ce_{1-x}Y_xO_{2-x/2}$. In the present study, the local environment of Y^{3+} ions in CeO_2 was examined by the Helmholtz free energies and XANES.

$Ce_{1-x}Y_xO_{2-x/2}$ was synthesized by CeO_2 and Y_2O_3 powders with the solid state reaction method. XANES measurements were carried out at BL-1A of UVSOR with double-crystal monochromator using InSb (111) (2d = 7.481Å) in the total electron yield method.

Four types of defect models were built by changing the positions of two Y ions and O vacancy according to the reaction [$2Ce^{4+} \leftrightarrow 2Y^{3+}+V_O$], which are shown in Fig. 1. In Y-O-Y and Y-Y models, two nearest neighboring Ce^{4+} are replaced by two Y^{3+} ions and an oxygen ion is removed between these two substituted Y^{3+} ions (Y-O-Y model) and at distant position from these Y^{3+} ions (Y-Y model). In Distant and Y-O models two distant Ce^{4+} ions are replaced by Y^{3+} ions and an oxygen ion is removed at the first nearest neighboring site from one of the substituted Y^{3+} ions (Y-O model), and at a distant site from both of the substituted Y^{3+} ions (Distant model).

We calculated Helmholtz free energies by the first principles PAW method in order to compare the relative defect formation energy among these models. Helmholtz free energy, F=U−TS, is obtained, where U is treated as a total electronic energy at 0K, S was calculated by $S=k_B \ln W$, in which W is atomic configurations in the system, and k_B and T are Boltzmann constant and temperature. Resultant F are -833.54, -833.50, -833.40 and -833.24 eV per supercell for Distant, Y-O, Y-Y, and Y-O-Y models, respectively, at 1773K, which is a present synthesized temperature. This result suggests two Y^{3+} ions and an oxygen vacancy are located apart as in Distant model.

We also performed XANES analysis. The first principles calculations for these four models within the density functional theory (DFT) were performed for the theoretical estimation of the XANES spectra with the all-electron linearized augmented plane wave package, WIEN2k [1]. Figure 2 shows the comparison between observed and four calculated XANES spectra of Y L_{III}-edge of $Ce_{1-x}Y_xO_{2-x/2}$. As shown in this figure Distant and Y-Y models, where the coordination number of two Y^{3+} ions is 6, show better comparisons than the others [2]. This result supports the above result by calculated Helmholtz free energy.

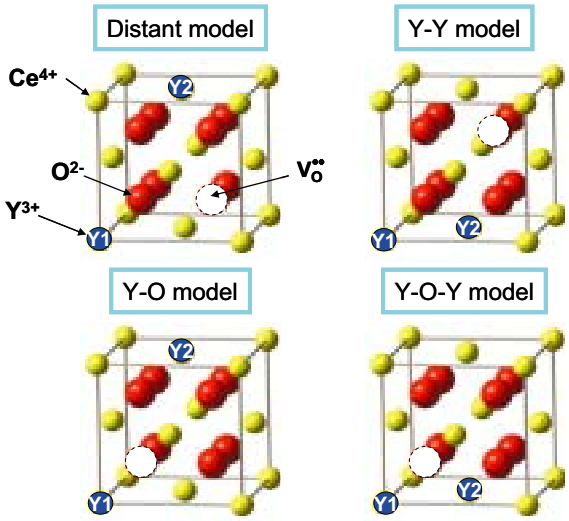

Fig. 1. Calculated models for $Ce_{1-x}Y_xO_{2-x/2}$.

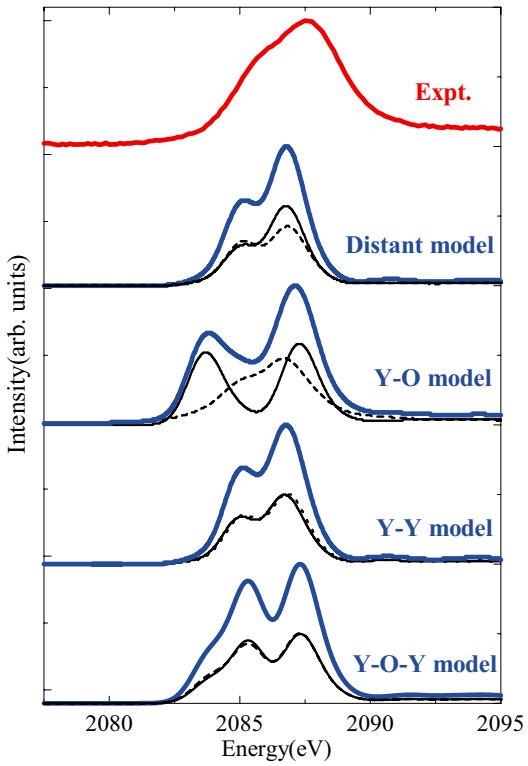

Fig. 2. Comparison between observed and calculated XANES spectra of Y L_{III}-edge of $Ce_{1-x}Y_xO_{2-x/2}$.

[1] P. Blaha *et al.*, http://www.wien2k.at
[2] T. Yamamoto *et al.*, J. Phys.:Condens. Matter, in press.

BL1A

Mg Local Structure in Ca,Mg Doped ZrO_2 for Artifical Joints with Good Biocompativility

A. Nakahira, T. Monden T. Kubo and T.Onoki

Faculty of Engineering, Osaka Prefecture University, Gakuencho, Sakai 599-8531, Japan

Introduction

Because ZrO_2 is one of high performance bioceramics with good properties, it is used as a biomaterial like knee and hip joints [1]. Many papers have investigated for Y_2O_3 or CeO_2 doped ZrO_2 due to their excellent mechanical properties. Y_2O_3 doped ZrO_2 and CeO_2 doped ZrO_2 have the good mechnical properties, such as high fracture toughness, high fracture strength, good wear resistance, high hardness, and good fatigue resistance etc.

Recently, the addition of Y and Ce into ZrO_2 raises question about the point of biological safety, although Y_2O_3 doped ZrO_2 and CeO_2 doped ZrO_2 have excelent mechanical properties. Therefore, the development of another element doped ZrO_2 are desired. For example, in this sutdy, CaO and MgO which are considered to be more biocompatible material, compared to Y_2O_3 and CeO_2, were selected as stabilizers for ZrO_2 based biomaterial. Moreover, in order to improve the mechanical properties of ZrO_2, we attempted to fabricate co-dope CaO and MgO to ZrO_2 by the spark plasma sintering (SPS) method in this sutdy. At UVsor station, we measured XANES of CaO,MgO-ZrO_2 prepared by the spark plasma sintering (SPS) method. The main purpose is to investigage the relationsip between mecahnical properties, microstructures and Mg local structure.

Experiments

Commercial CaO, MgO, and ZrO_2 powder were prepared as starting materials. Mixture of powder was mixed with wet ball-milling method. The mixed powders for CaO,MgO-ZrO_2 powders were sintered at 1300˚C by the spark plasma sintering (SPS) method.

Obtained samples were identified by XRD and SEM observation. Mg K-edge XANES spectra were obtained in a total electron yield mode at room temperature using KTP double–crystal monochrometer at BL01A station of the UVSOR. The spectra were collected in the photon energy range from 1300 to 1330 eV atintervals of 0.05 eV with a dwell time of 1 s.

Results

10Ca-10Mg-ZrO_2 had high hardness but the low fracture toughness with coarse microstructures. Figure 1 shows the results of Mg K-edge XANES of CaO,MgO-ZrO_2 prepared by the spark plasma sintering (SPS) method: a)3Ca and 3Mg, b)5Ca and 5Mg, c)10Ca and 10Mg doped, respectively. As the spectrum of the samples was obiously different between a), b) and c), there is some difference of chemical bonding of Mg between three CaO,MgO-ZrO_2 samples. Therefore, it is estimated that the microstructures are dependent on amount of dopant (Mg and Ca). These results of XANES spectra suggested that the Mg local structures influence mechanichal properties and microstructures for CaO,MgO-ZrO_2.

[1] J. M. Brown, B. Cales, J. Chevalier and G. Fantozzi, Journal of Biomedical Materials research **34** (1997) 149.

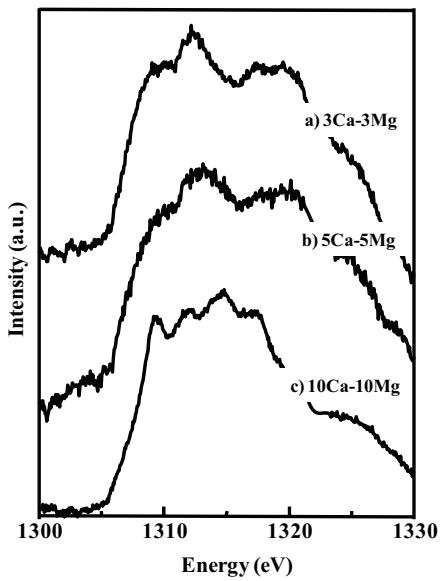

Fig. 1. Mg K-edge XANES spectra of ZrO_2 prepared by SPS method.

BL1A

Cation Disorder in Quenched $MgFe_2O_4$ Spinel

T. Nakashima and T. Yamamoto
Faculty of Science and Engineering, Waseda University, Shinjuku 169-8555, Japan

Magnetic properties of spinel-type oxides containing transition metal ions depend on the local environment of magnetic ions, especially the cation distribution in octahedral and tetrahedral sites [1, 2]. For the detailed understanding of the magnetic properties of these materials, it is crucial to know the cation distribution on an atomic scale. X-ray absorption near-edge structure (XANES) spectra have been widely used for the characterization of the electronic structures since it is sensitive to change in their local environment such as coordination number. In this study, the quenched $MgFe_2O_4$ spinels were investigated by utilizing Vibrating Sample Magnetometer (VSM) and XANES.

$MgFe_2O_4$ samples are synthesized by the conventional solid-state reaction method. The samples were annealed for 2 hours at intervals of 100 K from 973 K to 1273 K and then dropped in H_2O. Mg-K XANES spectra were observed at BL1A in UVSOR by the total electron yield (TEY) method. The incident beam was monochromatized with a beryl ($10\bar{1}0$) (2d = 15.965 Å) double crystal monochromator.

Prior to the VSM and XANES analysis, all the samples were characterized by the X-ray diffraction (XRD), in which no extra peaks can be found except for those of the spinel structured $MgFe_2O_4$.

The magnetic properties of the prepared samples were examined by VSM. The saturated magnetization increases incrementally with annealing temperature as shown in Fig. 1. It is considered that this variation of magnetic properties with annealing temperature reflects the change of the degree of cation disorder.

Observed Mg-K XANES spectra of the quenched $MgFe_2O_4$ spinels are shown in Fig. 2. The relative intensity of peak C decreases incrementally with annealing temperature up to 1273 K. This phenomenon suggests that the change in XANES spectra reflect the degree of cation disorder. Observed Mg-K XANES is the sum of those from Mg^{2+} ions at octahedral and tetrahedral sites. This change in the intensity of peak C should originate from the change in the ratio of the Mg^{2+} sites between octahedral and tetrahedral sites. From these experimental results we could conclude that Mg-K edge XANES spectra for the quenched $MgFe_2O_4$ spinels reflect magnetic properties. Thus, this combination of the VSM and XANES analysis with the assistance of XRD must be powerful tool to investigate the cation disordering in the spinel structured materials.

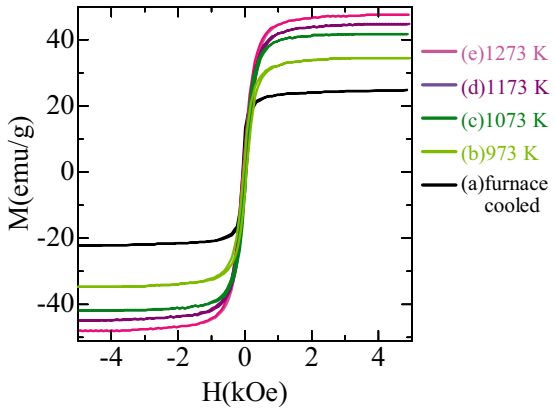

Fig. 1. Observed magnetization versus magnetic field curve of (a)furnace cooled $MgFe_2O_4$ and the samples quenched at (b)973 K, (c)1073 K, (d)1173 K and (e)1273 K.

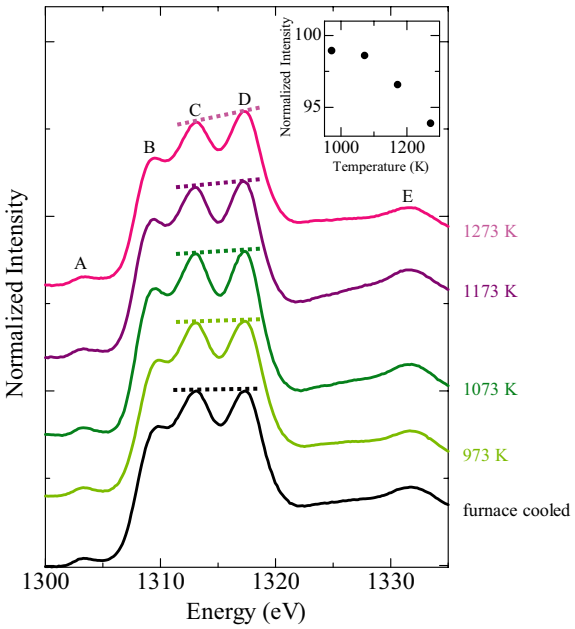

Fig. 2. Observed XANES spectra at Mg K-edge for $MgFe_2O_4$ spinels. Inset shows the relative intensity of peak C to that of furnace cooled one as a function of quenched temperature.

[1] S. Nakashima *et al.*, J. Magn. Magn. Mater. **310** (2007) 2543.
[2] H. St. C. O'Neil, Eur. J. Mineral. **4** (1992) 571.

BL1A & 8B1

XAFS Study on the Surface Structures of the Positive Electrodes for High Power-Type Lithium-Ion Battery Cells

M. Shikano[1], H. Nitani[1] and Y. Saito[2]

[1]*Research Institute for Ubiquitous Energy Devices, AIST, Ikeda, Osaka 563-8577, Japan*

[2]*Energy Technology Research Institute, AIST, Tsukuba, Ibaraki 305-8568, Japan*

Introduction

Lithium-ion battery is a key component of hybrid electric vehicle (HEV), plug-in HEV and electric vehicle (EV). For these applications, high specific power, long calendar life and safety are very important requirements. In our previous work, degradation mechanism of lithium-ion battery has been studied by various analyzing techniques and we concluded that the major factor of power fade was degradation of positive electrode surface [1-4]. However, the mechanism of degradation of the positive electrodes is still poorly understood. Detailed analysis on the structural changes of electrode material is essential in order to determine the origin of the degradation of battery performance.

In this study, we performed X-ray absorption fine structure (XAFS) analysis of $LiNi_{0.80}Co_{0.15}Al_{0.05}O_2$ positive electrodes in order to obtain information on their surfaces. The relationship between power fade and the surface structure of the positive electrode was studied.

Experimental

18650-type cylindrical lithium-ion cells with a capacity of 370 mAh were manufactured. Mixture of $LiCo_{0.15}Ni_{0.80}Al_{0.05}O_2$, acetylene black and poly vinylidene fluoride (PVDF) was used as positive electrode. The negative electrode was composed of hard carbon and PVDF. A 1 mol dm^{-3} of $LiPF_6$ in ethylene carbonate and dimethyl carbonate (DMC) in the 1:2 volume ratio was used as electrolyte. The state of charge (SOC) of assembled cell was adjusted to 0% or 100%. Then the cells were disassembled in order to obtain electrode materials. The obtained positive electrodes were washed by DMC and then dried under vacuum. We also prepared 'fresh' electrode by disassembling the cell before charging.

XAFS spectra of these positive electrodes were measured at UVSOR BL1A for P *K*-edge, Al *K*-edge, Ni *L*-edge and Co *L*-edge, and BL8B1 for O *K*-edge, F *K*-edge and Li *K*-edge. All measurements were performed with Total Electron Yield (TEY) technique at room temperature. Obtained XAFS spectra data were processed with Athena 0.8.057 software.

Results

Obtained P *K*-edge XANES spectra of the positive electrodes are shown in Fig. 1 with that of reference materials, $LiPF_6$, Li_3PO_4, $LiFePO_4$ and $NH_4H_2PO_4$. The spectrum of fresh electrode clearly indicated double peak feature at 2172.5 and 2177.5 eV. Though the SOC of electrode was changed, this double peak feature maintained and intensity of 1st and 2nd peak were almost same as fresh electrode. The peak position of 1st peak was close to $NH_4H_2PO_4$. And none of reference materials showed any peaks at 2nd peak position. Essentially, positive electrode material does not contain any P species. So, existence of P in positive electrode means adsorption of P species from electrolyte. However, electrolyte involves only $LiPF_6$ which was not observed in XANES measurements. From these results, we concluded that the adsorbed $LiPF_6$ reacted at the surface of positive electrode and changed into other chemical species. The more detailed structural analysis will be studied.

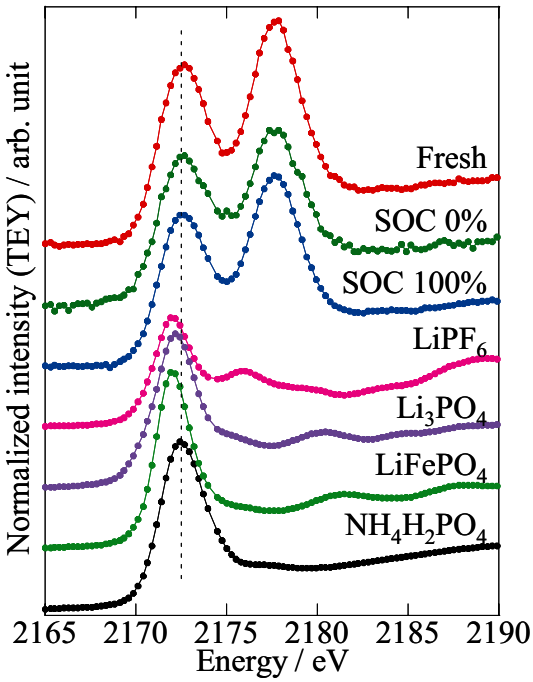

Fig. 1. P *K*-edge XANES spectra of positive electrodes and some reference materials. All spectra were normalized by Athena software.

[1] H. Kobayashi, M. Shikano, S. Koike, H. Sakaebe and K. Tatsumi, J. Power Sources **174** (2007) 380.

[2] M. Shikano, H. Kobayashi, S. Koike, H. Sakaebe, E. Ikenaga, K. Kobayashi and K. Tatsumi, J. Power Sources **174** (2007) 795.

[3] M. Rahman and Y. Saito, J. Power Sources **174** (2007) 889.

[4] Y. Saito and M. Rahman, J. Power Sources **174** (2007) 877.

BL1B

Luminescent Properties of $BaCl_2$ under VUV Excitation

M. Koshimizu, K. Onodera and K. Asai

Department of Applied Chemistry, Graduate School of Engineering, Tohoku University, Sendai, 980-8579, Japan

In recent years, the demand for fast scintillating materials has increased for applying in radiation detectors with an excellent timing property and the ability to operate at a high counting rate. BaCl2 is one of the promising candidates for such fast scintillating materials. In 1990, a fast scintillation component with a relatively high efficiency was reported for BaCl2 powder under X-ray irradiation [1]. Our recent research on the scintillation properties of a $BaCl_2$ single crystal revealed that this crystal includes a fast scintillation component of approximately 1.5 ns, and the timing property of $BaCl_2$ is comparable to that of a conventional fast scintillating material such as BaF_2 [2]. According to our previous study, the scintillation of $BaCl_2$ ranged over wavelengths region of 250–500 nm, and its spectra exhibited two distinct peaks at approximately 300 and 400 nm. In addition, it was revealed that the scintillation time profile comprised two lifetime components in the nanosecond regime, i.e., a 1.5-ns component and another of the order of tens of nanoseconds. However, the origin of the scintillation in $BaCl_2$ has not been revealed yet, and understanding the origin of scintillation is necessary in order to improve the scintillation properties of $BaCl_2$. In particular, it may be anticipated that the 1.5-ns component is ascribed to Auger-free luminescence because of its short lifetime and the scintillation wavelength in the UV region [2]. In this study, we present the luminescent properties of $BaCl_2$ under synchrotron VUV excitation, and discuss the origin of the emission.

A single crystal of $BaCl_2$ was grown by the Bridgman method. The emission and excitation spectra of $BaCl_2$ were measured at room temperature under the irradiation of synchrotron radiation having energies of 4–32 eV at the UVSOR facility (BL-1B).

Figure 1 shows the emission spectra of $BaCl_2$ under VUV excitation. Under 162-nm photon excitation, an emission band at 410 nm and a shoulder at 350 nm were observed. In contrast, an emission near 310 nm was observed under 176-nm photon excitation.

Figure 2 shows the excitation spectra for the emission bands at 410 nm and 310 nm. The 410-nm emission was observed over the broad excitation wavelength region including the sub-bandgap energy, suggesting that this band is caused by defects or impurities. The 160-nm sharp band of the excitation spectrum corresponds to the interband excitation. The excitation peak at 70 nm corresponds to twice the band-gap energy, suggesting that two electron-hole (e-h) pairs were created by one photon due to the impact ionization of the initially-excited e-h pair. The 310-nm emission was observed only for the near band-edge excitation, possibly corresponding to exciton absorption. This emission is considered to be an intrinsic one because this band was not observed under sub-bandgap excitation. Considering its large Stokes shift, this band is likely caused by impurities, defects, or self-trapped excitons. Thus, two emission bands are not ascribed to the Auger-free luminescence.

[1] S.E. Derenzo *et al.*, Conference Record of the 1991 IEEE, **1** (1991) 143.
[2] M. Koshimizu *et al.*, submitted to J. Appl. Phys.

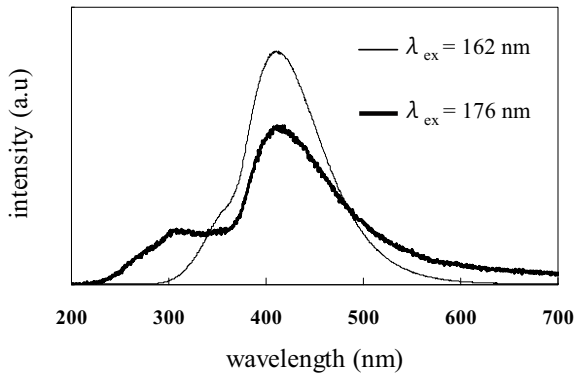

Fig. 1. Emission spectra of $BaCl_2$ under VUV excitation.

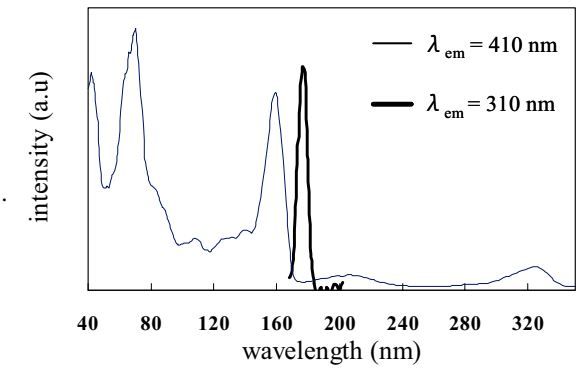

Fig. 2. Excitation spectra of $BaCl_2$ under VUV excitation.

BL1B

Luminescence Properties of $GdBO_3:Pr^{3+}$, Eu^{3+}

N. Ohno and K. Kohmoto

Division of Electronics and Applied Physics, Graduate School of Engineering, Osaka Electro-Communication University, Neyagawa, Osaka 572-8530, Japan

Recently, the phosphors to convert vacuum ultraviolet (VUV) light into visible light, which are used in mercury-free fluorescent lamps and plasma display panels, have been researched extensively. The materials with higher quantum efficiency for VUV light emitted from Xe dimers (173 nm) or monomers (147 nm) are quite needed.

Most borate hosts are transparent up to 140-180 nm, so that the VUV light can directly excite impurity activator in these hosts [1,2]. The strong absorption due to the impurity ions would give efficient conversion of the VUV light.

In the present study, luminescence properties of trivalent rare earth metal ion center in gadolinium borate have been studied in the UV and VUV region. The $GdBO_3:Pr^{3+},Eu^{3+}$ ($GdBO_3:Eu^{3+}$) phosphors were prepared by amounts of the appropriate starting compound powders of $GdBO_3$ adding and mixing Pr_2O_3 and Eu_2O_3 (1 mol %), and then firing in an alumina crucible at 1100℃ in the air atmosphere [3]. The impurity Pr^{3+} and Eu^{3+} ions would be substituted for Gd^{3+} ions in the host lattices.

Figure 1 shows the luminescence (red curve) and the photo-excitation (blue curve) spectra of $GdBO_3:Pr^{3+},Eu^{3+}$ measured at room temperature. Luminescence peaks located at around 600 nm are observed for the excitation of UV and VUV light. These luminescence peaks are attributed to the *f-f* transition from $^5D_0$ state to ^7F_J states in Eu^{3+} ion. It should be noted that no luminescence peaks due to Pr^{3+} ions were observed in this phosphor. The luminescence spectrum is almost the same as that of $GdBO_3:Eu^{3+}$ phosphor [4].

The luminescence due to Eu^{3+} ions is excited with lights of 275 nm, ~230 nm and 175 nm (blue curve in Fig.1). These excitation peaks are located at longer wavelength than the absorption edge of the host $GdBO_3$ (around 150 nm). The excitation band at around 225 nm is attributed to the Eu^{3+}– O^{2-} charge transfer transition in Eu^{3+} ion [4]. The excitation line at 275 nm was also observed in $GdBO_3:Eu^{3+}$, attributed to the transition from ^8S to ^6I state in Gd^{3+} ion. This indicates that the energy transfer from Gd^{3+} to Eu^{3+} ions occurs in $GdBO_3:Eu^{3+}$ and $GdBO_3:Pr^{3+}$, Eu^{3+}.

The excitation band at 175 nm would be ascribed to the *f-d* transition in Pr^{3+} ions since the structure is hardly observed in the excitation spectrum for the phosphor without Pr^{3+} ions, *i.e.* $GdBO_3:Eu^{3+}$. These results clearly show that the VUV light absorption in Pr^{3+} ions gives the red luminescence due to Eu^{3+} ions. It is concluded that the energy transfer from Pr^{3+} ions to Eu^{3+} ions through Gd^{3+} sublattices effectively occurs in $GdBO_3:Pr^{3+},Eu^{3+}$ as in the case of $NaGdF_4:Pr^{3+},Eu^{3+}$ phosphor [5].

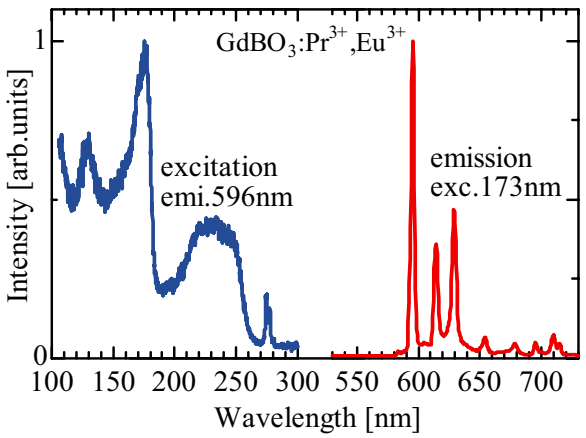

Fig. 1. Luminescence (red curve) and photo-excitation (blue curve) spectra of $GdBO_3:Pr^{3+},Eu^{3+}$ at room temperature.

[1] H. Lin, H. Liang, B. Han, J. Zhong, Q. Su, P. Dorenbos, M.D. Birowosuto, G. Zhang, Y. Fu and W. Wu, Phys. Rev. B **76** (2007) 035117.

[2] N. Ohno and K. Kohmoto, UVSOR Activity Report **35** (2008) 82.

[3] X.C. Jiang, C.H. Yan, L.D. Sun, Z.G. Wei, C.S. Liao, J. Solid State Chem. **175** (2003) 245.

[4] T. Kim and S. Kang, Mater. Res. Bull. **40** (2005) 1945.

[5] T. Hirai and N. Ohno, UVSOR Activity Report **28** (2001) 116.

BL1B

Optical Spectroscopy of YAG Ceramics Doped with Rare-Earth Ions

M. Yamaga, Y. Oda and N. Kashiwagura

Department of Mathematical and Design Engineering, Gifu University, Gifu 501-1193, Japan

Recently, ceramic lasers have been attractive since 1995 because ceramics can be produced in large volumes, made into composite media with complicated structures, and heavily and homogeneously doped with laser-active ions. Ceramic lasers with high power density and high resistance to laser damage are very useful for energy conversion system from inexhaustible solar energy to other optical energy. Absorption spectra of Cr^{3+} ions in ionic crystals, for example, $Y_3Al_5O_{12}$ (YAG) crystals cover the visible range (400-700 nm). YAG ceramics codoped with Nd^{3+} and Cr^{3+} ions are renewed as a laser medium with excitation of solar energy because of highly efficient energy transfer from Cr^{3+} to Nd^{3+} ions.

YAG ceramics codoped with 1at. % Nd^{3+} and 0.1 at. % Cr^{3+} were sintered by Konoshima Chemical Company. Optical absorption, fluorescence and excitation spectra were measured in the temperature range of 10-300 K.

Figure 1 shows the temperature dependence of optical absorption spectra in Nd: YAG and Nd: Cr YAG ceramics. Fairly broad bands below 240 nm are composed of band-to-band absorption and broad absorption due to the 4f-5d transitions of Nd^{3+} because the band-edge in pure YAG crystals is located around 180 nm. The sharp lines around 355 and 590 nm are due to the 4f-4f transitions of Nd^{3+}, while the broad band around 450 nm is due to the 3d-3d transition of Cr^{3+}.

Excitation below 240 nm in Nd:YAG ceramics produces several sharp lines of fluorescence in the visible (400-630 nm) and near-IR ranges, as shown in Fig. 2, being due to the transitions from $^2F_{5/2}$ and $^4F_{3/2}$ to other multiplets of Nd^{3+}, respectively. The near-UV and visible excitations produce only the near-IR fluorescence lines of Nd^{3+}. On the other hand, the excitation in Nd: Cr: YAG ceramics produces red fluorescence lines around 700 nm other than Nd^{3+}-lines. These lines are due to the $^2E \rightarrow {}^4A_2$ transition of Cr^{3+}.

Figure 3 shows the excitation spectra in Nd: YAG and Nd: Cr: YAG ceramics. The broad excitation bands of the visible Nd-fluorescence lines in Nd: YAG ceramics are due to the 4f-5d transition of Nd^{3+}. Similar excitation spectrum of the 400-nm Nd-fluorescence lines with five resolved bands were observed in Nd: Cr: YAG ceramics. The excitation spectrum of 707-nm Cr-fluorescence line is different from those of Nd-lines. The peaks of the Cr-bands are coincident with the bottoms of Nd-bands. This fact suggests that energy transfer occurs from Cr to Nd in Nd: Cr: YAG ceramics.

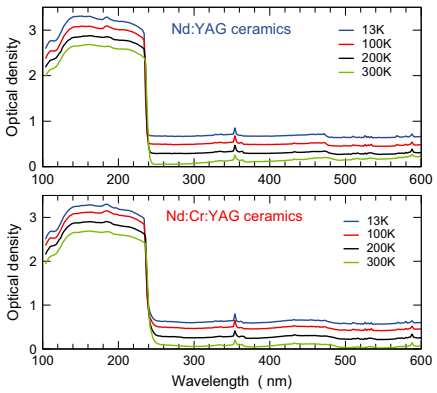

Fig. 1. Temperature dependence of absorption spectra for Nd:YAG and Nd:Cr:YAG ceramics.

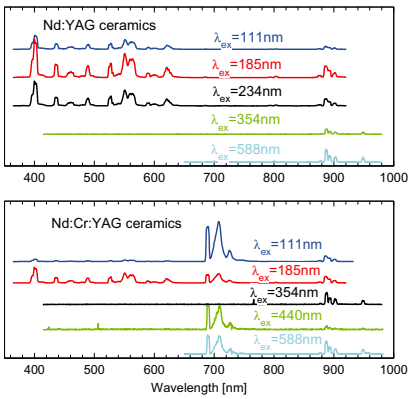

Fig. 2. Fluorescence spectra with various excitation wavelengths in Nd: YAG and Nd: Cr: YAG ceramics.

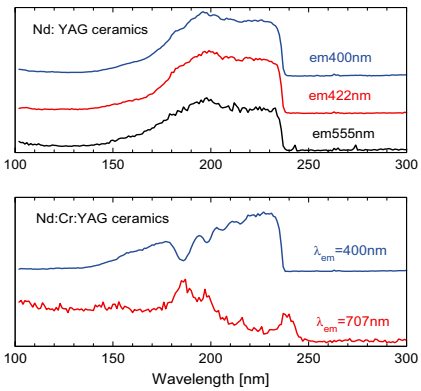

Fig. 3. Excitation spectra of Nd and Cr fluorescence in Nd: YAG and Nd: Cr: YAG ceramics.

BL1B

Excitation and Emission Spectra for Ce^{3+} in SrY_2O_4

M. Yoshino[1], S. Watanabe[2] and Y. Ichikawa[1]

[1] *Department of Materials, Physics and Energy Engineering, Nagoya University, Nagoya 464-8603, Japan*

[2] *Department of Chemistry, Kwansei Gakuin University, Sanda 669-1337, Japan*

The trivalent lanthanide ions (e.g. Nd^{3+}, Er^{3+}, Yb^{3+}) in Oxide crystals have drawn attentions due to their application for luminescent materials in NIR to UV regions such as solid-state lasers or phosphors. And, Ce^{3+} has also attracted attentions as luminescence centers. In this work, the 4*f*-5*d* excitation spectra and emission spectra for Ce^{3+} in SrY_2O_4 crystal have been measured. For the comparison, the excitation spectra and emission spectra for host oxide, SrY_2O_4 have been also measured. The Ce doped and pure SrY_2O_4 samples are produced by solid state reactions in 1373 K. The concentration of Ce^{3+} in the sample is 3 mol%. Figure 1 shows the emission spectrum for host oxide, SrY_2O_4. The broad peaks from interband optical transition exist around 300-600 nm. Then the excitation spectrum monitored 423 nm is shown in Fig. 2. The peak near 200 nm relates the absorption from the optical transition around the band edge in SrY_2O_4. The emission spectra for Ce^{3+} in SrY_2O_4 are shown in Fig. 3. In case of the excitation wavelength is 200 nm so as to excite the host, the broad peak appears below the peak relates to the emission of SrY_2O_4. The excitation spectrum monitored this emission (540 nm) is shown in Fig. 4. The broad peak appears below the peak relates to the absorption of SrY_2O_4 host. In case of the excitation wavelength is set in 320 nm so as to excite with the absorption band lies below the band edge absorption, only the broad peak around 600 nm appears as shown in Fig. 3. These emission and absorption peaks lie below the spectra relate to the host, are due to the Ce^{3+} 4*f*-5*d* transition.

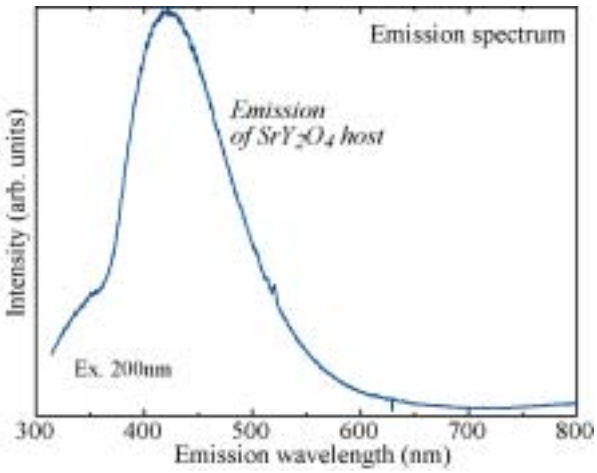

Fig. 1. Emission spectrum for SrY_2O_4.

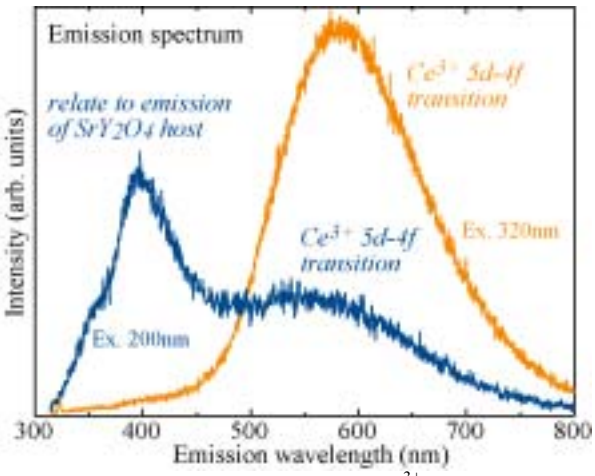

Fig. 3. Emission spectra for Ce^{3+} in SrY_2O_4.

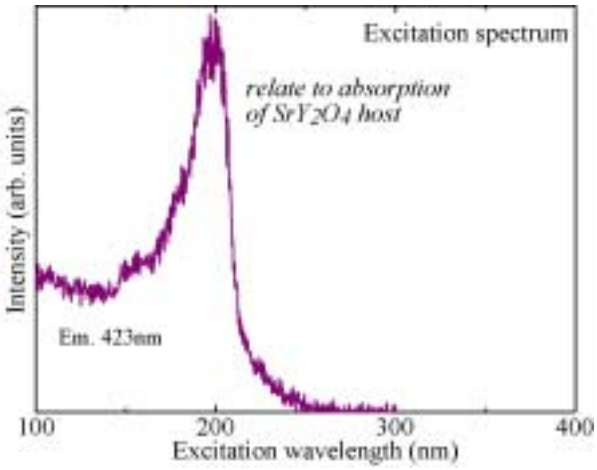

Fig. 2. Excitation spectrum for SrY_2O_4.

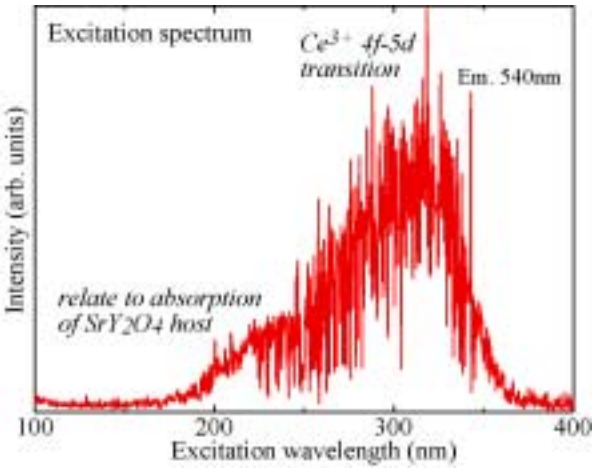

Fig. 4. Excitation spectrum for Ce^{3+} in SrY_2O_4.

BL4B & 8B1

Charging Behavior of Li_2MnO_3-Based Cathode Materials for Lithium-Ion Secondary Batteries from Metal L-Edge and Oxygen K-Edge Spectroscopy

Y. Arachi, M. Nakamura, K. Hinoshita and Y. Higuchi
Faculty of Engineering, Kansai University, Osaka 564-8680, Japan

New potential cathode materials to replace $LiCoO_2$ in Li-ion batteries are under extensive investigation. $LiNi_{0.5}Mn_{0.5}O_2$ has been proposed as a promising cathode material with attractive properties. Cells using this material exhibit a reversible capacity of c.a. 150 mAh/g within the voltage range of 2.5 to 4.3 V. Furthermore, the material shows superior characteristics for larger capacities when compared to $LiMn_2O_4$ and for better thermal stability when compared to $LiNiO_2$. This material is considered to be Li_2MnO_3-based solid solutions containing Ni. In this study, we have investigated the Fe^{3+} containing compositions, $Li[Li_{1/3-x/2}\ Fe_{3x/2}Mn_{2/3-x}]O_2$ with layered NaCl-type structure. It is of great important to understand the charging/discharging mechanism proceeding by Li-extraction/insertion. We have employed the variety of measurement techniques and specifically, examined the crystal structure and electronic structure using X-ray, neutron diffraction and XAFS measurements. In this study, the electronic structural changes were observed by XANES spectra of Fe, Mn L-edges and O K-edge respectively and the charging behavior was examined.

Experiment

$Li[Li_{1/3-x/2}\ Fe_{3x/2}Mn_{2/3-x}]O_2$ was prepared by co-precipitation method. $LiOH{\cdot}H_2O$ and precipitates of Fe, Mn hydroxides were mixed and then calcinated at 600°C for 12h. The obtained powders were pressed and sintered at 700-900°C for 12h in air. De-lithiated samples were electrochemically and chemically prepared. The former was used by coin-type cells with Li/1M LiPF6 in PC:DMC(1:1)/samples and the latter was by the chemical oxidants, ammonium persulfate as the following reaction:

$$S_2O_8^{2-} + 2e^- \rightarrow 2\ SO_4^{2-}$$

$$Li_{1.2}Fe_{0.4}Mn_{0.4}O_2 \rightarrow Li_{1.2-x}Fe_{0.4}Mn_{0.4}O_2 + xLi^+ + xe^-$$

X-ray absorption measurements at the Fe, Mn L-edges and O K-edge by total electron yield were performed on BL4B and BL8B1.

Results

Figures 1 and 2 show the selected XANES spectra of Fe L-edge for chemically and electrochemically oxidized $Li_{1.2-x}Fe_{0.4}Mn_{0.4}O_2$ respectively. The notation from CdeLi1 to CdeLi3 corresponds to the reaction time of 0.1 to 1.0 h at various steps. A remarkable difference is observed between these two results. As the samples are oxidized, a shift towards higher energy is clearly observed for chemically oxidized, but not for electrochemically.thresholds, which are completely absent from the ion yield spectrum. A similar enhancement of the neutral particle yield is observed around the N 1s ionization Electrochemical reaction occurs from the surface of the electrode. In contrast, chemical oxidation reaction proceeds throughout the sample. This result will strongly support the electrochemical properties for this material which shows a large irreversible capacity in the initial cycle. It indicates that an inhomogeneous reaction may occur on the surface of cathode materials.

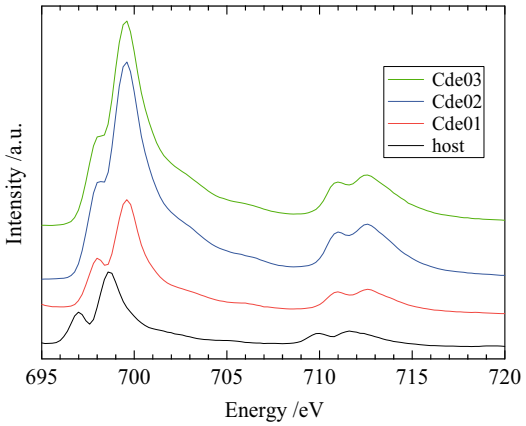

Fig.1. Fe L-edge XANES spectra of chemically oxidized $Li_{1.2-x}Fe_{0.4}Mn_{0.4}O_2$.

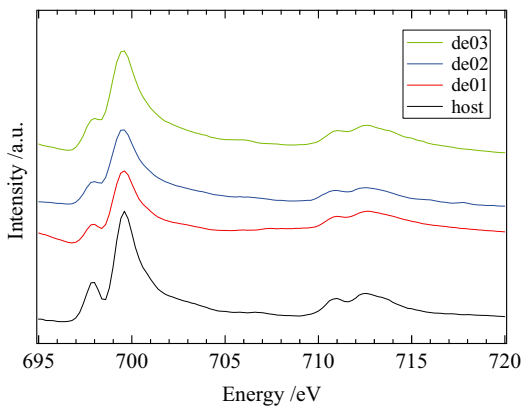

Fig. 2. Fe L-edge XANES spectra of electrochemically oxidized $Li_{1.2-x}Fe_{0.4}Mn_{0.4}O_2$.

BL4B

XAFS Study on the Surface Structures of the Positive Electrodes for High Power-Type Lithium-Ion Battery Cells

M. Shikano and H. Nitani

Research Institute for Ubiquitous Energy Devices, AIST, Ikeda, Osaka 563-8577, Japan

Introduction

Lithium-ion battery is one of the key component of fuel cell vehicles (FCVs), hybrid electric vehicles (HEVs), plug-in HEVs (PHEVs), and battery electric vehicles. In particular, for FCV, HEV and PHEV application, high specific power (> 1–2 kW/kg), long calendar life (> 10 years) and safety are very important requirements. In our previous work, degradation mechanism of lithium-ion batteries for HEV usage has been studied by various analyzing techniques and we concluded that the major factor of power fade was degradation of positive electrode structure near the surface [1-4]. However, the mechanism of degradation of the positive electrodes is still poorly understood. Detailed analysis on the structural changes of electrode material is essential in order to determine the origin of the degradation of battery performance.

In this study, $LiNiO_2$-based positive electrodes ($Li(NiCoAl)O_2$) in the initial cells were examined by X-ray absorption fine structure (XAFS) measurements to obtain information on the surface of the positive electrode.

Experimental

Cylindrical lithium-ion cells were used in this study. After adjusting the state of charge (SOC) of cell, the cells were disassembled under dry argon atmosphere in order to obtain materials. The obtained positive electrodes were washed by DMC and then dried under vacuum. Then the washed electrodes were cut into small pieces and fixed onto the aluminum plate by carbon tape.

XAFS spectra of these positive electrodes were measured at UVSOR BL4B for Co and Ni *L*III-edge. All measurements were performed with Total Electron Yield (TEY) technique by measuring the sample current in vacuumed chamber at room temperature. Obtained XAFS spectra data were processed with Athena 0.8.057 software.

Results

Figure 1 shows typical Co and Ni *L*III-edge X-ray absorption near-edge structure (XANES) spectra obtained of the positive electrodes. We could obtain good spectrum with very high energy-resolution. Especially, the double peak structure was clearly observed in Ni *L*III-edge spectrum. This feature means that Ni atoms existed with mixed atomic valences in the electrode sample. Furthermore, we found that the shape of this double peak drastically changes depends on the SOC of battery cell before disassembling (figure is not shown). The more detailed structural analysis and *ab initio* calculation are in progress in order to understand these changes in the XANES spectra.

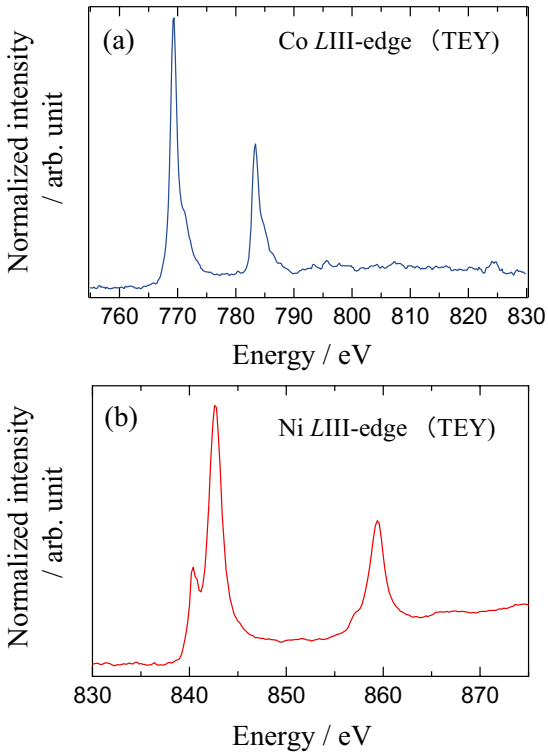

Fig. 1. (a) Co *L*III-edge and (b) Ni *L*III-edge XANES spectra of positive electrode (SOC90%).

[1] H. Kobayashi, M. Shikano, S. Koike, H. Sakaebe and K. Tatsumi, J. Power Sources **174** (2007) 380.
[2] M. Shikano, H. Kobayashi, S. Koike, H. Sakaebe, E. Ikenaga, K. Kobayashi and K. Tatsumi, J. Power Sources **174** (2007) 795.
[3] M. Rahman and Y. Saito, J. Power Sources **174** (2007) 889.
[4] Y. Saito and M. Rahman, J. Power Sources **174** (2007) 877.

BL5B

Photoinduced Change in the Total Photoyield of Amorphous Materials by Irradiation of Bandgap Light

K. Hayashi

Department of Electrical and Electronic Engineering, Gifu University, Gifu 501-1193, Japan

Introduction

The photoinduced change in photoconductivity during and after irradiation of bandgap light has been observed in many amorphous materials. [1, 2] This phenomenon is usually called the photodegradation and is explained in terms of photoinduced metastable defects. The creation of defects is a serious problem in the device application of these materials. The photodarkening is also a well-known phenomenon in amorphous chalcogenide materials. The photodarkening is a parallel shift to the optical absorption edge to lower energy side after irradiation of bandgap light. This darkened state is removed by annealing near the glass-transition temperature. The x-ray diffraction and the volume change of the films before and after irradiation of bandgap light suggest that photodarkening is due to a change of the local structure of the amorphous network. [3-5] Although a large number of studies have been done on the photoinduced phenomena, details of their underlying mechanisms are still not clear. Understanding the physical mechanisms of their underlying metastability is one of the fundamental problems associated with these materials.

The measurement of the total photoyield at the vacuum ultra-violet region is a powerful tool for the study of the energy structure. The photoyield will reflect optical absorption and the photoconductivity of the material. In this report, we investigate photoinduced change in the total photoyield of amorphous chalcogenide films.

Experimental

Thin films of amorphous chalcogenide materials (a-As_2S_3 and a-As_2Se_3) were prepared onto quartz substrates which fabricated Au electrodes by conventional evaporation technique. A typical thickness of an amorphous film was around 300 nm. The samples were annealed at the almost glass-transition temperature for two hours in a vacuum. A xenon arc lamp with IR-cut-off filter was used as a bandgap light source. The measurements of the total photoyield were performed at room temperature at the BL5B beam line of the UVSOR facility. The VUV light was fixed to the wavelength that was able to excite 3d core level of As atom of each material. To eliminate the higher order light from the monochromator, an aluminum thin film and a pinhole of 1.5 mm in a diameter were inserted between the monochromator and sample. We also monitored the intensity of the VUV light by measuring the total photoyield of two gold meshes.

Results and Discussion

Figure 1 shows the photoinduced change in the total photoyield of an a-As_2S_3 film by irradiation of bandgap light. This figure is obtained by normalizing the photoyield by the incident photon flux measured with Au mesh (Au-U) of the upstream. As shown in the figure, after irradiation of bandgap light the photoyield is gradually increased and it seems to be finally saturated. This change is similar to the previous report [6] in the total photoyield by irradiation of VUV light from the undulator light source. The relation among this photoyield change, the photodegradation, and the photodarkening will be more clarified in the next step.

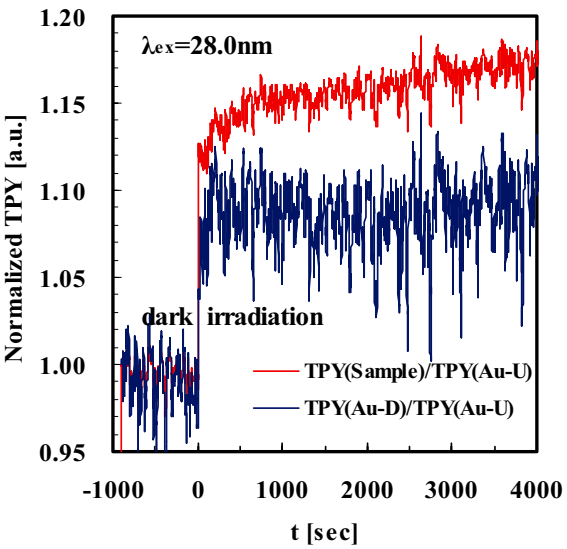

Fig. 1. The photoinduced change in the total photoyield of an a-As_2S_3 film by irradiation of bandgap light.

Acknowledgements

This work was partly supported by Saijiro Endo Memorial Foundation for Science & Technology.

[1] D. L. Staebler and C.R. Wronski, Appl. Phys. Lett. **31** (1977) 292.
[2] K.Shimakawa, S.Inami and S.R. Elliott, Phys. Rev. B **42** (1990) 11857.
[3] K. Tanaka, Rev. Solid State Sci. **4** (1990) 641.
[4] J. P. De Neuvile, S.C. Moss and S. R. Ovsinsky, J. Non-Cryst. Solids **13** (1973/1974) 191.
[5] A. J. Lowe, S. R. Elliot and G. N. Greaves, Philos. Mag. B **54** (1986) 483.
[6] K. Hayashi, UVSOR Activity Report **25** (1998) 118.

BL5B

Characterization of Novel Oxide Multilayer Reflectors at "Water-Window" Wavelengths Fabricated by Atomic Layer Epitaxy

H. Kumagai[1], Y. Masuda[1], Y.Tanaka[1], T. Shinagawa[2] and A. Kobayashi[1]

[1]*Graduate School of Engineering, Osaka City University, Sumiyoshi-ku, Osaka 558-8585, Japan*

[2]*Inorganic Materials Lab., Osaka Municipal Technical Research Institute, Joto-ku, Osaka 536-8553, Japan*

Since Barbee et al. successfully demonstrated near-normal-incidence (θ=15.5°) soft-x-ray reflectors with high reflectances of 67% at 17.0 nm using 20-bilayer Mo/Si multilayers deposited by magnetron sputtering [1], there have been various studies on the fabrication of soft-x-ray multilayer reflectors using electron beam evaporation and ion beam, rf and dc magnetron sputtering deposition. In particular, development of high-performance normal-incidence multilayer optics for the water-window wavelength region between the oxygen and carbon K absorption edges at 2.33 and 4.36 nm, respectively, where water is relatively transmissive and organic materials are absorptive, has been a technical challenge of great interest. The extremely small periods (1.2-2.2 nm) of soft-x-ray reflectors require very rigorous specifications to be met with respect to interface roughness and interlayer mixing, because interface roughness on an atomic scale has a substantial effect on soft-x-ray reflectance. Therefore, the highest reflectance achieved at water-window wavelengths (θ=3.18 nm) and near normal incidence (θ=9°) has been 3.3% [2], in spite of the various efforts which have been made in this field. The reason that the reflectances achieved at these wavelengths are so low is that the Fresnel coefficients of materials are so small at these wavelengths that a large number of bilayers must be used, which means that the problems of interface roughness and imperfect interfaces due to interlayer mixing become serious.

The authors have proposed the use of a novel metal oxide multilayer for soft-x-ray reflectors at water-window wavelengths [3], because an oxide multilayer can prevent the formation of an alloy at the interface, and the absorption of oxygen in oxides is negligible at the water-window wavelengths; moreover, the metal oxide multilayer can be fabricated by the atomic layer deposition or atomic layer epitaxy technique. These techniques can be used to control surfaces on an atomic scale by sequentially dosing the surface with appropriate chemical precursors and then promoting surface chemical reactions which are inherently self-limiting. We have found that the self-limiting adsorption mechanism works in the fabrication of oxide thin films such as aluminum oxide and titanium oxide. And we reported that we have experimentally demonstrated high reflectance of over 30% at a wavelength of 2.734 nm and an incident angle of 71.8° from the normal incidence using novel metal oxide multilayers of titanium oxide and aluminum oxide fabricated by the atomic layer deposition method of controlled growth with sequential surface chemical reactions.

In this study, the authors also demonstrated that novel oxide superlattice structures of crystalline ZnO/ TiO_2 on sapphire substrates were fabricated for high-reflection multilayer mirrors at 2.734 nm. Theoretical calculations also indicated that these structures could give high reflectance over 50% at the wavelength. In the experimental study, both rutile TiO_2 (200) and wurtzite ZnO (0001) thin films were grown epitaxially on the same sapphire (0001) substrates by atomic layer epitaxy (ALE) at 450°C. We demonstrated for the first time that the novel oxide superlattice structure of 10-bilayer ZnO/ TiO_2 on a sapphire substrate gave high reflectance of 33% at a wavelength of 2.734 nm, as shown in Fig. 1.

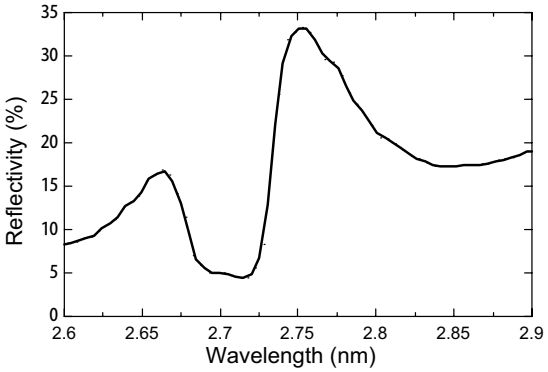

Fig. 1. Experimental reflectances of the ALE-grown 10-bilayer ZnO/ TiO_2 structure on a sapphire (0001) substrate. θ=86°.

[1] T. W. Barbee, Jr. *et al*., Appl. Opt. **24** (1985) 883.
[2] J. F. Seely *et al*., Appl. Opt. **32** (1993) 3541.
[3] H. Kumagai *et al*., Appl. Phys. Lett. **70** (1997) 2338.

BL5B

Measurement of Absolute Efficiency for Micro Channel Plates by Using Pure-Calibrated EUV Beam

G. Ogawa, K. Yoshioka, G. Murakami and I. Yoshikawa
Department of Earth and Planetary Science, Graduate School of Science, The University of Tokyo, Tokyo 113-0033, Japan

Introduction

We study to optically observe the Earth's plasmasphere, which is filled with cold plasmas (mainly H+, He+, O+ and electrons). The He+ and O+ ions have resonance scattering emission lines in the extreme ultraviolet region, at 30.4nm (HeII) and 83.4nm (OII) respectively. The intensity of each emission is proportional to column density of each scattered particle under the assumption of the optically thin condition.

EUVI (Extremity Ultra-Violet Imager) for the ISS-IMAP mission (Ionosphere, Mesosphere, upper Atmosphere and Plasmasphere mapping onboard the International Space Station) is under development. The instrument consists of two detectors, EUVI-HeII and EUVI-OII. The former observes resonantly-scatted light from He+ and the latter observes resonantly-scatted light from O+ in the plasmasphere. Both of them have band-pass filters and micro channel plates (MCPs), and look for the direction of the earth's limb. So, they can take images of the distribution of those ions in the plasmasphere over the limb.

The ISS-IMAP mission can make long-term (more than half year) and steady observations of the vertical and horizontal structure of the plasmasphere by using EUV light that cannot be observed on the ground. Furthermore, it can take images with higher special resolution comparing to the conventional spacecraft missions because the orbit of the ISS is closer to the plasmasphere than that of the other missions. So the ISS-IMAP mission will make up the interactions of the solar wind magnetic field variations and plasma transportation such as the supply from the ionosphere, pilling up and the ejection of the plasmas in the plasmasphere.

It is very important to get the absolute efficiency of the instrument in order to grasp the plasma density properly. In this experiment, we measure the quantum efficiency of the MCPs, which we use as the standard detector, at 30.4nm line.

Measurement and Result

We install an Al/C (1201Å/54Å) filter on the entrance of the SOR beam to eliminate the multi-order lines from 30.4nm line with PGM35. At first, we investigate the purity of the 30.4nm line through the Al/C filter. We judge the purity from the consistency between the wavelength characteristics of an Al/C filter for the particular lines at the EUV facilities of Institute of Space and Astronautical Science (ISAS) and those for the continuous lines at UVSOR. The former is measured for the emission lines of the helium gas with the discharge light source. Figure 1 shows the transmittances of the filter measured at ISAS and UVSOR. It is clear that both profiles of the filter are consistent in the wavelength region of 20-50nm. We interpret from the result that the pure 30.4nm can be introduced through the Al/C filter by using PGM35.

With the available pure 30.4nm line, then we measure the quantum efficiency of the MCPs. The quantum efficiency is calculated by the rate of the MCPs count to the electron yield of the photo diode which is absolutely calibrated. The result of the measurement shows that the quantum efficiency of the MCPs is 11.3% at 30.4nm line.

For the next step, in addition to the 30.4nm line, we plan to measure the quantum efficiency at the 83.4nm line, which is another observational object of EUVI. Then the purity of 83.4nm line is essential, and must be investigated for the next machine time.

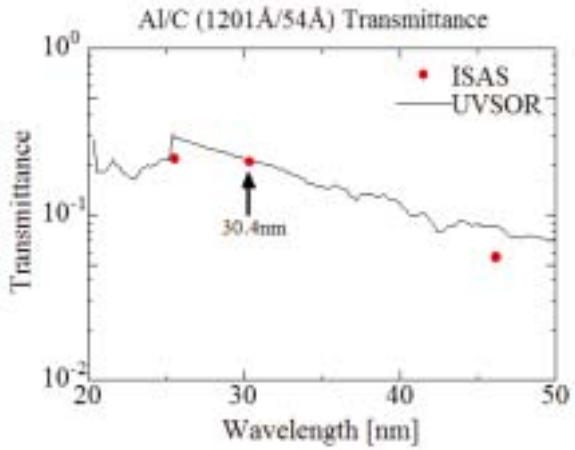

Fig. 1. The transmittance of an Al/C (1201Å/54Å) filter. The red dots show the results of the measurements at the EUV facility of ISAS and the solid line shows that at UVSOR.

[1] G. Murakami, K. Yoshioka, K. Hikosaka, A. Yamazaki and I. Yoshikawa, UVSOR activity report **34** (2007) 47.
[2] K. Yoshioka, G. Murakami, T. Toyota, G. Ogawa, A. Yamazaki and I. Yoshikawa, UVSOR activity report **35** (2008) 55.

BL6B

Far-Infrared Reflective Study of Alkali Niobate Ceramics

H. Matsudo, Y. Inagaki, T. Sumi, I. Kagomiya and K. Kakimoto
Graduate School of Engineering, Nagoya Institute of Technology, Showa-ku, Nagoya 466-8555, Japan

Introduction

$(Na_{0.5}K_{0.5})NbO_3$-$LiNbO_3$ (LNKN) is one of promising candidates of lead-free piezoelectric material because it shows the excellent piezoelectric property of d_{33}=235 pC/N when the Li content is 6.0 mol% [1]. The phase transition of LNKN varied with the content of Li, and it is considered that the phase transition between tetragonal and orthorhombic exist at the Li content of 5-7 mol% range at room temperature. LNKN undergoes the temperature-dependent successive phase transition. In our previous study, phase transition of LNKN was studied by using Raman scattering to clarify the origin of good piezoelectric property [2,3]. In this study, IR reflectivity of LNKN ceramics was measured in order to understand the effect of Li incorporation against the lattice vibration of LNKN.

Experimental procedure

The ceramic samples were sintered by the ordinal solid state reaction method. In this study, $Li_{0.06}(Na_{0.5}K_{0.5})_{0.94}NbO_3$ (L6) and $Na_{0.5}K_{0.5}NbO_3$ (NKN) were used for IR reflective study. The ceramics were polished to become specular surfaces.

Reflectivity far-infrared spectra of L6 and NKN ceramic samples were obtained at 78 and 300 K at the BL6B beam line of UVSOR. The spectra were corrected by using Michelson interferometer (Bruker, IFS66v) and synchrotron radiation source.

Result and Discussion

Figure 1 shows far-infrared reflectivity spectra of NKN at 78 and 300 K. Broad absorption was observed from 150 to 200 cm^{-1} at 300 K. This absorption was attributed by TO phonon of the vibration of Na and K ions against the NbO_6 unit. In addition, another absorption around 120 cm^{-1} was observed at 78 K. NKN shows the phase transition from rhombohedral to orthorhombic crystal structure at 125 K on heating process so that the phase transition of NKN includes the softening of translational modes of Na and K ions.

Figure 2 shows far-infrared reflectivity spectra of L6 at 78 and 300 K. The absorption of translational modes of Na and K ions were not clear and the softening of the translational modes was not observed between the spectrum at 78 K and that at 300 K in spite that the phase transition from rhombohedral to orthorhombic crystal structure exists at 270 K. In our previous study, Raman spectroscopy confirmed that NbO_6 unit receved an internal strain by increasing Li content [3]. It is believed that the distortion of NbO_6, which was induced by the small ion of Li, causes the suppression of the translational vibration of Na and K ions in unit-cell crystal structure.

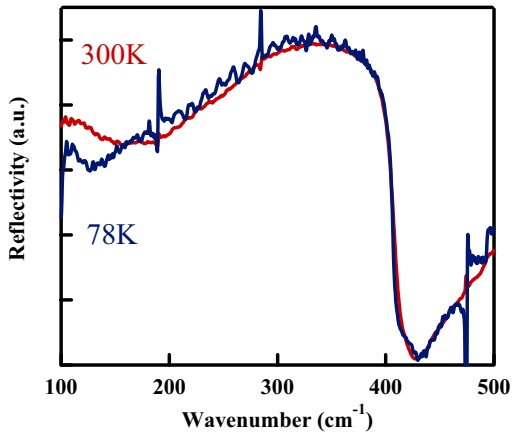

Fig. 1. Far-infrared reflectivity spectra of NKN ceramics at 78 and 300 K.

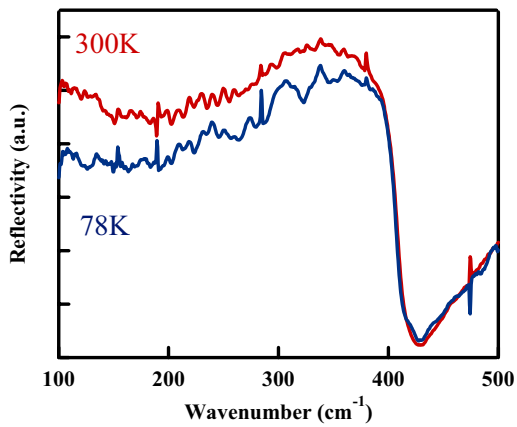

Fig. 2. Far-infrared reflectivity spectra of L6 ceramics at 78 and 300K.

Acknowledgement

This research was supported by the Industrial Technology Research Grant Program in 2007 from the New Energy and Industrial Technology Development Organization (NEDO) of Japan.

[1] Y. Guo, K. Kakimoto and H. Ohsato, Appl. Phys. Lett. **85** (2002) 4121.
[2] K. Kakimoto, K. Akao, Y. Guo and H. Ohsato, Jpn. J. Appl. Phys. **44** (2005) 7064.
[3] T. Hotta, K. Kakimoto and H. Ohsato, Key Eng. Mater. **368-372** (2008) 1893.

BL7B

Characterization of Highly Efficient Dye Sensitized Solar Cells Using Synchrotron Radiation

K. Nakajima[1, 2], H. Yagi[2], C. Huang[2], H. Katayanagi[2] and K. Mitsuke[2]
[1]*Science Research Center, Hosei University, Tokyo 102-8160, Japan*
[2]*Department of Photo-Molecular Science, Institute for Molecular Science, Okazaki 444-8585, Japan*

About two decades ago Grätzel et al. [1] first invented the dye sensitized solar cell (DSSC) with energy conversion efficiency of more than 10 %. Thereafter many relevant works have been reported, but significant improvement in the efficiency has not been achieved yet. In the present study we assembled DSSCs using a Ru dye and made them irradiated with monochromatized synchrotron radiation to observe electron injection process occurring at the interface between the dyes and semiconductor nanoparticles. The measurements of photoabsorption cross sections and output short-circuit currents by irradiation of synchrotron light allowed us to determine an incident photon-to-current efficiency (IPCE) of the DSSC and an absorbed photon-to-current efficiency (APCE) of the dye. The IPCE is calculated from the number of electrons $J_{SC}S/e$ fed into an external circuit divided by that of incident photons on the cell, $\Phi_P=I_PS=PS/h\nu$. The APCE is derived from $J_{SC}S/e$ divided by the number of photons absorbed by the sensitizer dye $\Delta\Phi_P$. Here, J_{SC} is the density of the output short-circuit current, S is the area of the DSSC, e is the elementary charge, I_P is the intensity of the incident photon, and P is the power density of the synchrotron radiation.

The DSSC was prepared as follows. Titanium dioxide TiO_2 paste (nanoparticles, 18 nm in diameter) was applied on an FTO glass by screen printing, and sintered at 450°C for 30 min. After soaking the glass in a Ru dye solution (N3 or N719), iodide electrolyte (PN-50 or AN-50) was dropped on the TiO_2 electrode which was combined with a counter electrode glass covered with Pt. Our DSSC exhibits a maximum energy conversion efficiency of about 7 %.

Figure 1 (a) shows an IPCE curve obtained from J_{SC} and Φ_P. Since the curve is in accordance with the curve (b) that was obtained using an instrument dedicated for the IPCE measurements (Peccell: PEC-S20DC), it was confirmed that synchrotron radiation can be used for the measurement of IPCE even though its flux is 2 – 3 orders of magnitude lower than that of the Xe lamp fitted in the above instrument. An IPCE value was improved to 0.7 when the layer of TiO_2 film is thicker than 16 μm. Figure 2 shows the two APCE curves calculated in different ways of estimation of $\Delta\Phi_P$, according as whether the scattered light in the TiO_2 film is partly absorbed by dye (b) or not (a). It is clear that such a reabsorption may favorably take place in a shorter wavelength and contributes to electron injection from the dye. The quantum yield of the electron injection is evaluated to be unity at shorter wavelengths, whereas it gradually decreases in longer wavelength.

The energy conversion efficiency of the DSSC will be improved when an appropriate conductive glass is selected and the best condition for sintering of a TiO_2 film is established. We are planning to observe fluorescence from the dye molecules adsorbed on several semiconductor films to study the rate of electron injection to TiO_2 film from the dye.

This research was partly supported by a grant from Hosei University.

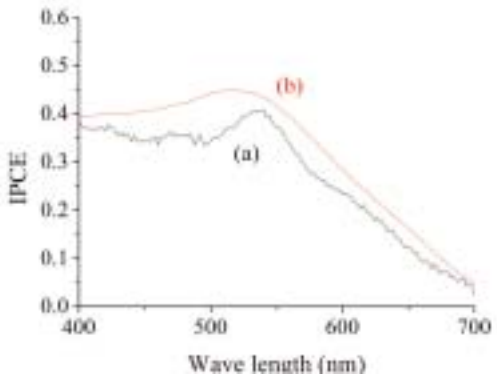

Fig. 1. IPCE curves obtained by (a) synchrotron radiation and (b) the PEC-S20DC spectrometer.

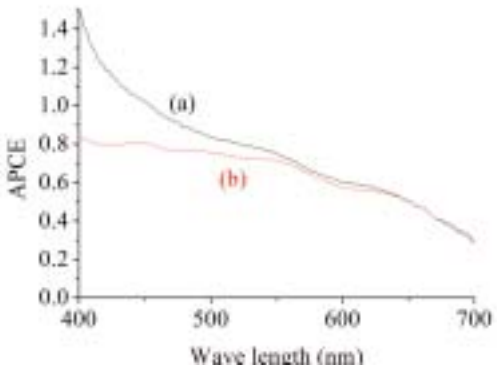

Fig. 2. Variation of APCE curves in different estimation of photons absorbed by dye.

[1] B. O'Regan, M. Grätzel, Nature **353** (1991) 737.

BL7B

Reflection Measurement on Si/W/Co and Si/W/C Multilayers for Use in 50-110 nm Region

T. Ejima[1], F. Suzuki[2], K. Fukui[2], M. Yanagihara[1], Z. Wang[3], J. Zhu[3], L. Bai[3], Z. Zhang[3], Q. Huang[3], J. Xu[3], X. Wang[3] and M. Watanabe[4, 5, 6]

[1]*IMRAM, Tohoku University, Sendai 980-8577, Japan*

[2]*Faculty of Engineering, University of Fukui, Fukui 910-8507, Japan*

[3]*Institute of Precision Optical Engineering, Tongji University, Shanghai 200092, China*

[4]*Shanghai Dianji University, Shanghai 200240, China*

[5]*Institute for Composite Materials, Shanghai Jiaotong University, Shanghai 200240, China*

[6]*Venture Business Laboratory, Saga University, Saga 840-8402, Japan*

High normal-incidence reflectivity mirrors with a flat top in 50–110 nm region are required not only for usual spectroscopy, but also some diagnosis of plasma. In this region, monolayers of Au, Pt and W are used as coating materials. Their reflectivity is about 30% and decreases around 50 nm down to 20% or less. The reflectivity of monolayer of SiC is higher than 40%, but the high reflectivity region is limited above 60 nm. Therefore, special multilayers are required to obtain such high reflectivity in this region. Composite multilayers consisting of a top single layer and piled periodic double layers have been developed to extend the region of reflectivity of more than 15% down to 30 nm [1], but their reflectivity around 50 nm is 20%. In this study, availability of non-periodic multilayers [2] has been investigated.

The multilayers were $[Si/W/Co]_2$ and $[Si/W/Co]_2$. Here the subscript "2" means 2 trilayers of different layer thicknesses. In both multilayers, the top layers were Si layers and the substrates were Si wafer. The multilayers were designed to have high reflectivity of 40–50% in this region at incident angle of 5°, which has not been obtained so far. In $[Si/W/Co]_2$, the designed value of layer thickness was respectively 8.96, 11.57, 6.07, 19.01, 12.47 and 11.68 nm from the top Si layer, and in $[Si/W/Co]_2$, 9.41, 3, 15.83, 23.48, 3, 14.42 nm. They were fabricated by magnetron sputtering at Tongji University. Near normal incidence reflectivity was measured at BL7B, which is equipped with a 3 m McPherson type monochromator. The p-reflectivity was measured at incident angles of 20° and 30°.

Figures 1 and 2 show the experimental and calculated reflectivity of $[Si/W/Co]_2$ and $[Si /W/C]_2$ multilayers for incident angle of 20°. The reflectivity was measured with good reproducibility. The calculated reflectivity is smaller at incident angle of 20° than 5°. It is due to the measurement of p-reflectivity. The experimental results at incident angle of 20° show the reflectivity of 50–60% of the calculated values. For investigation of this reason, the X-ray diffraction measurements on the multilayers were made to determine the actual layer thicknesses. It was found that the actual thicknesses did not deviate much more from the designed value except the top layers. On the top layers, about 2 nm SiO_2 layers were found. Taking into account this fact, the recalculation was performed and the discrepancy between experimental value and calculated value was well explained. It is an important subject of the next step how to reduce the amount of SiO_2.

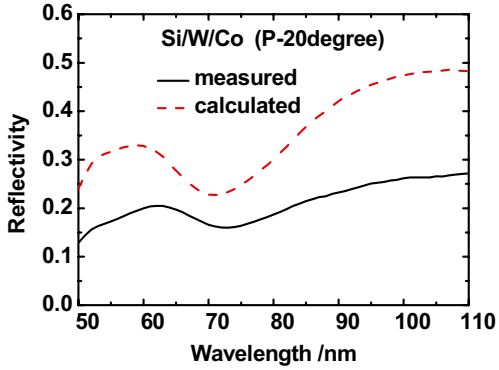

Fig. 1. Calculated and measured reflectivity of Si/W/Co multilayer at incident angle of 20°.

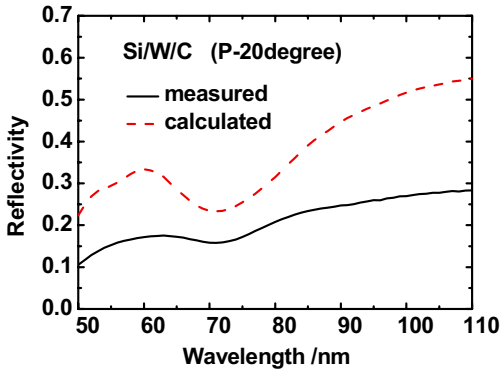

Fig. 2. Calculated and measured reflectivity of Si/W/C multilayer at incident angle of 20°.

[1] Y. Kondo *et al*, Nucl. Instr. Meth. A **467-468** (2001) 333.

[2] Z. Wang *et al*., J. Appl. Phys. **99** (2006) 056108.

List of Publications

M. Fujita, M. Itoh, T. Katagiri, D. Iri, M. Kitaura and V. B. Mikhailik, **"Optical Anisotropy and Electronic Structures of $CdMoO_4$ and $CdWO_4$ Crystals: Polarized Reflection Measurements, X-Ray Photoelectron Spectroscopy, and Electronic Structure Calculations"**, Phys. Rev. B **77** (2008) 155118.

Y. Hikosaka, T. Kaneyasu and E. Shigemasa, **"Formation of Metastable Fragments around the Cl 2p Ionization Thresholds of HCl"**, J. Korean Phys. Soc. **53** (2008) 3898.

Y. Hikosaka, P. Lablanquie, E. Shigemasa, T. Aoto and K. Ito, **"Sub-natural Linewidth Spectroscopy on Core-valence Doubly Ionized States of OCS"**, J. Phys. B: At., Mol. Opt. Phys. **41** (2008) 025103.

N. Hosaka, H. Yamada, Y. Shimada, J. Fujioka, S. Bordács, I. Kézsmárki, M. Kawasaki and Y. Tokura, **"Magneto-Optical Characterization on the Ferromagnetic-Paramagnetic Transitions in the Composition-Spread Epitaxial Film of $Sr_{1-x}Ca_xRuO_3$"**, Appl. Phys. Express **1** (2008) 113001.

H. J. Im, T. Ito, H. D. Kim, S. Kimura, K. E. Lee, J. B. Hong, Y. S. Kwon, A. Yasui and H. Yamagami, **"Direct Observation of Dispersive Kondo Resonance Peaks in a Heavy-Fermion System"**, Phys. Rev. Lett **100** (2008) 176402.

T. Inushima, K. Fukui, H. Lu and W. J. Schaff, **"Phonon Polariton InN Observed by Infrared Synchrotron Radiation"**, Appl. Phys. Lett. **92** (2008) 171905.

A. Irizawa, K. Sato, M. Kobayashi, K. Shimai, T. Murakami, H. Okamura, T. Nanba, M. Matsunami, H. Sugawara and H. Sato, **"Electronic State of $PrFe_4P_{12}$ under High Pressure Probed by Infrared Spectroscopy"**, Physica B **403** (2008) 948.

A. Irizawa, M. Kobayashi, K. Satoh, T. Nanba, L. Chen, T. Matsumoto, M. Matsunami, M. Ito, T. Suzuki and S. Nagata, **"Study on Cross-Over Change from Metal to Insulator in the Electronic States of Copper-Spinel Compounds under High Pressure"**, J. Phys. Soc. Jpn. **76** (2007) 13.

M. Ishii, T. Yoshida and K. Sakurai, **"X-Ray Excited 3.2 eV Luminescence from Amorphous Silica: Radiative Electron Relaxation Through an Unidentified Centre and Its Thermal Switching"**, J. Phys.:Codens. Matter **20** (2008) 255249.

M. Itoh, T. Katagiri, H. Mitani, M. Fujita and Y. Usuki, **"Comparative Study of Excitonic Structures and Luminescence Properties of $Bi_4Ge_3O_{12}$ and $Bi_{12}GeO_{20}$"**, Phys. Status Solidi B **245** (2008) 2733.

K. Kanda, J. Igaki, R. Kometani, S. Matsui and H. Ito, **"Characterization of High Nitrogen Content-Amorphous Carbon Nitride Films Using NEXAFS Spectroscopy"**, Diamond Rel. Mater. **17** (2008) 1755.

K. Kanda, N. Yamada, M. Okada, J. Igaki, R. Kometani and S. Matsui, **"Graphitization of Thin Films Formed by Focused-Ion-Beam Chemical-Vapor-Deposition"**, Diamond Rel. Mater. **18** (2009) 490.

T. Kaneyasu, M. Ito, Y. Hikosaka and E. Shigemasa,
"Stability and Fragmentation of OCS^{2+} Studied by Using Auger-Electron-Ion Coincidence Measurement", J. Korea. Phys. Soc. **54** (2009) 371.

H. Katayanagi, B. P. Kafle, J. Kou, T. Mori, K. Mitsuke, Y. Takabayashi, E. Kuwahara and Y. Kubozono, **"The 4*d*-4*f* Dipole Resonance of the Pr Atom in an Endohedral Metallofullerene, $Pr@C_{82}$"**, J. Quant. Spectrosc. Radiat. Transfer **109** (2008) 1590.

T. Kawai, **"Influence of the Next-Nearest-Neighbor Cations on Tl^+ Ions Doped in Ammonium Chloride Crystals"**, J. Phys. Soc. Jpn. **77** (2008) 094705.

T. Kawai and N. Ohno, **"Optical Studies of Hydrogen-Bonded Dielectrics TlH_2PO_4"**, Phys. Status Solidi C **6** (2009) 350.

S. Kimura, T. Iizuka and Y. Kwon, **"Origin of Middle-Infrared Peaks in Cerium Compounds"**, J. Phys. Soc. Jpn. **78** (2009) 013710.

M. Kitaura, **"Photoluminescence in $YPO_4:Mn^{2+}$ Codoped with Various tetravalent Cations Excited by VUV Radiation"**, Proceedings of The 15th International Display Workshop'08 **2** (2008) 947.

M. Kitaura and A. Ohnishi, **"Photoluminescence of Forsterite Single Crystals Excited by Vacuum Ultraviolet Radiation"**, Phys. Status Solidi C **6** (2009) 236.

H. Komoto and T. Takeuchi, **"Large Thermoelectric Power of $La_{2-x}Sr_xCuO_4$ Possessing Two-Dimensional Electronic Structure"**, J. Electron. Mater. (2009) 6 (*in press*).

K. Kurihara, T. Yanagawa, N. Nakagawa, K. Fukui and A. Yamamoto, **"Temperature Dependence of Infrared Reflectance Spectra of InN"**, Infrared Phys. Tech. **51** (2008) 482.

K. Kurihara, K. Fukui, T. Yanagawa and A. Yamamoto, **"Infrared Micro Optical Reflectance Spectra of InN"**, Phys. Status Solidi C **5** (2008) 1759.

M. Labat, G. Lambert, M. E. Couprie, M. Shimada, M. Katoh, M. Hosaka, Y. Takashima, T. Hara and A. Mochihashi, **"Coherent Harmonic Generation Experiments on UVSOR-II Storage Ring"**, Nucl. Instrum. Methods Phys. Res., Sect. A **593** (2008) 1.

M. Labat, H. Hosaka, A. Mochihashi, M. Shimada, M. Katoh, G. Lambert, T. Hara, Y. Takashima and M. E. Couprie, **"Coherent Harminic Generation at UVSOR-II Storage Ring"**, Eur. Phys. J. D **44** (2007) 187.

M. Labat, M. Hosaka, M. Shimada, N. Yamamoto, M. Katoh and M. E. Couprie, **"Observation of Synchrotron Sidebands in a Storage-Ring-Based Seeded Free-Electron Laser"**, Phys. Rev. Lett. **102** (2009) 014801.

M. Labat, M. Hosaka, M. Shimada, M. Katoh and M. E. Couprie, **"Optimization of a Seeded Free-Electron Laser with Helical Undulators"**, Phys. Rev. Lett. **101** (2008) 164803.

C. I. Lee, K. E. Lee, Y. Y. Song, H. J. Im, S. Kimura and Y. S. Kwon, **"Hybridization Gap-Open in $CeIn_3$"**, Infrared Phys. Tech. **51** (2008) 488.

K. E. Lee, C. I. Lee, H. J. Oh, M. A. Jung, B. H. Min, H. J. Im, T. Iizuka, Y. S. Lee, S. Kimura and Y. S. Kwon, **"Optical Properties of the Charge-Density-Wave Compound $CeTe_2$"**, Phys. Rev. B **78** (2008) 134408.

K. E. Lee, C. I. Lee, H. J. Oh, H. J. Im, T. Park, S. Kimura and Y. S. Kwon, **"Optical Evidence for a Change in the Heavy Electron Fermi Surface at a Magnetic Quantum Critical Point of $CeNi_{1-x}Co_xGe_2$"**, J. Phys.: Condens. Matter **20** (2008) 285202.

X. D. Ma, T. Nakagawa, Y. Takagi, M. Przybylski, F. M. Leibsle and T. Yokoyama, **"Magnetic Properties of Self-Assembled Co Nanorods Grown on Cu(110)-(2×3)N"**, Phys. Rev. B **78** (2008) 104420.

Y. Matsumoto, S. Sakai, Y. Takagi, T. Nakagawa, T. Yokoyama, T. Shimada, S. Mitani, H. Naramoto and Y. Maeda, **"X-Ray Absorption Spectroscopy and Magnetic Circular Dichroism in Codeposited C_{60}-Co Films with Giant Tunnel Magnetoresistance"**, Chem. Phys. Lett. **470** (2009) 244.

M. Matsunami, A. Chainani, M. Taguchi, R. Eguchi, Y. Ishida, Y. Takata, H. Okamura, T. Nanba, M. Yabashi, K. Tamasaku, Y. Nishino, T. Ishikawa, Y. Senba, H. Ohashi, N. Tsujii, A. Ochiai and S. Shin, **"Combining Photoemission and Optical Spectroscopies for Reliable Valence Determination in YbS and Yb Metal"**, Phys. Rev. B **78** (2008) 195118.

T. Mizoguchi, A. Seko, M. Yoshiya, H. Yoshida, T. Yoshida, W. Y. Ching and I. Tanaka, **"X-Ray Absorption Near-Edge Structures of Disordered $Mg_{1-x}Zn_xO$ Solid Solutions"**, Phys. Rev. B **76** (2007) 195125.

T. Mizuno, T. Iizuka, S. Kimura, K. Matsubayashi, K. Imura, H. S. Suzuki and N. K. Sato, **"Excitonic Instability in the Transition from the Black Phase to the Golden Phase of SmS under Pressure Investigated by Infrared Spectroscopy"**, J. Phys. Soc. Jpn. **77** (2008) 113704.

D. Mori, H. Kobayashi, M. Shikano, H. Nitani, H. Kageyama, S. Koike, H. Sakaebe and K. Tatsumi, **"Bulk and Surface Structure Investigation for the Positive Electrodes of Degraded Lithium-Ion Cell After Storage Test Using X-Ray Absorption Near-Edge Structure Measurement"**, J. Power Sources **189** (2009) 676.

M. Nagasaka, T. Hatsui and N. Kosugi, **"Exchange Interaction in Kr 3d Excitations of**

Small Krypton Clusters", J. Electron Spectrosc. Relat. Phenom. **166** (2008) 16.

K. Nakagawa, Z. Jin, I. Shimoyama, Y. Miyake, M. Ueno, Y. Kishigami, H. Horiuchi, M. Tanaka, F. Kaneko, H. Nishimagi, H. Kobayashi and Masahiro Kotani, **"Evolution of Energy Deposition Processes in Anthracene Single Crystal from Photochemistry to Radiation Chemistry under Excitation with Synchrotron Radiation from 3 to 700 eV"**, Radiat. Phys. Chem. **77** (2008) 1156.

T. Nakagawa, Y. Takagi, Y. Matsumoto and T. Yokoyama, **"Enhancements of Spin and Orbital Magnetic Moments of Submonolayer Co on Cu(001) Studied by X-Ray Magnetic Circular Dichroism Using a Superconducting Magnet and Liquid He Cryostat"**, Jpn. J. Appl. Phys. **47** (2008) 2132.

K. Nakata, T. Kubo, C. Numako, T. Onoki and A. Nakahira, **"Synthesis and Characterization of Silicon Doped Hydroxyapatite"**, Mater. Trans. **50 (5)** (2009) 1046.

Y. Nakayama, S. Machida, T. Minari, K. Tsukagoshi, Y. Noguchi and H. Ishii, **"Direct Observation of the Electronic States of Single Crystalline Rubrene under Ambient Condition by Photoelectron Yield Spectroscopy"**, Appl. Phys. Lett. **93** (2008) 173305.

T. Ogawa, S. Shima, T. Kaneko, K. Kobayashi, J. Takahashi, H. Mita, M. Hosaka and M. Kato, **"Asymmetric Synthesis and Decompoosition of Amino Acids by Circularly Polarized Light from Free Electron Laser"**, Origins of Life and Evolution of Biospheres (2009) (*in press*).

K. Ohgushi, Y. Okimoto, T. Ogasawara, S. Miyasaka and Y. Tokura, **"Magnetic, Optical, and Magnetooptical Properties of Spinel-Type ACr_2X_4 (A = Mn, Fe, Co, Cu, Zn, Cd; X = O, S, Se)"**, J. Phys. Soc. Jpn. **77** (2008) 034713.

J. Onoe, T. Ito and S. Kimura, **"Time Dependence of the Electronic Structure of an Electron-Beam-Irradiated C_{60} Film"**, J. Appl. Phys. **104** (2008) 103706.

A. A. Popov, V. M. Senyavin, V. I. Korepanov, I. V. Goldt, A. M. Lebedev, V. G. Stankevich, K. A. Menshikov, N. Yu. Svechnikov, O. V. Boltalina, I. E. Kareev, S. Kimura, O. Sidorova, K. Kanno and I. Akimoto, **"Vibrational, Electronic, and Vibronic Excitations of Polar $C_{60}F_{18}$ Molecules: Experimental and Theoretical Study"**, Phys. Rev. B **79** (2009) 045413.

Md. S. I. Prodhan, H. Katayanagi, C. Huang, H. Yagi, B. P. Kafle and K. Mitsuke, **"Velocity Map Imaging Apparatus Applicable to a Study of Multiple Photofragmentation of C_{60}"**, Chem. Phys. Lett. **469** (2009) 19.

Y. Y. Song, K. E. Lee, J. B. Hong, H. J. Im, S. Kimura and Y. S. Kwon, **"Dramatic Change of Optical Properties at a Quantum Critical Point in the Heavy Fermion System $CeNi_{1-x}Co_xGe_2$"**, Infrared Phys. Tech. **51** (2008) 485.

A. Tanaka, N. Takashima, M. Imamura, T. Kitagawa, Y. Murase and H. Yasuda, **"Surface Chemistry of Alkyl-Passivated Silicon Nanoparticles Studied by Synchrotron-Radiation Photoemission Spectroscopy"**, J. Phys. Soc. Jpn. **77** (2008) 094701.

A. Tanaka, N. Takashima, M. Imamura, Y. Murase and H. Yasuda, **"Electronic Structure and Surface Chemistry of Alkyl-Passivated Si Nanoparticles"**, J. Phys.: Conference Series **100** (2008) 052086.

H. Yagi, K. Nakajima, K. R. Koswattage, K. Nakagawa, C. Huang, Md. S. I. Prodhan, B. P. Kafle, H. Katayanagi and K. Mitsuke, **"Photoabsorption Cross Section of C_{60} Thin Films from the Visible to Vacuum Ultraviolet"**, Carbon **47** (2009) 1152.

T. Yokoyama, T. Nakagawa and Y. Takagi, **"Magnetic Circular Dichroism for Surface and Thin Film Magnetism: Measurement Techniques and Surface Chemical Applications"**, Int. Rev. Phys. Chem. **27** (2008) 449.

T. Yamamoto, Y. Kawashima, Y. Kusakabe, S. Matsuda, Y. Mizuoka, Y. Nakade and T. Okajima, **"Local Environment Analysis of Dopants in Ceramics by X-Ray Absorption Near-Edge Structure with the Aid of First-Principles Calculations"**, J. Phys. :Codens. Matter **21** (2009) 104211.

(in Japanese)
M. Katoh, T. Hara and M. Hosaka, **"Generation of Short Wavelength Coherent Radiation with Seeding"**, J. Jpn. Soc. Synchro. Rad. Res. **20 (4)** (2007) 226.

M. Katoh, M. Shimada, A. Mochihashi, M. Adachi, M. Hosaka, Y. Takashima and N. Yamamoto, **"Studies on Coherent Synchrotron Radiation at UVSOR-Ⅱ"** , J. Jpn. Soc. Synchrotron Radiat. Res. **21 (5)** (2008) 262.

"BL1B to BL3B" Kickoff Meeting

Dec. 2, 2008
Room 201, IMS Research Facilities Building

9:30	Reception	
10:00	Strategy etc.	N. Kosugi (Director UVSOR)
10:10	Beamline Optics of BL1B, 7B and 7U	S. Kimura (UVSOR)
10:30	User Research I : Oxides and Fluorides	T. Kawai (Osaka Pref. Univ.)
10:55	Coffee Break	
11:05	User Research II : Phosphors	M. Kitaura (Fukui Nat. Col. Tech.)
11:30	User Research III : Fullerenes	K. Mitsuke (IMS)
11:45	User Research IV : VUV detectors	T. Saito (AIST)
12:00	Lunch	
13:00	Research Surveys in VUV Region at Other Facilities	M. Itoh (Sinshu Univ.)
13:25	Spectroscopic Techniques for Normal Incidence Region	T. Ejima (Tohoku Univ.)
13:50	Coffee Break	
14:00	Discussion	Facilitator : K. Fukui (Univ. Fukui)

"BL1A to BL2A" Kickoff Meeting

Dec. 17, 2008
Room 304, UVSOR Facility

9:30	Strategy etc.	N. Kosugi (Director UVSOR)
10:00	User Research I : Structural Analysis of Catalytically Active Mo Species for GTL by Mo L-Edge XANES	H. Aritani (Saitama Inst. Tec. Univ,)
10:30	User Research II : Oscillator Strength Distribution of Biomolecules at the X-Ray Energy Range	K. Nakagawa (Kobe Univ.)
11:00	Coffee Break	
11:15	User Research III : Local Environment Analysis of Dopants in Functional Materials	T. Yamamoto (Waseda Univ.)
11:45	Lunch	
12:45	User Research IV : Attempts at the Band Structure Studies for the Compound Semiconductors Using Core Absorption and Core Excitation-Band to Band Photoluminescence Measurements	K. Fukui (Univ. Fukui)
13:15	User Research V : Analyses of Trace Components in Solid Materials Using by X-Ray Absorption and X-Ray Excited Optical Luminescence Spectra	T. Yoshida (Nagoya Univ.)
13:45	Discussion	Facilitator : T. Yoshida (Nagoya Univ.)

UVSOR Lunch Seminar

FY2008

Apr. 16 Prof. Iwao Matsuda, Institute for Solid State Physics, the University of Tokyo
Spin-split bands of Ag quantum film induced by Rashba effect at a surface

May 7 Dr. Masanori Tsunekawa, Research Center for Materials Science, Nagoya University and UVSOR
Probed bulk electronic structures of transition metal compounds by soft x-ray photoemission

Jun. 18 Prof. Tomoko Yoshida, Graduate School of Engineering, Nagoya University
XANES analysis of functional solid materials

Jul. 22 Prof. H. W. Yeom, Department of Physics, Yonsei University, Korea
Atomic Wires on Surfaces: metal-insulating transitions and electron correlation

Jul. 30 Prof. Takeo Ejima, Institute of Multidisciplinary Research for Advanced Materials, Tohoku University
Probing depth control of x-ray spectroscopies using phase measurement of standing wave: application to the Fe/Si interface

Nov. 12 Dr. Hojun Im, UVSOR Facility, Institute for Molecular Science
Electronic structure of strongly correlated Ce 4f-electrons systems

Nov. 25 Prof. Faris Gel'mukhanov, Royal Institute of Technology, Stockholm, Sweden
Lifetime broadening free X-ray absorption spectroscopy

Feb. 5 Dr. Tatsuo Kaneyasu, SAGA Light Source
Introduction of SAGA-LS

Feb. 10 Prof. Augusto Marcelli, Laboratori Nazionali Frascati INFN, Italy
IKNO a new user facility for coherent THz synchrotron radiation

Mar. 11 Prof. Kazuhiko Mase, KEK-PF
PF-BL13A project to develop a high brilliance VSX beamline for study of organic thin-films and biological molecules

Mar. 18 Dr. Takahiro Ito, UVSOR Facility, Institute for Molecular Science
Electronic structure of strongly correlated electron systems studied by three-dimensional angle-resolved photoemission spectroscopy at UVSOR-II BL5U and BL7U

Seminars